

Hydrodynamic Design Optimization of Wave Energy Converters Consisting of Heaving Point Absorbers

Griet De Backer

Dissertation submitted to obtain the academic degree of
Doctor of Civil Engineering

Supervisor:

prof. dr. ir. J. De Rouck
Coastal Engineering Division
Department of Civil Engineering
Faculty of Engineering
Ghent University
Technologiepark Zwijnaarde 904
B-9052 Zwijnaarde, Belgium
<http://awww.ugent.be>

Supervisor:

prof. dr. ir. M. Vantorre
Maritime Technology Division
Department of Civil Engineering
Faculty of Engineering
Ghent University
Technologiepark Zwijnaarde 904
B-9052 Zwijnaarde, Belgium
<http://www.maritiem.ugent.be>



Everything should be made as simple as possible but no simpler.

ALBERT EINSTEIN

Contents

Samenvatting	xi
Summary	xvii
List of Abbreviations	xxi
List of Symbols	xxiii
Glossary	xxvii
List of Publications	xxix
Introduction	3
1 Theoretical background	11
1.1 Introduction	11
1.2 Hydrodynamics	12
1.2.1 Fluid mechanics	12
1.2.2 Regular progressive waves	15
1.2.3 Wave-Body interactions	16
1.2.4 Pressures and forces	19
1.3 Point absorbers	21
1.3.1 Mass-spring-damper system	21
1.3.2 Equation of motion of a heaving point absorber	25
1.3.3 Power absorption	29
1.3.4 Absorption width	30
1.3.5 Phase control	33
2 Frequency domain modelling	37
2.1 Introduction	38
2.2 Concept	40
2.3 WAMIT	41

2.3.1	WAMIT input	41
2.3.2	WAMIT output	43
2.4	Design parameters	44
2.4.1	Buoy geometry	44
2.4.2	Wave climate	45
2.5	Hydrodynamic parameters	47
2.6	Power absorption	48
2.6.1	Response in irregular waves	48
2.6.2	Implementation of restrictions	51
2.6.3	Influence of design parameters	55
2.6.4	Influence of restrictions	61
2.7	Conclusion	69
3	Time domain model: implementation	75
3.1	Introduction	75
3.2	Equation of motion	76
3.3	Implementation	78
3.3.1	Prony's method	78
3.3.2	Selection of exponentials	79
3.4	Time domain solver	81
3.5	Conclusion	84
4	Experimental validation of numerical modelling	89
4.1	Introduction	90
4.2	Experimental setup	91
4.2.1	Wave flume	91
4.2.2	Scale model	91
4.2.3	Design parameters	95
4.2.4	Wave climate	96
4.3	Results	99
4.3.1	Decay tests	99
4.3.2	Heave exciting wave forces	101
4.3.3	Power absorption tests	103
4.4	Conclusion	122

5	Performance of closely spaced point absorbers with constrained floater motion	127
5.1	Introduction	128
5.2	Methodology	130
5.2.1	Equation of motion	130
5.2.2	Constraints	131
5.2.3	Optimization strategies	133
5.3	Case study specifications	135
5.3.1	Configuration	135
5.3.2	Wave climate	137
5.4	Results	138
5.4.1	Unconstrained	138
5.4.2	Constrained	139
5.5	Conclusion	150
6	Water impact on axisymmetric bodies: laboratory drop tests	155
6.1	Introduction	156
6.2	Slamming pressures and forces	159
6.2.1	Pressures	159
6.2.2	Vertical Slamming Forces	162
6.3	Experimental design	166
6.3.1	Test setup and test objects	166
6.3.2	Instrumentation	170
6.4	Experimental test results	174
6.4.1	Water uprise and impact velocity	174
6.4.2	Pressure distribution, impact velocity and deceleration	180
6.4.3	Comparison between shapes	187
6.4.4	Peak pressure	187
6.5	Conclusion	194
7	Large scale outdoor bottom slamming tests	201
7.1	Introduction	201
7.2	Test setup	202
7.3	Instrumentation	205
7.3.1	Pressure sensor and accelerometer	205
7.3.2	High speed camera	207
7.3.3	Data acquisition and synchronization	207

7.4	Test results	208
7.4.1	Visualization of impact phenomena	208
7.4.2	Pressure distribution, impact velocity and deceleration	208
7.4.3	Peak Pressures	212
7.5	Conclusion	221
8	Influence of constraints to reduce bottom slamming	225
8.1	Introduction	226
8.2	Different levels of slamming restrictions	226
8.3	Probability of emergence	234
8.4	Conclusion	240
9	Conclusion and future research	245
9.1	Discussion and conclusion	245
9.2	Recommendations for future research	248
9.2.1	Further improvements on the control and optimization process	248
9.2.2	Further research on multiple point absorbers	249
	Appendices	251
A	Steady-state solution of a mass-spring-damper system	253
B	Formulas for a floating reference case	257
B.1	Equation of motion	257
B.2	Restrictions	259
B.2.1	Slamming restriction	259
B.2.2	Stroke restriction	260
B.2.3	Force restriction	260
C	Simulation results	261
C.1	Constraint case 1	262
C.2	Constraint case 2	269
C.3	Constraint case 3	276
D	Prony's method	283
E	Reflection analysis	285

F	Test matrices	289
F.1	Decay tests	289
F.2	Heave exciting wave forces	289
F.3	Power absorption tests	290
F.3.1	Regular waves	290
F.3.2	Irregular waves	294
G	Large scale drop test results	297
G.1	Overview of performed tests	297
G.2	Drop test measurements	302
G.2.1	Buoy with foam	302
G.2.2	Buoy without foam	307

Samenvatting

Inleiding

De wereldwijde energieproblematiek wordt momenteel frequent onder de aandacht gebracht. Gedurende de voorbije decennia is de vraag naar energie aanzienlijk toegenomen. De Europese Unie importeert circa 50 % van haar energie en er wordt verwacht dat dit cijfer zal stijgen tot 70 % in 2030. Dit brengt de Europese Unie in een afhankelijke en dus economisch kwetsbare positie. Het grootste deel van die energie-import bestaat bovendien uit fossiele brandstoffen, die bijdragen tot de opwarming van de aarde. Een van de antwoorden om deze problemen tegen het lijf te gaan, ligt in de exploitatie van hernieuwbare energiebronnen. Hoewel grote hoeveelheden energie beschikbaar zijn in de oceaangolven, is golfenergie waarschijnlijk de minst gekende hernieuwbare energiebron. Er werden reeds verschillende conversietechnologieën uitgevonden, waaronder overtoppingssystemen, oscillerende waterkolommen en point-absorbersystemen. Point-absorbersystemen bestaan uit kleine boeien die oscilleren in de oceaangolven. Door het dempen van hun beweging wordt elektriciteit geproduceerd. Zoals windmolens in parken geïnstalleerd worden, is het ook de bedoeling om point-absorbersystemen in een park te plaatsen om grotere vermogens te leveren. Sommige toestellen zijn zelfs opgebouwd uit verschillende, interagerende point-absorbers, die geïntegreerd zijn in één eenheid.

Probleemstelling en doelstellingen

Point-absorbers worden vaak afgestemd ('getuned') op de karakteristieken van de invallende golffrequenties om de vermogensabsorptie te verhogen. Deze tuning vergroot de boeibewegingen aanzienlijk. In sommige vroegere onderzoeken werden point-absorbers ofwel gemodelleerd zonder tuning, wat resulteerde in ontgoochelende vermogensabsorptiewaarden, ofwel werd tuning wel beschouwd, maar lag de focus vaak op de maximalisatie van de vermogensabsorptie in onbegrensde condities. Dit leidt tot extreem grote

boei-uitwijkingen en kan er zelfs voor zorgen dat de vlotter uit het water rijst. Wanneer de vlotter terug in het water treedt, kan hij onderhevig zijn aan ‘slamming’, een verschijnsel dat geassocieerd is met grote impactdrukken en -krachten. Naast dit probleem, kan ook de geldigheid van de vaak gebruikte lineaire theorie in vraag gesteld worden in deze gevallen.

Om te grote vlotteruitwijkingen, excessieve controlekrachten en slammingproblemen te vermijden, werden in dit werk verschillende praktische beperkingen opgelegd op de vlotterbeweging. De invloed van deze restricties op de optimale controleparameters en op de vermogensabsorptie werd onderzocht voor geïsoleerde en meerdere, dicht bij elkaar geplaatste point-absorbersystemen. Ten tweede werd de geldigheid van de lineaire theorie, voor de beschrijving van de vlotterbeweging, geëvalueerd aan de hand van fysische modelproeven. Tot slot werden de effecten van slamming meer in detail bestudeerd, in het bijzonder met betrekking op drukken en krachten alsook voorkomensfrequenties van slamming. Het doel hiervan is om realistische, toereerbare slammingniveaus te formuleren.

Methodologie en resultaten

Numerieke modellen in het frequentie- en tijdsdomein werden ontwikkeld, die het hydrodynamisch gedrag beschrijven van dompende point-absorbers in regelmatige en unidirectionele onregelmatige golven. Het model is gebaseerd op lineaire theorie en het krijgt input in verband met de hydrodynamische parameters van het commerciële pakket WAMIT, dat gebaseerd is op de randelementenmethode. De point-absorber wordt extern geregeld door middel van een lineaire dempingskracht en een lineaire tuningskracht. Het frequentiedomeinmodel werd gebruikt om de vermogensabsorptie te optimaliseren voor verschillende vlottergeometrieën, rekening houdend met bepaalde beperkingen. Het tijdsdomeinmodel werd aangewend om de voorkomensfrequenties van slamming onder de loep te nemen voor verschillende vlottervormen en slammingrestricties. De numerieke modellen werden **gevalideerd door middel van fysische modelproeven** met een dompende point-absorber in de golfgoet van het Waterbouwkundig Laboratorium in Antwerpen. Een goede overeenkomst werd gevonden tussen de experimentele resultaten en de resultaten van de numerieke modellering. In regelmatige golven is de overeenkomst goed buiten de resonantiezone. In onregelmatige golven die typische golfklassen op het Belgisch Continentaal Plat voorstelden, overschatten de

numerieke simulaties het experimenteel geabsorbeerde vermogen slechts met 10 % tot 20 %, afhankelijk van de vlottervorm. Bijgevolg produceren de numerieke modellen bevredigende resultaten voor die toepassingen die van belang zijn.

Met het frequentiedomeinmodel werden numerieke simulaties in onregelmatige golven uitgevoerd voor **variërende geometrische parameters**, zoals de vlotterdiameter, de diepgang en de vorm. Een grotere vlotterdiameter geeft aanleiding tot een behoorlijke stijging van de vermogensabsorptie, terwijl variaties in de vlotterdiepgang de vermogensextractie slechts beperkt beïnvloeden. Voor eenzelfde diameter (gemeten aan de waterlijn) en diepgang is de vermogensabsorptie bij een conische boei met een tophoek van 90° slechts 4 % tot 8 % beter dan bij een hemisferische boei. Aangezien de hydrodynamische performantie vrij gelijkaardig blijkt te zijn voor vormen die dezelfde dimensies hebben en die geassocieerd zijn met kleine visceuze verliezen, kan verwacht worden dat andere aspecten, zoals slammingskrachten, membraanactie en materiaalkosten, mogelijk een meer dominante invloed zullen hebben op de finale vormlayout dan de hydrodynamische performantie van de vorm.

Zoals reeds eerder vermeld, werden bepaalde **restricties** in rekening gebracht in het optimalisatieproces van het geabsorbeerd vermogen. De geïmplementeerde restricties zijn slammingsrestricties, slaglengterestricties en restricties op de controlekracht. De eerste restrictie is bedoeld om de voorkomingsfrequentie te verminderen van het fenomeen waarbij de boei uit het water rijst. De slaglengterestrictie beperkt de maximale uitwijking van de vlotter en de krachtrestrictie vermindert de controlekrachten voor het geval waarbij deze door de generator worden geleverd. Algemeen leiden deze beperkingen tot een verhoging van de demping en een verlaging van de tuning, waarmee bedoeld wordt dat de vlotter verder buiten de resonantiezone wordt gehouden. Deze maatregelen resulteren in kleinere vermogensabsorptiewaarden dan de optimale waarden die kunnen bereikt worden zonder restricties.

Slammingverschijnselen hangen enorm af van de evenwichtsdiepgang van de vlotter. Indien een voldoende diepgang kan voorzien worden in vergelijking met de relatieve beweging van de vlotter ten opzichte van de golven, zullen slammingverschijnselen zelden voorkomen. Indien echter - om eender welke reden- de vlotterdiepgang toch vrij klein is, is het raadzaam

om een vlottervorm te kiezen die slechts kleine impactdrukken en -krachten ondervindt. Valtesten werden uitgevoerd op zowel kleine als grote schaal om slamming op point-absorbers te onderzoeken. Zoals verwacht, zijn de drukken gemeten nabij de onderkant van de hemisfeer significant groter dan deze waargenomen op de conus met een tophoek van 90° .

Wanneer de diepgang groot genoeg is, blijken realistische **slaglengte-restricties** dominant te zijn dan slammingrestricties. Een grotere slaglengte is in het bijzonder voordelig in de meer energetische golfklassen. Het is echter niet steeds praktisch haalbaar om de maximale slaglengte te vergroten, aangezien ze meestal onderhevig is aan technische restricties, zoals de beperkte hoogte van het platform waarin de vlotters zich bevinden of de beperkte grootte van hydraulische zuigers in het geval een hydraulische conversie gebruikt wordt. De gevolgen van de geïmplementeerde slaglengterestricties voor het geabsorbeerd vermogen zouden minder ernstig kunnen zijn dan in dit werk werd vastgesteld, indien een tijdsafhankelijke controle toegepast zou worden, die de vlotter extra kan afremmen wanneer zijn verplaatsing te groot dreigt te worden. In dat geval is de optimale tuning slechts negatief beïnvloed gedurende enkele kortstondige momenten, in plaats van tijdens de volledige golfklasse. Het vergt echter een zeer nauwkeurig en betrouwbaar controlesysteem.

In energetische golven met lange periodes worden de optimale **contro-lekrachten** zeer groot. De optimale tuningskracht, in het bijzonder, kan enorm groot worden in verhouding tot de benodigde dempingskracht. Als de generator verondersteld is om deze tuningskracht te leveren, zou dat kunnen resulteren in een oneconomisch ontwerp van de generator. De krachtrestrictie kan deze tuningskracht substantieel verkleinen, echter, met een aanzienlijke vermindering van de absorptieperformantie tot gevolg. Een tweede probleem dat kan opduiken, als de generator de tuningskracht levert, is dat kleine afwijkingen in de grootte en fase van deze tuningskracht nefast kunnen zijn voor het geabsorbeerd vermogen van de vlotter. Om die reden is het aan te raden de boei te tunen met een mechanisme dat onafhankelijk is van de generator, bijvoorbeeld met latching of door het toevoegen van een supplementaire massa.

Tot zover werden de ontwerpaspecten toegepast op een geïsoleerde point-absorber. In praktijk bestaan verscheidene point-absorbertoestellen uit **meerdere oscillerende vlotters**. Bijgevolg is het van belang nader te onderzoeken

hoe deze interagerende vlotter zich gedragen en wat de invloed van hun interactie is op de ontwerpparameters en op het geabsorbeerd vermogen. Configuraties van 12 en 21 dicht bij elkaar geplaatste vlotter, met een diameter van 5 m, respectievelijk 4 m, werden nader bestudeerd. Zoals verwacht is het geabsorbeerd vermogen van een vlotter in een raster met meerdere, dicht bij elkaar geplaatste vlotter gemiddeld kleiner dan dat van een geïsoleerde boei, als gevolg van het schaduweffect. Hoe strenger de restricties, hoe minder uitgesproken dit effect is, aangezien de voorste vlotter minder vermogen absorberen en er dus meer vermogen overblijft voor de achterste vlotter in het raster. Om die reden werd ook vastgesteld dat de reductie in geabsorbeerd vermogen, als gevolg van de implementatie van restricties, minder ernstig is voor een groep point absorbers dan voor één point absorber alleen. De restricties hebben een ‘afvlakkend’ effect op het geabsorbeerd vermogen van de boeien, wat betekent dat het verschil in vermogen tussen de voorste en achterste boeien in het raster vermindert naarmate de restricties strenger zijn.

Tevens bleek dat toepassing van de optimale controleparameters voor een enkele boei resulteert in een suboptimaal functioneren van de groep point absorbers. De beste performantie voor een groep werd bereikt door elke vlotter individueel te tunen, m.a.w. elke vlotter heeft zijn eigen optimale controleparameters, afhankelijk van de positie in het raster. Met deze individuele tuning en voor de vermelde configuraties, met 12 grote of 21 kleinere boeien, werd geschat dat ter hoogte van Westhinder op het Belgisch Continentaal Plat een jaarlijkse hoeveelheid energie in de grootteorde van 1 GWh geabsorbeerd kan worden.

Summary

Introduction

The global energy problem is frequently spotlighted nowadays. Over the last decades, the energy demand has considerably increased. The European Union imports approximately 50 % of its energy and this number is estimated to increase to 70 % by 2030. This puts the European Union in a dependent and hence economically vulnerable position. Most of the energy imports concern fossil fuels which contribute to global warming. One of the answers to overcome these problems lays in the exploitation of renewable energy sources. Although huge amounts of power are available in the ocean waves, wave energy is probably the least-known resource among the renewable energies. Several conversion technologies have been invented, such as overtopping devices, oscillating water columns and point absorber systems. Point absorber systems consist of small buoys oscillating in the ocean waves. By damping their motion, electricity is produced. Similar to wind energy farms, point absorbers are intended to operate in arrays to produce considerable amounts of power. Some devices are even composed of several, interacting point absorbers, integrated in one unit. The design and optimization of single and multiple, closely spaced point absorbers is the subject of this thesis.

Problem statement and objectives

Point absorbers are often tuned towards the characteristics of the incident wave frequencies to increase the power absorption. This tuning enlarges the buoy motions significantly. In some earlier research, point absorbers were either modelled without tuning, yielding disappointing power absorption numbers, or tuning was considered, but the focus often lied on power absorption maximization in unconstrained conditions. This may result in extremely large strokes and may even cause the buoy to rise out of the water and experience slamming phenomena upon re-entry. Apart from this problem, the validity of linear theory -which is often applied- can be questioned in those cases.

To avoid too large strokes, excessive control forces and slamming problems, several practical restrictions are imposed on the buoy motions in this work. The influence of those restrictions on the optimal control parameters and power absorption is assessed for single and multiple, closely spaced point absorbers. Secondly, the validity of linear theory to describe the motion of a point absorber is evaluated by means of experimental tests. Finally, the effects of slamming have been studied more in detail, in terms of pressures and loads as well as occurrence probabilities in order to obtain realistic, tolerable slamming levels.

Methodology and results

Numerical models in frequency and time domain have been developed to describe the hydrodynamic behaviour of a heaving point absorber in regular and unidirectional irregular waves. The model is based on linear theory and receives input on the hydrodynamic parameters from the commercial BEM code WAMIT. The point absorber can be externally controlled by means of a linear damping and a linear tuning force. The frequency domain model is used to optimize the power absorption for different buoy geometries, within certain constraints. The time domain model is used to assess the occurrence probabilities of emergence for different buoy shapes and slamming constraints. The numerical models have been **validated by experimental tests** with a heaving point absorber in the wave flume of Flanders Hydraulics Research in Antwerp. A good correspondence is found between the experimental results and the results from the numerical modelling. In regular waves, the agreement is good in non-resonance zones. In irregular waves, representing typical sea states on the Belgian Continental Shelf, the numerical simulations overestimated the experimental power absorption generally only with 10 % to 20 %, dependent on the shape. Hence, the numerical models produce satisfying results for those applications that are of interest.

With the frequency domain model, numerical simulations in irregular waves are run for **varying geometrical parameters**, such as the buoy diameter, draft and shape. An increase of the buoy diameter leads to a significant rise of the absorbed power, whereas variations in the buoy draft influence the power extraction only to a limited extent. For the same waterline diameter and draft, the power absorption by a conical buoy with apex angle 90° is only 4 % to 8 % better than a hemispherical buoy. Since the

hydrodynamic performance appears to be quite similar for shapes with the same size and small viscous losses, it is expected that other aspects, like slamming loads, membrane action and material costs, are likely to have a more dominant influence in the final shape layout than the hydrodynamic performance of the shape.

As mentioned earlier, the optimization process of the absorbed power takes into account certain **constraints**. The implemented restrictions are a slamming, stroke and force constraint. The first restraint is intended to reduce the occurrence probability of rising out of the water. The stroke constraint limits the maximum buoy displacement and the force constraint diminishes the control forces, in case they are to be generated by the power take-off system. The three limiting conditions are satisfied by adapting the control parameters. Generally the damping is increased and the buoy needs to be tuned away from resonance. These measures lead to smaller power absorption values than the optimal values obtained without restrictions.

Slamming phenomena depend significantly on the equilibrium draft. If a sufficient buoy draft can be provided compared to the relative motion of the buoy to the waves, slamming problems will rarely occur. If -for any reason- the buoy draft is rather small, it is advised to choose a buoy shape that experiences small impact pressures and loads. Drop tests have been performed to assess bottom slamming on small and large scale point absorber buoys. As expected, the pressures measured near the bottom of the hemisphere are significantly larger than those registered on a cone with an apex angle of 90° .

When the buoy draft is large enough, realistic **stroke restrictions** are found to be more dominant than the slamming constraints. A larger stroke length is particularly beneficial in the more energetic sea states. However, increasing the maximum stroke in the design is often practically not feasible, since it is usually determined by technical restraints, such as the limited height of the platform enclosing the floaters or the limited height of the hydraulic rams if a hydraulic conversion is used. The penalty of the implemented stroke constraints in this work could be less severe if a time-dependent control is applied which additionally brakes the floater, when its displacement becomes too large. In that case the optimal tuning is only negatively affected during some temporary time frames, instead of during the entire sea state. However, a very accurate and reliable control system is required.

In energetic waves with large periods, the optimal **control forces** become

very large. In particular the optimal tuning force might be enormous, compared to the required damping force. If this tuning force is supposed to be delivered by the power take-off system, it could result in an uneconomic design of the latter. The force restriction may reduce this tuning force substantially, however, with a serious drop in absorption performance as a consequence. A second problem that may arise if the tuning is to be provided by the power take-off, is that small deviations in the magnitude and phase of this tuning force may be pernicious for the power absorption of the buoy. For these reasons it is advised to tune the buoy with a mechanism that is independent of the power take-off, e.g. with latching or by adding a supplementary inertia.

So far, the described design aspects have been applied to a single body. In practice, several point absorber devices consist of **multiple oscillating buoys**. Hence, it is of interest to investigate how these interacting bodies behave and what the influence of their interaction is on the design parameters and power absorption. Array configurations of 12 and 21 closely spaced buoys, with diameters of 5 m and 4 m, respectively, have been studied. As expected, the power absorption of a point absorber in an array of closely spaced bodies is on average smaller than that of an isolated buoy, due to the wake effect. For more stringent constraints, this effect is less pronounced, since the front buoys absorb less power and thus more power remains available for the rear buoys in the array. For this reason, it is found that the power absorption reduction due to the implementation of constraints is less severe for an array configuration than for a single buoy. Hence, the restrictions have a ‘smoothing’ effect on the power absorption of the buoys, meaning that the difference in performance between the front and rear buoys is diminished as the constraints are more restrictive.

It is also observed that applying the optimal control parameters for a single body, results in a suboptimal performance of the array. The best array performance is obtained with individually tuned buoys, i.e. each buoy has its own optimal control parameters, dependent on the position in the array. With this individual tuning, it is estimated that the yearly energy absorption at Westhinder on the Belgian Continental Shelf of the considered arrays, with 12 large or 21 smaller buoys, is in the order of magnitude of 1 GWh.

List of Abbreviations

abs	absorption
AM	Added Mass method
BCS	Belgian Continental Shelf
BEM	Boundary Element Method
BIEM	Boundary Integral Equation Method
BWF	Buoy With Foam
BWOF	Buoy Without Foam
cc	cone-cylinder
CAD	Computer-Aided Design
CFD	Computational Fluid Dynamics
CP	Control Parameters
CPU	Central Processing Unit
DO	Diagonal Optimization
hc	hemisphere-cylinder
FEM	Finite Element Method
fps	frames per second
F2T	Frequency to Time domain
HSC	High Speed Camera
IO	Individual Optimization
ICP	Integrated Circuit Piezoelectric
IRF	Impulse Response Function
ODE	Ordinary Differential Equation
OF	Occurrence Frequency
OPSB	Optimal Parameters Single Body
OWC	Oscillating Water Column
PA	Point Absorber
PI	Pressure Integration method
PTO	Power Take-Off
RAO	Response Amplitude Operator
SEEWEC	Sustainable Economically Efficient Wave Energy Converter

SS	Sea State
SWL	Still Water Level
WEC	Wave Energy Converter
2D	two-dimensional
3D	three-dimensional

List of Symbols

A_w	waterline area = πR^2 [m ²]
b_0	wet radius at $z = 0$ [m]
b	wet radius at the immediate free water surface [m]
b_c	critical damping coefficient [kg/s]
b_d	damping coefficient [kg/s]
b_{ext}	external damping coefficient [kg/s]
\mathbf{B}_{ext}	external damping matrix (NxN) [kg/s]
b_{hyd}	hydrodynamic damping coefficient (heave mode) [kg/s]
\bar{b}_{hyd}	normalized hydrodynamic damping coefficient [kg/s]
\mathbf{B}_{hyd}	hydrodynamic damping matrix (NxN) [kg/s]
C	wave velocity [m/s]
C_f	constant factor [-]
C_g	group velocity [m/s]
C_p	slamming pressure coefficient [-]
C_r	reflection coefficient [-]
C_s	slamming coefficient [-]
C_v	coefficient of variation [-]
C_w	wetting factor [-]
d	buoy draft [m]
d_{cc}	centre-to-centre distance between neighbouring bodies [m]
d_w	water depth [m]
D	buoy waterline diameter [m]
D_f	depth function [-]
EI	bending stiffness [N/m ²]
f	frequency [Hz]
f_n	natural frequency [Hz]
f_p	peak frequency [Hz]
F	force [N]
F_{arch}	Archimedes force [N]
F_d	damping force [N]

F_{ex}	exciting force (heave mode) [N]
\bar{F}_{ex}	normalized exciting force [N]
F_g	gravity force [N]
F_{fric}	friction force [N]
F_{PTO}	control force [N]
F_{rad}	radiation force [N]
F_{res}	restoring force [N]
F_{tun}	tuning force [N]
g	gravitational acceleration [m/s ²]
h	drop height [m]
h^*	equivalent drop height corresponding to the measured impact velocity [m]
h^{**}	equivalent drop height corresponding to the measured instantaneous velocity [m]
I	identity matrix (NxN) [-]
j	imaginary unit ($\sqrt{-1}$) [-]
k	hydrostatic restoring coefficient or stiffness [kg/s ²]
k_{SS}	dimensionless value to describe impact force (Shiffman and Spencer) [-]
k_w	wavenumber [1/m]
\mathbf{K}	stiffness matrix (NxN) [kg/s ²]
K_r	radiation impulse response function [kg/s ²]
l_{jet}	jet height [m]
L	wave length [m]
H	wave height [m]
m	buoy mass [kg]
m_a	added mass (heave mode) [kg]
\bar{m}_a	normalized added mass (for heave motion) [kg]
$m_{a,\infty}$	high frequency limit of the added mass (for heave motion) [kg]
m_{br}	mass to brake the buoy motion [kg]
m_{sm}	small mass (used to estimate the friction force) [kg]
m_{sup}	supplementary mass [kg]
m_{tot}	total mass [kg]
\mathbf{M}	buoy mass matrix (NxN) [kg]
\mathbf{M}_a	added mass matrix (NxN) [kg]
\mathbf{M}_{sup}	supplementary mass matrix (NxN) [kg]

N	number of buoys [-]
\mathbf{n}	vector normal to body surface [-]
n_f	number of frequencies [-]
p	pressure [bar = 10^5 Pa]
p_0	arbitrary constant in Bernoulli's equation [bar = 10^5 Pa]
P_{abs}	absorbed power [W]
$P_{abs,av}$	average power absorption [W]
P_{avail}	available power (per m crest length) [W/m]
$P_{avail,D}$	available power over the device width D [W]
q	ratio of maximum power absorption by N interacting bodies to N isolated bodies [-]
\tilde{q}	power absorption ratio of N interacting bodies and N isolated bodies in suboptimal conditions [-]
r	radial coordinate [m]
R	radius of hemisphere - waterline radius of point absorber [m]
R_*	Pearson correlation coefficient [-]
R_b	distance to body [m]
S_{FA}	force amplitude spectrum [N^2s]
S_{z_A}	buoy displacement amplitude spectrum [m^2s]
S_{ζ}	wave amplitude spectrum [m^2s]
t	time [s]
T	period [s]
T_n	natural period [s]
T_p	peak period [s]
U	entry velocity [m/s]
U_{0m}	measured velocity at initial time step [m/s]
\mathbf{v}	velocity vector [m/s]
V	submerged buoy volume [m^3]
z	buoy position - vertical coordinate [m]
z_{pl}	platform motion [m]
\mathbf{Z}	buoy position vector (Nx1)[m]
Z_m	mechanical impedance [m/s]
Z_{rad}	radiation impedance [m/s]
β	deadrise angle [deg][rad]
β_i	angle of wave incidence [deg][rad]
β_{mot}	position phase angle [deg][rad]

$\beta_{F_{ex}}$	heave exciting force phase angle [deg][rad]
β_v	velocity phase angle [deg][rad]
γ	peak enhancement factor [-]
ζ	wave elevation, in slamming context: water elevation at intersection with body [m]
ζ_d	damping factor [-]
η	power absorption efficiency (= ratio of incident power to power available within the device width) [-]
λ_p	capture width [m]
ρ	mass density of fluid [kg/m ³]
σ	spectral width parameter [-]
ϕ	velocity potential [m ² /s]
ϕ_I	incident wave potential [m ² /s]
ϕ_R	radiation potential [m ² /s]
ϕ_D	diffraction potential [m ² /s]
ω	angular frequency [rad/s]
ω_n	natural angular frequency [rad/s]

Glossary

The glossary is partly based on the ‘Marine Energy Glossary’, developed by The Carbon Trust and Entec (2005).

Absorption efficiency	The ratio of the absorbed power to the incident power available within the width of the device (see also efficiency).
Absorption width	Width of the wave front containing the same available power as the power ‘absorbed’ by the device in the same wave climate.
Buoy	Floating body, part of a point absorber system. Its horizontal dimensions are small compared to the incident wavelengths.
Capacity factor	The ratio of the average power production of a device to the rated power production. This corresponds to the energy production during a large period of time divided by the installed capacity multiplied by the same time period.
Capture width	Width of the wave front containing the same available power as the useful power captured by the device in the same wave climate. (Capture width is sometimes used to refer to the ‘produced’ power instead of the ‘absorbed’ power.)
Efficiency	Ratio of output power to input power. However, the exact meaning is context dependent. In the context of this work, it means the ratio of the absorbed power to the incident power available within the width of the device (‘Absorption efficiency’). Component efficiencies, e.g. turbine efficiency and generator efficiency are not included. The ‘overall efficiency’ is the multiple of the absorption efficiency with the component efficiencies.

Heave	Vertical motion of object.
Ideal fluid	An inviscous fluid.
Installed capacity	The maximum power that the device can deliver, generally corresponding to the installed capacity of the generator.
Irrotational flow	Flow with zero vorticity.
Latching	A way to realize phase control. In case of point absorbers, the body is locked or 'latched' during a certain time and then released. Latching can make the buoys operate closer to or in resonance conditions and may hence increase the power absorption. It is particularly interesting for systems with a smaller natural period than the incident wave periods.
Power matrix	A table displaying the power production for different sea states. Since a sea state is characterized by a representative height (e.g. H_s) and a representative period (e.g. T_z or T_p), the power matrix has axes of height and period.
Rated power	Maximum power that can be produced, generally determined by the installed capacity of the generator.
Response amplitude operator	Frequency dependent parameter, describing the response of a system to a wave with amplitude equal to unity.
Scatter diagram	A table showing the occurrence frequencies of several sea states at a certain location. With a scatter diagram and a power matrix of a device, the yearly energy production can be determined.
Tuning ratio	Ratio of the natural period of the tuned point absorber (including the supplementary mass) to the period of the incident wave.

List of Publications

Articles in international journals

- G. De Backer, M. Vantorre, C. Beels, J. De Pré, S. Victor, J. De Rouck, C. Blommaert and W. Van Paepegem, “Experimental investigation of water impact on axisymmetric bodies,” accepted for publication in *Applied Ocean Research*, 2009.
- G. De Backer, M. Vantorre, P. Frigaard, C. Beels and J. De Rouck, “Bottom slamming on heaving point absorber wave energy devices,” conditionally accepted for publication in *Journal of Marine Science and Technology*, 2009.
- C. Beels, P. Troch, K. De Visch, J.P. Kofoed and G. De Backer, “Application of the time-dependent mild-slope equations for the simulation of wake effects in the lee of a farm of Wave Dragon wave energy converters,” accepted for publication in *Renewable Energy*, 2009.
- C. Beels, P. Troch, J. De Rouck, M. Vantorre and G. De Backer, “Numerical implementation and sensitivity analysis of a wave energy converter in a time-dependent mild-slope equation model,” submitted for publication in *Coastal Engineering*, 2008.
- C. Beels, G. De Backer and P. Matthys, “Wave energy conversion in a sheltered sea,” *Sea Technology*, vol. 49(9), pp. 21-24, 2008.

Articles in national journals

- G. De Backer, C. Beels, T. Mertens and L. Victor, “Golfenergie : groene stroom uit de zeegolven,” *De Grote Rede*, vol. 22, pp. 2-8, 2008.
- G. De Backer and T. Mertens, “Golfenergie op het Belgisch Continentaal Plat?,” *Het Ingenieursblad*, vol. 5, pp. 44-50, 2006.

Articles in conference proceedings

- G. De Backer, M. Vantorre, C. Beels, J. De Rouck and P. Frigaard, “Performance of closely spaced point absorbers with constrained floater motion,” Proceedings of the 8th European Wave and Tidal Energy Conference, Sweden, 2009.
- G. De Backer, M. Vantorre, K. De Beule, C. Beels and J. De Rouck, “Experimental investigation of the validity of linear theory to assess the behaviour of a heaving point absorber at the Belgian continental shelf,” Proceedings of the 28th International Conference on Ocean, Offshore and Arctic Engineering, Hawaii, 2009.
- W. Van Paeppegem, C. Blommaert, J. Degrieck, G. De Backer, J. De Rouck, J. Degroote, S. Matthys and L. Taerwe, “Slamming wave impact of a composite buoy for wave energy applications: design and large-scale testing,” 9th Seminar on Experimental Techniques and Design in Composite Materials, Italy, 2009.
- C. Blommaert, W. Van Paeppegem, P. Dhondt, G. De Backer, J. Degrieck, J. De Rouck, M. Vantorre, J. Van Slycken, I. De Baere, H. De Backer, J. Vierendeels, P. De Pauw, S. Matthys and L. Taerwe, “Large scale slamming tests on composite buoys for wave energy applications,” 17th International Conference on Composite Materials, United Kingdom, 2009.
- C. Beels, P. Troch, K. De Visch, G. De Backer, J. De Rouck and J.P. Kofoed, “Numerical simulation of wake effects in the lee of a farm of Wave Dragon wave energy converters,” Proceedings of the 8th European Wave and Tidal Energy Conference, Sweden, 2009.
- C. Beels, P. Troch, T. Versluys, J. De Rouck and G. De Backer, “Numerical simulation of wave effects in the lee of a farm of wave energy converters,” Proceedings of the 28th International Conference on Ocean, Offshore and Arctic Engineering, Hawaii, 2009.
- G. De Backer, M. Vantorre, J. De Pré, J. De Rouck, P. Troch, C. Beels, J. Van Slycken and P. Verleysen “Experimental study of bottom slamming on point absorbers using drop tests” Proceedings of 2nd International

Conference on Physical Modelling to Port and Coastal Protection, Italy, 2008.

- G. De Backer, M. Vantorre, S. Victor, J. De Rouck and C. Beels “Investigation of vertical slamming on point absorbers” Proceedings of 27th International Conference on Offshore Mechanics and Arctic Engineering, Portugal, 2008.
- C. Beels, P. Mathys, V. Meerschaert, I. Ydens, J. De Rouck, G. De Backer and L. Victor “The impact of several criteria on site selection for wave energy conversion in the North Sea” Proceedings of the 2nd International Conference on Ocean Energy, France, 2008.
- G. De Backer, M. Vantorre, R. Banasiak, J. De Rouck, C. Beels and H. Verhaeghe “Performance of a point absorber heaving with respect to a floating platform” Proceedings of 7th European Wave and Tidal Energy Conference, Portugal, 2007.
- G. De Backer, M. Vantorre, R. Banasiak, C. Beels and J. De Rouck “Numerical Modelling of Wave Energy Absorption by a Floating Point Absorber System” Proceedings of 17th International Offshore and Polar Engineering Conference, Portugal, 2007.
- C. Beels, J.C.C. Henriques, J. De Rouck, M.T. Pontes, G. De Backer and H. Verhaeghe “Wave energy resource in the North Sea” Proceedings of the 7th European Wave and Tidal Energy Conference EWTEC, Portugal, 2007.
- C. Beels, P. Troch, G. De Backer, J. De Rouck, T. Moan and A. Falco “A model to investigate interacting wave power devices”, pp. 94-101, Proceedings of the International Conference Ocean Energy - From Innovation to Industry, Germany, 2006.

Symposium Abstracts

- G. De Backer, “Closely spaced point absorbers with constrained floater motion,” submitted for the 10th Ph.D. Symposium FirW Ugent, Belgium, 2009.

- G. De Backer, M. Vantorre and J. De Rouck “Wave energy absorption by point absorber arrays,” submitted for the VLIZ Young Scientists’ Day, Belgium, 2009.
- G. De Backer, C. Beels and J. De Rouck “Waves in the North Sea: Powering our future,” Book of Abstracts of the VLIZ Young Scientists’ Day, Belgium, 2008.
- G. De Backer “Wave energy extraction in the southern North Sea by a heaving point absorber” Proceedings of the 1st International PhD Symposium on Offshore Renewable energy, INORE, Norway, 2007.
- G. De Backer “Wave energy extraction in the North Sea by a heaving point absorber” Book of Abstracts of the VLIZ Young Scientists’ Day, Belgium, 2007.
- G. De Backer, M. Vantorre, J. De Rouck “Numerical modelling of wave energy absorption by a floating point absorber system” Proceedings of 7th Ph.D. Symposium FirW Ugent, Belgium, 2006.

Scientific Award

- Best Poster Award, VLIZ Young Scientists’ Day, Belgium, 2007.

**HYDRODYNAMIC DESIGN OPTIMIZATION OF WAVE
ENERGY CONVERTERS CONSISTING OF HEAVING
POINT ABSORBERS**

Introduction

Situation and history

The development of renewable energy technologies is gaining considerable importance nowadays. A particular incentive for some developed regions like the European Union to stimulate the development of renewable energy applications is their vulnerable position, due to the dependence on imports of fossil fuels from other countries. A second reason is the shortage of supply of those fossil fuels and a third motivation comprehends the global warming issues. Inspired by these concerns, the European Council has set some targets in 2007 to tackle climate change and the energy problem, known as '20 20 20 by 2020'. These key targets are [1]:

- A 20 % share of renewable energy in 2020. For comparison, in 2005, only 8.5 % of the final energy consumption in the European Union was covered by renewable energy [2].
- A reduction of at least 20 % in greenhouse gas emissions by 2020 compared to the values of 1990 [3], which might rise to 30 % if other developed countries are committing to comparable emission reductions.
- A saving of 20 % in energy consumption through energy efficiency.

Renewable energy sources are defined as sources that are 'inexhaustible' or than can be replenished in a short period of time. Examples are solar, wind and geothermal energy, hydropower, biomass (wood waste, municipal solid waste and biogas) and ocean energy. Compared to other, well-established renewable energy technologies, ocean energy applications are generally still in the testing-phase or pre-commercial stage. They can be subdivided in five categories: wave energy, tidal energy, marine current, temperature gradient and salinity gradient [4]. The focus of this work lies on wave energy, which is a concentrated form of wind energy. Waves originate from wind passage over the surface of the sea.

Research on wave energy was initiated after the oil crisis in 1973. Pioneering researchers were Salter [5], Budal and Falnes [6–8] and Evans [9, 10]. Most of the research at the time was dedicated to oscillating bodies. In the 1980s, when the oil prices declined, the interest in wave energy nearly disappeared. Funding for wave energy research increased again in the late nineties, due to the Kyoto conference on the reduction of CO₂ emissions and the growing awareness of shortness and insecurity of energy supply. Up to date, several different techniques have been invented to convert the energy from the waves into electrical energy. In 2006, about 53 different wave energy technologies have been reported in [4]. They are typically classified according to the type of conversion:

- A **point absorber** consists of a buoy with horizontal dimensions that are small compared to the incident wave lengths. The buoy oscillates according to one or more degrees of freedom. Energy is absorbed by damping the buoy motion and it is converted into electricity by a generator. An example of a pitching point absorber is Salter's duck [5]. Some heaving multi-point absorber systems are the FO³ [11], the Manchester Bobber [12] and the Wave Star [13].
- An **oscillating water column** generally consists of a hollow structure that is partially submerged below the mean sea level. Due to the waves, the water level in the chamber rises and falls and the air above the water column is compressed, respectively, expanded through a turbine. The turbine is connected to a generator, which converts the mechanical energy into electrical energy. Pico power plant [14] is an example of an oscillating water column.
- An **overtopping device** captures overtopped waves in a reservoir above sea level. The water is returned to the sea through low-head turbines. Examples are the Wave Dragon [15] and the Sea Slot-cone Generator (SSG) [16].
- An **attenuator** is typically a slender, flexing device, installed parallel to the wave propagation direction. A well-known example is the Pelamis [17].

Devices that are facing the waves (installed parallel to the wave crests) are called terminators. Some oscillating water columns and overtopping

devices operate as a terminator.

- **Others.** The last category comprises all other technologies that do not fit the aforementioned descriptions. Some sources [4, 18, 19] have additional categories such as the ‘submerged device based on pressure differential’. The Archimedes Wave Swing is an example of this type, but it might also be regarded as a special, submerged point absorber.

Those numerous devices are based on a whole range of different technologies. Even within the category of point absorbers, several ideas and concepts have been launched, involving a variety of engineering disciplines. Hence, wave energy research is spread over many different topics. Since most of the concepts are not yet in a mature nor commercial stage, it might not be surprising that various aspects have not yet been fully studied up to date. This study focuses on some specific hydrodynamic design aspects and tries to highlight some important phenomena that need to be taken into account in the design process of heaving point absorber systems.

Objective and approach

Earlier research on point absorbers mainly focussed on power absorption maximization, often in unconstrained conditions. Although substantial theoretical work as well as numerical and experimental studies have been performed, almost none of the projects resulted in the construction of a prototype device. Gradually, the practical feasibility became more important, mainly through the impulse of private investors. More recently, for instance, some researchers implemented motion constraints or slamming restrictions in their control to avoid unrealistic results, e.g. [20,21]. The basis of the present work is inspired on the latter study by Vantorre, Banasiak and Verhoeven.

The aim of this research work is to optimize the design of heaving point absorbers, taking into account several realistic restrictions, originating from practical limitations. For this purpose, a numerical model has been developed in MATLAB that solves the equation of motion of heaving point absorbers in frequency and time domain. The model is fed with input on the hydrodynamic parameters, obtained with a commercial BEM code, WAMIT [22]. It has been validated by means of experimental tests in the wave flume

of Flanders Hydraulics Research. With the numerical model, the influence of the geometrical buoy parameters is investigated in irregular unidirectional waves. Furthermore, the performance of closely spaced, interacting bodies is studied for the wave conditions on the Belgian Continental Shelf. The control parameters of the different point absorbers are individually optimized, leading to a non-negligible increase in power absorption, compared to applying the optimal control parameters of a single body.

The restrictions implemented in the numerical model are stroke, control force and slamming constraints. The stroke constraint originates from mechanical limitations on the stroke of the point absorber, e.g. imposed by the limited height of a hydraulic piston. The force control restriction is introduced to decrease the control forces, particularly for the case where the tuning is to be delivered by the power take-off system. This restriction is imposed by electromechanical and/or economic limitations. The third constraint is the slamming constraint, intended to reduce the probability of the buoys to rise out of the water and being subjected to bottom slamming. This constraint is imposed by the hydrodynamic limitations and for this reason, special attention will be drawn to this phenomenon. Water-entry phenomena are associated with certain hydrodynamic pressures and loads. These impact problems are studied by means of small scale and large scale drop tests. In addition, occurrence probabilities of slamming phenomena have been assessed numerically. The hydrodynamic impacts and occurrence probabilities may serve as input for the structural design of the floater.

This PhD research is funded by a PhD grant of the Institute for the Promotion of Innovation through Science and Technology in Flanders. Some of this work has been conducted within the framework of the SEEWEC¹ project. SEEWEC is European project in which 11 different research institutions collaborated to ameliorate the design of a multiple point absorber system, called the FO³, developed by Fred Olsen Ltd. Figure 1 shows a picture of the laboratory rig, named Buldra, built on a scale 1/3.

¹SEEWEC: Sustainable Economically Efficient Wave Energy Converter, EU project within the 6th framework programme.



Figure 1: Picture of Buldra at Jomfruland, Norway. ©Fred Olsen

Outline of this work

The first Chapter of this work provides the reader with a short theoretical background. The basics of hydrodynamics theory are outlined and the fundamental principles of point absorber theory are explained. A literature review on the state of the art of the different aspects treated in this thesis, is given at the beginning of each Chapter.

In the second Chapter, the considered point absorber concept is described and an introduction to WAMIT is given. Next, the details of the frequency domain model are given. The calculation of the power absorption and implementation of the constraints are explained. Finally, simulation results for different geometrical design parameters and constraints are presented.

The third Chapter contains the implementation of the time domain model and a comparison of the outcome with the results of the frequency domain model.

Chapter four deals with the physical tests in the wave flume of Flanders Hydraulics Research in Antwerp. The hydrodynamic parameters obtained with WAMIT are compared with the experimental data obtained from decay tests and wave exciting force experiments. Performance tests in regular and irregular waves have been carried out for different buoy shapes and drafts and are used for the validation of the numerical models.

In Chapter five, the methodology to assess the performance of multiple closely spaced point absorbers is described and applied to two array configurations. Three different strategies to determine the optimal control parameters of multiple bodies are compared. The influence on the angle of wave incidence and effects of tuning errors on the array performance is assessed in this Chapter. In a last part, the yearly energy absorption at Westhinder on the Belgian Continental Shelf is estimated.

Chapter six starts with an extensive description of literature results on water-entry problems of axisymmetric bodies. Next, the laboratory test-setup and results of small scale drop tests are given. The drop tests are performed with three test objects: a hemisphere and two cones with deadrise angles of 20° and 45° .

In Chapter seven, large scale outdoor drop tests are presented. Two large composite test bodies are lifted up to 5 m by a crane and then dropped in the Watersportbaan, a canal in Ghent. The pressure, deceleration and deformation of the bodies are measured and presented.

Chapter eight combines the knowledge on bottom slamming loads with time domain simulations of oscillating point absorbers. The time domain model is used to determine occurrence probabilities of emergence and the probability of the associated impact loads for a buoy operating in three different sea states. Several levels of slamming restrictions are implemented and the required stringency of slamming constraints is evaluated.

In the final Chapter, the most important findings of this work are highlighted and some recommendations for future research are given.

Chapters 2, 4, 5, 6 and 8 are partly or nearly entirely based on peer-reviewed conference papers or journal papers.

Bibliography

- [1] European Commission, 20 20 by 2020 - Europe's climate change opportunity. Communication from the Commission to the European Parliament, the Council, the European Economic and Social Committee and the Committee of the Regions, 2008.
- [2] Nikolaos Roubanis and Carola Dahlström, Renewable energy statistics 2005. Eurostat data in focus, website: <http://epp.eurostat.ec.europa.eu>, 2007.
- [3] Boosting growth and jobs by meeting our climate change commitments, Europe Press Releases Rapid. 2008.
- [4] Review and analysis of ocean energy systems - development and supporting policies. AEA Energy & Environment on the behalf of Sustainable Energy Ireland for the IEAs Implementing Agreement on Ocean Energy Systems, 2006.
- [5] Salter S., Wave power. *Nature* 1974;249:720–724.
- [6] Budal K., Falnes J., A resonant point absorber of ocean waves. *Nature* 1975;256:478–479.
- [7] Budal K., Theory for absorption of wave power by a system of interacting bodies. *Journal of Ship Research* 1977;21:248–253.
- [8] Budal K., Falnes J., Interacting point absorbers with controlled motion, in *Power from Sea Waves*. B. Count: Academic Press, 1980.
- [9] Evans D., A theory for wave-power absorption by oscillating bodies. *Journal of Fluid Mechanics* 1976;77:1–25.
- [10] Evans D., Some analytic results for two- and three-dimensional wave-energy absorbers. B. Count: Academic Press, 1980.

-
- [11] Taghipour R., Arswendy A., Devergez M., Moan T., Efficient frequency-domain analysis of dynamic response for the multi-body wave energy converter in multi-directional waves. In: The 18th International Offshore and Polar Engineering Conference, 2008.
- [12] <http://www.manchesterbobber.com/>.
- [13] Bjerrum A., The Wave Star Energy concept. In: 2nd International Conference on Ocean Energy, 2008.
- [14] Neumann F., Winands V., Sarmento A., Pico shoreline OWC: status and new perspectives. In: 2nd International Conference on Ocean Energy, France, 2008.
- [15] Soerensen H., Hansen R., Friis-Madsen E., Panhauser W., Mackie G., Hansen H., Frigaard P., Hald T., Knapp W., Keller J., Holmén E., Holmes B., Thomas G., Rasmussen P., Krogsgaard J., The Wave Dragon - now ready for test in real sea. In: 4th European Wave Energy Conference, Denmark, 2000.
- [16] L. Margheritini D. Vicinanza P.F., SSG wave energy converter: Design, reliability and hydraulic performance of an innovative overtopping device. *Renewable Energy* 2009;34(5):1371–1380.
- [17] Pizer D., Retzler C., Yemm R., The OPD Pelamis: Experimental and numerical results from the hydrodynamic work program. In: 4th European Wave and Tidal Energy Conference, Denmark, 2000, pp. 227–234.
- [18] Callaway E., To catch a wave. *Nature* 2007;450(8):156–159.
- [19] The European Marine Energy Centre, website: <http://www.emec.org.uk/>.
- [20] Korde, Use of oscillation constraints in providing a reaction for deep water floating wave energy devices. *International Journal of Offshore and Polar Engineering* 2001;11(2):155–160.
- [21] Vantorre M., Banasiak R., Verhoeven R., Modelling of hydraulic performance and wave energy extraction by a point absorber in heave. *Applied Ocean Research* 2004;26:61–72.
- [22] WAMIT user manual: <http://www.wamit.com/manual.htm>.

CHAPTER 1

Theoretical background



In this Chapter, a theoretical background is given on hydrodynamics theory and point absorber theory in a concise way. This Chapter is particularly intended for the reader who is not familiar with these subjects. The purpose of the first part is to briefly describe the underlying theory of WAMIT, the software program used to study the wave-body interactions in the next Chapters. The basics of linear potential theory as well as the assumptions behind it are reviewed. It is clarified how the forces acting on the floating body are determined. In a second part, the solution of the differential equation, describing the motion of the oscillating body, is derived. At first, the solution for a mass-spring-damper system is considered, which is then extended for a point-absorber subjected to external control forces, such as tuning and damping forces. Finally, some important point absorber characteristics are described and explained.

1.1 Introduction

In the next Chapters, the software program WAMIT [1] will be utilized to determine the hydrodynamic forces, experienced by the oscillating point absorber. The outcome of WAMIT is used as input in the frequency and time domain models that solve the equation of motion of a controlled, heaving point absorber. Since it is essential to have a good understanding of the theory and assumptions behind the ‘black box’, some principles of hydrodynamics theory

based on linear potential theory are described in the next Sections as well as some basics about point absorbers. Further elaboration and more details can be found in the literature. A large amount of books and courses is available, particularly on hydrodynamics theory, among them [2–5].

1.2 Hydrodynamics

1.2.1 Fluid mechanics

The equation of continuity together with the Navier-Stokes equations describe the motion of a fluid. The continuity equation is based on the concept of conservation of mass, the Navier-Stokes equations are based on the conservation of momentum. The latter equations express that changes in momentum of fluid particles are dependent on an internal viscous term and on the external pressure applied on the fluid. The Navier-Stokes equations are the fundamental basis of almost all Computational Fluid Dynamics (CFD) codes. Consisting of a coupled system of non-linear partial differential equations, the Navier-Stokes equations are generally difficult and time-consuming to solve. Hence, to facilitate the practical applicability, some assumptions are often introduced. Since the purpose of this Section is to briefly describe the theory on which WAMIT is based, the emphasis is laid on linear potential theory for inviscid fluids. The assumptions made are: the fluid is incompressible and inviscid (= ideal); the flow is irrotational and the effect of surface tension is neglected.

Potential flow

In the next paragraphs, a Cartesian coordinate system is adopted with three orthogonal axes: x , y and z . The z -axis is assumed vertical and upward directing. The velocity vector of a fluid particle is indicated with the symbol $\mathbf{v} = [v_1; v_2; v_3]$. Since the flow is assumed irrotational, i.e. $\nabla \times \mathbf{v} = 0$, the velocity vector can be written as the gradient of the velocity potential, denoted by the scalar ϕ :

$$\mathbf{v} = \nabla\phi \quad (1.1)$$

Combining this equation with the equation of continuity for incompressible fluids, i.e. $\nabla \cdot \mathbf{v} = 0$, results in the Laplace equation:

$$\nabla^2\phi = \frac{\partial^2\phi}{\partial x^2} + \frac{\partial^2\phi}{\partial y^2} + \frac{\partial^2\phi}{\partial z^2} = 0 \quad (1.2)$$

Bernoulli's equation

For inviscid fluids, the Navier-Stokes equations can be simplified, resulting in equations known as the Euler equations. Integration of the latter yields Bernoulli's equation:

$$p = -\rho \frac{\partial\phi}{\partial t} - \frac{1}{2}\rho(\nabla\phi)^2 - \rho gz + p_0(t) \quad (1.3)$$

where p_0 is an arbitrary constant, that is independent of space for irrotational flow. Linearizing Bernoulli's equations leads to Eq. (1.4):

$$p = -\rho \frac{\partial\phi}{\partial t} - \rho gz + p_0(t) \quad (1.4)$$

The pressure consists of a hydrodynamic and a hydrostatic part, corresponding to the first and second term, respectively, in Eq. (1.4). In order to determine the hydrodynamic pressures, a velocity potential needs to be found that satisfies the Laplace equation (1.2). Moreover, the velocity potential must satisfy several boundary conditions. These conditions are divided in kinematic and dynamic boundary conditions and will be discussed in the next Section.

Boundary conditions

Kinematic boundary conditions

In an ideal fluid, a fluid particle located at the surface of a body at a certain time instant, will remain lying on that body surface. The fluid particle can neither go through nor come out of the body boundary. In other words, the normal velocity component of a fluid particle on a motionless solid surface must be equal to zero:

$$\frac{\partial\phi}{\partial n} = 0 \quad \text{on the body surface} \quad (1.5)$$

where \mathbf{n} denotes the unit vector normal to the body surface in the considered point. For instance on the seabed, this condition must be fulfilled for $z = -d_w$, with the water depth denoted by d_w . For a moving body, with a normal velocity

component v_n at its surface in the considered point, the boundary condition is given by:

$$\frac{\partial \phi}{\partial n} = \mathbf{v} \cdot \mathbf{n} = v_n \quad \text{on the body surface} \quad (1.6)$$

The kinematic boundary condition on the free surface expresses that a fluid particle initially lying on the free surface will remain on the free surface. This means that $z - \zeta(x, y, t)$ must be a constant at the free surface or alternatively:

$$\frac{D}{Dt}[z - \zeta(x, y, t)] = 0 \quad \text{on the free surface} \quad (1.7)$$

where the operator $\frac{D}{Dt}$ is the total derivative: $\frac{D}{Dt} = \frac{\partial}{\partial t} + v_1 \frac{\partial}{\partial x} + v_2 \frac{\partial}{\partial y} + v_3 \frac{\partial}{\partial z}$. Hence, Eq. (1.7) is equivalent with:

$$\frac{\partial \phi}{\partial z} = \frac{\partial \zeta}{\partial t} + v_1 \frac{\partial \zeta}{\partial x} + v_2 \frac{\partial \zeta}{\partial y} \quad \text{on the free surface} \quad (1.8)$$

The particle velocity components are small compared to the wave velocity and the derivatives of the wave elevation along x and y direction, i.e. $\frac{\partial \zeta}{\partial x}$ and $\frac{\partial \zeta}{\partial y}$ are also small, since the wave elevation is assumed small compared to the wave length. Hence, the products in the second and third term of Eq. (1.8) are of second order and can be omitted. This results in the linearized kinematic boundary condition:

$$\frac{\partial \zeta}{\partial t} = \frac{\partial \phi}{\partial z} \quad \text{on the free surface} \quad (1.9)$$

Dynamic boundary conditions

The dynamic boundary condition on the free surface relies on the assumption that the pressure outside the fluid is constant. This can be expressed as:

$$\frac{Dp}{Dt} = 0 \quad \text{on the free surface} \quad (1.10)$$

Substitution of the expression for the pressure (1.4) in Eq. (1.10) yields:

$$\frac{D}{Dt}(-\rho \frac{\partial \phi}{\partial t} - \rho g z + p_0(t)) = 0 \quad \text{on the free surface} \quad (1.11)$$

Combining the latter expression (1.11) with the kinematic boundary condition on the free surface, i.e. $z = \zeta(x, y, t)$, gives:

$$\frac{\partial^2 \phi}{\partial t^2} + g \frac{\partial \zeta}{\partial t} = 0 \quad \text{on the free surface} \quad (1.12)$$

If the wave amplitude is small compared to the wave length, which is assumed within linear theory, the free surface conditions may be linearized, i.e. the kinematic and dynamic boundary conditions may be applied at the still water level (SWL), instead of at $z = \zeta$, as it actually should be. Taking this linearization into account and substituting Eq. (1.9) in condition (1.12) gives the linearized boundary condition on the free surface:

$$\frac{\partial^2 \phi}{\partial t^2} + g \frac{\partial \phi}{\partial z} = 0 \quad \text{at } z = 0 \quad (1.13)$$

1.2.2 Regular progressive waves

A progressive wave travels in a particular direction and transfers energy, in contradiction to a standing wave. The first to develop the theory for linear progressive waves was Airy. The theory is based on the assumption of small amplitudes and is therefore called the small amplitude wave theory or Airy theory.

The velocity potential ϕ_I (in literature also often indicated by ϕ_0) of an incident regular progressive wave must satisfy the Laplace equation (Eq. (1.2)) and the following boundary conditions:

- the boundary condition at the seabed (Eq. (1.5))
- the boundary condition at the free surface (Eq. (1.13))

The solution for a regular, plain progressive wave is given by:

$$\phi_I = \frac{g\zeta_A}{\omega} \frac{\cosh(k_w(z + d_w))}{\cosh(k_w d_w)} \sin(k_w x - \omega t + \delta) \quad (1.14)$$

The derivation of this solution can be found in many reference works, among them in Chapter 3 of [2] and Chapter 1 of [3]. In Eq. (1.14), the gravitational acceleration is denoted by g , the amplitude of the undisturbed wave is given by ζ_A , the angular frequency of the wave is indicated with ω and the phase angle with δ . The symbol k_w is the wavenumber and is defined as:

$$k_w = \frac{2\pi}{L} \quad (1.15)$$

where L is the wavelength, that can be derived from the dispersion relation:

$$\frac{\omega^2}{g} = k_w \tanh(k_w d_w) \quad (1.16)$$

Eq. (1.16) expresses a relationship between the wave frequency and the wavelength. With linear potential theory, the dynamic wave pressure and the fluid particle velocities can be obtained. Both quantities are used to determine the mean available power per unit crest length, as the time averaged product of the hydrodynamic plus hydrostatic force and the particle velocities in the direction of the wave propagation:

$$P_{avail} = \frac{1}{T} \int_0^T \int_{-d_w}^{\zeta} p v_1 (dz \cdot 1) dt = \frac{1}{8} \rho g H^2 C_g \quad (1.17)$$

where T is the wave period, H the wave height ($= 2 \cdot \zeta_A$), C_g is the group velocity given by:

$$C_g = nC = \frac{C}{2} \left(1 + \frac{2k_w d_w}{\sinh(2k_w d_w)} \right) \quad (1.18)$$

and C is the wave velocity, defined as the ratio of the wavelength to the wave period.

The depth function D_f is introduced as:

$$D_f(k_w d_w) = 2n \tanh(k_w d_w) = \left[1 + \frac{2k_w d_w}{\sinh(2k_w d_w)} \right] \tanh(k_w d_w) \quad (1.19)$$

Substitution of Eqs. (1.16) and (1.19) in Eq. (1.17), yields the following expression for the average available wave power per unit crest length:

$$P_{avail} = \frac{\rho g^2 D_f(k d_w) \zeta_A^2}{4\omega} \quad (1.20)$$

1.2.3 Wave-Body interactions

An offshore structure that is freely floating in ocean waves has six degrees of freedom: three translational and three rotational degrees of freedom (Figure 1.1).

- Surge: horizontal, longitudinal motion along the x -axis.
- Sway: horizontal, transverse motion along the y -axis.
- Heave: vertical motion along the z -axis.
- Roll: angular motion around the x -axis.
- Pitch: angular motion around the y -axis.
- Yaw: angular motion around the z -axis.

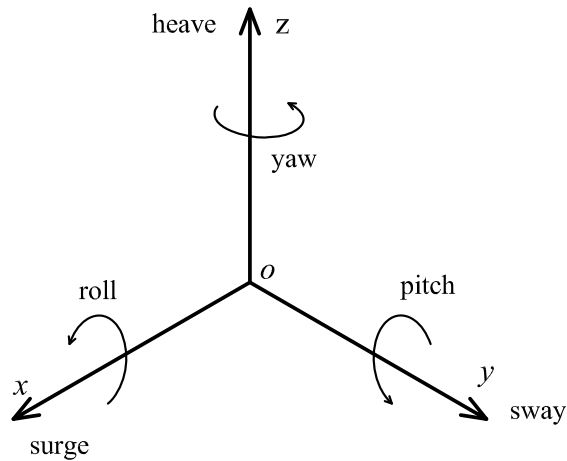


Figure 1.1: Definition of the coordinate system and the 6 degrees of freedom.

Some structures are not freely floating, but are restrained to fewer degrees of freedom due to e.g. their connection to the seabed. For instance, the point absorber that will be considered in this study, is restrained to heave mode only. For generality, the described theory in this Section will be applied to all six modes of motion. The body displacements and rotations are comprised in the six-dimensional generalized vector ξ and the velocity components are comprised in the generalized vector \mathbf{v} .

When wave-body interactions are considered, a velocity potential needs to be found that does not only satisfy the Laplace equation and the boundary conditions on the seabed and the free surface, but also the boundary conditions on the submerged body surface and a boundary condition at infinity. To find a

solution for the velocity potential, the problem is split up in subproblems, each resulting in a velocity potential. The appropriate velocity potential of the entire problem is then obtained by linearly superimposing the velocity potentials of the subproblems. Two additional problems need to be considered: the radiation problem and the diffraction problem.

The radiation problem

The body undergoes a forced harmonic motion in originally still water. Due to this forced motion, waves are radiated. The corresponding flow is described by the radiation potential, indicated by ϕ_R . The potential can be expressed as:

$$\phi_R = \sum_{i=1}^6 \xi_i \phi_i^{(1)} \quad (1.21)$$

where $\phi_i^{(1)}$ is the potential per unit displacement amplitude in mode i . The radiation potential must fulfill the previously described boundary conditions plus the boundary condition on the body:

$$\frac{\partial \phi_i}{\partial n} = v_i n_i \quad (1.22)$$

Moreover, the velocity potential must fulfill a radiation condition at infinity, also called the ‘far field radiation condition’, expressing the conservation of energy. It can be shown [3] that the potential must be of the form:

$$\phi_i = j C_f \frac{e^{jk_w R_b}}{\sqrt{R_b}} \quad \text{for } R_b \rightarrow \infty \quad (1.23)$$

where R_b is the distance to the body and C_f a constant. The conservation of radiated energy is expressed in the denominator with $\sqrt{R_b}$.

The diffraction problem

The diffraction problem is studied on the body, while it is kept fixed in a regular wave field. The flow of the diffracted waves is described by the diffraction potential, indicated by ϕ_D or also commonly denoted by ϕ_7 . The diffraction potential must satisfy the Laplace equation (1.2), the boundary condition on the seabed (1.5) and on the free surface (1.9). Furthermore, the sum of the

incident and diffracted potential must fulfill the body boundary condition, i.e. $\partial(\phi_I + \phi_D)/\partial n = 0$ on the submerged surface of the body, S_b . This leads to:

$$\frac{\partial\phi_D}{\partial n} = -\frac{\partial\phi_I}{\partial n} \quad \text{on } S_b \quad (1.24)$$

The diffraction potential must also satisfy the far field radiation as formulated in (1.23) for the radiation potential. Hence, most of the boundary conditions are identical to those described for the radiation potential. However, the boundary condition at the body surface is different: the flow has a prescribed velocity normal to the body surface.

Note that some authors indicate the previously mentioned diffraction potential by ϕ_s , the ‘scattered potential’. In that case, the term ‘diffraction potential’ is then often used to refer to the sum of the incident potential and scattered potential.

1.2.4 Pressures and forces

When a solution is found for each of the subproblems, the total velocity potential ϕ can be computed and is given in Eq. (1.25), assuming that all phenomena are harmonic in time with angular frequency ω .

$$\begin{aligned} \phi &= \phi_I + \phi_R + \phi_D \\ &= \text{Re} \left[\left(\sum_{i=1}^6 \hat{\xi}_i \hat{\phi}_i + \hat{\phi}_I + \hat{\phi}_D \right) e^{j\omega t} \right] \end{aligned} \quad (1.25)$$

where $\phi(t; x, y, z) = \text{Re}[\hat{\phi}(x, y, z) \cdot e^{j\omega t}]$. The hat symbol signifies the complex amplitude of the velocity potential and the body displacement vector. The pressure is then obtained from Bernoulli’s equation (1.4), assuming $p_0 = 0$.

$$\begin{aligned} p &= -\rho \frac{\partial\phi}{\partial t} - \rho g z \\ &= -\rho \text{Re} \left[j\omega \left(\sum_{i=1}^6 \hat{\xi}_i \hat{\phi}_i + \hat{\phi}_I + \hat{\phi}_D \right) e^{j\omega t} \right] - \rho g z \end{aligned} \quad (1.26)$$

The hydrodynamic and hydrostatic forces (\mathbf{F}_h) and moments (\mathbf{M}_h) are determined by integration of the pressure on the submerged body surface S_b :

$$\mathbf{F}_h = \iint_{S_b} p \mathbf{n} dS \quad (1.27)$$

$$\mathbf{M}_h = \iint_{S_b} p(\mathbf{r} \times \mathbf{n}) dS \quad (1.28)$$

where \mathbf{n} denotes the normal vector on S_b and \mathbf{r} is the position vector. The forces and moments are often expressed in one generalized force vector with six degrees of freedom, denoted by \mathbf{F} . The first term in Eq. (1.26) becomes the ‘radiation force’, indicated with F_{rad} . It consists of a part in phase with the acceleration and a part in phase with the velocity:

$$F_{rad,j} = \sum_{i=1}^6 -m_{a_{ji}} \frac{d^2 \xi_i}{dt^2} - b_{hyd_{ji}} \frac{d\xi_i}{dt} \quad (1.29)$$

where $m_{a_{ji}}$ is known as the ‘added inertia’ and $b_{hyd_{ji}}$ as the linear ‘hydrodynamic damping’. The index ji denotes that the force acts in the direction of j and is induced by an oscillation in the direction of i . Integration of the second term, containing the incident wave potential, gives the ‘Froude-Krylov force’. This is the force which the body experiences from the incoming wave, as if the body itself does not disturb the wave field. Integration of the third term, with the diffraction potential, results in the ‘diffraction force’. The sum of the Froude-Krylov force and the diffraction force is called the ‘exciting wave force’ or shortly ‘exciting force’, denoted by F_{ex} . Integration of the last term in Eq. (1.26) yields -after subtraction of the gravity forces- the hydrostatic restoring force, indicated with F_{res} .

When all the forces acting on a floating structure are known, the motion of the structure can be derived from Newton’s second law of motion:

$$\sum_{i=1}^6 \left[(m_{ji} + m_{a_{ji}}) \frac{d^2 \xi_i}{dt^2} + b_{hyd_{ji}} \frac{d\xi_i}{dt} + k_{ji} \xi_i \right] = \hat{F}_{ex_j} e^{j\omega t} \quad (1.30)$$

where m_{ji} and k_{ji} are the elements on the j^{th} row and i^{th} column of the inertia matrix and stiffness matrix, respectively. Eq. (1.30) contains a set of coupled differential equations. When the body is restricted to one degree of

freedom (e.g. a freely heaving buoy), only a single differential equation is left. In the next Section the solution of this differential equation is discussed. In the subsequent Sections, external damping and tuning forces will be added to obtain the equation of motion of the considered point absorber. Since only heave mode is considered in the rest of this thesis, the index ‘3’ will be dropped to denote the heave mode. Hence, in the next Sections and Chapters, the following notation will be used:

$$\begin{aligned}
 m &= m_{33} \\
 m_a &= m_{a33} \\
 b_{hyd} &= b_{hyd33} \\
 k &= k_{33} \\
 F_{ex} &= F_{ex3} \\
 v &= v_3
 \end{aligned}$$

1.3 Point absorbers

1.3.1 Mass-spring-damper system

The behaviour of a heaving point absorber can be compared to that of a mechanical oscillator, composed of a mass-spring-damper system with one degree of freedom, subjected to an external force in the direction of the degree of freedom. A schematic representation is given in Figure 1.2. Some basic principles of mass-spring-damper systems will be rehearsed in this Section in a concise way. More details can be found in the literature, e.g. [2], [5].

The system is linearly damped with damping coefficient b_d . An external harmonic force is applied on the system, with amplitude F_A and angular frequency ω . According to Newton’s law, the equation of motion, Eq. (1.31), consists of an inertia force $m \frac{d^2z}{dt^2}$, a damping force $b_d \frac{dz}{dt}$, a restoring force kz , and the external force $F_A \sin(\omega t)$:

$$m \frac{d^2z}{dt^2} + b_d \frac{dz}{dt} + kz = F_A \sin(\omega t) \quad (1.31)$$

The homogeneous or transient solution of this differential equation corresponds with the solution for a free oscillation. Omitting the external force

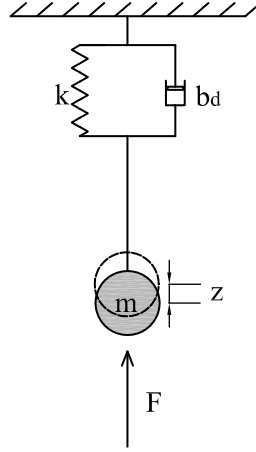


Figure 1.2: Schematic representation of a mass-spring-damper system.

($F_A \sin(\omega t) = 0$) results in Eq. (1.32):

$$m \frac{d^2 z}{dt^2} + b_d \frac{dz}{dt} + kz = 0 \quad (1.32)$$

Assuming a solution of the form:

$$z = z_A \cdot e^{qt} \quad (1.33)$$

with z_A and q unknown constants. Substitution of z in Eq. (1.32) gives:

$$(mq^2 + b_d q + k = 0) \cdot z_A e^{qt} = 0 \quad (1.34)$$

Since Eq. (1.34) must be fulfilled for all t , it can be simplified to:

$$mq^2 + b_d q + k = 0 \quad (1.35)$$

This quadratic equation has two solutions for q :

$$q_{1,2} = -\frac{b_d}{2m} \pm \sqrt{\left(\frac{b_d}{2m}\right)^2 - \frac{k}{m}} \quad (1.36)$$

When the discriminant D equals zero, Eq. (1.35) has only one solution. In that case the oscillation is critically damped, meaning that the systems returns to its equilibrium position in the quickest possible way without vibrating

around the equilibrium position. The damping coefficient associated with this case, is called the critical damping coefficient, b_c . Solving $D = 0$ for b_d gives the critical damping coefficient:

$$b_c = 2\sqrt{km} = 2m\omega_n \quad (1.37)$$

with ω_n the natural pulsation of the system, given by Eq. (1.38):

$$\omega_n = \sqrt{\frac{k}{m}} \quad (1.38)$$

The ratio of the damping coefficient to the critical damping coefficient is called the damping ratio and is denoted by ζ_d :

$$\zeta_d = \frac{b_d}{b_c} \quad (1.39)$$

If $\zeta_d > 1$, the system is overcritically damped. An overdamped system returns to its equilibrium position in a non-oscillatory way, requiring more time than a critically damped system (with the same initial conditions). In case $\zeta_d < 1$, the system is called an underdamped system. The considered heaving point absorber can generally be considered as an underdamped mechanical oscillator.

Figure 1.3 shows the difference in response between an overdamped, underdamped and critically damped system.

For an underdamped system, the values of q can be rewritten as Eq. (1.40), utilizing Eqs. (1.37-1.39):

$$q_{1,2} = -\zeta_d\omega_n \pm i\omega_n\sqrt{1 - \zeta_d^2} \quad (1.40)$$

According to Eq. (1.33) and Eq. (1.36) the solution of z becomes:

$$z = A_1e^{q_1t} + A_2e^{q_2t} \quad (1.41)$$

The constants A_1 and A_2 are determined by the initial conditions of the system. Since $q_{1,2}$ are complex conjugate values, A_1 and A_2 need to be a complex conjugate pair as well for z to be real. Replacing A_1 and A_2 by the expressions in Eq. (1.42) results in an equivalent expression for the motion z , which is given in Eq. (1.43):

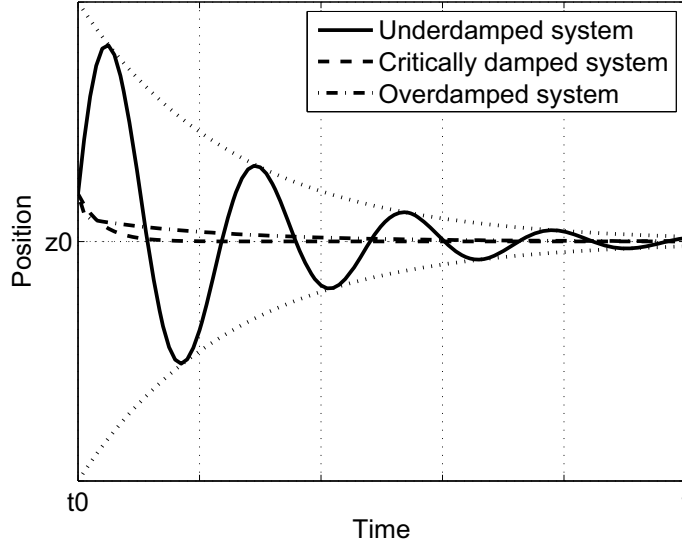


Figure 1.3: Motion curves of an underdamped, overdamped and critically damped system.

$$\begin{cases} A_1 = \frac{1}{2}z_{Af}(\sin\beta_f - i \cos\beta_f) \\ A_2 = \frac{1}{2}z_{Af}(\sin\beta_f + i \cos\beta_f) \end{cases} \quad (1.42)$$

$$z = z_{Af} e^{-\zeta_d \omega_n t} \sin(\sqrt{1 - \zeta_d^2} \omega_n t + \beta_f) \quad (1.43)$$

where the index f denotes ‘free oscillation’. The exponential function $e^{-\zeta_d \omega_n t}$ is responsible for the decreasing amplitude effect. This function is represented by black dotted lines in Figure 1.3. The sine function causes the oscillations at a frequency equal to the damped natural angular frequency, ω_d :

$$\omega_d = \sqrt{1 - \zeta_d^2} \omega_n \quad (1.44)$$

The damped free oscillations of a system disappear after a number of oscillations. The number of oscillations depends on the damping in the system. The equation of motion can alternatively be expressed in the form of Eq. (1.45), which is equivalent with Eq. (1.43), adopting the following relationships: $C_1 = z_{Af} \cos\beta_f$ and $C_2 = z_{Af} \sin\beta_f$.

$$z = e^{-\zeta_d \omega_n t} (C_1 \cos \omega_d t + C_2 \sin \omega_d t) \quad (1.45)$$

When an external force is applied on the system, as in Eq. (1.31), the complete solution of the equation of motion consists of the sum of the free oscillation, dependent on the initial conditions, and the forced oscillation or steady-state oscillation, which is called the particular solution of the differential equation. This particular solution of Eq. (1.31) is of the form:

$$z = z_{As} \sin(\omega t + \beta_s) \quad (1.46)$$

with z_{As} the amplitude of the steady-state oscillation and β_s the phase angle between the external force and the motion of the system. The index s denotes 'steady state'. The parameters, z_{As} and β_s , can be found as explained in Appendix A:

$$z_{As} = \frac{F_A}{\left[(k - m\omega^2)^2 + (b\omega)^2 \right]^{1/2}} \quad (1.47)$$

and

$$\tan \beta_s = \frac{-b_d \omega}{k - m\omega^2} \quad (1.48)$$

To conclude, the complete response of a mass-spring-damper system subjected to a regular external force is given by:

$$\begin{aligned} z_{total} &= z_{free} + z_{forced} \\ &= z_{Af} e^{-\zeta_d \omega_n t} \sin(\sqrt{1 - \zeta_d^2} \omega_n t + \beta_f) \\ &\quad + z_{As} \sin(\omega t + \beta_s) \end{aligned} \quad (1.49)$$

$$(1.50)$$

1.3.2 Equation of motion of a heaving point absorber

In this Section, the response of a point absorber, oscillating in a harmonic wave with respect to a fixed reference is discussed. The motion of the point absorber is restricted to the heave mode only. A schematic view of the considered point absorber is given in Figure 1.4.

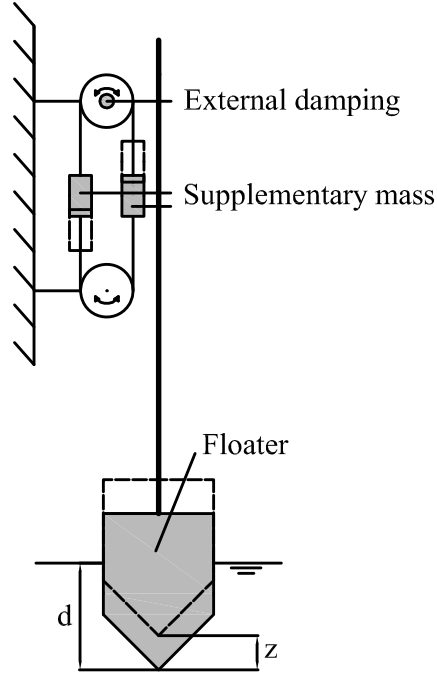


Figure 1.4: Schematic representation of a heaving point absorber with applied supplementary mass.

In equilibrium position the floater has a draft d . Due to the vertical wave action, the floater has a position z from its equilibrium position. The equation of motion of this point absorber can be described by Newton's second law:

$$m \frac{d^2 z}{dt^2} = F_{ex} + F_{rad} + F_{res} + F_{damp} + F_{tun} \quad (1.51)$$

where m is the mass of the buoy and $d^2 z/dt^2$ the buoy acceleration. F_{ex} is the exciting wave force, F_{rad} the radiation force. As stated in Section 1.2, the radiation force can be decomposed -with linear theory- in a linear added mass term and a linear hydrodynamic damping term:

$$F_{rad} = -m_a(\omega) \frac{d^2 z}{dt^2} - b_{hyd}(\omega) \frac{dz}{dt} \quad (1.52)$$

The hydrostatic restoring force, F_{res} , is the Archimedes forces (F_{arch}) minus the gravity force (F_g). This force corresponds to the spring force in

Eq. (1.31). With a linear spring constant k , the hydrostatic restoring force can be expressed as:

$$F_{res} = F_{arch} - F_g = \rho V(t) - mg = -kz \quad (1.53)$$

where $V(t)$ is the instantaneous, submerged buoy volume. The spring constant or hydrostatic restoring coefficient is expressed as: $k = \rho g A_w$, where A_w is the waterline area.

F_{damp} is the external damping force, exerted by the power take-off (PTO) system and F_{tun} the tuning force to phase-control the buoy. In Section 1.3.5, it will be explained why a point absorber is typically phase-controlled. The damping and tuning forces are determined by the power take-off and control mechanism, respectively, and are in practical applications typically non-linear. However, for simplicity, they are often assumed linear. In that case the damping force becomes:

$$F_{damp} = b_{ext} \frac{dz}{dt} \quad (1.54)$$

with b_{ext} the linear external damping coefficient originating from the PTO and enabling power extraction.

A linear tuning force can be realized for instance by means of a supplementary mass term [6] or an additional spring term [7]. A supplementary mass term has been applied in the present study. A principal representation of the supplementary mass, m_{sup} , is given in Figure 1.4. The supplementary inertia is realized by adding two equal masses at both sides of a rotating belt. In that way, the inertia of the system can be increased without changing the draft of the floater. The tuning force is expressed as:

$$F_{tun} = m_{sup} \frac{d^2z}{dt^2} \quad (1.55)$$

Other possibilities to effectuate phase-control are discussed in Section 1.3.5. Taking into account the previous considerations, the equation of motion of the presented heaving point absorber can be rewritten as:

$$(m + m_{sup} + m_a(\omega)) \frac{d^2 z(t)}{dt^2} + (b_{hyd}(\omega) + b_{ext}) \frac{dz(t)}{dt} + kz(t) = F_{ex}(\omega, t) \quad (1.56)$$

The two external parameters, b_{ext} and m_{sup} , have to be optimized in order to maximize the absorbed power. These optimizations will be described in Chapter 2. Several restrictions will be introduced, in order to avoid unrealistic solutions, such as extremely large buoy motions.

The steady state solution of Eq. (1.56) has been determined in Section 1.3.1 by Eq. (1.46): $z = z_A \sin(\omega t + \beta_{mot})$, where z_A en β_{mot} are given by:

$$z_A(\omega) = \frac{F_{ex,A}(\omega)}{\sqrt{[k - (m + m_{sup} + m_a(\omega)) \cdot \omega^2]^2 + [(b_{hyd}(\omega) + b_{ext})\omega]^2}} \quad (1.57)$$

$$\beta_{mot} = \beta_{F_{ex}} - \arctan\left(\frac{(b_{hyd}(\omega) + b_{ext})\omega}{k - (m + m_{sup} + m_a(\omega))\omega^2}\right) \quad (1.58)$$

Alternatively, complex notation can be used, simplifying the mathematical expressions. With v the vertical velocity component and j the imaginary unit, the buoy motion parameters become:

$$\begin{aligned} v &= \frac{dz}{dt} = v_A \cos(\omega t + \beta_v) = \text{Re}[\hat{v} e^{j\omega t}] \\ z &= \int_0^t v dt = \frac{v_A}{\omega} \sin(\omega t + \beta_v) = \text{Re}\left[\frac{\hat{v}}{j\omega} e^{j\omega t}\right] \\ \frac{dv}{dt} &= \frac{d^2 z}{dt^2} = -v_A \omega \sin(\omega t + \beta_v) = \text{Re}[j\omega \hat{v} e^{j\omega t}] \end{aligned}$$

The equation of motion Eq. (1.56) becomes:

$$\text{Re}\left[\left[j\omega (m + m_{sup}) + b_{ext} + \frac{k}{j\omega}\right] \hat{v} e^{j\omega t}\right] = (\hat{F}_{ex} + \hat{F}_{rad}) e^{j\omega t} \quad (1.59)$$

with \hat{F}_{ex} and \hat{F}_{rad} , the complex amplitudes of F_{ex} and F_{rad} . Introducing the mechanical impedance, $Z_m = j\omega m + b_{ext} + \frac{k}{j\omega}$, Eq. (1.59) is expressed as:

$$Z_m \hat{v} = \hat{F}_{ex} + \hat{F}_{rad} \quad (1.60)$$

Analogous, the radiation force in Eq. (1.52) can be formulated as:

$$F_{rad} = \text{Re} \left[[-j\omega m_a(\omega) - b_{hyd}(\omega)] \hat{v} e^{j\omega t} \right] \quad (1.61)$$

The radiation impedance, Z_{rad} , is introduced as: $Z_{rad} = -j\omega m_a(\omega) - b_{hyd}(\omega)$. Hence, the complex amplitude of the radiation force can be written as:

$$\hat{F}_{rad} = -Z_{rad} \hat{v} \quad (1.62)$$

This results in a concise expression for the equation of motion:

$$(Z_m + Z_{rad}) \hat{v} = \hat{F}_{ex} \quad (1.63)$$

1.3.3 Power absorption

A harmonically oscillating body is assumed, with velocity v , and subjected to a force $F(t)$:

$$F(t) = F_A \cos(\omega t + \beta_F)$$

$$v(t) = v_A \cos(\omega t + \beta_v)$$

The power averaged over a period T can be expressed as:

$$P_{av} = \frac{1}{2} F_A v_A \cos(\beta_F - \beta_v) \quad (1.64)$$

In complex notation, Eq. (1.64) becomes:

$$P_{av} = \frac{1}{2} \text{Re}[\hat{F} \cdot \hat{v}^*] \quad (1.65)$$

$$(1.66)$$

with * indicating the complex conjugate. The average absorbed power of a point absorber is equal to the average excited power minus the average radiated power:

$$P_{abs,av} = P_{ex,av} - P_{rad,av} \quad (1.67)$$

According to Eq. (1.64), the average exciting power can be expressed as:

$$P_{ex,av} = \frac{1}{2} F_{e,A} v_A \cos(\gamma) \quad (1.68)$$

with $\gamma = \beta_{F_{ex}} - \beta_v$ the phase shift between $F_{ex,A}$ and v_A . Combining Eq. (1.52) and Eq. (1.64) gives the average radiated power:

$$P_{rad,av} = \frac{1}{2} \text{Re}[Z_{rad} v v^*] = \frac{1}{2} b_{hyd} v_A^2 \quad (1.69)$$

with $b_{hyd} = \text{Re}[Z_{rad}]$.

Hence, the average power absorption is given by:

$$P_{abs,av} = \frac{1}{2} F_{e,A} v_{A,i} \cos(\gamma) - \frac{1}{2} b_{hyd} v_A^2 \quad (1.70)$$

or, alternatively, $P_{abs,av}$ can be expressed as the power absorbed by the power take-off system:

$$P_{abs,av} = \frac{1}{2} b_{ext} v_A^2 = \frac{1}{2} b_{ext} \omega^2 z_A^2 \quad (1.71)$$

Note that the term ‘power absorption’ is generally used to indicate the ‘average power absorption’ and is simply denoted by ‘ P_{abs} ’. When the time-dependent power absorption is meant, it is usually explicitly mentioned.

1.3.4 Absorption width

The ‘absorption width’ or ‘absorption length’, denoted by λ_p , is the crest length over which the total available power corresponds to the absorbed power or, in other words, the ratio of the absorbed power to the average available power per unit crest length. It is also called the ‘capture width’. However, the term capture width generally takes into account the useful power instead of the absorbed power and thus includes the power losses.

$$\begin{aligned} \lambda_p &= \frac{P_{abs}}{P_{avail}} \\ &= \frac{2L}{\pi} \frac{b_{hyd}(\omega) b_{ext} \omega^2}{[k - (m + m_a(\omega) + m_{sup}) \omega^2]^2 + (b_{hyd}(\omega) + b_{ext})^2 \omega^2} \quad (1.72) \end{aligned}$$

Dividing the absorption width by the diameter of the device results in the ‘efficiency’. Note that the meaning of the word ‘efficiency’ is context-

dependent. In this case, it only refers to the absorption efficiency and not to the efficiency during any other conversion step, e.g. turbine efficiency, generator efficiency, etc. The absorption efficiency can be very large, even larger than 100 %. This phenomenon is called the ‘point-absorber effect’ or ‘antenna effect’ and is explained by the fact that the point absorber is able to absorb a larger fraction of the power than what is available over its diameter.

In a regular wave with wave length, L , the maximum absorption width of a heaving point absorber is theoretically (with linear theory) equal to the wave length divided by 2π .

$$\lambda_{p,max} = \frac{L}{2\pi} \quad (1.73)$$

This result was independently derived by Budal and Falnes [8], Evans [9] and Newman [10]. For an axisymmetric body with three degrees of freedom: heave, surge and sway, the maximum absorption width is equal to: $\lambda_p = \frac{3}{2\pi}L$ [10].

The proof of Eq. (1.73) is given here, according to Falnes [5].

The maximum power absorption occurs when the derivative to the velocity of Eq. 1.70 equals zero: $dP_{abs,av}/dv_A = 0$. Hence, the optimum amplitude of the velocity is:

$$v_{A,opt} = \frac{F_{ex,A}}{2b_{hyd}} \cos(\gamma) \quad (1.74)$$

Consequently, the maximum value of the average power absorption is:

$$P_{abs,av,max} = \frac{|F_{ex,A}|^2}{8b_{hyd}} \cos^2(\gamma) \quad (1.75)$$

The optimum phase shift is obtained for $\gamma = 0$. This means that, in optimal conditions, the buoy velocity is in phase with the heave exciting force. The amplitude of the exciting force is rewritten as follows, with f_{ex} the transfer function for the heave exciting force:

$$F_{ex,A} = f_{ex} \cdot \zeta_A \quad (1.76)$$

The expression for the maximum average absorbed power becomes:

$$P_{abs,av,max} = \frac{f_{ex,A}^2}{8b_{hyd}} \zeta_A^2 \quad (1.77)$$

The hydrodynamic damping coefficient for heave is [5]:

$$b_{hyd} = \frac{\omega k_w}{2\rho g^2 D(k_w d_w)} f_{ex,A}^2 \quad \text{for heave} \quad (1.78)$$

with k_w the wave number and $D(k_w d_w)$ the depth factor.

Substitution of Eq. (1.78) in Eq. (1.77) gives:

$$P_{abs,av,max} = \frac{\rho g^2 D(k_w d_w)}{4\omega k_w} \zeta_A^2 \quad (1.79)$$

The total available average power is given by Eq. (1.80):

$$P_{avail} = \frac{\rho g^2 D(d_w k_w)}{4\omega} \zeta_A^2 \quad (1.80)$$

The maximum absorption width is found to be equal to $L/2\pi$:

$$\lambda_p = \frac{P_{abs,av,max}}{P_{avail}} = \frac{1}{k_w} \stackrel{!}{=} \frac{L}{2\pi} \quad (1.81)$$

Eq. (1.78) expresses a relationship between the exciting wave force F_{ex} and the hydrodynamic damping coefficient b_{hyd} . A large hydrodynamic damping coefficient at an angular frequency ω indicates that the system has a large capacity to radiate waves at that frequency. According to Eq. (1.78), the body experiences for that frequency also a large excitation force. Hence, a point absorber that is a good damper at an angular frequency ω is also a good receiver for waves with the same frequency.

The maximum absorption width can also be obtained directly from Eq. (1.72). The denominator is minimal when the term $[k - (m + m_a(\omega) + m_{sup})\omega^2]$ is equal to zero. This means that the angular frequency of the system must equal to the natural angular frequency ω_n :

$$\omega = \sqrt{\frac{k}{m + m_a\omega + m_{sup}}} \equiv \omega_0 \quad (1.82)$$

The numerator is maximal for $b_{hyd}(\omega) = b_{ext}$. When both conditions are fulfilled, the value for the maximum absorption width is indeed $L/(2\pi)$. Note that this is a theoretical optimum. In reality, the buoy velocities will be so large that second order effects become important. Maximum experimental absorption widths are smaller and occur for larger damping values as will be

illustrated in Chapter 4.

1.3.5 Phase control

Generally, the natural frequency of a point absorber system is higher than the wave frequency so that the condition in Eq. (1.82) is not fulfilled if no supplementary mass is applied. The natural frequency can be decreased by adding supplementary mass, as explained in Section 1.3.2, by a flywheel mechanically coupled with the vertical motion of the buoy, or by an additional spring term with negative spring coefficient. The effect of this tuning is shown in Figure 1.5. The solid line shows the water elevation. This line would correspond to the buoy position if the mass of the buoy were negligible. The dashed line illustrates the position of the buoy in case the inertia of the point absorber is increased so that the natural frequency of the device corresponds to the wave frequency. This is called ‘optimal’ control (tuning).

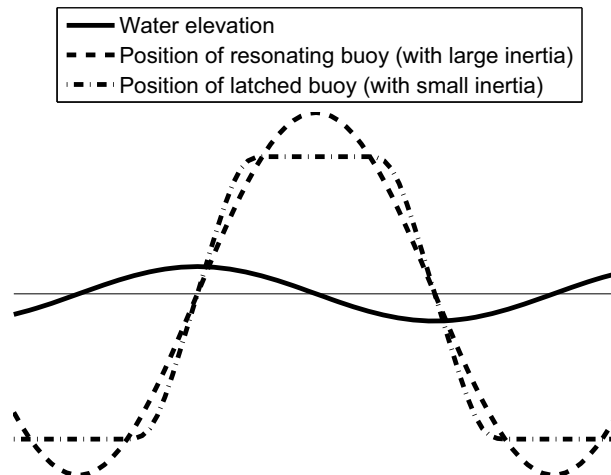


Figure 1.5: Schematic representation of phase control, based on Falnes [5].

In practical applications it might be difficult to realize the tuning by changing the supplementary inertia dependent on the incoming waves. The tuning force, as described in Eq. (1.55) can also be delivered by the power take-off system. In that case, it might be required to return some energy back to the sea during some small fractions of each oscillation cycle and

benefit from this during the remaining time, as stated by Falnes [11]. For this reason ‘optimum control’ is also denoted by ‘reactive control’. It is clear that in order to obtain this optimum control in practice, a reversible energy-converting mechanism with very low conversion losses is required [11]. It will be shown in this PhD thesis that the required tuning forces and associated instantaneous power levels might be much larger than the damping force and the corresponding power absorption values, respectively. Hence, these tuning forces will influence the design of the power take-off system and might possibly result in an uneconomic solution. The tuning forces can be limited, however, this can be associated with large power losses, depending on the restrictions and the sea states, which will be illustrated in the next Chapters.

Another phase control technique is ‘latching’. A mechanism holds the floater in a fixed position when it has reached an extreme excursion, i.e. when the velocity equals zero. The floater is released again at a certain time (approximately one quarter of the natural period T_n [11]) before the next extremum in the exciting force occurs. The motion of a point absorber subjected to latching control is illustrated with the dash-dotted line in Figure 1.5. Latching induces a non-linear response of the point absorber. This control technique has been applied in experimental test setups, for instance with the SEAREV device, resulting in a significant increase in power absorption [12].

Bibliography

- [1] WAMIT user manual: <http://www.wamit.com/manual.htm>.
- [2] Chakrabarti S., Hydrodynamics of Offshore Structures. WIT press, 1987.
- [3] Vantorre M., Wave forces on floating and fixed constructions (in Dutch). Ghent University, 1997.
- [4] Payne G., Numerical modelling of a sloped wave energy device. Ph.D. thesis, The University of Edinburgh, United Kingdom, 2006.
- [5] Falnes J., Ocean Waves and oscillating systems, linear interactions including wave-energy extraction. Cambridge University Press, 2002.
- [6] Vantorre M., Banasiak R., Verhoeven R., Modelling of hydraulic performance and wave energy extraction by a point absorber in heave. Applied Ocean Research 2004;26:61–72.
- [7] Ricci P., Saulnier J.B., Falcao A., Point-absorber arrays: a configuration study off the Portuguese west-coast. In: 7th European Wave and Tidal Energy Conference, Portugal, 2007.
- [8] Budal K., Falnes J., A resonant point absorber of ocean waves. Nature 1975;256:478–479.
- [9] Evans D., A theory for wave-power absorption by oscillating bodies. Journal of Fluid Mechanics 1976;77:1–25.
- [10] Newman J., The interaction of stationary vessels with regular waves. In: 11th Symposium on Naval Hydrodynamics, United Kingdom: Mechanical Engineering Pub, 1976.
- [11] Falnes J., Principles for capture of energy from ocean waves. phase control and optimum oscillation. Annex Report B1: Device fundamentals/Hydrodynamics, an annex to the main report ‘Wave

Energy Converters: Generic Technical Evaluation Study', B-study of the DG XII Joule Wave Energy Initiative, 1993.

- [12] Durand M., Babarit A., Pettinotti B., Quillard O., Toularastel J., Clément A., Experimental validation of the performances of the SEAREV wave energy converter with real time latching control. In: 7th European Wave and Tidal Energy conference, Portugal, 2007.

CHAPTER 2

Frequency domain modelling



A linear frequency domain model has been employed to compute the behaviour of a heaving point absorber system. The hydrodynamic parameters are obtained with WAMIT, a software package based on boundary element methods. A linear external damping coefficient is applied to enable power absorption and a supplementary mass is introduced to tune the point absorber to the incoming wave conditions. The external damping coefficient and supplementary mass are the control parameters, which need to be optimized to maximize the power absorption. Two buoy shapes are evaluated with different waterline diameters and drafts. Several constraints are implemented: two restrictions are imposed on the (relative) buoy motion, i.e. a slamming and a stroke restriction. A third constraint is imposed on the total control force that can be applied on the buoy. These restrictions appear to have a slightly negative to seriously harmful impact on the power absorption.

This Chapter is partly based on ‘Numerical Modelling of Wave Energy Absorption by a Floating Point Absorber System’ by G. De Backer et al. [1] and ‘Performance of a point absorber heaving with respect to a floating platform’ by G. De Backer et al. [2].

2.1 Introduction

Whether the numerical models, used to simulate wave energy converters, are based on frequency or time domain approaches, they usually rely on the application of boundary element methods (BEM), also referred to as boundary integral equation methods (BIEM) or panel methods. Boundary element methods are applied in many different areas such as fluid dynamics, acoustics and electromagnetics. They have been extensively used in the offshore industry for over 30 years [3]. With a boundary element method, the numerical discretization is performed on the boundary of an object, contrary to the finite element method (FEM), where -in fluid dynamics- the fluid volume is discretized. BEM are used to solve partial differential equations that can be formulated as integral equations, with the velocity potential as the unknown in fluid dynamics applications. Since the numerical simulations in this study are also based on a BEM package, a short review is given on numerical modelling of wave energy devices, focussing on BEM applications.

In 1980 Standing [4] predicted the hydrodynamic damping, the added mass and the pressure amplification ratio at the centre of a submerged duct device (Vickers device) and calculated the pitch response, the power absorption efficiency and reaction forces of a 2D pitching ‘duck’ with a BEM code named NMIWAVE. The results from the 2D duck were compared with experiments by Salter and a good agreement was found. In the nineties, Pizer [5] employed a custom made BEM code to evaluate the performance of a solo duck. Later on Yemm [6] and Pizer [7] numerically modelled the Pelamis wave energy converter with the BEM approach. In 1996 Lee et al. [8] studied three types of oscillating water columns with the low-order 3D BEM version of WAMIT [9]. An additional difficulty with OWCs is the presence of an interior domain within the chamber. Lee et al. applied two different approaches to deal with this problem. The ‘direct approach’ consists of adapting the dynamic boundary conditions on the free surface of the aperture. The second approach is based on the application of ‘generalized modes’, which are extra modes of motions that are introduced to describe the motion of a virtual, weightless and deformable piston, representing the free surface of the OWC chamber. Two years later Brito-Melo et al. [10] presented an adaptation of the BEM code AQUADYN [11], developed at the Ecole Centrale de Nantes, France, to study OWCs. The direct method was applied to account for the imposed oscillatory pressure within the chamber of the OWC. The use of BEM codes for the prediction

of the performance of OWCs has been experimentally validated by Delauré and Lewis [12, 13], by applying the technique based on generalized modes in WAMIT.

Apart from oscillating water columns, BEM packages have been used to model the performance of point absorber systems. Arzel [14] studied the hydrodynamic parameters of a heaving buoy, oscillating with respect to a submerged reference plate. Energy is absorbed from the relative motion between the two bodies. AQUADYN has been used to determine the exciting and radiation parameters in frequency and time domain; the time domain impulse response functions are obtained by inverse Fourier transform of the frequency domain parameters. Justino [15] studied the performance of five spherical, submerged point absorbers, also with the numerical program AQUADYN. He evaluated heaving, surging and swaying spheres with different interdistances.

Vantorre et al. [16] investigated the hydrodynamic performance of several buoy shapes with the BEM code Aquaplan [17]. The considered shapes are a hemisphere, a cone with apex angle 90° and a compound shape, combining two conical surfaces (a shape with 60° top angle combined with a conical part with a 120° top angle). All shapes have a submerged, cylindrical upper part. The compound shape was expected to be most favourable, because of the large wetted area close to the free water surface, making the buoy benefit from higher wave excitation forces. The smaller top cone assures a sufficient draft, reducing the probability of slamming. However, physical experiments revealed that high viscous losses due to intensive vortex shedding were associated with this compound shape, resulting in less power absorption.

Payne et al. [18] have used the higher-order method of WAMIT to investigate the performance of a sloped wave energy device. The device consists of an oscillating buoy rigidly connected to an inclined submerged tube which is open at both ends. The tube is fitted with a piston that can translate along the tube axis. The body of water contained inside the tube provides the piston with a large added inertia. Energy is extracted by damping the relative motion between the piston and the rest of the device. The numerical results are validated with experimental tests in [3].

The SEAREV device, developed at the Ecole Centrale de Nantes by Clément et al. [19], has also been extensively numerically modelled with - among others- BEM codes, more specifically AQUADYN and ACHILD3D

[20]. More recently, Taghipour et al. [21] numerically modelled the FO³ device in WAMIT. The interaction between the platform and multiple bodies are studied, by introducing generalized modes. Since many WEC developers and researchers are currently using BEM codes to model their devices, the mentioned list is non-exhaustive. A more elaborate review on the use of BEM packages to model wave energy devices is given by Payne in [22].

2.2 Concept

The point absorber concept has been discussed in Section 1.3.2 of Chapter 1. A similar schematic representation is given in Figure 2.1. The point absorber system consists of a buoy that is restricted to heave mode only. The motion of the buoy with respect to a fixed reference is linearly damped to enable power absorption.

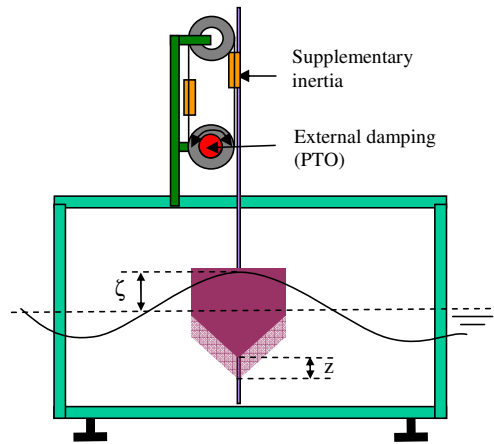


Figure 2.1: Schematic representation of a heaving point absorber with applied supplementary mass.

In the frequency domain, the equation of motion of the point absorber (Eq. (1.56)), subjected to a harmonic excitation with angular frequency ω , can be formulated as:

$$[-\omega^2(m + m_a + m_{sup}) + j\omega(b_{ext} + b_{hyd}) + k] \hat{z} = \hat{F}_{ex} \quad (2.1)$$

where \hat{z} is the complex amplitude of the buoy position and \hat{F}_{ex} the complex amplitude of the heave exciting force. As aforementioned in Chapter 1, the mass of the buoy is denoted by m , the added mass by m_a , the hydrodynamic damping coefficient by b_{hyd} and the hydrostatic restoring coefficient by k . The force associated with b_{ext} has to be exerted by the power take-off (PTO) and is called the damping force. A supplementary mass term is added to the equation to realize a tuning force proportional with the acceleration of the buoy, as explained in Chapter 1. The hydrodynamic parameters m_a , b_{hyd} and F_{ex} are dependent on both the buoy shape and wave frequency and are calculated with the BEM software package WAMIT.

2.3 WAMIT

WAMIT [9] is a software program developed for the computation of wave loads and motions of floating or submerged offshore structures. It is based on linear (and second-order) potential theory. As stated before, the velocity potential is determined with the boundary element method. WAMIT solves the diffraction and radiation problem for a given geometry and for given frequencies and returns the first order hydrostatic and hydrodynamic parameters. A separate version (6S) has a second-order module, capable of computing second-order non-linear quantities. The version employed in this work (v6) is restricted to first order potential theory only.

2.3.1 WAMIT input

Generally, four input files need to be prepared by the user to run WAMIT, namely the potential control file, the force control file, the configuration file and the geometry definition file. Different input possibilities exist, which are well explained in the user manual [9]. Although several input manners are possible and some parameters may be specified in more than one file, a general idea of the input expected in the four input files is given below.

- Potential Control file (.pot file). In this file, the number of bodies, N , and the water depth are specified. The position of each body with respect to a fixed xyz -axis must be mentioned too. Hence, in case N identical bodies are to be evaluated, only one geometry definition file of a single body is required and the positions of the N bodies are listed here. The user must

also indicate whether the radiation and/or the diffraction problem need to be solved. The frequencies of interest and the wave heading angles are listed in this file.

- Force Control file (.frc file). Here, the user indicates the hydrodynamic parameters that have to be calculated. The centre of gravity of the body must be specified as well as the matrix of the body radii of gyration and the coordinates of field points, if needed.
- Configuration file (.cfg file). In this input file, the user can specify several parameters and computation options. Examples are: the choice between the direct or iterative solver, the maximum number of iterations in case the latter solver is chosen, etc.
- Geometry Definition file (.gdf file). This file contains the geometrical description of the body. Since the free surface boundary conditions are linearized, only the part of the body below the mean water level needs to be specified. In the next Section, some more light will be shed on the description of the geometry.

Geometry description

Two different approaches are possible to discretize the body surface. The first method is the low-order method (or panel method), the second method is the higher-order method.

In the low-order method, the body surface is approximated with small quadrilateral panels. The velocity potential is assumed constant in each panel. Hence, the integral equations with the velocity potential as unknown, consist of a set of piecewise constant integrals that must be satisfied at the centroid of each panel.

The panels are described by the coordinates of each vertex. This coordinate list can be generated in several ways, but probably the most easy way is by using the CAD package MultiSurf [23]. MultiSurf is a geometric modelling program, providing the tools to create the body surfaces. An example of a mesh is presented in Figure 2.2. The generated mesh can be exported to a PAT-file, which is then converted into the required GDF file with a special MultiSurf add-on.

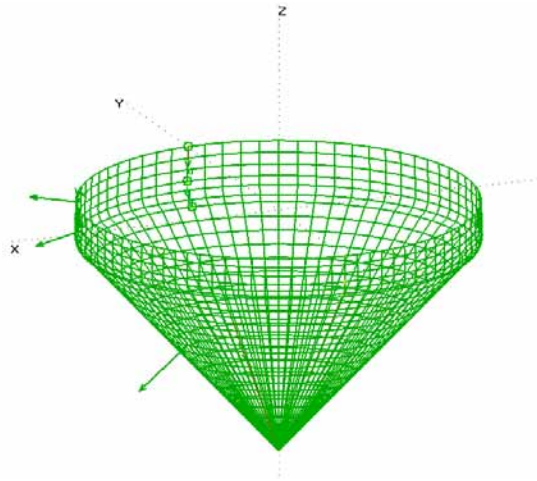


Figure 2.2: MultiSurf mesh, representing the cone-cylinder body surface.

A more efficient method is the higher order method, where the velocity potential is represented by continuous B-splines and the body surface by smooth continuous surfaces, called ‘patches’. The patches can be described analytically or by means of B-spline functions. This higher-order option generally leads to more accurate results than the low-order method for the same CPU time. However, CPU time is generally not an issue in the present work, since the considered bodies are small and axisymmetric. Due to the axisymmetry only a quarter of the body needs to be modelled, requiring very few computation time. Hence, both methods have been applied, but no significant differences were found.

2.3.2 WAMIT output

Several quantities can be evaluated with WAMIT, among them added mass and damping coefficients, exciting forces and moments, response amplitude operators, hydrodynamic pressure and fluid velocity on the body surface and in the fluid domain, free-surface elevation, drift forces and moments, etc. [9]. WAMIT also has a frequency to time domain (F2T) option to compute the impulse response functions based on the frequency domain hydrodynamic output parameters.

For the present study, the relevant output parameters are the added mass

(m_a) and hydrodynamic damping (b_{hyd}) coefficients for heave mode and the heave wave exciting force (F_{ex}). These parameters are returned by WAMIT in a normalized form (Chapter 4 of [9]). The normalized added mass and hydrodynamic damping are indicated with a bar and are defined as:

$$\bar{m}_a = \frac{m_a}{\rho L_s^3} \quad \text{for heave mode} \quad (2.2)$$

$$\bar{b}_{hyd} = \frac{b_{hyd}}{\rho L_s^3 \omega} \quad \text{for heave mode} \quad (2.3)$$

$$\bar{F}_{ex,A} = \frac{F_{ex,A}}{\rho g \zeta_A L_s^2} \quad \text{for heave mode} \quad (2.4)$$

$$(2.5)$$

where L_s is the length scale and ζ_A the wave amplitude. Note that other normalization rules may apply for other modes than the heave mode. A MATLAB script has been written to facilitate the dimensionalization process and to extract the relevant parameters from the WAMIT output files to be used as input for the MATLAB frequency domain program.

2.4 Design parameters

2.4.1 Buoy geometry

Shape

Two buoy shapes are considered: a conical shape with an apex angle of 90° and a hemisphere, both extended by a cylindrical part. The shapes are shown in Figure 2.3. In the framework of the SEEWEC project, some additional shapes have been evaluated, among them a tulip-like shape and a number of cylindrical shapes with small draft.

Draft and diameter

Simulations are run for five different waterline diameters, D , ranging between 3.0 and 5.0 m. For each buoy diameter, three different drafts are evaluated, corresponding to a submerged cylindrical part of 0.5, 1.0 and 2.0 m. Figure 2.4 gives an overview of the considered buoy diameters and drafts.

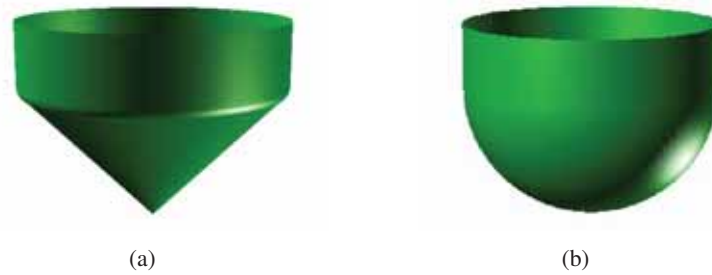


Figure 2.3: Evaluated buoy shapes: (a) cone-cylinder: 'cc', (b) hemisphere-cylinder: 'hc'.

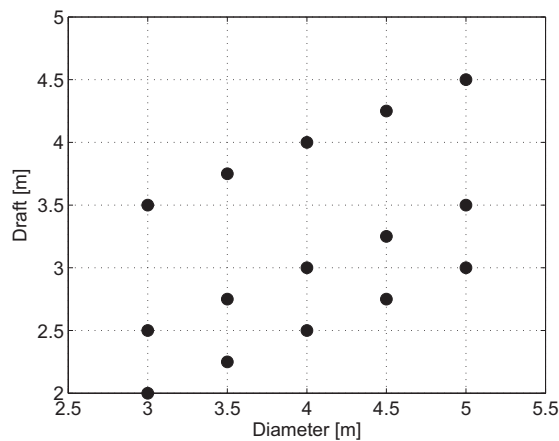


Figure 2.4: Evaluated buoy diameters and drafts.

2.4.2 Wave climate

The calculations in this Chapter are performed for eight reference sea states, displayed in Table 2.1. The first sea state covers H_s values from 0.00 to 0.50 m, the second sea state covers the range between 0.50 m and 1.00 m, and so on. The combinations of H_s and T_p are representative for the North Sea area. The considered reference water depth is 50 m. In the next Chapters, the focus will be laid on the Belgian Continental Shelf, more specifically on the Westhinder buoy location.

Table 2.1: Reference sea states

Sea state	H_s [m]	T_p [s]
1	0.25	6.70
2	0.75	6.70
3	1.25	6.70
4	1.75	7.40
5	2.25	8.11
6	2.75	8.81
7	3.25	8.81
8	3.75	9.52

The wave amplitude spectra, $S_{\zeta_A}(f)$, are based on the parameterized JONSWAP spectrum [?, 24]:

$$S_{\zeta_A}(f) = \alpha_s H_s^2 f_p^4 f^{-5} \gamma^{\beta_s} \exp\left(\frac{-5}{4} \left(\frac{f_p}{f}\right)^4\right) \quad (2.6)$$

with γ the peak enhancement factor ($\gamma = 3.3$), f_p the peak frequency and α_s and β_s :

$$\alpha_s = \frac{0.0624}{0.230 + 0.0336 \gamma - \left(\frac{0.185}{1.9+\gamma}\right)} \quad (2.7)$$

$$\beta_s = \exp\left(-\frac{(f - f_p)^2}{2\sigma^2 f_p^2}\right) \quad (2.8)$$

The value of the spectral width parameter σ depends on the frequency:

$$\sigma = \begin{cases} 0.07 & f < f_p \\ 0.09 & f \geq f_p \end{cases} \quad (2.9)$$

The calculated wave amplitude spectra corresponding with the eight sea states are shown in Figure 2.5.

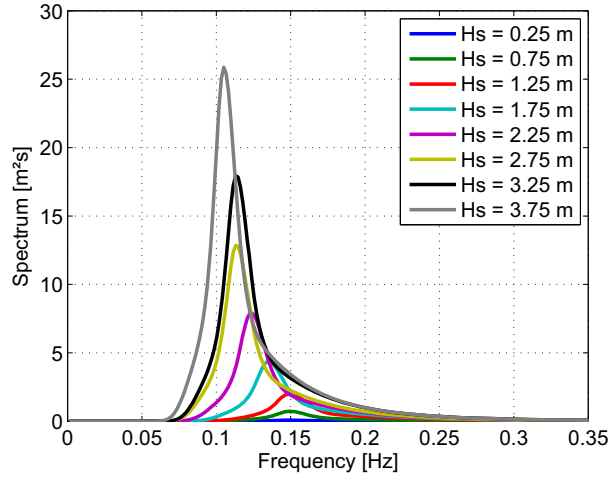


Figure 2.5: JONSWAP wave amplitude spectrum for 8 sea states.

2.5 Hydrodynamic parameters

Figure 2.6 gives the hydrodynamic parameters of the cone-cylinder shape, denoted by ‘cc’, with waterline diameter $D = 5$ m versus the frequency bandwidth relevant to cover the spectra of the above defined sea states. The added mass is shown in Figure 2.6(a). Note that a smaller draft is associated with a larger added mass in this frequency range. This is also observed for the hydrodynamic damping coefficient and the amplitude of the heave exciting force, as presented in Figures 2.6(b) and 2.6(c), respectively. This feeds the supposition that a smaller draft will result in a larger power absorption. For the zero frequency limit of the heave exciting force, a value of approximately 197.5 kN/m^1 is obtained with WAMIT. This corresponds to the value of the hydrostatic force per unit displacement: $\rho g A_w$, with A_w the waterline area ($= \pi R^2$). Figure 2.6(d) shows the phase angle of the heave exciting force as a function of the frequency. The phase difference between the exciting force and incident wave is very small ($\beta_{F_{ex}} < 5^\circ$) in the range of the peak frequencies, i.e. f_p between 0.1 and 0.17 Hz ($6 \text{ s} < T_p < 10 \text{ s}$). The hydrodynamic parameters for the hemisphere cylinder shape (hc) with a waterline diameter of 5 m are shown in Figure 2.7. Those parameters appear to be somehow smaller

¹Value computed for $f = 0.008$ Hz.

compared to the cone-cylinder shape, so it might be expected that the latter will be a slightly better wave absorber.

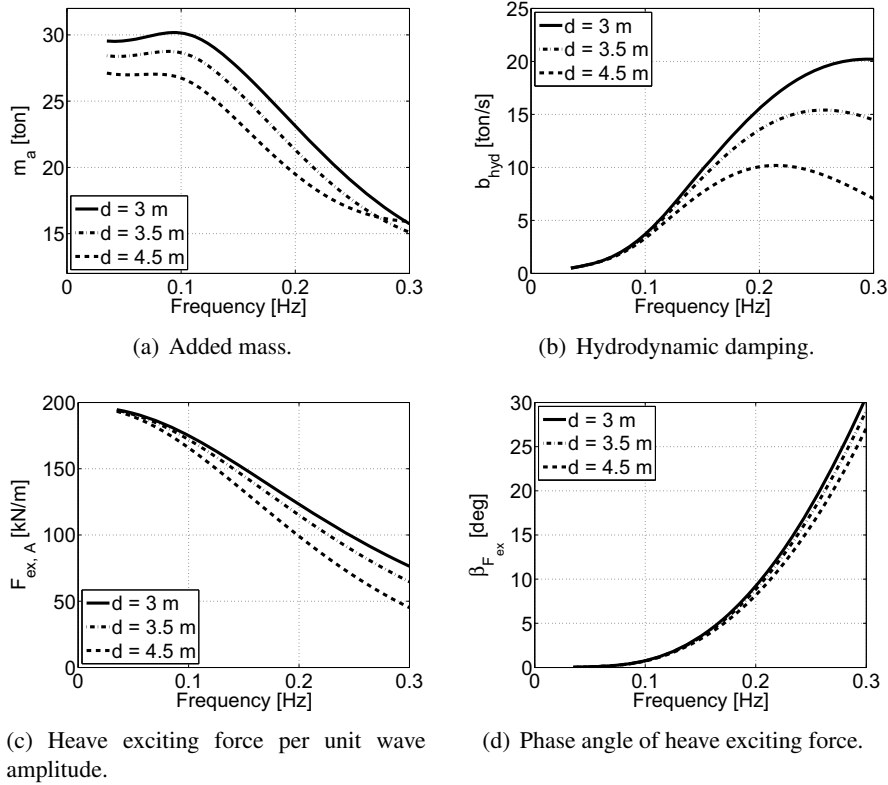


Figure 2.6: Hydrodynamic parameters for the cone-cylinder shape, $D = 5$ m, $d = 3, 3.5, 4.5$ m.

2.6 Power absorption

2.6.1 Response in irregular waves

The response in irregular long-crested waves is obtained by superimposing the responses in regular waves. The wave amplitude of those regular wave components is derived from the JONSWAP spectrum (Section 2.4.2):

$$\zeta_A = 2\sqrt{S_{\zeta_A}(\omega)\Delta\omega} \quad (2.10)$$

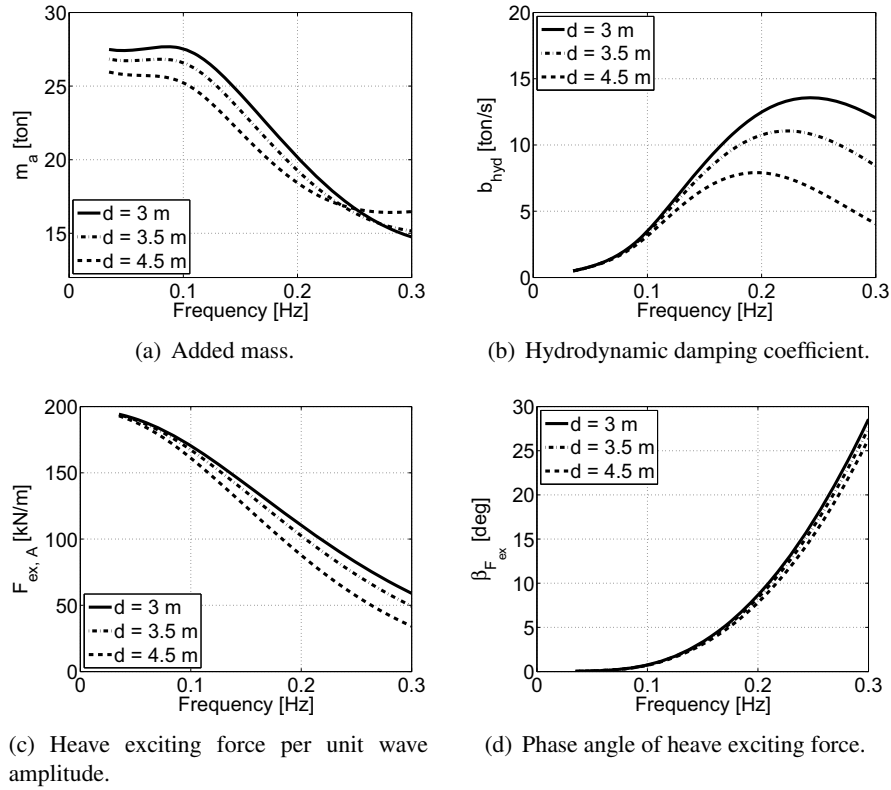


Figure 2.7: Hydrodynamic parameters for the hemisphere-cylinder shape, $D = 5$ m, $d = 3, 3.5, 4.5$ m.

The spectrum has been covered by 40 equidistant frequencies, ranging between 0.22 rad/s and 1.88 rad/s with $\Delta\omega = 0.043$ rad/s (or 0.035 Hz $< f < 0.3$ Hz with $\Delta f = 0.0068$ Hz). For comparison Vantorre and Banasiak et al. [16] applied the superposition principle with 20 frequencies and Ricci et al. [25] with 75 frequencies. It has been observed that simulations based on 20 frequency components are reliable, except in unconstrained conditions. In that case, the buoy resonates and its response is overpredicted for supplementary mass values corresponding to a natural period that is equal to a discrete frequency component close to the peak frequency in the spectrum. Hence, power absorption peaks are observed for those particular values of the natural frequency of the system, which do not occur if the spectrum is composed

of a larger number of frequencies with smaller Δf . In the latter case, the power absorption varies smoothly for varying supplementary mass. Since CPU time is generally not an issue (except when multiple bodies are considered), the number of frequencies for single body simulations has been increased in more recent applications (Chapter 8) to 150 frequencies. The difference in power absorption², obtained with 40 and 150 frequency components, was found to be not significant: in unconstrained conditions the difference was smaller than 1.5 %, in constrained conditions the difference is even smaller than 1 %, which is not necessarily due to the number of frequencies. Such small differences may also be attributed to the selected accuracy settings of the optimizer. However, since the computation time is relatively small in most cases, it is advised to use a large number of frequency components for future work.

The spectrum of the amplitude of the floater position is defined as:

$$S_{z_{Ai}}(\omega) = S_{\zeta_{Ai}}(\omega) \frac{z_{Ai}^2}{\zeta_{Ai}^2} \quad (2.11)$$

Assuming Rayleigh distribution of the floater motion amplitudes, some characteristic values can be obtained such as the significant amplitude of the buoy motion:

$$z_{A,sign} = 2 \sqrt{\int_0^{\infty} S_{z_{Ai}} d\omega} \quad (2.12)$$

In irregular waves, the available power over the diameter D of the point absorber is expressed by [26]:

$$P_{avail,D} = D \int_0^{\infty} \rho g C_g(\omega) S_{\zeta}(\omega) d\omega \quad (2.13)$$

The absorbed power in a regular wave has been given by Eq. (1.71) in Chapter 1. By applying linear superposition of the buoy responses, expression (2.14) for the power absorption in irregular waves can be obtained:

²Power absorption determined on a cone-cylinder shape with waterline diameter 5 m and draft 3 m.

$$P_{abs} = \int_0^{\infty} b_{ext} \omega^2 \left(\frac{z_A}{\zeta_A} \right)^2 S_{\zeta}(\omega) d\omega \quad (2.14)$$

The absorption efficiency, or briefly efficiency, denoted by η , is defined as the ratio of the absorbed power to the incident wave power within the device width:

$$\eta = \frac{P_{abs}}{P_{avail,D}} \quad (2.15)$$

The absorbed power, and hence the efficiency, are influenced by the external damping coefficient, b_{ext} , and the buoy velocity, which is dependent on both b_{ext} and m_{sup} . These two parameters have to be optimized to maximize the power absorption, taking into account several constraints. The optimization is carried out in MATLAB with an exhaustive searching method. Vantorre et al. [16] determined the hydrodynamic parameters with Aquaplan [17] and performed the optimization process in Microsoft Excel. Both methods gave very similar results, which differed usually less than 5 %, except in unconstrained conditions or conditions where the imposed constraints did not have any influence. This is due to the relatively small number of frequencies in [16]. When 20 frequencies are adopted in the MATLAB model, the results correspond well with [16]. Kaasen performed also frequency domain simulations on a single point absorber and on multiple point absorbers [27]. The hydrodynamic parameters are calculated with WAMIT. Comparable simulations have been run in the framework of the SEEWEC project yielding similar results. For instance, the difference in maximum power absorption that has been found for a hemisphere-cylinder shape with $D = 3.5$ m in unconstrained conditions, is less than 1 % compared with the present model.³

2.6.2 Implementation of restrictions

Slamming restriction

Slamming is a phenomenon that occurs when the buoy re-enters the water, after having lost contact with the water surface. The buoy experiences a slam, which may result in very high hydrodynamic pressures and loads. These impacts have a very short duration, with a typical order of magnitude of milliseconds.

³This comparison is based on the results of slide 32 of [27].

Fatigue by repetitive slamming pressures can be responsible for structural damage of the material. More information on slamming will be given in Chapters 6-8.

A restriction has been implemented, requiring that the significant amplitude of each buoy position relative to the free water surface elevation should be smaller than a fraction α of the draft d of the buoy:

$$(z - \zeta)_{A,sign} \leq \alpha \cdot d \quad (2.16)$$

where the index ' $A,sign$ ' stands for significant amplitude and α is a parameter that is arbitrarily chosen equal to unity in this Chapter. This means that slamming is still allowed in the 13.5 % highest waves, if Rayleigh distribution is assumed for the relative buoy positions. In Chapter 8 several levels of slamming restrictions are investigated by varying this α -value.

In order to implement this restriction in the numerical model, the motion of the point absorber relative to the wave needs to be known. Considering a harmonic wave component $\zeta_A \cos\omega t$, this relative buoy motion can be written as:

$$z_{rel,wave} = z_A \cos(\omega t + \beta_{mot}) - \zeta_A \cos\omega t \quad (2.17)$$

where β_{mot} is the phase angle of the buoy position. Using the trigonometric sum formulas, this expression becomes:

$$z_{rel,wave} = (z_A \cos\beta_{mot} - \zeta_A) \cos\omega t - z_A \sin\beta_{mot} \cdot \sin\omega t \quad (2.18)$$

from which the relative motion amplitude can be easily derived:

$$z_{A,rel,wave} = \sqrt{(\zeta_A - z_A \cos\beta_{mot})^2 + z_A^2 \sin^2\beta_{mot}} \quad (2.19)$$

The significant value of this relative motion amplitude can be determined in an analogous way as was done for the absolute motion $z_{A,sign}$ in Eqs. (2.11 - 2.12).

The velocity of the buoy relative to the vertical velocity of the water surface, v_{rel} can be expressed as follows:

$$v_{rel} = -\omega z_A \sin(\omega t + \beta_{mot}) + \omega \zeta_A \sin\omega t \quad (2.20)$$

The amplitude of this relative velocity is:

$$v_{rel,A} = \omega \sqrt{(\zeta_A - z_A \cos \beta_{mot})^2 + (z_A \sin \beta_{mot})^2} \quad (2.21)$$

It will be shown that the slamming restriction might require a decrease of the tuning parameter m_{sup} and/or an increase of the external damping coefficient b_{ext} . Not only the occurrence probability of slamming will be reduced by this measure, but also the magnitude of the associated impact pressures and loads will decrease, since they are dependent on the impact velocity of the body relative to the water particle velocity and this impact velocity will decrease when the control parameters of the buoy are adapted according to the imposed restriction.

Stroke restriction

In practice, many point absorber devices are very likely to have restrictions on the buoy motion, e.g. imposed by the limited height of the rams in case of a hydraulic conversion system or by the limited height of a platform structure enclosing the oscillating point absorbers (e.g. as in Figure 1 of the introductory Chapter). Therefore a stroke constraint is implemented, imposing a maximum value on the significant amplitude of the body motion:

$$z_{A,sign} \leq z_{A,sign,max} \quad (2.22)$$

Three maximum levels are considered: a maximum significant amplitude of 1.34 m, 2.00 m and 2.68 m. Assuming Rayleigh distribution of the buoy motions, this restriction means that a stroke of e.g. 5.00 m is exceeded for 0.09 %, 4.39 % and 17.55 % of the waves, respectively⁴. The first constraint is rather stringent: in less than one oscillation out of 1000 the maximum stroke is exceeded. For comparison, the third stroke constraint is very weak for the same maximum stroke of 5 m: in almost one oscillation out of five the available stroke is surpassed. In practice, when the maximum stroke is nearly reached, an additional mechanism will have to brake the floater motion. The kinetic energy of the floater might be absorbed by e.g. fenders attached to the structure

⁴A maximum stroke of 5.00 m was considered as a realistic constraint within the SEEWEC project.

that encloses the point absorber. When the floater frequently hits the fender, the average power absorption will be negatively influenced, as well as the lifetime of the structure. To reduce the probability of this phenomenon, either a more stringent constraint must be chosen, or a larger available stroke length must be considered. If, for instance, the maximum available stroke length is 10 m, then the latter constraint would correspond to an exceedance probability of 0.09 %, whereas the first constraint ($z_{A,sign,max} = 1.34$ m) would correspond to an exceedance probability of only $0.8 \cdot 10^{-10}\%$. This is clearly too strict and will affect the power absorption significantly. Hence, the relative stringency of a certain constraint depends on the available stroke length. The implementation of constraints on the body motion also increases the reliability of the linear model, which is based on the assumption of small body motions.

Force restriction

In some cases, the optimal control parameters for maximum power absorption, result in very large control forces. The tuning force, in particular, might become very large and can even be a multiple of the damping force. If this tuning force is to be delivered by the PTO, it might result in a very uneconomic design of the PTO system. For this reason it is relevant to study the response of the floaters in case the total control force is restricted. If the force spectrum is expressed as: $S_{F_{A,i}} = F_{A,i}^2 / (2\Delta f)$ and the significant amplitude of the force is defined as $F_{A,sign} = 2\sqrt{\int_0^\infty S_{F_{A,i}}(f)df}$, then the significant amplitude of the damping and tuning force, respectively, are given by:

$$F_{bezt,A,sign} = 2\sqrt{\int_0^\infty S_{F_{bezt,A}}(f)df} \quad (2.23)$$

$$F_{msup,A,sign} = 2\sqrt{\int_0^\infty S_{F_{msup,A}}(f)df} \quad (2.24)$$

A restriction will be imposed on the significant amplitude of the total force,

expressed as:

$$F_{tot,A,sign} = 2 \sqrt{\int_0^{\infty} (S_{F_{bext,A}}(f) + S_{F_{msup,A}}(f)) df} \quad (2.25)$$

Simulation results will be presented where $F_{tot,A,sign}$ is limited⁵ to 100 kN and 200 kN.

In case the tuning is not provided by the generator, e.g. when applying latching or a supplementary inertia, it would be appropriate to consider separate restrictions on the tuning and damping force. However, in that case, no major problems are expected, since the damping force is found to be small, as aforementioned, and the tuning force is expected to be significantly smaller when latching is applied or even inexistent when a supplementary inertia is added to the system.

The equation of motion of a heaving point absorber with respect to a floating reference (e.g. a floating platform) is given in Appendix B. It concerns a simplified case in which the point absorber is positioned in the centre of the platform. Hence, only the heave mode of the platform needs to be taken into account. More general applications of oscillating point absorbers with respect to a floating platform can be found in [21] and [27].

2.6.3 Influence of design parameters

Buoy shape and draft

Figure 2.8 shows the simulation results for the two buoy shapes with varying draft. Optimal control parameters have been determined, taking into account the slamming restriction and the stroke restriction defined as: $z_{A,sign,max} = 2.00$ m. All buoys have a diameter of 5 m.

Figure 2.8(a) presents the power absorption versus the significant wave height. The H_s -values are associated with peak periods as defined in Table 2.1. The results of the cone-cylinder are presented in solid lines, those of the hemisphere-cylinder are given in dashed lines. For the three different drafts, it turns out that the cone-cylinder performs slightly better than the hemisphere-cylinder shape, however, the difference between both shapes is very small

⁵In the framework of the SEEWEC project, limitations of the total control force to the presented magnitudes were considered as reasonable constraints.

(between 4 % and 8%). Furthermore, the power absorption is larger for smaller drafts. This was expected, since it was observed from Figures 2.6(b)-2.6(c) that the hydrodynamic damping coefficient and heave exciting force are larger for smaller drafts. The presented figures do not take into account any losses due to mechanical friction, viscous losses, turbine nor generator losses in the conversion system and are therefore not equal to the produced electrical power.

The absorption efficiency is shown in Figure 2.8(b). Figures 2.8(c) and 2.8(d), show the significant amplitude of the buoy position and of the relative buoy position divided by the draft of the buoy, respectively. Note that the applied stroke restriction is dominant on the slamming restriction: the significant amplitude of the relative buoy position is smaller than the draft of the buoy for all sea states; it is never equal to the draft, because the applied stroke constraint appears to be more stringent. Indeed, the absolute motion of the buoy is limited for the intermediate and larger sea states, as can be seen in Figure 2.8(c). This explains the drop of the absorption efficiency for larger sea states. In the smaller sea states, the buoys oscillate in unconstrained conditions. The absorption efficiency is large, however, smaller than the theoretical maximum absorption efficiency in regular waves ($L/(2\pi D)$, Chapter 1), since the applied control in irregular waves is always ‘suboptimal’ due to the use of frequency-invariant parameters of supplementary mass and external damping. Hence, pure resonance cases as for regular waves are not obtained. It is expected that especially in these smaller sea states the power absorption can be increased by applying frequency-dependent control forces.

The control parameters are presented in Figures 2.8(e) and 2.8(f). Note that the peak periods of the three smallest sea states are equal, yielding the same optimal values for the external damping and supplementary mass. The peak period of the sixth and seventh sea states ($H_s = 2.75$ m and 3.25 m) are also equal, however, in order to satisfy the stroke restriction, the supplementary mass is slightly decreased and the external damping is increased for $H_s = 3.25$ m compared to $H_s = 2.75$ m. When comparing Figures 2.6(b) and 2.7(b) with Figure 2.8(e), it may be observed that the external damping coefficient is significantly larger than the hydrodynamic damping coefficient for the more energetic sea states. These large values are required to satisfy the stroke restriction.

The significant amplitude of the damping and tuning force is shown in Figures 2.8(g) and 2.8(h), respectively. The significant amplitude of the total

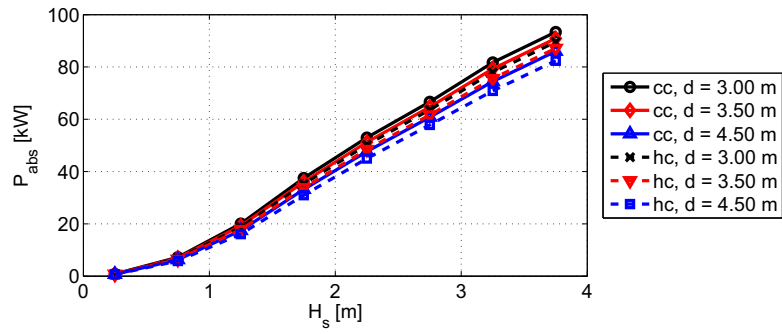
force is plotted in Figure 2.8(i). This total force is particularly relevant in case the tuning force has to be provided by the generator, apart from the damping force. Except for the large sea states, the tuning force is considerably larger than the damping force. For this reason it might of interest to realize the tuning in another way (e.g. with latching, by means of a flywheel, etc.) than with the generator, in order to avoid an uneconomic design of the latter. Further considerations on this aspect will be mentioned in Chapter 4. In the intermediate and large waves, the tuning force remains more or less constant and the damping force is considerably increased compared to the smaller waves as a result of the stroke constraint.

Similar results are presented in Appendix C for the five different diameters and for three combinations of constraints:

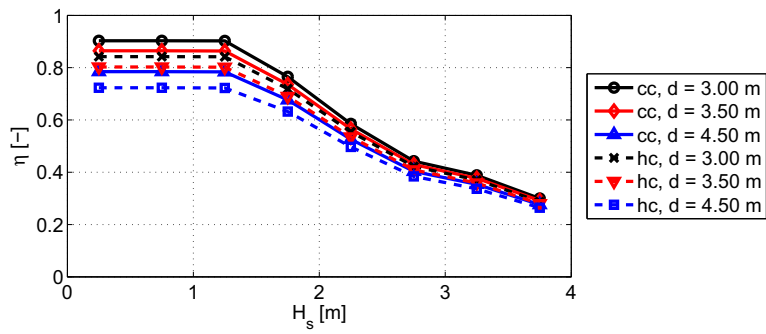
- (1) only the slamming restriction,
- (2) the slamming restriction, combined with the intermediate stroke restriction, i.e. $z_{A,sign,max} = 2.00$ m,
- (3) the slamming restriction, combined with the same stroke restriction and the least stringent force constraint, i.e. $F_{tot,A,sign,max} = 200$ kN.

Buoy diameter

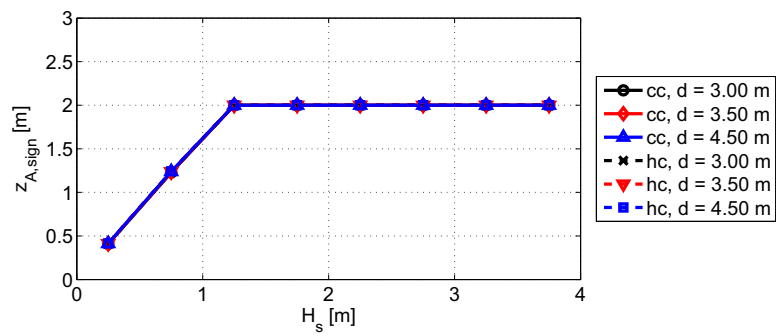
The impact of the diameter is illustrated in Figure 2.9 displaying the power absorption of a cone-cylinder with diameters of 3 and 5 m. Whereas the selected drafts seemed to limitedly influence the power absorption, changing the diameter has a significant effect on the absorbed power. When comparing two buoys with the same draft ($d = 3.5$ m), the volume ratio is 2.0 and the ratio of the absorbed power varies between a factor of 1.8 (smallest sea state) and 2.7 (largest sea state). Hence, the smallest diameter is only beneficial in the two smallest sea states, assuming the volume is a measure for the material cost. However, since each unit is assumed to be equipped with its own PTO-system, important additional costs per unit will exist, most probably making the larger diameter also economically more attractive in the smaller sea states. Attention must be drawn to the fact that the influence of the diameter on the power absorption depends on the applied restrictions. In Appendix C, simulation results are presented for a case where also a force restriction is applied. In that case, the advantage of the larger diameters is somehow diminished, since larger diameters involve larger forces, resulting in an increased penalty when the same force restrictions are applied as for the smaller buoys. Hence, it



(a) Power absorption.

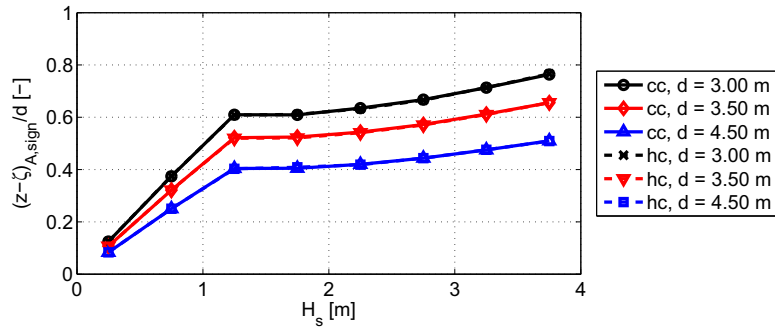


(b) Absorption efficiency.

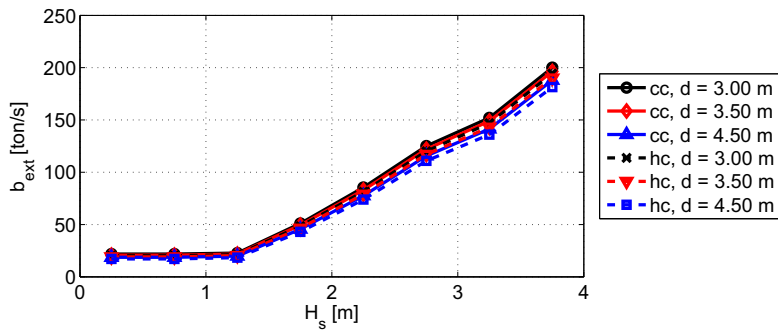


(c) Significant amplitude of the buoy position.

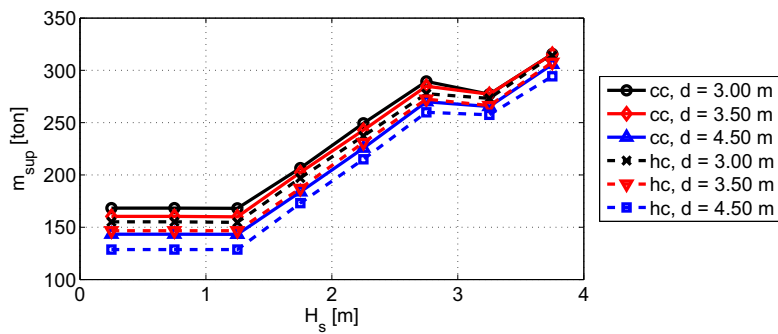
Figure 2.8: Figure continues on next page.



(d) Significant amplitude of the relative buoy position divided by the draft.

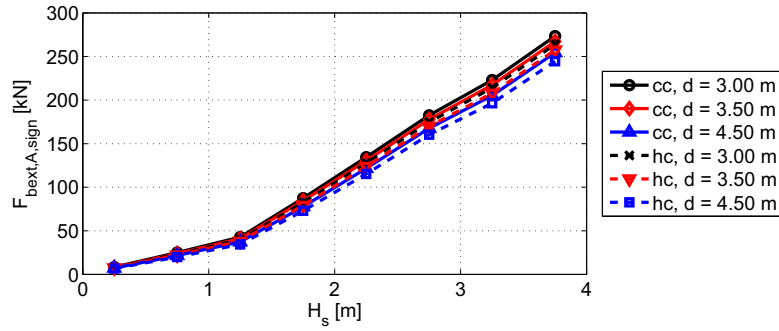


(e) External damping coefficient.

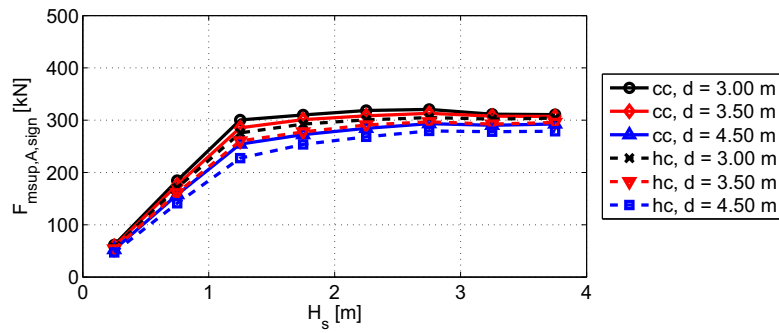


(f) Supplementary mass.

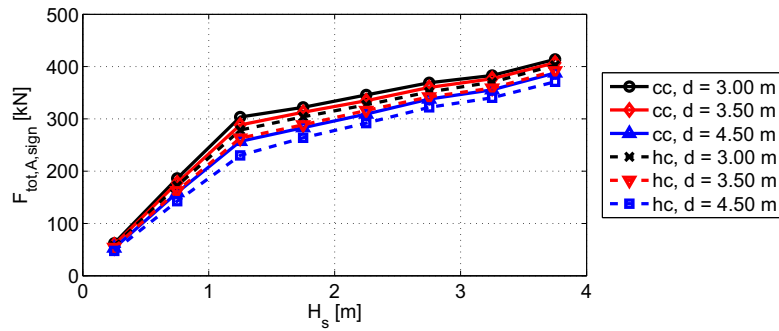
Figure 2.8: Figure continues on next page.



(g) Significant amplitude of the damping force.



(h) Significant amplitude of the tuning force.



(i) Significant amplitude of the total control force.

Figure 2.8: Comparison between cone-cylinder and hemisphere-cylinder for different drafts. H_s -classes: defined in Table 2.1, diameter = 5 m, constraints: slamming restriction, stroke restriction: $z_{A,sign,max} = 2.00$ m, no force constraint.

would be beneficial to adjust the force restrictions to the dimensions of the buoy, however, this will result in raised costs for larger buoys. To conclude, the optimum diameter has to be determined for a particular device and a particular location, taking into account the relevant restrictions and incorporating a cost assessment. In the next Chapters of this work, a diameter of 5 m will generally be adopted.

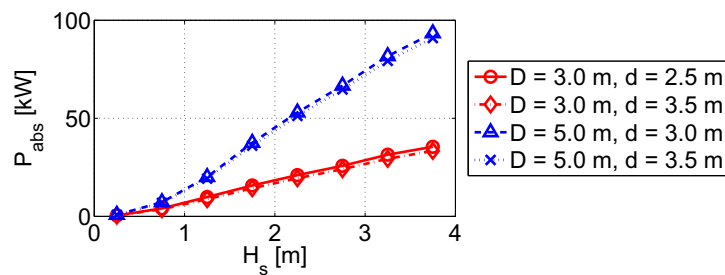


Figure 2.9: Power absorption for the cone-cylinder: comparison between diameters. H_s -classes: defined in Table 2.1.

2.6.4 Influence of restrictions

The effect of different restrictions will be investigated for the cone-cylinder shape with a diameter of 5 m and a draft of 3 m. The evaluated restriction combinations are:

- **SL:** Slamming constraint, no stroke nor force constraint.
- **SL-STR1.34:** Slamming constraint, stroke constraint: $z_{A,sign,max} = 1.34$ m, no force constraint.
- **SL-STR2.00:** Slamming constraint, stroke constraint: $z_{A,sign,max} = 2.00$ m, no force constraint.
- **SL-STR2.68:** Slamming constraint, stroke constraint: $z_{A,sign,max} = 2.68$ m, no force constraint.
- **SL-STR2.00-F100:** Slamming constraint, stroke constraint: $z_{A,sign,max} = 2.00$ m, force constraint: $F_{tot,A,sign,max} = 100$ kN.

- **SL-STR2.00-F200:** Slamming constraint, stroke constraint: $z_{A,sign,max} = 2.00$ m, force constraint: $F_{tot,A,sign,max} = 200$ kN.

Simulation results are presented in Figure 2.10. The first graph (Figure 2.10(a)) shows the average power that can be absorbed with optimized control parameters satisfying the constraints. As noticed before, the slamming constraint is the weakest constraint in this case. For bodies with a very small draft, this constraint may, however, transform into a quite stringent restriction. The power absorption for limited stroke cases is presented in black, showing that a large amount of power is lost when only a small stroke is possible. The most stringent constraints are clearly the force restrictions, given in red. The penalty of the most stringent force constraint is extremely large. The tuning and damping force have to be so small that serious amounts of power cannot be absorbed anymore in the intermediate and higher sea states. This is also illustrated in Figure 2.10(b) where the power absorption efficiency is shown. The large available power in the higher sea states is not efficiently absorbed.

Figures 2.10(c) and 2.10(d) show the significant amplitude of the buoy position and of the relative buoy position divided by the buoy draft, respectively. It can be seen from which sea state the stroke constraints and slamming constraint, respectively, start to effectuate their influence. The external damping coefficient and supplementary mass are given in Figures 2.10(e) and 2.10(f). It is remarkable how the damping coefficient is increased in order to satisfy the stroke constraints. In order to fulfill the force constraints, the damping is kept rather constant, but the supplementary mass is extremely small. The value of the supplementary mass even decreases for increasing H_s and thus for generally increasing T_p . This means that the buoy is tuned further away from resonance in the large sea states to avoid very large control forces. The damping and tuning forces are indeed significantly smaller in those cases where the force restrictions apply, as can be seen in Figures 2.10(g) and 2.10(h). The significant amplitude of the total control force is given in Figure 2.10(i). However, note the very large tuning forces that are required to deliver the power levels, associated with the weakest constraints (SL and SL-STR2.68). Attention should be drawn to the fact that these are only the significant amplitudes of the tuning forces. The maximum forces that are involved are even larger. Hence, it is very unlikely that the generator will be designed to deliver these tuning forces and the corresponding instantaneous, large power levels. As stated before, it is expected to be more beneficial to

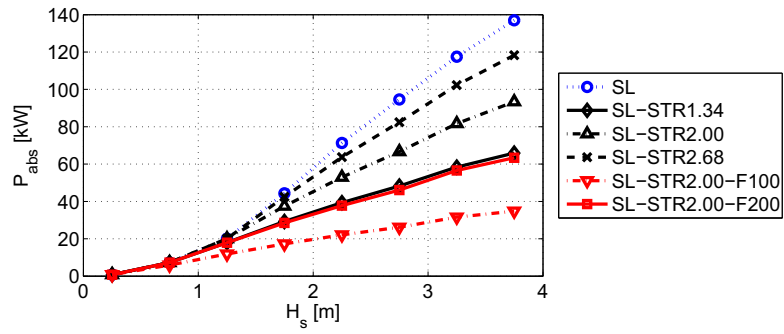
realize the control with a separate control mechanism, e.g. through latching.

Figure 2.11(a) shows the power absorption⁶ as a function of the supplementary mass and external damping coefficient for sea state 4, i.e. $H_s = 1.75$ m and $T_p = 7.40$ s. The magnitude of the power absorption is indicated by the colour bar legend. Note that similar power absorption values can be obtained with different combinations of supplementary mass and external damping coefficients. The dotted contour line on the graph represents the slamming constraint. The area enclosed by this line has to be avoided to fulfill the slamming restriction. The optimal power absorption in the remaining area is 44 kW for this sea state, which is indicated by a circle on the graph. The Figure clearly illustrates the effect of tuning the point absorber, which is effectuated here by adding inertia (m_{sup}) to the device. The tuning ratio T_n/T_p in this case is 99 %. The power that can be absorbed with an untuned buoy is significantly smaller than that of a tuned buoy.

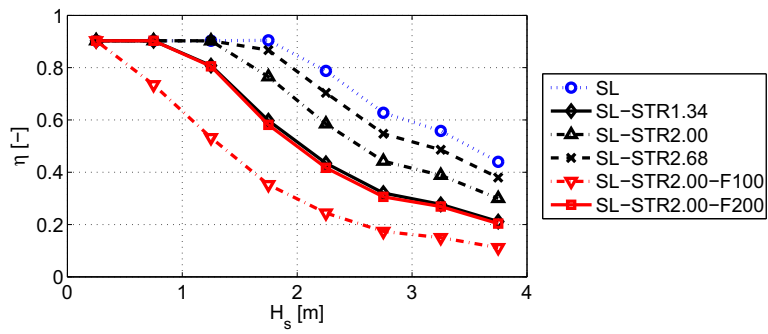
When adding the stroke restrictions to this graph, Figure 2.11(b) is obtained. To fulfill these restrictions, the damping is considerably raised, and the tuning is slightly decreased. The optimal power absorption levels drop from 42 kW to 37 kW and 29 kW when going from the weakest to the most stringent stroke constraint. In Figure 2.11(c) the two force constraints are displayed as well. As observed before, the force restrictions require much smaller values of the supplementary mass. The tuning ratio T_n/T_p drops to 87 % and 67 %, respectively, considering the aforementioned force constraints ($F_{tot,A,sign} \leq 200$ kN and $F_{tot,A,sign} \leq 100$ kN). The power that can be absorbed within these constraints is only 28 kW and 17 kW, respectively, as indicated with the red circles.

Similar results are displayed in Figure 2.12 for sea state 7 ($H_s = 3.25$ m and $T_p = 8.81$ s). The optimum values are again indicated with circles. The influence of the restrictions is even more significant for this more energetic sea state. The maximum power that can be absorbed, by imposing only the slamming constraint is 117 kW ($T_n/T_p = 94$ %). When the stroke restrictions are taken into account (from weak to stringent) the power absorption decreases from 102 kW to 82 kW and finally to 58 kW. Note that the contour lines around the optimum values are locally parallel with the power absorption colours. This means that similar power absorption values might be obtained with slightly different control parameters, dependent on the accuracy settings

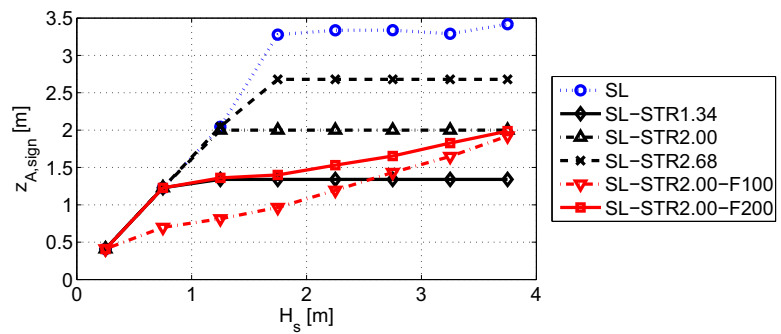
⁶These plots are based on 150 frequency components.



(a) Power absorption.

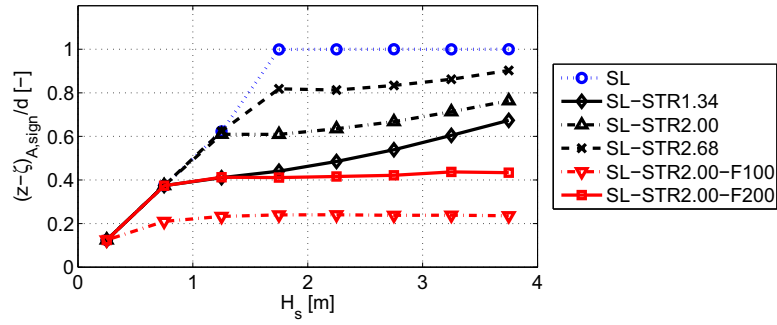


(b) Absorption efficiency.

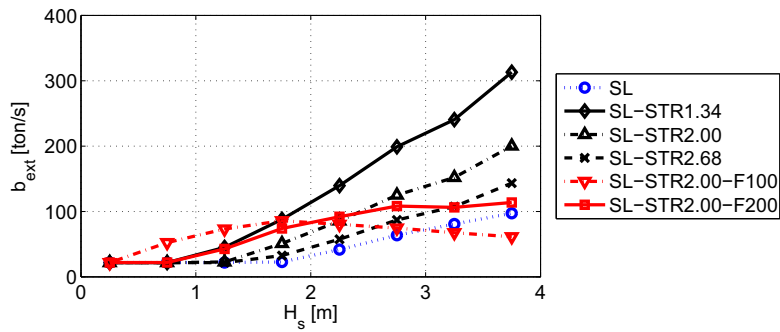


(c) Significant amplitude of the buoy position.

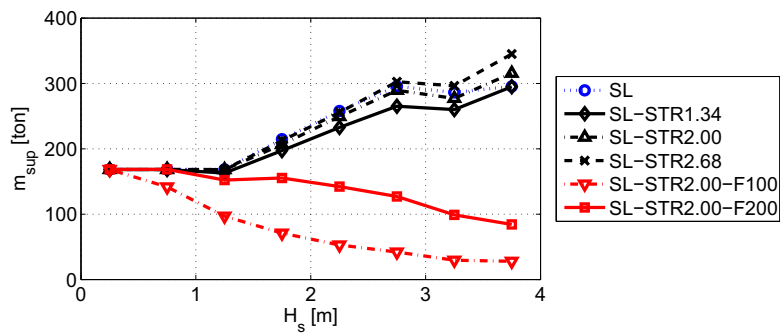
Figure 2.10: Figure continues on next page.



(d) Significant amplitude of the relative buoy position divided by the draft.

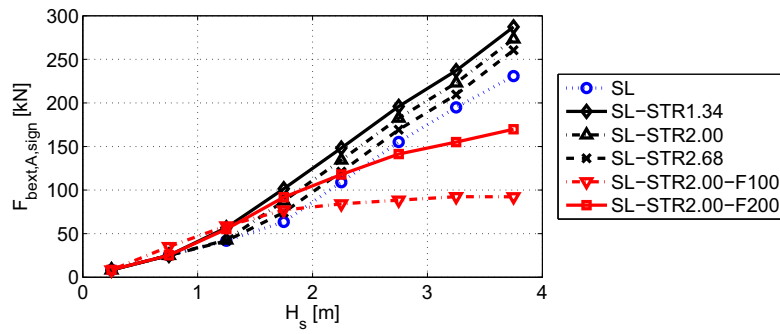


(e) External damping coefficient.

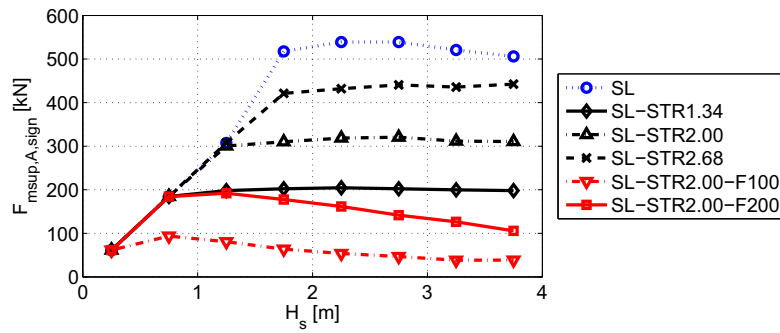


(f) Supplementary mass.

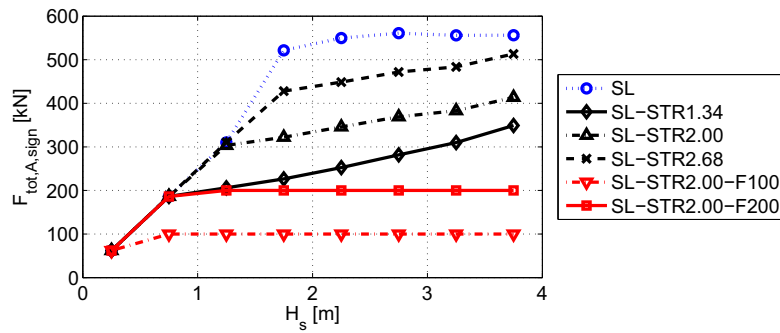
Figure 2.10: Figure continues on next page.



(g) Significant amplitude of the damping force.

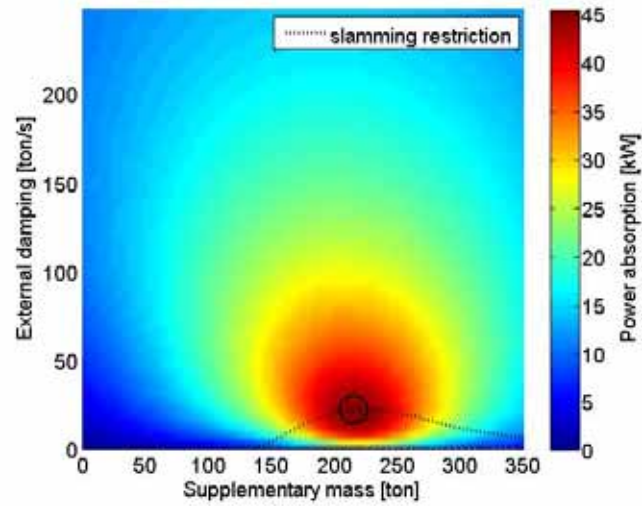


(h) Significant amplitude of the tuning force.

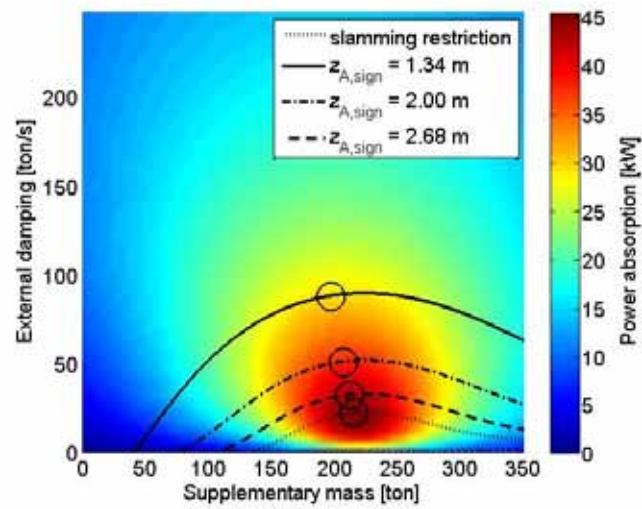


(i) Significant amplitude of the total control force.

Figure 2.10: Evaluation of different restrictions for the cone-cylinder shape. H_s -classes: defined in Table 2.1, diameter = 5 m, draft = 3 m.

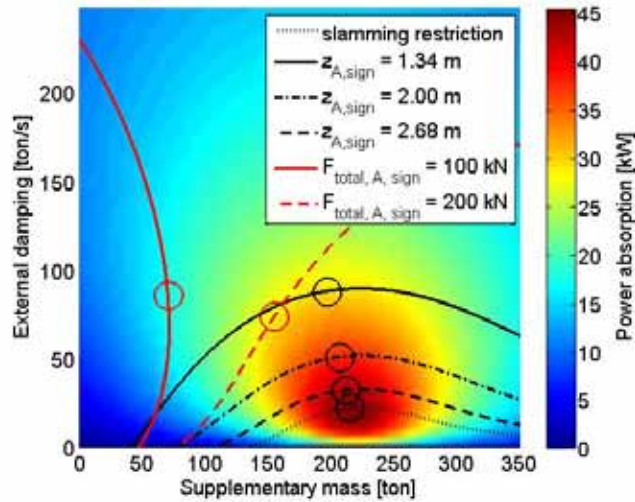


(a) Slamming restriction.



(b) Slamming and stroke restriction.

Figure 2.11: Figure continues on next page.



(c) Slamming, stroke and force restriction

Figure 2.11: Power absorption [kW] versus b_{ext} [ton/s] and m_{sup} [ton]. Buoy: cc, $D = 5$ m, $d = 3$ m, H_s -class: $H_s = 1.75$ m and $T_p = 7.40$ s.

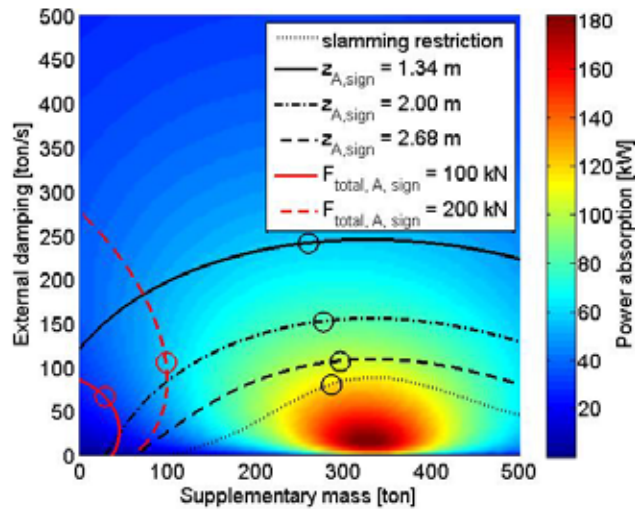


Figure 2.12: Power absorption [kW] versus b_{ext} [ton/s] and m_{sup} [ton]. Buoy: cc, $D = 5$ m, $d = 3$ m, H_s -class: $H_s = 3.25$ m and $T_p = 8.81$ s.

of the optimizer. The power absorption drops even further when the force restrictions are taken into account: the weakest constraint gives a maximum power level of 57 kW ($T_n/T_p = 63\%$), the most stringent constraint allows only to absorb 32 kW ($T_n/T_p = 47\%$). This is about one third of the power that can be absorbed when only the weakest stroke constraint is implemented. Hence, the impact of the constraints is illustrated once more. The graphs are also useful to get an idea of the sensitivity of the control parameters. In practical cases the applied control parameters might be erroneously slightly different from the intended control parameters and the influence of ‘mistuning’ effects can be derived from those figures.

2.7 Conclusion

By means of a linear frequency domain model, the behaviour of a heaving point absorber is simulated and the absorbed power is assessed. The hydrodynamic parameters of the oscillating buoys are derived with the BEM code WAMIT. A conical and hemispherical buoy shape are evaluated, both with a cylindrical upper part. Five different waterline diameters (between 3 m and 5 m) and three different drafts are considered. Three types of constraints are introduced: a slamming restriction, a stroke restriction and a force restriction. The first constraint reduces the occurrence probability of emergence events. The stroke restriction limits the point absorber stroke length and the force constraint limits the total force that is required to realize the control and damping of the system. The influence of several combinations of these restrictions is evaluated.

The main conclusions that may be drawn are:

- Only small differences in performance between the conical and hemispherical shapes are noticed. Generally, the cone-cylinder performs slightly better than the hemisphere-cylinder.
- The power absorption rises for larger waterline diameters and smaller drafts (if the draft is large enough to avoid slamming). However, the waterline diameter significantly influences the power absorption, whereas the impact of the evaluated buoy drafts appeared to be rather limited.
- For the considered test cases, the slamming restriction had a smaller impact on the power absorption compared to the stroke restrictions. However, the stringency of this restriction is dependent on the draft of the buoy and on the probability of slamming that can still be allowed. These aspects will be studied

more in detail in Chapter 8.

- The stroke restrictions decrease the power extraction significantly, especially in more energetic waves.
- The required tuning forces have a much higher contribution to the total force than the required damping forces. Restricting those forces may have a very negative influence on the power absorption. Hence, it might be advantageous to realize the tuning of the system in another way than by making use of the PTO.

Bibliography

- [1] De Backer G., Vantorre M., Banasiak R., Beels C., De Rouck J., Numerical modelling of wave energy absorption by a floating point absorber system. In: 17th International Offshore and Polar Engineering Conference, Portugal, 2007.
- [2] De Backer G., Vantorre M., Banasiak R., De Rouck J., Beels C., Verhaeghe H., Performance of a point absorber heaving with respect to a floating platform. In: 7th European Wave and Tidal Energy Conference, Portugal, 2007.
- [3] Payne G., Taylor J., Bruce T., Parkin P., Assessment of boundary-element method for modelling a free-floating sloped wave energy device. part 2: Experimental validation. *Ocean Engineering* 2008;35:342–357.
- [4] Standing M., Use of potential flow theory in evaluating wave forces on offshore structures, in *Power from Sea Waves*. B. Count: Academic Press, 1980.
- [5] Pizer D., The numerical prediction of the performance of a solo duck. In: *European Wave Energy Symposium*, Edingburgh, 1993, pp. 129–137.
- [6] Yemm R., Pizer D., Retzler C., The WPT-375 - a near-shore wave energy converter submitted to Scottish Renewables Obligation 3, 1998. In: *3rd European Wave Energy Conference*, vol 2, Greece, 1998, pp. 243–249.
- [7] Pizer D., Retzler C., Yemm R., The OPD Pelamis: Experimental and numerical results from the hydrodynamic work program. In: *4th European Wave and Tidal Energy Conference*, Denmark, 2000, pp. 227–234.
- [8] Lee C., Newman J., Nielsen F., Wave interactions with an oscillating water column. In: *6th International Offshore and Polar Engineering Conference*, vol 1, USA, 1996, pp. 82–90.

- [9] WAMIT user manual: <http://www.wamit.com/manual.htm>.
- [10] Brito-Melo A., Sarmiento A., Clément A., Delhommeau G., Hydrodynamic analysis of geometrical design parameters of oscillating water column devices. In: 3rd European Wave Energy Conference, vol 1, Greece, 1998, pp. 23–30.
- [11] Delhommeau G., Ferrant P., Guilbaud M., Calculation and measurement of forces on a high speed vehicle in forced pitch and heave. *Applied Ocean Research* 1992;14(2):119–126.
- [12] Delauré Y., Lewis A., A comparison of OWC response prediction by a Boundary Element Method with scaled model test results. In: 4th European Wave Energy Conference, Denmark, 2000, pp. 275–282.
- [13] Delauré Y., Lewis A., 3D hydrodynamic modelling of fixed oscillating water column wave power plant by boundary element methods. *Ocean Engineering* 2003;30:309–330.
- [14] Arzel T., Bjarte-Larsson T., Falnes J., Hydrodynamic parameters for a floating wec force-reacting against a submerged body. In: 4th European Wave and Tidal Energy Conference, Denmark, 2000, pp. 267–274.
- [15] Justino P., Clément A., Hydrodynamic performance of small arrays of submerged spheres. In: 5th European Wave Energy Conference, Ireland, 2003, pp. 266–273.
- [16] Vantorre M., Banasiak R., Verhoeven R., Modelling of hydraulic performance and wave energy extraction by a point absorber in heave. *Applied Ocean Research* 2004;26:61–72.
- [17] Carrico V., Maisonneuve J., Aqua+, User's manual. SIREHNA, 1995.
- [18] Payne G., Taylor J., Bruce T., Parkin P., Assessment of boundary-element method for modelling a free-floating sloped wave energy device. part 1: Numerical modelling. *Ocean Engineering* 2008;35:333–341.
- [19] Clément A., Babarit A., Gilloteaux J.C., Josset C., Duclos G., The SEAREV wave energy converter. In: 6th European Wave and Tidal Energy Conference, Ireland, 2003, pp. 81–89.

- [20] Clément A., Using differential properties of the green function in seakeeping computational codes. In: 7th International Conference on Numerical Ship Hydrodynamics, France, 1999, volume 6, pp. 1–15.
- [21] Taghipour R., Arswendy A., Devergez M., Moan T., Efficient frequency-domain analysis of dynamic response for the multi-body wave energy converter in multi-directional waves. In: The 18th International Offshore and Polar Engineering Conference, 2008.
- [22] Payne G., Numerical modelling of a sloped wave energy device. Ph.D. thesis, The University of Edinburgh, United Kingdom, 2006.
- [23] MultiSurf user manual and tutorials:
<http://www.multisurf.com/tutorials.htm>.
- [24] Liu Z., Frigaard P., Random seas. Aalborg University, 1997.
- [25] Ricci P., Saulnier J.B., Falcao A., Point-absorber arrays: a configuration study off the Portuguese west-coast. In: 7th European Wave and Tidal Energy Conference, Portugal, 2007.
- [26] Crabb J., Synthesis of a directional wave climate. B. Count: Academic Press, 1980.
- [27] Kaasen K., Solaas F., Presentation of MARINTEK work and plans. SEEWEC Project Technical Committee meeting (confidential), 2008.

CHAPTER 3

Time domain model: implementation

★ ★ ★

In this Chapter the implementation of a time domain solver is described. The equation of motion of the point absorber buoy is expressed with Cummins' integro-differential equation. The hydrodynamic parameters are determined with the boundary element package WAMIT and its F2T tool. Prony's method has been applied to transform the integro-differential equation into a set of ordinary differential equations that are solved with the common fourth-order Runge-Kutta method. A comparison between the results obtained with the frequency and time domain models is presented.

3.1 Introduction

Up to now, in the majority of applications, frequency domain models have been used to describe the behaviour of wave energy converters (WECs) [1]. However, the use of time domain models is indispensable in some cases, e.g. when non-linear effects need to be included, such as non-linear power take-off forces or viscous forces. Time domain implementations are also required if time series responses are of interest, or when responses in transient regime are important. The most complete approach is probably offered by Computational Fluid Dynamics (CFD) models, dealing with -approximations of- the Navier-Stokes equations. Since CFD models are complex and time-

consuming, even with current computer capacity, the use of boundary element methods combined with potential theory is still very important. Most authors have used the latter approach to model the behaviour of a WEC in time domain [2–7] and also the presented implementation is based on this approach.

3.2 Equation of motion

With linear theory, the equation of motion of a floating body, oscillating in heave mode is written as (see Chapter 1):

$$m \frac{d^2 z}{dt^2} = F_{ex} + F_{rad} + F_{res} + F_{damp} + F_{tun} \quad (3.1)$$

If the power take-off forces are assumed linear and the body is responding to a harmonic excitation, the ordinary differential equation has an analytical solution, as described in Chapter 1 and the time-dependent response in irregular waves can be obtained with the superposition principle. However, when non-linear effects are included, e.g. in F_{damp} or F_{tun} , the superposition principle cannot be applied. Therefore, in naval hydrodynamics the body response in irregular seas is often expressed as an integro-differential equation, based on Cummins' decomposition [8]. For a heaving point absorber, this results in:

$$\begin{aligned} & (m + m_{a,\infty}) \frac{d^2 z(t)}{dt^2} + F_{damp} \left(\frac{d^2 z(t)}{dt^2}, \frac{dz(t)}{dt}, z(t) \right) \\ & + F_{tun} \left(\frac{d^2 z(t)}{dt^2}, \frac{dz(t)}{dt}, z(t) \right) + \int_0^t K_r(t - \tau) \frac{dz(\tau)}{d\tau} d\tau + kz(t) = F_{ex}(t) \end{aligned} \quad (3.2)$$

The radiation forces are expressed as an instantaneous added mass term $m_{a,\infty} \frac{d^2 z(t)}{dt^2}$ and a convolution product $\int_0^t K_r(t - \tau) \frac{dz(\tau)}{d\tau} d\tau$, where $m_{a,\infty}$ is the infinite frequency limit of the added mass and K_r the radiation impulse response function (IRF), also called radiation force kernel, retardation function or memory function. The radiation impulse response function (IRF) can be computed directly in time domain with boundary element methods such as ACHIL3D [9] or TiMIT [10]. The radiation IRF can also be obtained indirectly by Fourier transformation of the frequency domain hydrodynamic parameters

of added mass and damping, which can be computed with frequency domain BEM codes like WAMIT [11] and AQUAPLUS [12] as pointed out previously. In that case the memory function K_r is obtained from [8]:

$$K_r(t) = \frac{2}{\pi} \int_0^{\infty} b_{hyd}(\omega) \cos(\omega t) d\omega \quad (3.3)$$

where b_{hyd} is the hydrodynamic damping coefficient. The indirect method has been applied and the frequency to time domain (F2T) utility provided by WAMIT has been used to determine K_r . Figure 3.1 shows the radiation impulse response function for a heaving hemisphere with radius 1 m, determined by WAMIT F2T. The correspondence with the result obtained with Achil3D is very satisfying. The difference between both curves is displayed by making use of the y -axis on the right-hand side. Mind the different scale of this axis compared to the left y -axis.

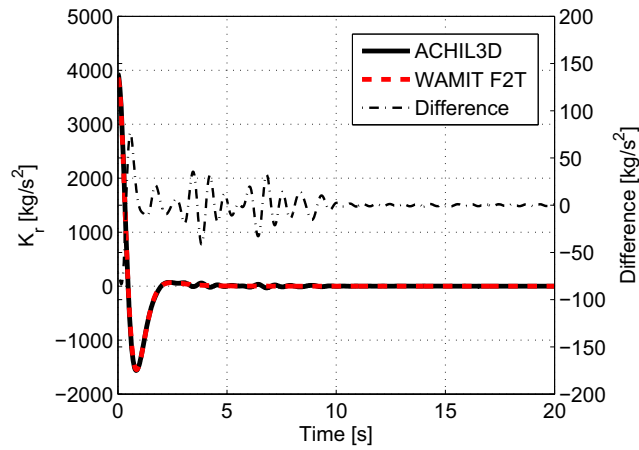


Figure 3.1: Radiation impulse response function for a hemisphere ($R = 1$ m) oscillating in heave mode.

3.3 Implementation

3.3.1 Prony's method

In order to solve Eq. (3.2) directly, the solution of the convolution integral has to be known at every time step, which might require considerable CPU time. Therefore, the impulse response function is approximated by a sum of exponential functions with Prony's method and the integro-differential equation can be transformed into a system of ordinary differential equations (ODEs), as explained below. The method has been developed by Duclos and Clément et al. [13] from the Ecole Centrale de Nantes. Apart from this method, other techniques exist to obtain a state-space representation of Eq. (3.2), e.g. the method of Yu and Falnes [14]. However, the method by Duclos and Clément et al. [13] is applied here, since it is very fast and efficient, as stated by Ricci [2]. For completeness, the algorithm of Prony is included in Appendix D.

With Prony's method, the retardation function, K_r , is expressed as:

$$K_r(t) = \sum_{i=1}^{N_e} \alpha_i e^{\beta_i t} \quad (3.4)$$

with N_e the number of exponential functions. The couples (α_i, β_i) are either real values, either complex values. In the latter case they are always associated with a complex conjugate couple.

Introducing $I(t)$ as:

$$I(t) = \int_0^t K_r(t - \tau) \frac{dz(\tau)}{d\tau} d\tau \quad (3.5)$$

and combining equations (3.4) and (3.5), we get:

$$I(t) = \int_0^t \sum_{i=1}^{N_e} \alpha_i e^{\beta_i(t-\tau)} \frac{dz(\tau)}{d\tau} d\tau$$

$$I(t) = \sum_{i=1}^{N_e} \int_0^t \alpha_i e^{\beta_i(t-\tau)} \frac{dz(\tau)}{d\tau} d\tau \quad (3.6)$$

$I_i(t)$ is defined as:

$$I_i(t) = \int_0^t \alpha_i e^{\beta_i(t-\tau)} \frac{dz(\tau)}{d\tau} d\tau \quad (3.7)$$

Deriving the latter expression to time results in:

$$\dot{I}_i = \beta_i I_i + \alpha_i \frac{dz(t)}{dt} \quad (3.8)$$

In this way the convolution integral can be replaced by a sum of first order differential equations with constant coefficients:

$$\begin{cases} I = \sum_{i=1}^{N_e} I_i \\ \dot{I}_i = \beta_i I_i + \alpha_i \frac{dz(t)}{dt} \\ I_i(0) = 0 \end{cases} \quad (3.9)$$

With $y_1 = z(t)$ and $y_2 = \frac{dz(t)}{dt}$, the system of differential equations to be solved, can be written as:

$$\begin{cases} \dot{y}_1 = y_2 \\ \dot{y}_2 = \frac{F_{ex}(t) - ky_1 - F_{damp} - F_{tun} - \sum_{i=1}^{N_e} I_i}{m + m_{a,\infty}} \\ \dot{I}_1 = \beta_1 I_1 + \alpha_1 y_2 \\ \vdots \\ \dot{I}_{N_e} = \beta_{N_e} I_{N_e} + \alpha_{N_e} y_2 \end{cases} \quad (3.10)$$

These differential equations are numerically integrated with the fourth-order Runge-Kutta method. The implementation has been carried out in MATLAB [15].

3.3.2 Selection of exponentials

With Prony's method we approximate the radiation kernel by a sum of a hundred or two hundred exponential functions at first. Thereafter a selection is made of a few couples (α_i, β_i) who have the most important contribution.

To evaluate the quality of the approximation the relative error is calculated at each time step:

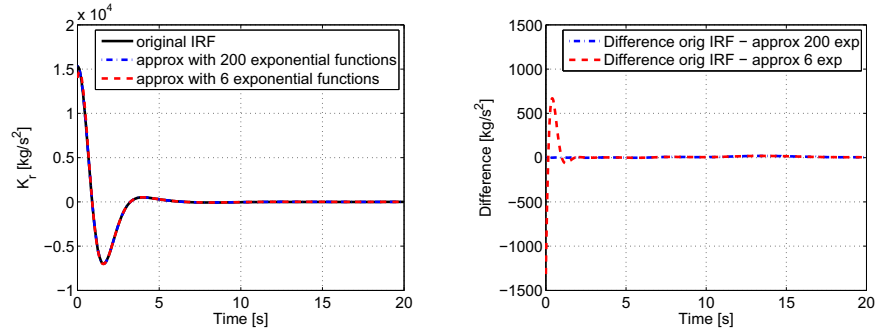
$$E_k = \frac{|\sum_{i=1}^{N_e} \alpha_i e^{\beta_i t_k} - K_r(t_k)|}{\max_{t_k \in [0, t_{N_t}]} |K_r(t_k)|} \quad (3.11)$$

In order to have an idea of the overall error, the mean relative error is calculated as:

$$E = \frac{1}{N_t} \sum_{k=1}^{N_t} E_k \quad (3.12)$$

where N_t is the number of time steps. The number of exponential functions can be reduced significantly without exceeding a predefined mean relative error level. An example is given in Figure 3.2(a) for a hemisphere with diameter 5 m and a cylindrical upper part of 0.5 m. The original radiation IRF, calculated with WAMIT F2T, is shown in a black solid line together with 2 approximations. The blue dash-dot line represents an approximation with 200 exponential functions, the red dashed line shows an approximation with only 6 exponential functions. The difference between the original IRF and the two approximations is shown in Figure 3.2(b), obtained by subtracting the approximations from the original IRF. The approximation with 200 exponential functions corresponds nearly perfectly with the original IRF. The approximation based on 6 exponential functions deviates locally from the original IRF, however, the difference is relatively small. The good agreement between these approximate curves and the original IRF is confirmed by the error calculations. The mean relative error for the first approximation is only 0.02 %, whereas for the second approximation it is 0.31 %, which is still a very small number.

The time gain on the other hand is significant: only 6 additional differential equations have to be integrated instead of 200. The number of exponential equations, N_e , is selected automatically, based on two conditions: N_e should be as small as possible and the mean relative error for the approximation should be smaller than 1.00 %. For the considered shapes, this requirement is easily fulfilled with 5 to 6 exponential functions.



(a) Original IRF (WAMIT) and 2 approximations.

(b) Difference between the original IRF and the two approximations.

Figure 3.2: Radiation impulse response function on a hemisphere-cylinder shape ($D = 5$ m, $d = 3$ m) for heave mode.

3.4 Time domain solver

In this Section some results of the time domain solver are shown and compared to frequency domain results.

The response amplitude operator (RAO) of the buoy position is defined as the ratio between the displacement amplitude of the uncontrolled floater, responding to a harmonic excitation, and the incident wave amplitude. The RAO can be calculated directly with WAMIT. It has been computed with the time domain model from the steady state response of the floater to a regular incident wave. The input parameters for the time domain model, i.e. the radiation impulse response function and the exciting force transfer function, are obtained with WAMIT. Figures 3.3(a) and 3.3(b) show the comparison between the RAO values obtained directly with WAMIT and indirectly with the time domain model for the shapes described in Chapter 2, i.e. the hemisphere-cylinder and cone-cylinder shape, respectively ($D = 5$ m, $d = 3$ m). The differences between both outputs can be read from the y -axis on the right side of the Figures. The RAO has been evaluated for 140 equidistant frequencies ranging between $7.958 \cdot 10^{-3}$ Hz and 1.114 Hz ($\omega \in [0.05, 7.00]$, $T \in [0.90$ s, 125.76 s]). As expected, the time domain RAOs correspond very well to those calculated by WAMIT. Only very small differences are observed around the resonance frequency where the models are sensitive to slight differences in

input parameters.

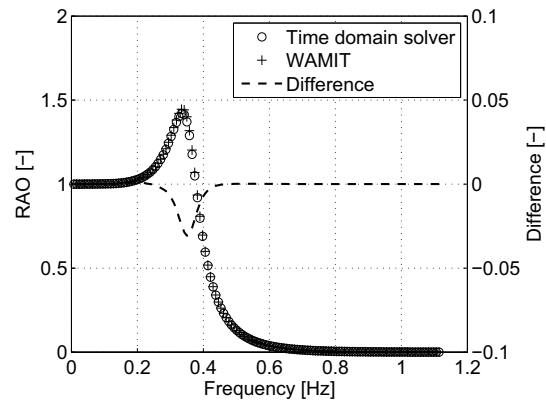
The time domain model has been used with a linear damping force (proportional to the velocity) and a force with constant amplitude (and sign equal to the velocity sign) to simulate the power extraction force. A linear damping force has been applied for the comparison with the frequency domain model. An example of a simulated body response is given in Figure 3.4. The body position and velocity are given for the cone-cylinder shape ($D = 5$ m, $d = 3$ m) with control parameters $m_{sup} = 100$ ton and $b_{ext} = 80$ ton/s, in an irregular wave characterized by $H_s = 2.75$ m and $T_p = 7.78$ s. The incident wave has been generated with WaveLab [16] using the parameterized JONSWAP spectrum. The effect of the tuning can be clearly observed from the graph. The point absorber displacement is lagging compared to the incident wave and it experiences a slightly larger elevation. This kind of time domain simulations will be extensively treated in Chapter 4, where the results will be compared with experimentally measured time series.

Power absorption results are presented in Figures 3.5(a) and 3.5(b) for the cone-cylinder and hemisphere-cylinder shape ($D = 5$ m, $d = 3$ m), respectively. The Figures show the time-averaged power absorption for varying values of the supplementary mass and external damping coefficient in the same irregular wave.

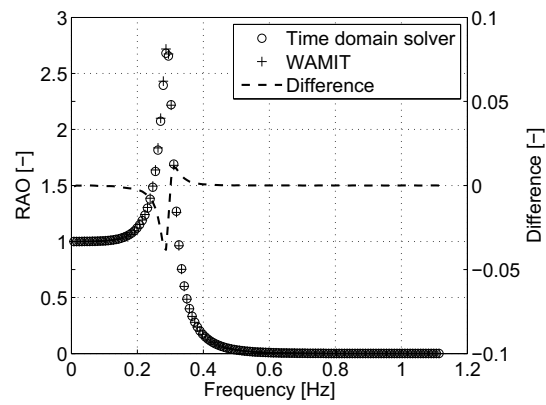
The incident wave has a duration of 5000 s. This duration should be long enough to give a representative value of the time-averaged power absorption, as pointed out by Ricci [2]. The time step is set at 0.02 s and hence, the number of time steps to be evaluated equals 250 000. The CPU time for one simulation -with given control parameters m_{sup} and b_{ext} - is almost 15 minutes on an 1.83 GHz Intel processor with 1 GB RAM. With a time step of 0.50 s, the simulation time is approximately 10 s and the accuracy is still good (difference in power absorption compared to $\Delta t = 0.02$ s is $< 0.5\%$). The graph shows a very good agreement between the time domain and frequency domain results¹.

As mentioned before, further applications of the time domain model will be presented in Chapter 4, where it is validated with physical test results.

¹Note that for the same control parameters the hemisphere absorbs more power than the cone in some cases. This is due to the fact that the mass of the hemisphere is 62 % larger than the mass of the cone. Consequently, the hemisphere has a larger natural period and is thus better tuned towards the incident wave characteristics than the cone shape. If the control parameters are optimized for both shapes, then the cone shape will generally perform better, which has been illustrated in Chapter 2.



(a) Response amplitude operator of a cone-cylinder shape ($D = 5$ m, $d = 3$ m) for heave mode.



(b) Response amplitude operator of a hemisphere-cylinder shape ($D = 5$ m, $d = 3$ m) for heave mode.

Figure 3.3: RAO obtained with the time domain solver compared to the RAO directly determined with WAMIT.

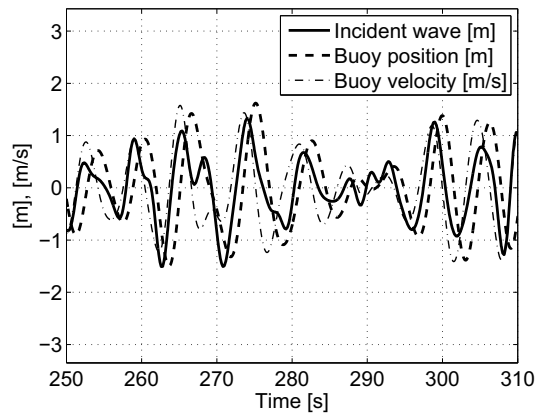
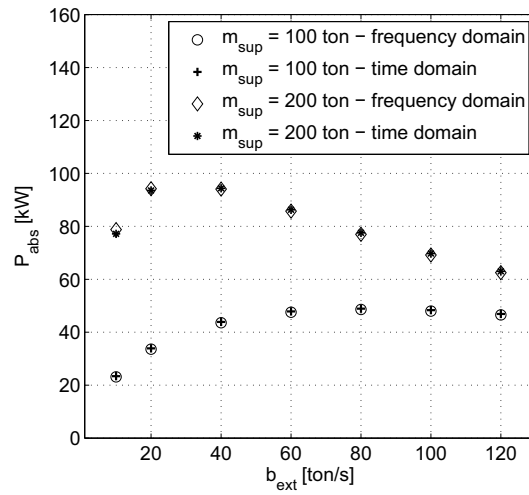


Figure 3.4: Body response determined with the time domain model for $m_{sup} = 100$ ton and $b_{ext} = 80$ ton/s in an irregular wave characterized by $H_s = 2.75$ m and $T_p = 7.78$ s.

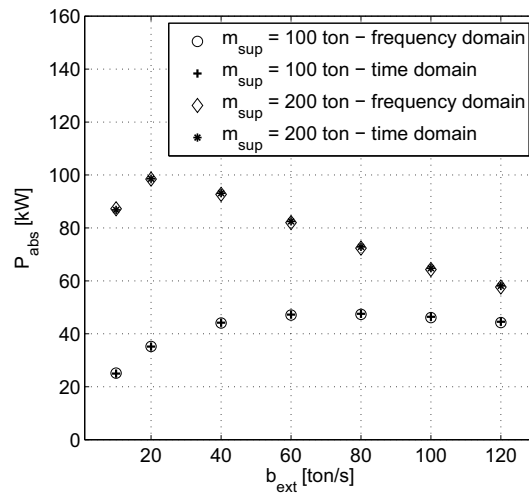
Furthermore the model will be utilized in Chapter 8 to estimate floater impact velocities and occurrence probabilities of slamming phenomena.

3.5 Conclusion

A time domain model has been implemented in MATLAB. The equation of motion of the heaving point absorber is described by Cummins' integro-differential equation and converted into a set of ordinary differential equations. This has been done by approximating the radiation impulse response function by a sum of exponential functions with Prony's method. The time domain model uses input from WAMIT for the hydrodynamic parameters (infinite frequency limit of the added mass, exciting force and radiation impulse response function). The output results are in good agreement with the frequency domain results.



(a) Absorbed power by a cone-cylinder shape $D = 5$ m, $d = 3$ m.



(b) Absorbed power by a hemisphere-cylinder shape $D = 5$ m, $d = 3$ m.

Figure 3.5: Comparison between frequency and time domain model for an irregular wave characterized by $H_s = 2.75$ m and $T_p = 7.78$ s.

Bibliography

- [1] Cruz (editor) J., Ocean energy: current status and perspectives. Springer, 2008.
- [2] Ricci P., Saulnier J., ao A.F., Pontes T., Time-domain models and wave energy converters performance assessment. In: 27th International Conference on Offshore Mechanics and Arctic Engineering, Portugal, 2008, pp. 1–10.
- [3] Babarit A., Optimisation hydrodynamique et contrôle optimal d'un récupérateur de l'énergie des vagues. Ph.D. thesis, Ecole Centrale de Nantes, France, 2005.
- [4] Babarit A., Duclos G., Clément A., Comparison of latching control strategies for a heaving wave energy device in random sea. Applied Ocean Research 2004;26(5):227–238.
- [5] da Costa J., Sarmiento A., Gardner F., ao P.B., Brito-Melo A., Time domain model of the AWS wave energy converter. In: 6th European Wave and Tidal Energy Conference, United Kingdom, 2005, pp. 91–98.
- [6] Gilloteaux J.C., Babarit A., Ducrozet G., Durand M., Clément A., A non-linear potential model to predict large-amplitude motions: application to the SEAREV wave energy converter. In: 26th International Conference on Offshore Mechanics and Arctic Engineering, USA, 2007.
- [7] Hals J., Taghipour R., Moan T., Dynamics of a force-compensated two-body wave energy converter in heave with hydraulic power take-off subject to phase control. In: 7th European Wave and Tidal Energy Conference, Portugal, 2007.
- [8] Cummins W., The impulse response function and ship motions. Schiffstechnik 1962;(9):101–109.

- [9] Clément A., Using differential properties of the green function in seakeeping computational codes. In: 7th International Conference on Numerical Ship Hydrodynamics, France, 1999, volume 6, pp. 1–15.
- [10] Korsmeyer F., Bingham H., Newman J., TiMIT A panel method for transient wavebody interactions. Research Laboratory of Electronics, M.I.T.
- [11] WAMIT user manual: <http://www.wamit.com/manual.htm>.
- [12] Carrico V., Maisonneuve J., Aqua+, User's manual. SIREHNA, 1995.
- [13] Duclos G., Clément A., Chatry G., Absorption of outgoing waves in a numerical wave tank using a self-adaptive boundary condition. *International Journal of Offshore and Polar Engineering* 2001;11(3):168–175.
- [14] Yu Z., Falnes J., State-space modelling of a vertical cylinder in heave. *Applied Ocean Research* 1980;17:265–275.
- [15] MATLAB: <http://www.mathworks.com/>.
- [16] WaveLab: <http://hydrosoft.civil.aau.dk/wavelab/>.

CHAPTER 4

Experimental validation of numerical modelling



The results of an experimental investigation on a heaving point absorber are presented. The physical tests are used to validate numerical simulations of the behaviour of the point absorber based on linear theory. Floater response and power absorption are evaluated in regular and irregular waves representing a mild wave climate. A good correspondence is found between the physical and numerical results. In irregular waves the difference between numerical and experimental power absorption is generally smaller than 20%. In regular waves the correspondence is good as well, except in the resonance zone; i.e. when the natural frequency of the buoy is tuned towards the resonance frequency of the incident wave. In this case, non-linear effects such as viscous damping and a non-linear hydrostatic restoring force become important due to the high velocities and displacements of the point absorber. However, pure resonance cases are often not preferred in practical applications. In general it is concluded that the numerical results are in good accordance with the experimental results and hence, linear theory can be used to predict the point absorber behaviour in mild energetic waves in non-resonance conditions.

This Chapter is partly based on ‘Experimental investigation of the validity of linear theory to assess the behaviour of a heaving point absorber at the Belgian Continental Shelf’ by G. De Backer et al. [1].

4.1 Introduction

Wave energy converters are often designed and optimized by means of numerical methods. The behaviour of point absorbers and oscillating water columns (OWCs) has also been extensively described analytically. These numerical and analytical methods are generally based on assumptions, of which some are not always well satisfied for wave energy applications. For example, linear theory assumes small waves and small body motions, a condition that might be violated when phase-control is applied to point absorbers. In spite of this, linear theory is still often used to assess the performance of point absorbers. In Chapter 2 and 3 numerical simulations have been presented based on linear water wave theory and a linearized equation of motion. The validity of linear theory for point absorber applications will be assessed in this Chapter by means of experimental wave flume tests.

Pioneering experimental research work on point absorbers has been performed by Budal et al. in 1981 [2]. They presented tests of a point absorber oscillating in heave mode, in irregular waves and subjected to phase control. In the eighties as well, Vantorre [3] performed numerical and experimental tests on a two-body point absorber system. In 2005 Vantorre, Banasiak and Verhoeven [4] compared numerical and experimental results of the hydraulic performance of a heaving point absorber. The numerical simulations were performed with the 3D panel method software AQUAPLUS. The present research work is a sequel of this study.

At the Ecole Centrale de Nantes (France) the SEAREV device has been extensively studied both numerically and experimentally. Validations of linear and non-linear models are presented in [5–7]. Payne et al. [8] compared numerical BEM simulations of the sloped IPS buoy, with experimental tests carried out in the Edinburgh Curved Tank. Fairly good agreements between numerical and experimental heave responses were obtained for large damping values. For smaller damping values the correspondence was good outside the resonance frequency bandwidth. Experimental research on closely spaced arrays of point absorbers has been carried out by Weller [9] and Stallard [10] and initial comparisons with the BEM software WAMIT are presented in [11].

In this Chapter, the hydrodynamic parameters and the performance of a point absorber will be investigated for different tuning and damping conditions. Several types of tests have been conducted: decay tests, wave exciting force tests and power absorption performance tests in regular and irregular waves.

The majority of tests in the wave flume have been run by Kim De Beule [12] in the framework of a master dissertation, supervised by the author of this PhD thesis. The experimental results are compared with numerical simulations, based on linear theory. The numerical hydrodynamic parameters are computed with WAMIT, and the equation of motion has been solved in the frequency and time domain models described in Chapters 2 and 3.

4.2 Experimental setup

4.2.1 Wave flume

The experimental tests are conducted in the wave flume of Flanders Hydraulics Research (FHR) in Antwerp, Belgium. The flume has a length of 70 m, a width of 4 m and a depth of 1.45 m. The wave paddle is driven by a hydraulic piston. The water depth in the flume is 1 m for all test cases. The model is installed at a distance of 12 m from the paddle. At 15 m from the paddle a screed beach was built in the wave flume with a small slope of 1/40, as indicated in Figure 4.1. At a distance of 43 m, respectively 55 m from the paddle a protection dam and breakwater were built in the flume for other experimental purposes. Since active absorption is not applied in the flume, absorbing material was placed in front of the dam at a distance of 35.7 m from the paddle in order to avoid too much disturbance due to reflection in the wave flume. Three wave gauges are placed in front of the point absorber and one behind the point absorber. A reflection analysis is carried out with the three wave gauges in front of the test object. In order to assess the reflection in the wave flume, the test setup is removed from the flume. The position of the wave gauges is determined according to the criteria of Mansard and Funke [13]. The analysis is performed in WaveLab, a software tool for data acquisition and data analysis developed at Aalborg University (Denmark) [14]. Reflection coefficients, C_r , between 9 to 18 % have been found. More details about the reflection analysis can be found in Appendix E.

4.2.2 Scale model

The test setup consists of a floating body, oscillating with respect to a fixed structure. The buoy is connected to a rod, which is attached to a rotating belt (Figure 4.2). The belt is supported by three bearings and a pulley

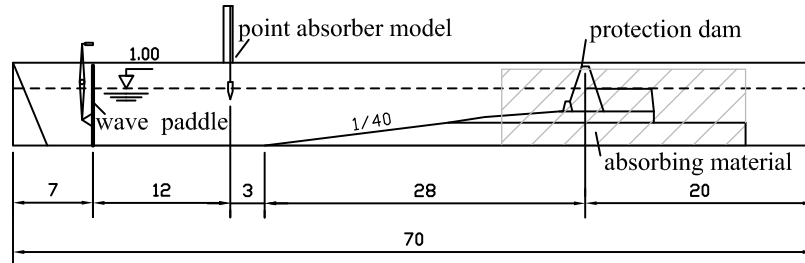


Figure 4.1: Position of test setup in wave flume (dimensions in [m]).

that is connected to rotating shaft. On this rotating shaft, the measurement instrumentation is installed. The test setup is modelled on a scale 1/15.9. This scale is based on the ratio of the diameter of the test body to a full scale diameter of 5 m (see Section 4.2.3). The experimental investigation is a continuation of the study carried out by Vantorre et al. [4]. The test setup has been rebuilt and is improved in some ways: the internal friction in the model has been reduced by a factor of two and the measurement of the damping force and buoy motion has been enhanced. A picture of the new test setup is given in Figure 4.3.

The floating body is indicated by number 1. The bottom part is made of polyurethane and it is connected to a cylindrical part of PVC. In order to reduce the friction, the number of bearings is reduced and higher quality bearings are used. The original steel guiding rod with circular cross section significantly bended under the action of large horizontal hydrodynamic forces. This resulted in large friction forces in the bearings and even in damage of those bearings. For this reason the steel bar has been replaced by a stiff aluminium profile (no 2), with cross section 7.4 x 1.9 cm, increasing the bending stiffness by a factor of 6.4 ($EI = 4.3 \text{ kN/m}^2$). The aluminium profile is guided by two carriages which are mounted on the frame structure. Furthermore, the motion of the point absorber is registered by an optical encoder (no 3) instead of a potentiometer. The encoder is mounted on a horizontal, rotating shaft connected to the pulley. The damping force is realized by means of a mechanical brake (no 4) consisting of a circular element covered by a felt that can be pressed on a wheel that is mounted on the rotating shaft (Figure 4.4). The damping force is measured by a force transducer (no 5) and torque sensor (no 6) which gave very similar results. A tuning force proportional to the buoy

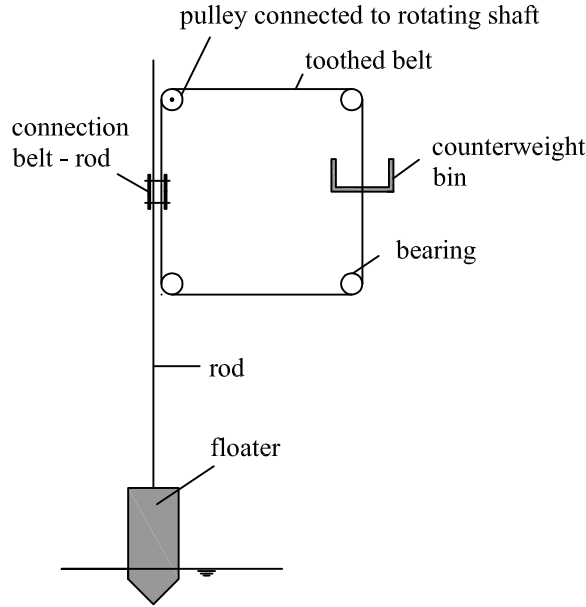


Figure 4.2: Schematic representation of test model.

acceleration has been applied by adding supplementary mass. Weights are placed on top of the buoy and in the counterweight bin (no 7) at the other side of the belt [4].

It is important to know the magnitude of the internal friction in the test setup in order to be able to implement this friction force in the numerical model. The friction force is measured outside the flume. An equilibrium position of the system is obtained by putting weights in the counterweight bin so that the total mass on the one side of the belt is equal to the total mass on the other side. In a next step, a small mass m_{sm} (approx 1 kg) is added to induce the motion of the point absorber. The acceleration \ddot{z} is measured and the friction force F_{fric} is determined from Eq. (4.1), assuming a constant acceleration, and hence, a constant internal friction force.

$$(m_{tot} + m_{sm}) \ddot{z} = F_{fric} - m_{sm}g \quad (4.1)$$

where m_{tot} is the total mass of the system that is accelerated (without the extra small mass). In this way, the magnitude of the internal friction force has been estimated at 2.2 N for the enhanced test setup.

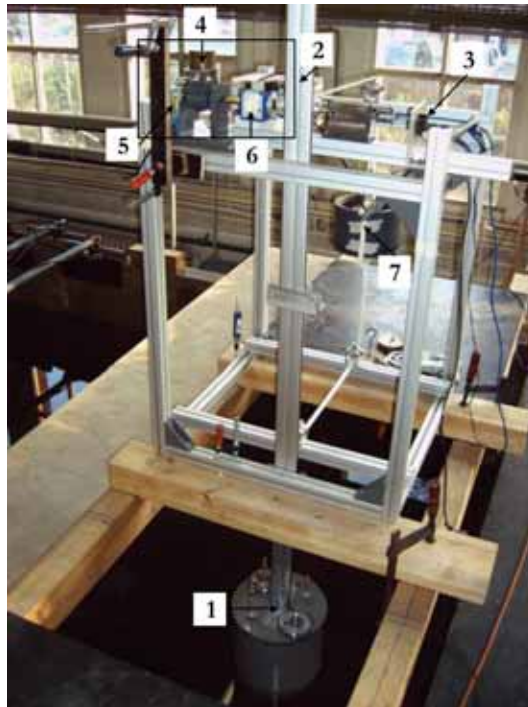


Figure 4.3: Experimental setup: point absorber with test rig.

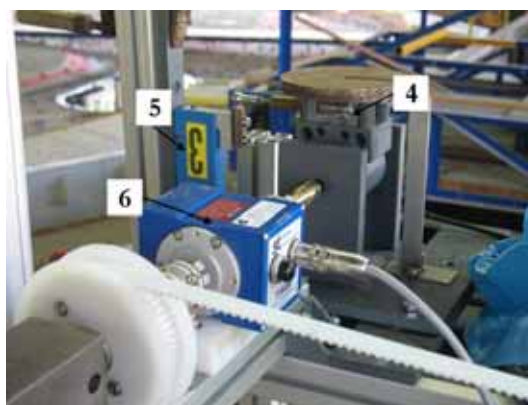


Figure 4.4: Measurement instrumentation.

4.2.3 Design parameters

Buoy geometry

Two buoy shapes have been tested: a cone and hemisphere shape, both with a cylindrical upper part. The cone has an apex angle of 90° . The diameter D of the cylinders is 31.5 cm, which is equivalent to a prototype diameter of 5 m on a scale 1/15.9. Three different drafts are evaluated ($d = 18.9$ cm, 22.1 cm and 28.4 cm) corresponding to a draft of 3 m, 3.5 m and 4.5 m in prototype size, as indicated in Fig. 4.5. The draft is varied by adapting the weights on top of the floater.

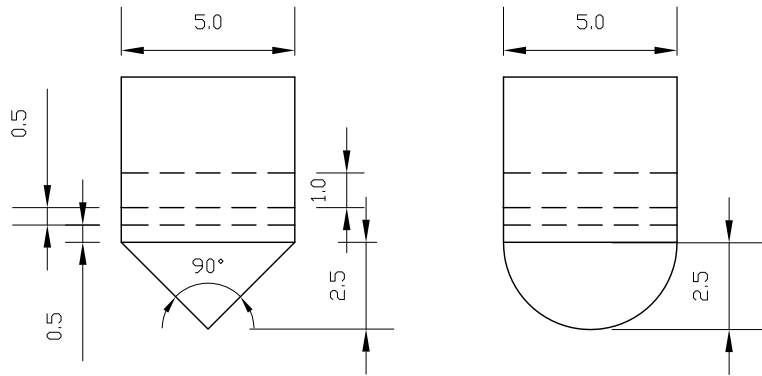


Figure 4.5: Cone-cylinder and hemisphere-cylinder shapes with three different drafts (prototype dimensions in m).

Damping and tuning forces

The damping force, F_d , is varied by changing the masses on top of the mechanical brake in Fig. 4.4 (no 4). The resulting damping force is a block signal, i.e. a force with a constant magnitude and a sign dependent on the sign of the velocity. This magnitude will be indicated as $F_{d,A}$ and will be further referred to as the amplitude of the damping force, although -strictly speaking- it is not a real amplitude.

$$F_d = F_{d,A} \operatorname{sgn}\left(\frac{dz}{dt}\right) \quad (4.2)$$

The tuning force is proportional to the acceleration of the buoy and can be changed by varying the weights on top of the floater and in the counterweight bin. Since the weight is varied at both sides of the belt, changing the supplementary mass has no influence on the draft of the buoy. The adjustable supplementary mass allows for covering a frequency zone further from and closer to resonance. Since the point absorber system is a mass-spring-damper system, the relationship between the supplementary mass and the natural frequency of the floater can be expressed as:

$$\omega_n = \sqrt{\frac{k}{m + m_a(\omega) + m_{sup}}} \quad (4.3)$$

where k is the hydrostatic restoring coefficient, m the mass of the buoy, $m_a(\omega)$ the added mass and m_{sup} the supplementary mass.

4.2.4 Wave climate

Sea states

The point absorber has been tested in both regular and irregular waves. The latter characterize the wave conditions on the Belgian Continental Shelf (BCS). Scatter diagrams based on buoy measurements at Westhinder, located 32 km from shore on the Belgian Continental Shelf, have been used to define nine sea states. Table 4.1 displays the sea states and Figure 4.6 shows the corresponding occurrence probabilities (OP). Note that more than 80 % of the H_s -values is smaller than 1.5 m. The average available wave power at Westhinder is 4.64 kW/m [15].

Table 4.2 shows the regular and irregular wave characteristics selected for the power absorption tests in the wave flume. Froude scaling has been used to obtain the prototype values. The figures represent the measured values, based on the measurements of a wave gauge placed at the position of the point absorber, when the device was removed from the flume. The waves in the flume are generated based on the parameterized JONSWAP spectrum with peakedness factor $\gamma = 3.3$. The analysis of the wave gauge signals has been performed with the software programme WaveLab [14]. The wave data is registered at 50 Hz, the data from the other measurement equipment is registered at 25 Hz. It was found that the measured wave heights in the flume are slightly smaller than the target wave heights, whereas the measured

Table 4.1: Sea states at Westhinder based on measurements from 1-7-1990 until 30-6-2004 (Source of original scatter diagram: Flemish Ministry of Transport and Public Works (Agency for Maritime and Coastal Services, Coastal Division) [16]).

Sea state	H_s [m]	T_p [s]
1	0.0-0.5	5.24
2	0.5-1.0	5.45
3	1.0-1.5	5.98
4	1.5-2.0	6.59
5	2.0-2.5	7.22
6	2.5-3.0	7.78
7	3.0-3.5	8.29
8	3.5-4.0	8.85
9	4.0-4.5	9.10

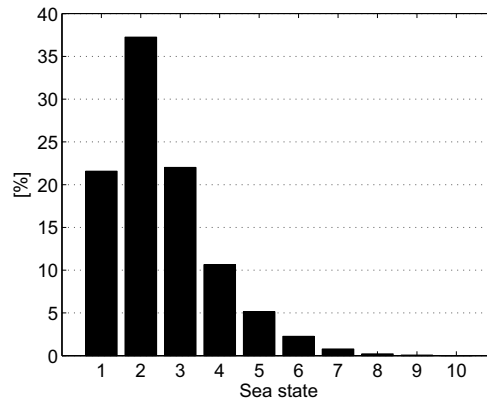


Figure 4.6: Occurrence probability of sea states (SS) at Westhinder buoy in Belgium, based on [16].

and target periods correspond well. Therefore, the measured sea states do not correspond exactly to the sea states of the BCS. It must be noted as well that the reliability of the H_s - and T_p -values is small, since they are based on very short time series (approx 118 s). This rather short duration has been chosen to avoid influences of any energy building up effects in the flume. The measured irregular wave trains are used as input in the numerical time

Table 4.2: Regular and irregular waves at prototype and model scale.

Regular waves	Prototype scale		Model scale	
	H [m]	T [s]	H [cm]	T [s]
	1.65	5.42	10.4	1.36
	1.62	6.37	10.2	1.60
	2.29	6.97	14.4	1.75
Irregular waves	H_s [m]	T_p [s]	H_s [cm]	T_p [s]
	0.98	6.33	6.2	1.59
	1.52	7.29	9.6	1.83

domain model. Hence, the small reliability of the H_s - and T_p -values is of less importance, since the main purpose is to compare numerical and experimental results, based on the same time series.

Wave generation and time series selection

When a test is started on the control computer, a pressure of more than a hundred bar is exerted on the wave paddle, causing slight paddle oscillations. Consequently small waves are generated disturbing the water surface. Therefore a rest period of 600 s is introduced after the start of a test to obtain a still water surface before the paddle is instructed to generate the wave series. The wave generation lasts 200 s in case of regular waves and 400 s in case of irregular waves. The selected wave trains for data analysis are much shorter in order to minimize the influence from the waves reflected on the absorbing material. Since no active absorption is applied in the flume, rather small durations and a small start cutoff point need to be chosen. The start cutoff point is determined by the sum of:

- The time Δt_1 for the wave to be totally developed, preferably ≥ 10 s (including the 2 s wave ramp time).
- The time Δt_2 for the wave to travel from the paddle to the model, depending on the wave period. For a wave period of 1.36 s, respectively 1.75 s the required time is 8.8 s, respectively 6.9 s.

It has been decided to choose the start cutoff point at 15 s after the start of the wave generation. The time domain model is started at least 5 s before the start cutoff point to avoid any influence from the initial conditions. The duration of the time frame to be analysed can be quite short for regular waves,

since the point absorber response in regime conditions remains identical. Hence, a time frame of 20 s is sufficient for data analysis of regular waves. For irregular waves, the considered time frame is set at 118 s. As pointed out before, this rather short duration makes it difficult to characterize the waves statistically in an accurate way. However, the numerical and experimental models can be compared in a correct manner, since exactly the same wave trains are considered in both cases.

4.3 Results

4.3.1 Decay tests

In a decay test, the buoy is released from an initial position different from its equilibrium position in originally still water. Hence, the buoy undergoes a damped free oscillation. From the recorded decaying motion, relevant hydrodynamic parameters of the point absorber can be derived, such as the hydrodynamic coefficients of added mass and damping. Decay tests have been performed for the hemisphere-cylinder (hc) shape for different drafts and different values of supplementary mass. A test matrix is given in Table F.1 of Appendix F. An example of a decaying buoy motion is given in Figure 4.7, showing the measured and numerically determined buoy position for the hc, with draft 22.1 cm and $m_{sup} = 8.1$ kg. The point absorber is initially submerged at a distance equal to its draft plus 0.15 m. The same initial condition is implemented in the numerical model, resulting in very similar results. The correspondence is particularly good in the beginning. About 6 s after releasing the floater, the influence of the radiated waves reflected on the side walls of the flume become clearly visible in the experiment. Furthermore, the amplitude of the numerical oscillations is slightly higher and the damped natural period in the numerical decay curve seems to be slightly smaller than in the experimental curve.

From a decay test, the natural angular frequency ω_n , the added mass m_a and the damping factor ζ_d can be derived. The floater describes a free damped oscillation, which can be mathematically expressed as:

$$z(t) = a \exp(-\zeta_d \omega_n t) \sin(\omega_d t + \phi) \quad (4.4)$$

Eq. (4.4) is fitted to the measured position of the buoy, as shown in

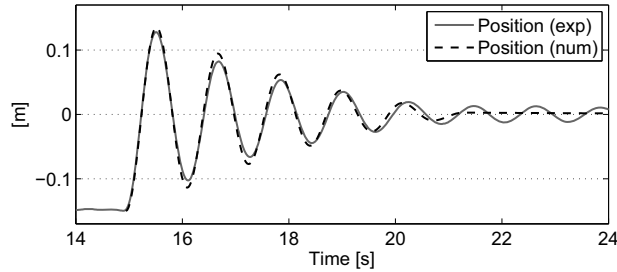


Figure 4.7: Measured and numerically determined buoy position during decay test. Test object: hc, $d = 22.1$ cm, $m_{sup} = 8.1$ kg.

Figure 4.8. The very initial part of the curve is omitted for the fitting to avoid the influence of static friction and the last part is excluded too to avoid the influence of reflected waves.

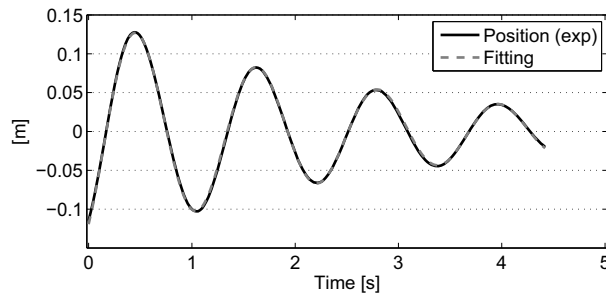


Figure 4.8: Fitting of expression for a damped free oscillation to the experimentally measured buoy position. Test object: hc, $d = 22.1$ cm, $m_{sup} = 8.1$ kg.

The added mass is obtained from the measured natural angular frequency ω_n of the buoy with Eq. (4.5):

$$m_a = \frac{k}{\omega_n^2} - m_{\text{buoy}} - m_{\text{sup}} \quad (4.5)$$

By performing these tests for varying supplementary masses, the added mass is obtained for different natural frequencies. Figure 4.9 shows a comparison between the experimental and numerical values of the dimensionless added mass for three different drafts d of the hemisphere-cylinder. The numerical

results are obtained with WAMIT. The values in the experiments are found to be somewhat higher than the numerical results. This corresponds with the fact that the damped natural period appeared to be slightly smaller in the numerical simulations, compared to the experimental results, as observed in Figure 4.7. The hydrodynamic damping could not be derived in an accurate way due to the influence of the internal friction in the system.

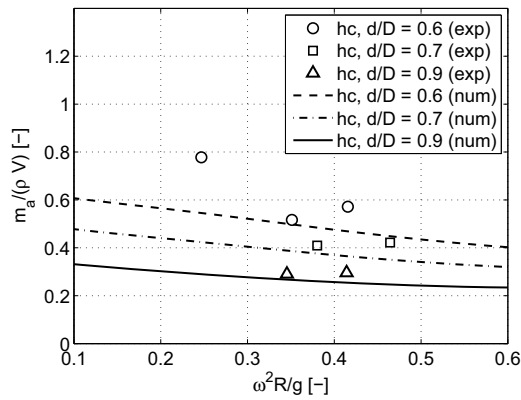


Figure 4.9: Experimentally and numerically determined added mass for three different drafts (d/D is the draft to diameter ratio). Test object: hc.

4.3.2 Heave exciting wave forces

The heave exciting wave forces are measured on the buoy while it is held fixed in regular waves with varying period. The brake is tightly screwed on the shaft, so that the exciting force on the buoy is entirely transferred to the load cell. With the torque sensor mounted on the shaft, the exciting wave force is derived as well. Note that the internal friction force needs to be added to the value obtained from the measurements, since only the part larger than the friction force is transferred to the sensors.

Figures 4.10 and 4.11 show the amplitudes of the first harmonic component of the heave exciting forces as a function of the (dimensionless) frequency on the cone-cylinder (cc) and hemisphere-cylinder (hc) shapes for two different drafts. The tests are performed in regular waves with a wave height of 8.0 cm and wave periods of 1.11, 1.35, 1.60 and 1.75 s ($\omega^2 R / g = 0.51, 0.35, 0.25$

and 0.21). The test matrix is given in Table F.2 of Appendix F. The numerical findings are quite well confirmed by the experiments. Firstly, the exciting forces are higher for the cone shape than for the hemisphere shape. Secondly, for both shapes, larger exciting forces are associated with smaller buoy drafts. At a period of 1.59 s ($\omega^2 R/g = 0.25$) an increased value of the exciting force is measured. This effect has also been observed by Vantorre et al. [4] and is caused by wave reflection from the side walls of the flume.

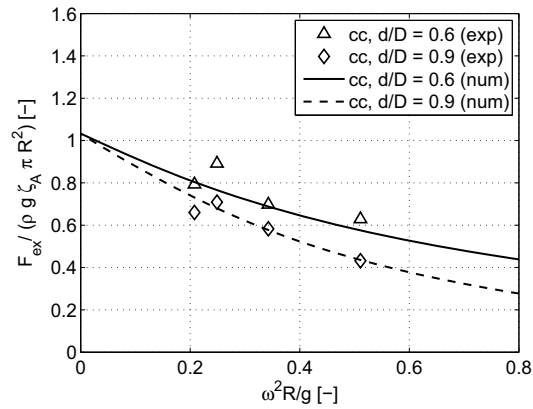


Figure 4.10: Measured and numerically determined heave exciting force on the cone-cylinder.

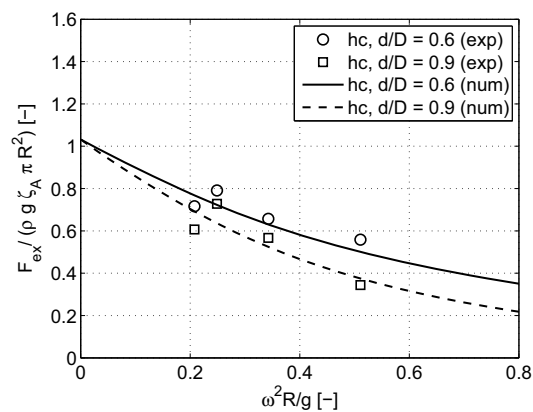


Figure 4.11: Measured and numerically determined heave exciting force on the hemisphere-cylinder.

4.3.3 Power absorption tests

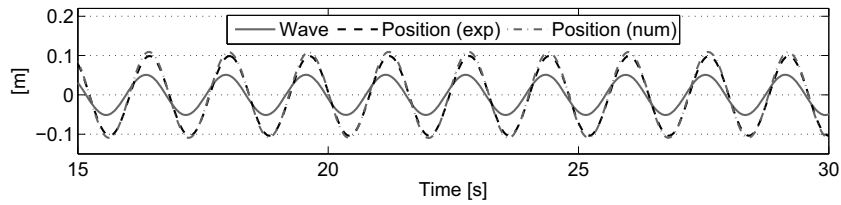
In regular and irregular waves, tests are run for several values of the damping force and supplementary mass. The variation of the supplementary mass leads to different ratios of the natural period of the system to the incident (peak) wave period or, in other words, different levels of tuning are obtained. The absorbed power is determined by multiplying the buoy velocity with the total damping force, consisting of the measured damping force and the friction force in the system, estimated as described in Section 4.2.2. The test matrices for regular and irregular waves are presented in Tables F.3-F.6 of Appendix F.

Regular waves

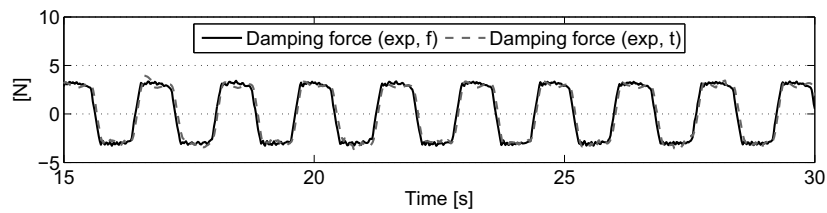
The response of the heaving cone-cylinder buoy in a regular wave with a wave height of 10.2 cm and a period of 1.60 s is shown in Figure 4.12(a). The buoy draft is 22.1 cm and the applied damping force (with constant magnitude) is 3.0 N (excluding the friction force). This corresponds to a damping force of 12 kN in prototype. A supplementary mass of 18.5 kg (74.12 ton in prototype) has been added to the system, which is about twice the buoy mass, resulting in a ratio ω_n/ω equal to 83 %. This explains the phase lag between the buoy position and the wave on the one hand and the large buoy amplitude of almost two times the wave amplitude on the other hand. The buoy is not yet fully operating at resonance, since in that case the phase lag would be approximately 90°, assuming the phase of the exciting force is close to zero degrees for this frequency range¹. Furthermore, it can be noticed that the numerical and experimental buoy response correspond quite well in these conditions. Figure 4.12(b) shows the damping force measured by the force transducer (exp, f) and torque sensor (exp, t). The damping force is a block wave, instead of a harmonic wave, which is in phase with the buoy velocity.

In Figure 4.12(c) the measured damping force and tuning force are compared for the same test conditions. Note the large amplitude of the tuning force, even for this suboptimal tuning case. The amplitude of the tuning force is 10 times larger than the amplitude of the measured damping force and corresponds to a value of 120 kN in prototype dimensions. When the tuning ratio of this buoy is increased to 90 %, the amplitude of the registered tuning force is multiplied by a factor of two. This illustrates that

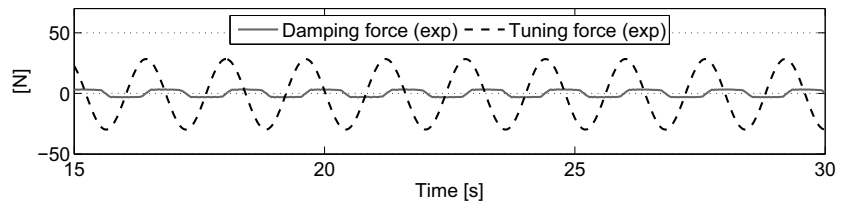
¹The phase of the exciting force is 4.0° for this shape and for $T = 1.60$ s.



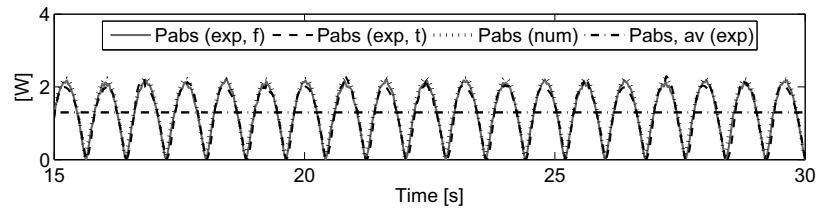
(a) Measured wave, measured and numerically determined buoy position.



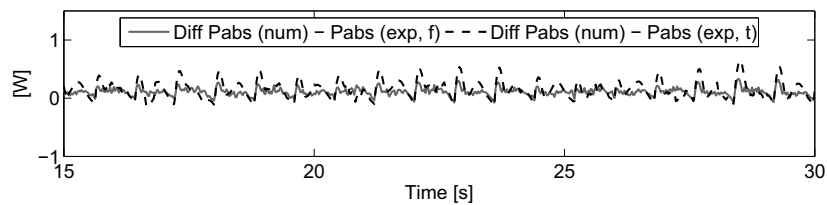
(b) Damping force measured with the force transducer (exp, f) and torque sensor (exp, t).



(c) Measured damping force and tuning force.



(d) Measured and numerically determined power absorption (measurements by force transducer (exp, f) and torque sensor (exp, t)).



(e) Difference between measured and numerically determined power absorption.

Figure 4.12: Experimentally and numerically determined time series. Test object: cc, $d = 22.1$ cm, $m_{sup} = 18.5$ kg, $F_{d,A} = 3.0$ N, wave characteristics: $H = 10.2$ cm and $T = 1.60$ s.

operating close to resonance might require very large tuning forces, if the intrinsic inertia of the device is rather small. Figure 4.12(d) gives the time-dependent power absorption, experimentally and numerically determined. The difference between the numerical and experimental power absorption is shown in Figure 4.12(e). Mind the different scale of the y -axis. The numerical average power is 1.4 W, indicated by the dash-dotted line in Figure 4.12(d). The measured averaged power is 1.3 W, which is a difference of 7 %. When the supplementary mass is increased, the difference becomes much larger, as will be shown later. The ratio between the maximum instantaneous power and the average power is about 1.6. Note that viscous losses are not included in the numerical model, which might explain the difference between the numerical and experimental values. Both numerical and experimental power absorption figures do not represent produced power values, since PTO losses or other conversion losses are not taken into account in the presented numbers.

Figure 4.13 shows the power absorption efficiency as a function of the dimensionless damping coefficient applied on the cone-cylinder (cc) buoy. The absorption efficiency is defined as the ratio of the absorbed power to the incident wave power, available over the diameter of the buoy. An ‘equivalent’ external damping, b_{ext} , has been derived for the experiments, based on the expression for the average power (Eq. (1.71) of Chapter 1):

$$P_{abs} = \frac{1}{2} \omega^2 b_{ext} z_A^2 \quad (4.6)$$

The experimental data are compared with the numerical frequency domain model for different tuning levels. Near resonance ($T_n/T = 96\%$) the motion amplitudes become very large and linear theory is not able to predict the point absorber behaviour anymore. However, when the buoy operates further from resonance ($T_n/T = 83\%$), the numerical and experimental values correspond well. This is in agreement with Durand et al. [5] where numerical simulations based on linear and non-linear theory are validated with experimental tests on the SEAREV device. In the resonance zone only the non-linear model is able to predict the power absorption in an accurate way.

The discrepancy in this near resonance case is particularly large for small external damping values. At low damping, the buoy motion is large and the influence of the non-linear hydrostatic restoring force becomes important. Also the buoy velocity is large, which is associated with viscous effects causing energy dissipation. These effects are not taken into account in WAMIT.

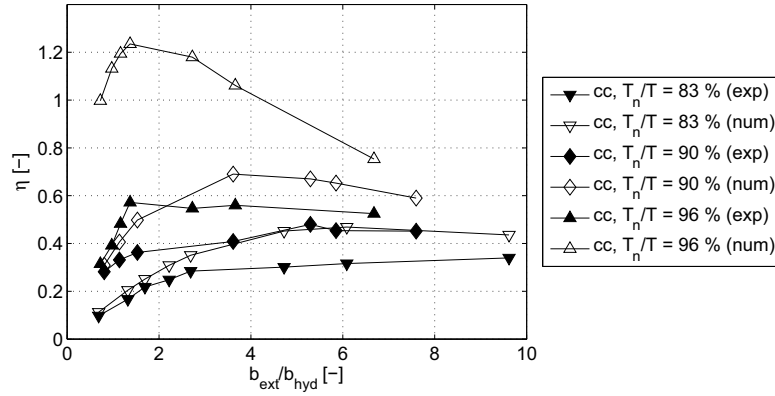


Figure 4.13: Power absorption efficiency as a function of the dimensionless damping coefficient for several ratios of T_n/T . Test object: cc, $D = 5$ m, $d = 3.5$ m, wave characteristics: $H = 1.62$ m, $T = 6.37$ s.

Similar conclusions can be drawn, based on the measurements of the heave response of a sloped wave energy converter concept by Payne et al. [8]. Only for low damping values, the numerically predicted amplitude (with WAMIT) appeared to be much larger (about 65 %) than the experimental values at resonance frequency. For increased external damping, the agreement between measurements and numerical simulations significantly improved. The correspondence was also very good for small damping values in the frequency ranges outside resonance. This is also observed in Figure 4.13. The correspondence between numerical and experimental values seems to worsen somehow for larger damping values in the off-resonance zone. It is not entirely clear why this happens, but it could be attributed to the friction force. This force might have been larger than estimated when the external damping is increased, since the buoy motions are quite small in that case and the static friction, being larger than the dynamic friction, becomes important.

According to linear theory, efficiencies larger than 100 % are found -due to the point absorber effect described in Chapter 1- whereas the experiments have a maximum efficiency of almost 60 % for this particular tuning case. Theoretically, maximum power absorption is obtained at $T_n/T = 100$ % and $b_{ext} = b_{hyd}$. However, in practice the optimal damping will be higher, in order to reduce undesired energy losses, related to large buoy velocities.

Note that for smaller tuning ratios T_n/T , the maximum power absorption occurs for larger damping values, in both the experiments and numerical simulations. Similar findings were formulated by Vantorre et al. [4]. However, the experimental efficiencies measured in [4] are about 10 to 20 % higher in absolute figures. Several differences may have caused this dissimilarity. First of all, a different test setup has been employed, with different intrinsic properties. For example the internal friction in the new setup is estimated to be reduced by a factor of two. Since the contribution of the friction force is considered in the total power absorption, possible inaccuracies in the estimation of this force result in inaccurate power absorption values. Secondly, the data processing has been performed in a different way. For instance small under- or overestimations of the incident wave amplitude may induce a considerable error in the incident wave power, since a quadratic relationship exists between the available power and wave amplitude, having its direct implication on the absorption efficiency.

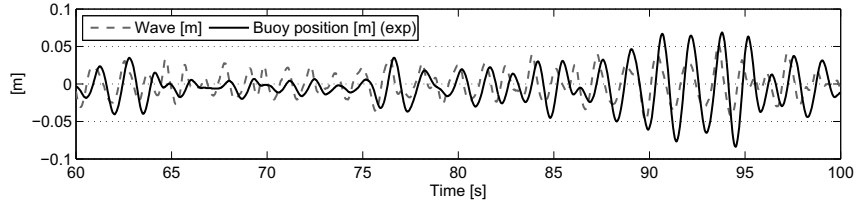
Irregular waves

The cone and hemisphere have been tested in two irregular wave trains with varying tuning parameters and damping forces. The measured wave elevations, the measured damping force and estimated friction force (Section 4.2.2) are used as input in the numerical time domain model. Figure 4.14 displays the measured and calculated buoy motion parameters, forces and power absorption as a function of time for the cone-cylinder with a draft of 22.1 cm, a supplementary mass of 18.5 kg ($= 2 \cdot m_{\text{buoy}}$; $T_n/T_p = 83\%$) and a measured damping force of 3.5 N. The wave is characterized by a significant wave height of 6.2 cm and a peak period of 1.59 s. In Figure 4.14(a) the wave elevation is shown, together with the measured buoy position. Even though the tuning is suboptimal, it is clearly visible how the buoy motion is lagging relative to the wave, resulting in larger buoy motions. Figure 4.14(b) compares the measured buoy motion and the numerically determined buoy position. The correspondence is excellent, showing that linear theory can indeed be used to predict the point absorber behaviour for small waves and small buoy motions. Figures 4.14(c) and 4.14(d) display the wave elevation, together with the buoy velocity and acceleration, respectively. Note that the buoy velocity is more or less in phase with the wave elevation, as a result of the tuning. Figure 4.14(e) illustrates the tuning and damping forces. The tuning

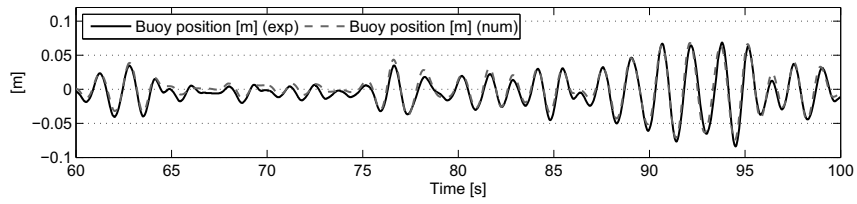
force fluctuates significantly, dependent on the acceleration of the buoy. In Figure 4.14(f) the numerically determined radiation force and exciting wave force are plotted. The radiation force is rather small, particularly in comparison to the hydrostatic force, which is shown in Figure 4.14(g). The hydrostatic force (or hydrostatic restoring force) is calculated as the Archimedes force minus the gravity force. A constant spring coefficient has been considered.

Finally, Figure 4.14(h) displays the instantaneous power absorption, numerically determined and experimentally measured based on the force transducer signal. The difference between both curves is shown in Figure 4.14(i) on a different scale. As expected, the correspondence between numerical and experimental results is quite good, particularly in the zone where the buoy motions are small. Note the large fluctuations in instantaneous power absorption in Figure 4.14(h). If no intermediate storage, e.g. by a hydraulic accumulator, is provided, the produced power will also significantly vary in time. However, the problem might not be too bad, since in practical applications, multiple point absorbers will be installed in array configurations. Hence, the total produced power will fluctuate less compared to a single body, resulting in a higher quality of the power to be delivered to the grid. The time-averaged power absorption of the considered time frame (118 s) is 0.42 W for the experiments and 0.43 W for the numerical simulation. For clarity, only the experimentally determined average value is indicated in Figure 4.14(h). The ratio between the average power and the maximum value in this time frame of 118 s is about 6.7. Note that this ratio would even be quite larger if a much longer, and hence more representative, time frame is considered. In practice, the generator will not be designed for the very high, but exceptional peaks in the design waves. Instead, these peaks are more likely to be truncated, with power absorption losses as a consequence. The magnitude of these losses is dependent on the rated (= maximum) power of the generator. It is obvious that, if this rated power is close to the average power determined without truncation, a considerable amount of power will be lost and the true average power will be significantly smaller. Hence, these observations indicate that, in case the device is not equipped with an intermediate storage, the capacity factor is expected to be lower than for devices with a storage system.

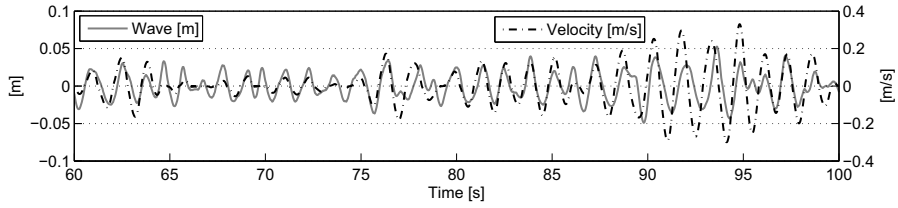
In Figure 4.15 the results of a different test case have been displayed. The buoy shape is the hemisphere-cylinder (hc) with a draft of 18.9 cm. It has been employed in a more energetic irregular wave, characterized by H_s



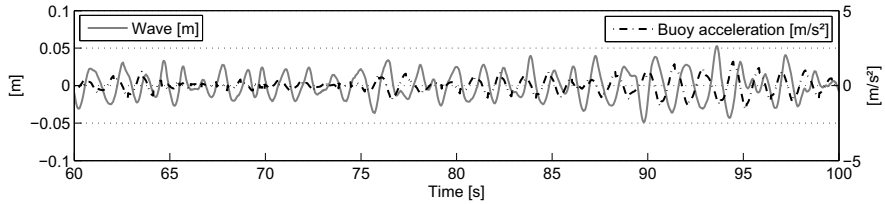
(a) Measured wave and measured buoy position.



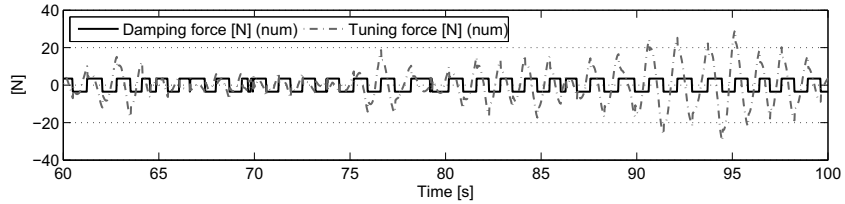
(b) Measured and numerically determined buoy position.



(c) Measured wave and numerically determined buoy velocity.

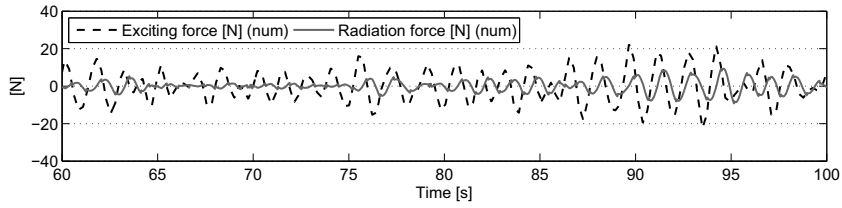


(d) Measured wave and numerically determined buoy acceleration.

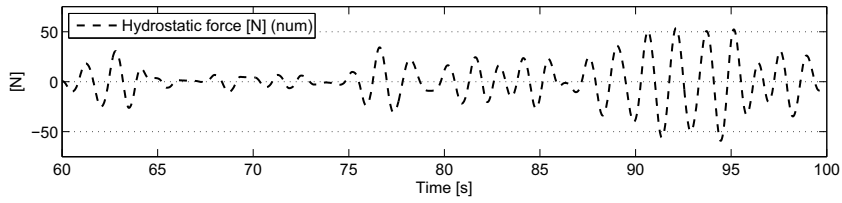


(e) Applied damping and tuning force (num).

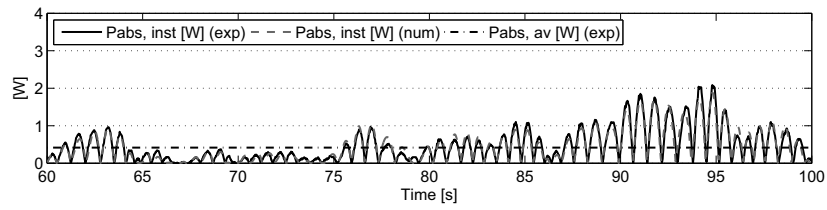
Figure 4.14: Figure continues on next page.



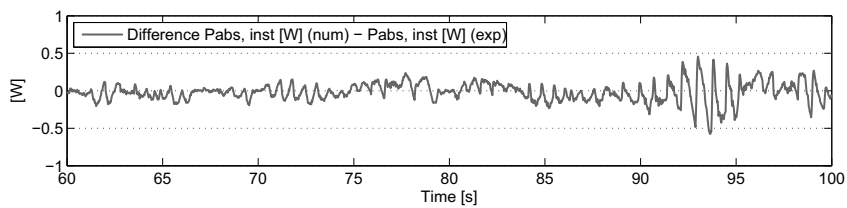
(f) Radiation and exciting force (num).



(g) Hydrostatic force (num).



(h) Experimentally and numerically determined power absorption.

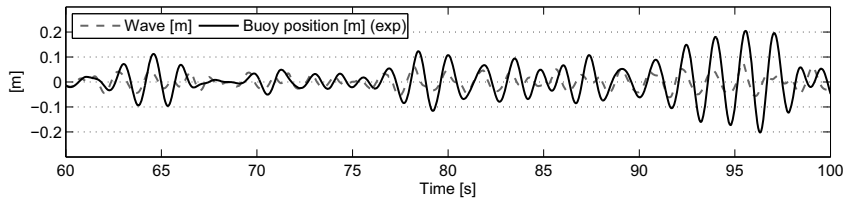


(i) Difference between experimentally and numerically determined power absorption.

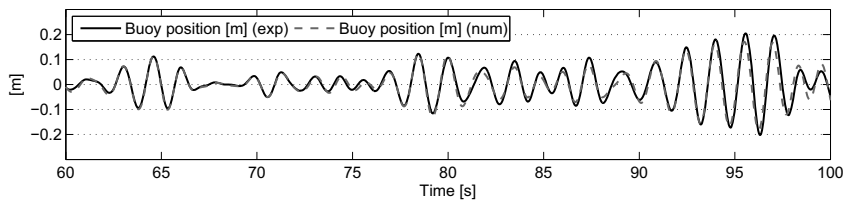
Figure 4.14: Experimentally and numerically determined time series. Test object: cc, $d = 22.1$ cm, $m_{sup} = 18.5$ kg, $F_{d,A} = 3.5$ N, wave characteristics: $H_s = 6.2$ cm, $T_p = 1.59$ s.

= 9.6 cm and $T_p = 1.83$ s. The inertia of the system has been increased: the buoy mass of the hemisphere is slightly larger than the cone (although the applied draft is smaller) and the supplementary mass of the system has been increased. Nevertheless, the tuning ratio T_n/T_p is only 76 %, since the peak period is also increased. Additional to the friction force, a small external damping force of 1.7 N has been applied. Figure 4.15(a) shows the measured wave elevation and buoy motion. Again, the influence of the tuning can be observed in the phase lag and motion amplification of the body response. The correspondence between numerical and experimental buoy motions is very good, as can be seen in Figure 4.15(b). Figures 4.15(c) and 4.15(d) present the buoy velocity and acceleration. The forces acting on the body are shown in Figures 4.15(e)-4.15(g). Mind the large tuning forces that occur, due to the large inertia of the system on the one side and the large body accelerations on the other side. The maximum tuning force in the considered time frame of 118 s is 79 N (prototype: 316 kN), whereas the maximum total damping force (sum of friction force and external damping force) is only 3.9 N (prototype: 16 kN). The ratio between both values is approximately equal to 20 and it is clear that it might be necessary to limit the tuning force to a certain value. A restriction on the tuning force is particularly required if this force needs to be delivered by the PTO system, in order to avoid overdimensioning of the PTO. Figure 4.15(h) compares the numerical and experimental power absorption and Figure 4.15(i) shows the difference between both power absorption time series. Instantaneous deviations occur particularly when the buoy motions are larger (e.g. during the last 6 s of the presented time frame). However, the average power absorption values of the considered time frame (118 s) correspond very well. The experimental average power absorption figure is 0.77 W and the numerical value is 0.78 W. This results in a ratio of maximum power absorption to average power absorption of 4.5. Again, this ratio would considerably increase as the length of the time frame increases, but it already gives an idea of the large difference between maximum and average power that occurs even in a short time frame.

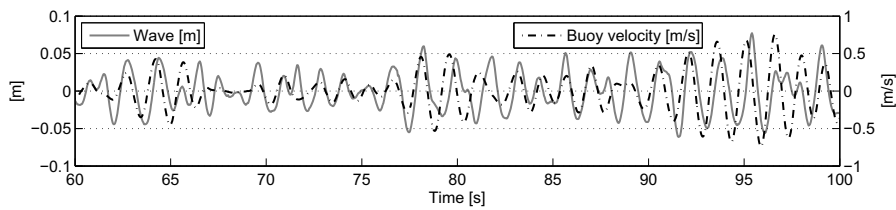
Figure 4.15(j) illustrates the instantaneous power that is associated with the tuning force. Huge instantaneous power levels are observed compared to the useful power absorption. This is not surprising, since the control force appeared to be a multiple of the damping force in Figure 4.15(e). It must be stressed that the average power related to the tuning force is zero, since it



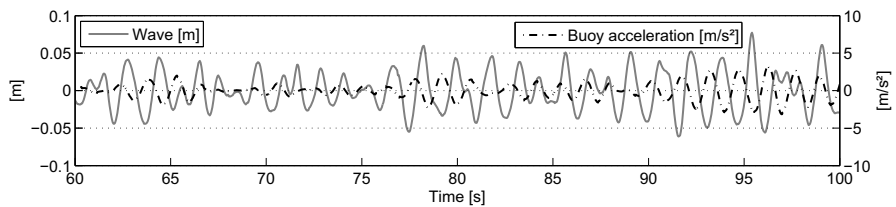
(a) Measured wave and measured buoy position.



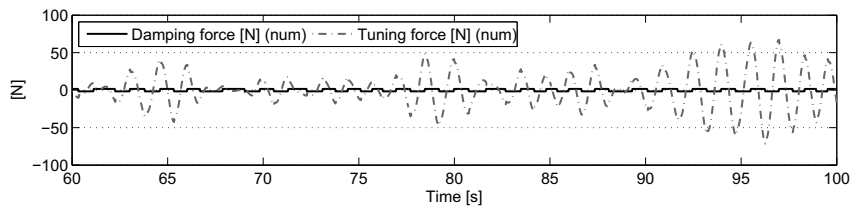
(b) Measured and numerically determined buoy position.



(c) Measured wave and numerically determined buoy velocity.

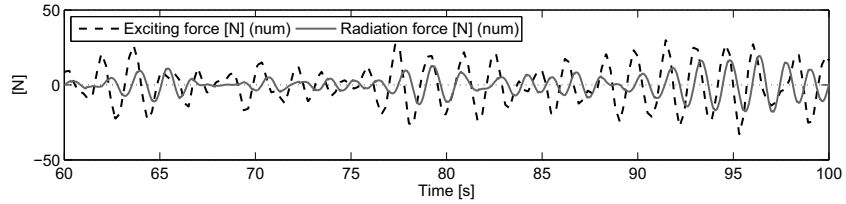


(d) Measured wave and numerically determined buoy acceleration.

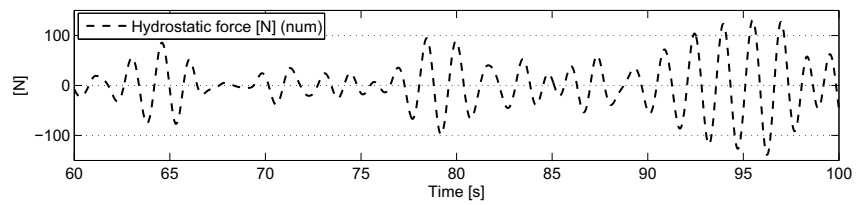


(e) Applied damping and tuning force (num).

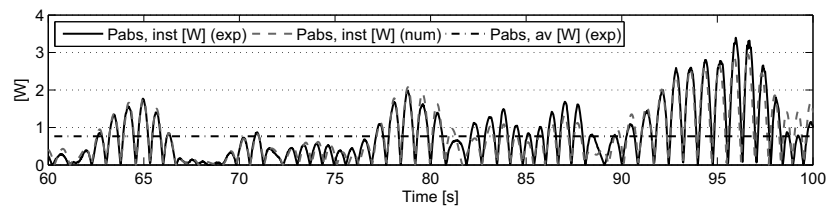
Figure 4.15: Figure continues on next page.



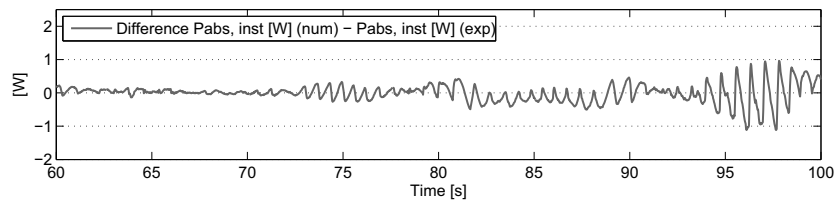
(f) Radiation and exciting force (num).



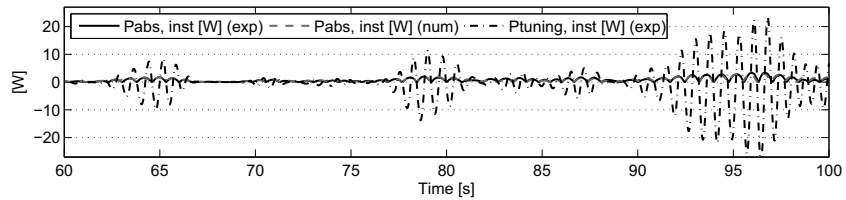
(g) Hydrostatic force (num).



(h) Experimentally and numerically determined power absorption.



(i) Difference between experimentally and numerically determined power absorption.



(j) Power absorption and power associated with the tuning force.

Figure 4.15: Experimentally and numerically determined time series. Test object: hc, $d = 18.9$ cm, $m_{sup} = 21.2$ kg, $F_{d,A} = 1.7$ N, wave characteristics: $H_s = 9.6$ cm, $T_p = 1.83$ s.

contains the product of the buoy acceleration and velocity, which have a phase difference of 90° . Nevertheless, it seems unreasonable that an economical design of the PTO will allow such a large power range, except in very small waves where the useful power is small compared to the rated power. In addition, small inaccuracies in the control may have a drastic effect on the net power absorption.

These observations lead to two preliminary conclusions. First of all, a large device inertia is very important. Systems with a relatively large inertia, e.g. due to supplementary mass or a flywheel, may need only smaller additional control forces to tune the buoys to the incident wave frequencies. Another valuable alternative is the application of latching, i.e. locking and releasing the point absorber at certain time instants to create the desired phase shift between the exciting force and the buoy motion. This is likely to be more practically feasible than realizing the tuning with the PTO.

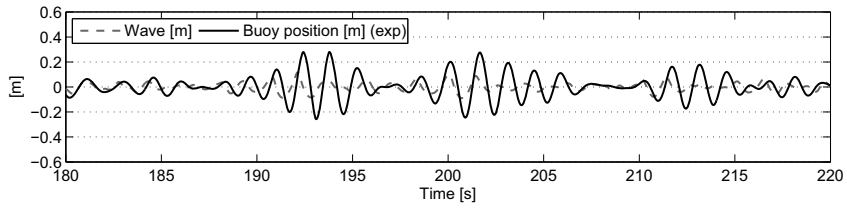
Secondly, if the PTO is supposed to deliver the control forces, it is advisable to implement restrictions on the control force in numerical models, e.g. as introduced in Chapter 2 in order to obtain realistic power output results. These restrictions are generally also associated with a reduction in the occurrence probability of slamming and in the required maximum stroke, since the buoys operate further away from resonance. It would be even better to implement absolute restrictions, instead of constraints based on a statistical parameter, and to apply control parameters that are adjustable in time even within a certain sea state. In that case large control forces and large body motions can be avoided in a specific time frame, without violating the power absorption in the majority of the time. Since this requires more complicated control engineering, it is beyond the scope of this work. However, it remains an important issue, that should be addressed in future work.

Figure 4.16 shows the results of the same measurement, from 180 s after the start of the wave generation. Due to energy building up effects in the flume, most probably due to reflected waves to the side walls, the significant wave height in the flume has been increased and the peak period decreased. Within the time frame of 180 s to 220 s, the wave characteristics are: $H_s = 13.8$ cm and $T_p = 1.28$ s. Note that the wave data analysis is not that reliable for such a small number of waves (27), but at least it gives a rough idea of the characteristics. Similar graphs as in Figures 4.14 and 4.15, showing buoy responses and forces, are plotted. The reason why this time frame is shown too, is because of the

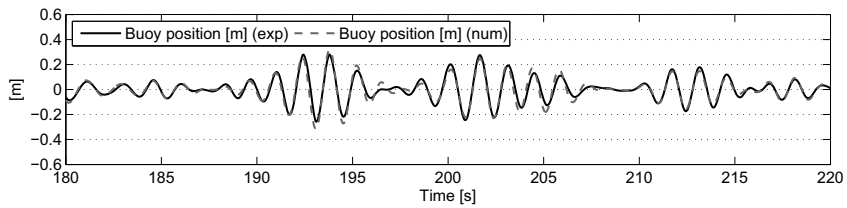
large buoy responses that occur. Since the wave period has been decreased, the buoy is tuned closer towards resonance ($T_n/T_p = 109\%$ instead of 76%), and the buoy even rises out of the water several times. This is illustrated in Figure 4.16(j), showing the relative buoy motion, i.e. the position of the buoy relative to the wave elevation. The draft of the buoy is indicated with a dashed line. When the relative motion of the buoy is larger than the buoy draft, the buoy emerges and might be subjected to slamming. This happens five times during the presented 40 s. This is an undesired control situation for practical applications, since the occurrence probability of slamming is too large, as well as the buoy motions and the tuning forces.

Figure 4.17(a) shows the power absorption efficiency for the cone-cylinder as a function of the total damping force. The efficiency is numerically and experimentally determined for two different buoy drafts with approximately the same tuning ratio: $T_n/T_p = 96\% - 97\%$ in the smallest irregular wave: $H_s = 0.98$ m, $T_p = 6.33$ s (prototype dimensions). In Chapter 2 it was shown numerically that buoys with a smaller draft -and similar waterline diameters- absorb more power than buoys with a larger draft. This finding is confirmed by the experiments. Furthermore, it is observed that the numerical power absorption efficiencies, based on linear theory, are somewhat higher than the experimental values. Similar conclusions can be made for the hemisphere, of which the results are shown in Figure 4.17(b). Both the numerical and experimental power absorption efficiencies are slightly smaller for the hemisphere than the cone. This observation was also already pointed out in Chapter 2.

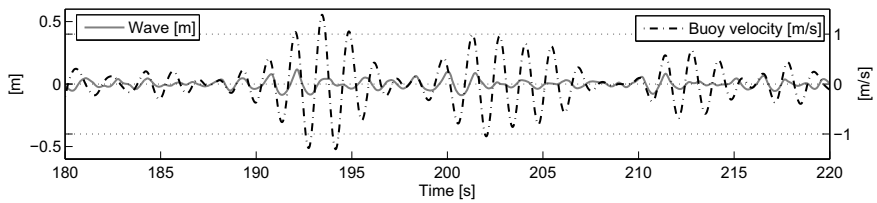
In irregular waves, the general difference in power absorption is smaller than 10% in almost 70% of the cone test cases and in 33% of the hemisphere test cases. In 76% of the hemisphere tests, the difference in power absorption is smaller than 20% , which is still very good. In regular waves the correspondence depended a lot on the ratio between the natural period of the buoy to the wave period. In irregular waves, the technique of applying a fixed supplementary mass for a certain sea state only allows the buoy to be tuned towards a certain predominant frequency, such as the peak frequency. Pure resonance cases, which can be obtained with latching, are not achieved. Often they are even avoided, because they are associated with very high buoy motions. Since the evaluated draft is rather large and the buoy motions are relatively small in our test cases, the influence of non-



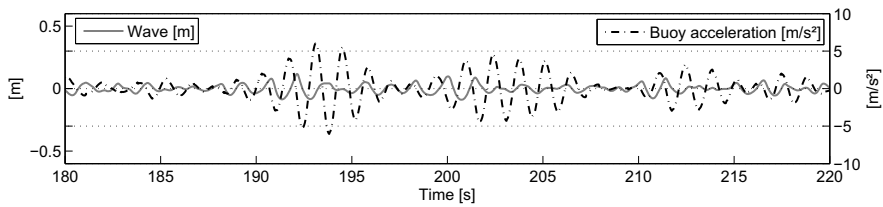
(a) Measured wave and measured buoy position.



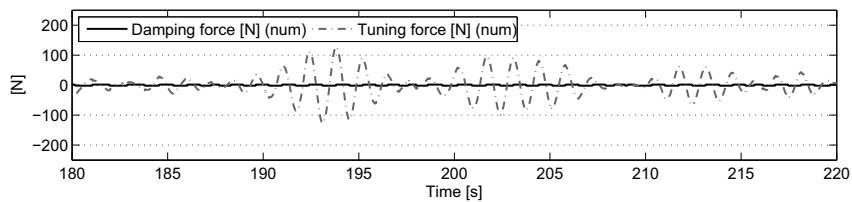
(b) Measured and numerically determined buoy position.



(c) Measured wave and numerically determined buoy velocity.

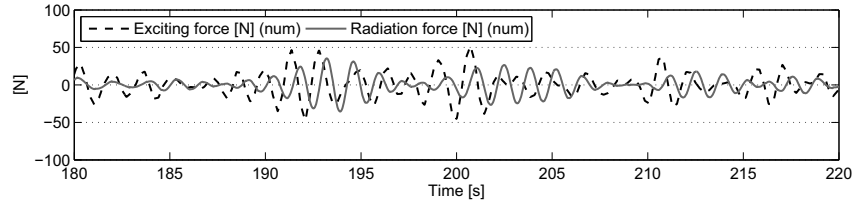


(d) Measured wave and numerically determined buoy acceleration.

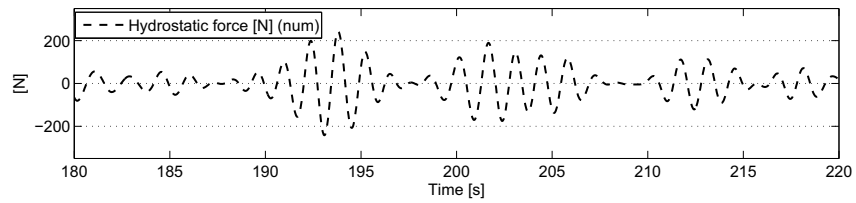


(e) Applied damping and tuning force (num).

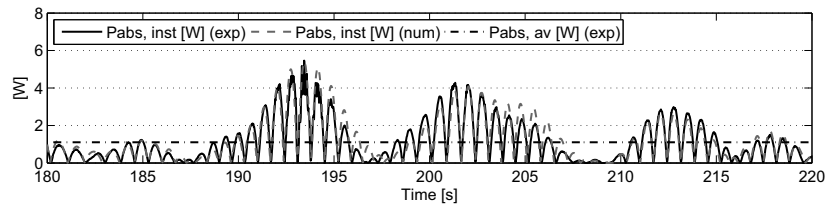
Figure 4.16: Figure continues on next page.



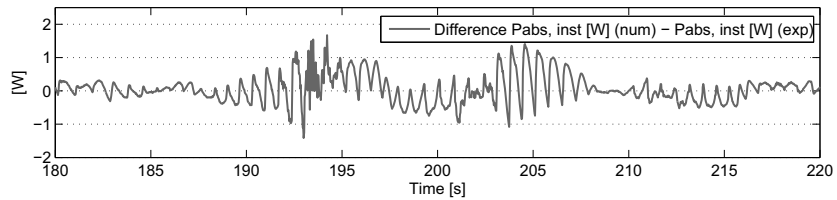
(f) Radiation and exciting force (num).



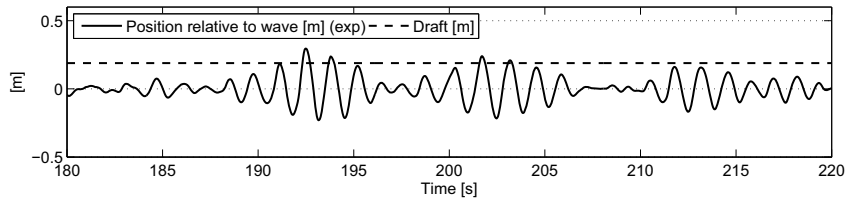
(g) Hydrostatic force (num).



(h) Experimentally and numerically determined power absorption.



(i) Difference between experimentally and numerically determined power absorption.



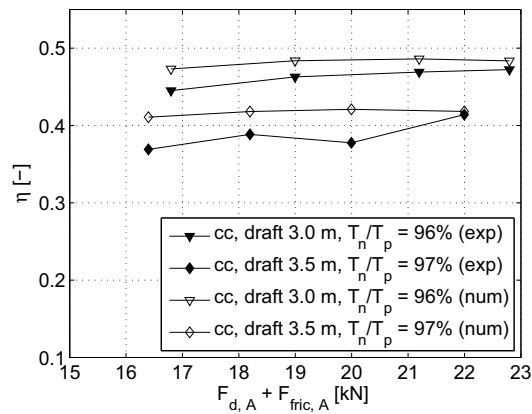
(j) Buoy position relative to wave.

Figure 4.16: Experimentally and numerically determined time series. Test object: hc, $d = 18.9$ cm, $m_{sup} = 21.2$ kg, $F_{d,A} = 1.7$ N, wave characteristics: $H_s = 13.8$ cm, $T_p = 1.28$ s.

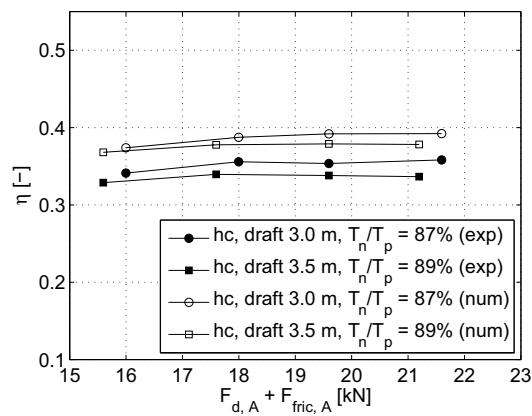
linear effects, from e.g. viscous damping, and from the non-linearity of the hydrostatic and hydrodynamic coefficients, remains at an acceptable level.

In general, smaller experimental power absorption efficiencies are found compared to Vantorre et al. [4]. Some possible reasons have already been mentioned in the Section about regular waves. The presented efficiencies are based on short wave trains (118 s), which has its implication on the reliability of the sea state characteristics (H_s , T_p and the available power). Nevertheless, the influence of different parameters can still be investigated and the numerical model can be validated with the experiments, by comparing the same wave trains.

Figure 4.18 shows the power absorption efficiency as a function of the ratio of the natural period of the point absorber versus the peak period in the smallest irregular wave ($H_s = 0.98$ m, $T_p = 6.33$ s). Experimental and numerical values are given for both the hemisphere and cone shapes with a similar damping force of approximately 10 kN. As expected, the power absorption rises for increasing values of the tuning ratio (T_n/T_p). It could seem remarkable that the experiments with the cone-cylinder shape give a maximum power output for a sub-optimal tuning case ($T_n/T_p = 92$ %). This can be explained by the fact that the hydrostatic restoring coefficient k is assumed constant when calculating the natural period. However, when the buoy amplitudes are larger, the hydrostatic restoring coefficient becomes smaller, due to the smaller waterline diameter, resulting in a higher natural period. This means that the real ratio T_n/T_p is increased and resonance phenomena occur for smaller values of the supplementary mass than initially expected. Although the performance of the cone-cylinder shape and hemisphere-cylinder shape seems to be quite equivalent, it should be mentioned that the required supplementary mass to tune the hemisphere-cylinder is smaller, since its own weight is 41 % higher than that of the cone-cylinder shape with the same draft ($d = 3.5$ m). This requires smaller control forces for the hemisphere, probably resulting in a cost reduction. However, the latter shape will be exposed to much higher impact pressures and forces when bottom slamming on the buoy occurs [17]. This might increase the floater costs. On the other hand, the hemisphere is able to withstand these forces better than the cone due to the membrane action effect. Consequently, the choice between a hemispherical buoy, a conical buoy or an intermediate shape will be more affected by other aspects than only by its hydrodynamic performance.



(a) Test object: cc.



(b) Test object: hc.

Figure 4.17: Power absorption efficiency for different drafts as a function of the total damping force (sum of the external damping force and friction force). Wave characteristics: $H_s = 0.98$ m, $T_p = 6.33$ s.

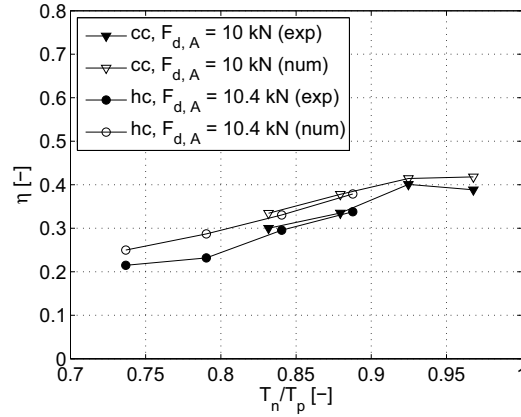


Figure 4.18: Power absorption efficiency as a function of the relative natural period of the system (T_n/T_p) for the cone- and hemisphere-cylinder with $d = 3.5$ m and a damping force of 10 kN and 10.4 kN respectively. Wave characteristics: $H_s = 0.98$ m, $T_p = 6.33$ s.

Figure 4.19(a) gives the power absorption efficiency as a function of the dimensionless total damping force for the cone-cylinder shape in two different irregular waves. For both sea states, a similar supplementary mass of 128 ton has been applied. Since the peak periods of the two sea states are different, this corresponds with different tuning ratios: $T_n/T_p = 96\%$ ('small' wave: $H_s = 0.98$ m - $T_p = 6.33$ s) and 84% ('large' wave: $H_s = 1.52$ m - $T_p = 7.29$ s). Hence, the buoy is better tuned in the smaller wave and absorbs a larger fraction of the available power, although in absolute values the power absorption is largest in the more energetic wave (between 50% and 110% larger than in the smaller wave). For the smaller wave, the power absorption is not much affected by the value of the damping force. For the larger wave though, the power absorption rises for increased damping force values and the optimum is not yet obtained. The results for the hemisphere-cylinder shape are presented in Figure 4.19(b). The supplementary mass is 85 ton, corresponding to tuning ratios of 87% and 76% for the two respective sea states.

Figures 4.20(a) and 4.20(b) show the power absorption efficiency of the cone and hemisphere, respectively, as a function of the dimensionless total damping force for several tuning ratios T_n/T_p . The effect on the power absorption of varying the tuning is significant and much more pronounced

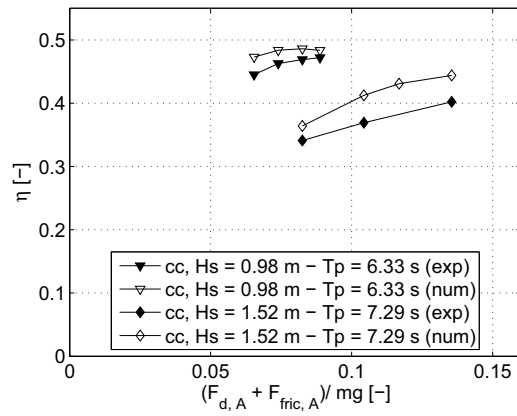
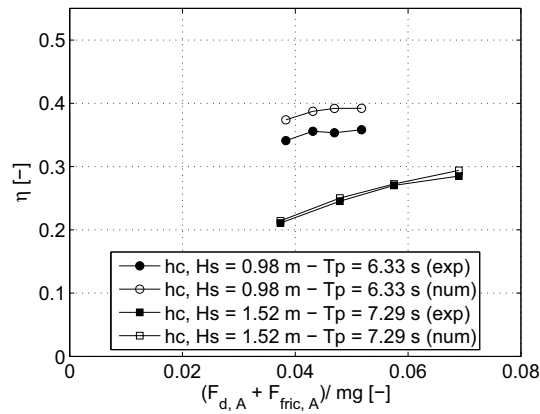
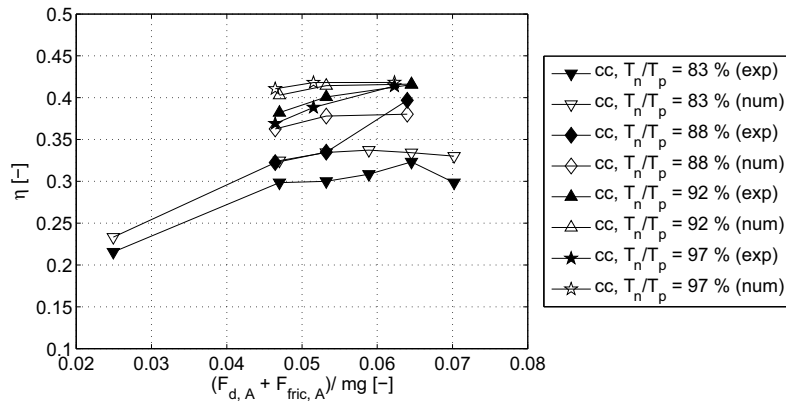
(a) Test object: cc, $d = 3$ m.(b) Test object: hc, $d = 3$ m.

Figure 4.19: Power absorption efficiency as a function of the dimensionless total damping force for the two different sea states.

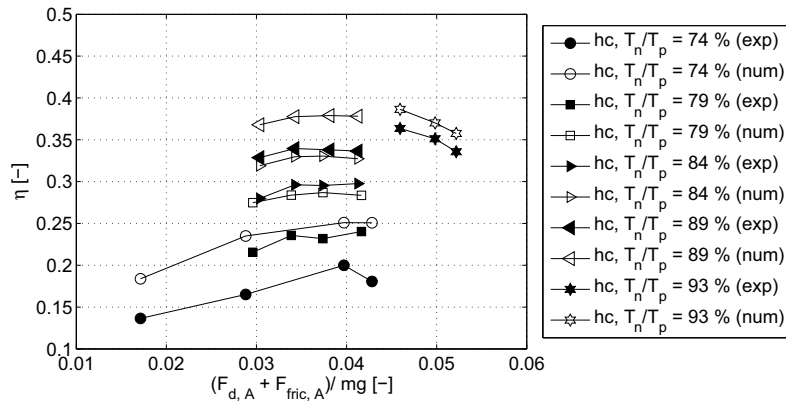
than the effect of changing the damping. For the hemisphere for instance, if the tuning ratio is increased from 74 % to 93 %, the power absorption is increased with a factor of approximately 2.3. However, as noted before, such a large tuning ratio might not be practically interesting, because of the large buoy motions that are involved and the large tuning forces that are required. For the cone shape, the experimental efficiencies are observed to be slightly larger for a tuning ratio of 92 % compared to a ratio of 97 %, due to the non-constant hydrostatic restoring coefficient. This is in agreement with the findings from Figure 4.18.

4.4 Conclusion

Experimental measurements have been performed to validate numerical simulations based on linear potential theory and a linearized equation of motion. A block shaped damping force has been applied to simulate power extraction and a control force proportional to the acceleration has been realized by adding supplementary mass to the system. The selected wave characteristics are based on the measurements of Westhinder buoy, which is located at the Belgian Continental Shelf. Generally, a satisfying correspondence is found between the results from the experimental model and the numerical model. For regular waves, the correspondence between experimental and numerical power absorption is good in non-resonance frequency zones. When resonance occurs, the buoy motions become large and the assumptions behind linear theory are violated. In that situation linear theory overestimates the power absorption by a large margin. In irregular waves, a difference of less than 10 % and 20 %, respectively, is generally found on the average experimental and numerical power absorption for the cone-cylinder and hemisphere-cylinder shape in the selected test cases. It is expected that a larger difference would be found in more energetic waves and for tuned buoys with a smaller draft. In that case slamming phenomena might occur and a non-linear model is required to obtain accurate results. However, in practical situations slamming must be avoided. Hence, it can be concluded that the linear model can be used for most applications that are of practical interest.



(a) Test object: cc, $d = 3.5$ m.



(b) Test object: hc, $d = 3.5$ m.

Figure 4.20: Power absorption efficiency as a function of the total damping force (sum of external damping force and friction force) for different ratios of T_n/T_p . Wave characteristics: $H_s = 0.98$ m, $T_p = 6.33$ s.

Bibliography

- [1] De Backer G., Vantorre M., De Beule K., Beels C., De Rouck J., Experimental investigation of the validity of linear theory to assess the behaviour of a heaving point absorber at the Belgian Continental Shelf. In: 28th International Conference on Ocean, Offshore and Arctic Engineering, Hawaii, 2009.
- [2] Budal K., Falnes J., Iversen L., Hals T., Onshus T., Model experiment with a phase controlled point absorber. In: 2nd International Symposium on Wave and Tidal Energy, United Kingdom, 1981, pp. 191–206.
- [3] Vantorre M., Third-order potential theory for determining the hydrodynamic forces on axisymmetric floating and submerged bodies in a forced periodic heave motion. Ph.D. thesis, Ghent University, Belgium, 1985.
- [4] Vantorre M., Banasiak R., Verhoeven R., Modelling of hydraulic performance and wave energy extraction by a point absorber in heave. *Applied Ocean Research* 2004;26:61–72.
- [5] Durand M., Babarit A., Pettinotti B., Quillard O., Toularastel J., Clément A., Experimental validation of the performances of the SEAREV wave energy converter with real time latching control. In: 7th European Wave and Tidal Energy conference, Portugal, 2007.
- [6] Gilloteaux J.C., Babarit A., Ducrozet G., Durand M., Clément A., A non-linear potential model to predict large-amplitude motions: application to the SEAREV wave energy converter. In: 26th International Conference on Offshore Mechanics and Arctic Engineering, USA, 2007.
- [7] Babarit A., Mouslim H., Clément A., Laporte-Weywada P., On the numerical modelling of the non-linear behaviour of a wave energy converter. In: 28th International Conference on Ocean, Offshore and Arctic Engineering, Hawaii, 2009.

-
- [8] Payne G., Taylor J., Bruce T., Parkin P., Assessment of boundary-element method for modelling a free-floating sloped wave energy device. part 2: Experimental validation. *Ocean Engineering* 2008;35:342–357.
- [9] Weller S., Stallard T., Stansby P.K., Experimental measurements of irregular wave interaction factors in closely spaced arrays. In: 8th European Wave and Tidal Energy Conference, Sweden, 2009.
- [10] Stallard T., Stansby P.K., Williamson A., An experimental study of closely spaced point absorber arrays. In: 18th International Offshore and Polar Engineering Conference, Canada, 2008.
- [11] Thomas S., Weller S., Stallard T., Comparison of numerical and experimental results for the response of heaving floats within an array. In: 2nd International Conference on Ocean Energy, France, 2008.
- [12] De Beule K., Experimental research on point absorber characteristics aiming at the optimization of energy absorption. Master dissertation. (in Dutch). Ghent University, Belgium, 2008.
- [13] Mansard E., Funke E., The measurement of incident and reflected spectra using a least square method. In: 17th Coastal Engineering Conference, Australia, 1980.
- [14] WaveLab: <http://hydrosoft.civil.aau.dk/wavelab/>.
- [15] Beels C., De Rouck J., Verhaeghe H., Geeraerts J., Dumon G., Wave energy on the Belgian Continental Shelf. In: *Oceans 07*, United Kingdom, 2007.
- [16] Flemish Ministry of Transport and Public Works, Haecon, Probabilitas, Hydro Meteo Atlas Measurement grid Flemish banks.
- [17] De Backer G., Vantorre M., De Pré J., De Rouck J., Troch P., Beels C., Van Slycken J., Verleysen P., Experimental study of bottom slamming on point absorbers using drop tests. In: 2nd International Conference on Physical Modelling to Port and Coastal Protection, Italy, 2008.

CHAPTER 5

Performance of closely spaced point absorbers with constrained floater motion

★ ★ ★

In this Chapter the performance of point absorber arrays is numerically assessed in a frequency domain model. Each point absorber is assumed to have its own linear power take-off. The impact of slamming, stroke and force restrictions on the power absorption is evaluated and optimal power take-off parameters are determined. For multiple bodies optimal control parameters are not only dependent on the incoming waves, but also on the position and behaviour of the other buoys. Applying the optimal control values for one buoy to multiple closely spaced buoys results in a suboptimal solution, as will be illustrated. Other ways to determine the power take-off parameters are diagonal optimization and individual optimization. The latter method is found to increase the power absorption on average with about 16 % to 18 %, compared to diagonal optimization. At the end of the Chapter, the yearly absorbed energy at Westhinder on the Belgian Continental Shelf is estimated. This Chapter is an extension of 'Performance of closely spaced point absorbers with constrained floater motion' by G. De Backer et al. [1].

5.1 Introduction

Point absorbers are oscillating wave energy converters with dimensions that are small compared to the incident wave lengths. In order to absorb a considerable amount of power, several point absorbers are grouped in one or more arrays. Some point absorber devices under development consist of a large structure containing multiple, closely spaced oscillating bodies. Examples are Wave Star [2], Manchester Bobber [3] and FO³ [4].

Several theoretical models dealing with interacting bodies have been developed. Budal [5], Evans [6] and Falnes [7] adopted the ‘point absorber approximation’ to derive expressions for the maximum power an array can absorb. The approximation relies on the assumption that the bodies are small compared to the incident wave lengths, so the wave scattering within the array can be neglected while calculating the interactions. This means that the exciting forces on the fixed devices are equal to those of isolated bodies. The scattering of the radiated waves within the array is also neglected. The point absorber theory gives good results for $k_w R \ll 1$, with k_w the wavenumber ($= 2\pi/L$) and R the floater radius [8]. A theory accounting more accurately for the body interactions is the ‘plane-wave approximation’ [9–11], which is based on the assumption that the bodies are widely spaced relative to the incident wavelengths, so the radiated and circular scattered waves can be locally approximated by plane waves. For closely spaced bodies, which is the focus of this Chapter, this theory is not suitable as the wide spacing requirement is not fulfilled, except for very short wave lengths. Satisfying computation results are obtained with this method for values of $k_w d_{cc}$ greater than unity [10, 12], where d_{cc} denotes the centre-to-centre spacing between two neighbouring bodies. In the majority of studies, both theories have been applied to arrays for unconstrained conditions. Contrary to the point absorber approximation, the plane wave approximation is also suitable to study the power absorption of an array in suboptimal conditions, as scattering might be relatively important in that case [9, 13]. Heaving point absorbers with constrained displacements have been studied by McIver [13, 14] by means of the plane wave approximation and by Thomas and Evans [15] with the point absorber approximation, although less suitable. Motion restrictions appeared to significantly reduce the power absorption capability of the array for longer wave lengths [13]. Apart from regular waves, McIver et al. [14] also studied array interactions in irregular unidirectional and directionally spread seas for a varying number of oscillators

between 5 and 20, arranged in one or two lines. In unidirectional irregular normal waves, the power absorption in unconstrained motions outperforms the power extraction in constrained motions. In multidirectional seas, this effect seemed to be clearly less pronounced.

More exact results on array hydrodynamics can be obtained by the ‘multiple scattering’ theory of Mavrakos [16]. This theory has been extensively compared with the above mentioned approximate theories (the point absorber approximation and plane wave approximation) [8, 17].

With current computer capacity, Boundary Element Methods (BEM) are becoming more and more important to investigate interacting point absorbers. Ricci et al. [18] compared results obtained with a BEM code to the point absorber approximation and optimized the point absorber geometry and interbody distance of two array configurations, each consisting of 5 floaters in irregular waves with and without directional spreading. Taghipour et al. [4] investigated the interaction of 21 heaving point absorbers in a floating platform, known as the FO³ device, in unconstrained conditions. By means of a mode expansion method, he was able to reduce the computation time to calculate the body responses by a factor of 10 to 15. Recently, numerical simulations of interacting floaters using the BEM package WAMIT [19] have been successfully validated with experimental tests on arrays by Thomas et al. [15].

The impact of constraints on a single point absorber has been described in Chapter 2, showing that stroke and force restrictions might have a significant impact on the power absorption. In this Chapter, the influence of slamming and stroke restrictions as well as limitations on the power take-off (PTO) forces are investigated for an array in a frequency domain model with WAMIT. The results are compared with the performance of an isolated buoy under the same restrictions. Apart from the total amount of power absorbed by multiple bodies, attention is paid to the individual power absorption and the difference in performance between the buoys within a certain configuration. The control parameters are optimized with different strategies, among them diagonal optimization and individual optimization.

5.2 Methodology

5.2.1 Equation of motion

The equation of motion of an oscillating point absorber has been given in Chapter 1, Eq. (1.51):

$$m\ddot{z} = F_{ex} + F_{rad} + F_{res} + F_{damp} + F_{tun} \quad (5.1)$$

where m is the mass of the buoy and \ddot{z} its acceleration. F_{ex} is the exciting force, F_{rad} the radiation force, F_{res} the hydrostatic restoring force, F_{damp} the external damping force to extract power and F_{tun} the tuning force for phase-controlling the buoy. The damping force is delivered by the power take-off (PTO) system, whereas the tuning force can be exerted by the PTO or another control mechanism. For simplicity, the PTO is assumed linear.

The equation of motion of N multiple bodies, oscillating in heave in a regular wave with angular frequency ω , can be expressed as follows with linear theory in the frequency domain:

$$-\omega^2(\mathbf{M} + \mathbf{M}_a(\omega) + \mathbf{M}_{sup}) \hat{\mathbf{Z}} + j\omega(\mathbf{B}_{ext} + \mathbf{B}_{hyd}(\omega)) \hat{\mathbf{Z}} + \mathbf{K} \hat{\mathbf{Z}} = \hat{\mathbf{F}}_{ex}(\omega) \quad (5.2)$$

where $\hat{\mathbf{Z}}$ is the complex amplitude of the buoy positions, \mathbf{M} the mass matrix of the buoys, and \mathbf{K} the matrix with hydrostatic restoring coefficients or stiffness matrix. The added mass matrix and hydrodynamic damping matrix are denoted by \mathbf{M}_a and \mathbf{B}_{hyd} , respectively. They are both symmetric $N \times N$ matrices with the hydrodynamic interaction coefficients on the non-diagonal positions. The vector $\hat{\mathbf{F}}_{ex}$ contains the complex amplitudes of the heave exciting forces. The hydrodynamic parameters \mathbf{M}_a , \mathbf{B}_{hyd} and $\hat{\mathbf{F}}_{ex}$ are obtained from the BEM software WAMIT [19]. Since the natural frequency of the buoys is generally smaller than the incident wave frequencies, the buoys are often tuned towards the characteristics of the incident waves to augment power absorption. Similar to the previous Chapters, a tuning force proportional to the acceleration has been implemented by means of a supplementary mass matrix, \mathbf{M}_{sup} . \mathbf{M}_{sup} is a diagonal matrix, containing the supplementary mass coefficients of each buoy on the diagonal: $\mathbf{M}_{sup_{jk}} = m_{sup}^{(j)} \mathbf{I}_{jk}$, with $m_{sup}^{(j)}$ the supplementary mass for buoy j , \mathbf{I} the $N \times N$ identity matrix and $j, k \in [1, N]$. A linear external damping matrix, \mathbf{B}_{ext} , has been applied, enabling power

extraction. The external damping matrix -also a diagonal matrix- is defined as: $\mathbf{B}_{\text{ext}_{jk}} = b_{\text{ext}}^{(j)} \mathbf{I}_{jk}$.

The superposition principle is used to obtain the time-averaged power absorption in irregular waves:

$$\mathbf{P}_{\text{abs}} = \sum_{i=1}^{n_f} \frac{1}{2} \omega_i^2 \mathbf{Z}_i^* \mathbf{B}_{\text{ext}} \mathbf{Z}_i \quad (5.3)$$

where n_f is the number of frequencies and \mathbf{Z}_i^* the complex conjugate transpose of \mathbf{Z}_i . The calculations are performed for 40 frequencies, ranging between 0.035 and 0.300 Hz. All buoys are assumed to be equipped with their own power take-off system.

5.2.2 Constraints

Slamming constraint

In Chapter 2, a slamming restriction has been introduced to reduce the probability of rising out of the water. A similar constraint is implemented on each buoy of the array, requiring that the significant amplitude of the buoy position relative to the free water surface elevation should be smaller than a fraction α of the draft d of the buoy:

$$(z^{(j)} - \zeta^{(j)})_{A,\text{sign}} \leq \alpha \cdot d \quad (5.4)$$

where $z^{(j)}$ is the position of buoy j , $\zeta^{(j)}$ the water elevation at the centre of buoy j and α a parameter that is arbitrarily chosen equal to one. The water elevation has been determined with the incident wave only, thereby neglecting the radiated and diffracted waves from the buoys¹.

This slamming restriction might require a decrease of the tuning parameter m_{sup} and/or an increase of the external damping coefficient b_{ext} . Not only the occurrence probability of slamming will be reduced by this measure, but also the magnitude of the associated impact pressures and loads will drop, since they are dependent on the impact velocity of the body relative to the water particle velocity and this impact velocity will decrease when the control parameters of the buoy are adapted according to the restriction imposed.

¹Radiated and diffracted waves from the considered buoy j are neglected too, similar to the method applied for an isolated buoy.

Bottom slamming phenomena will be addressed more in depth in Chapters 6-8.

Stroke constraint

Several point absorber devices are very likely to have practical restrictions on the buoy motion. Therefore a stroke constraint is implemented, similar to the restriction implemented in Chapter 2, i.e. a maximum value on the significant amplitude of the body motion is imposed:

$$z_{A,sign}^{(j)} \leq z_{A,sign,max}^{(j)} \quad (5.5)$$

In the examples that will be presented, a maximum value of the significant amplitude of 2.00 m is chosen. Assuming Rayleigh distribution of the buoy motions, this restriction means that a stroke of 4.90 m is exceeded for 5.0 % of the waves. The implementation of constraints on the body motion increases the reliability of the linear model, which is based on the assumption of small body motions.

Force constraint

As illustrated in Chapters 2 and 4, the optimal control parameters for maximum power absorption, may result in very large control forces, in particular caused by large tuning forces. If this tuning force is to be exerted by the PTO, it might result in a very uneconomic design of the PTO system. In that case it is interesting to study the response of the floaters in case the total control force is restricted, similar to the force constraint introduced in Chapter 2. If the force spectrum is expressed as: $S_{F,i}^{(j)} = F_{A,i}^{(j)2} / (2\Delta f)$ and the significant amplitude of the force is defined as $F_{A,sign}^{(j)} = 2\sqrt{\int_{i=1}^{n_f} S_{F,i}^{(j)} \cdot df}$, then the significant amplitude of the damping and tuning force, respectively, for buoy j are given by:

$$F_{bext,A,sign}^{(j)} = 2\sqrt{\int_0^{\infty} S_{F_{bext,A}}^{(j)}(f)df} \quad (5.6)$$

$$F_{msup,A,sign}^{(j)} = 2\sqrt{\int_0^{\infty} S_{F_{msup,A}}^{(j)}(f)df} \quad (5.7)$$

The significant amplitude of the total force, expressed in Eq. (5.8) will be limited to 100 kN and 200 kN.

$$F_{tot,A,sign}^{(j)} = 2 \sqrt{\int_0^{\infty} \left(S_{F_{bext},A}^{(j)}(f) + S_{F_{msup},A}^{(j)}(f) \right) df} \quad (5.8)$$

5.2.3 Optimization strategies

The relative performance of an array is often expressed by means of the ‘ q -factor’, defined as the maximum time-averaged total power absorbed by the N bodies in the array divided by N times the maximum time-averaged power absorption by a single point absorber.

$$q = \frac{P_{\text{abs, max by array of } N \text{ floaters}}}{N \cdot P_{\text{abs, max by an isolated floater}}} \quad (5.9)$$

The q -factor expresses the performance of the array compared to isolated buoys in ideal circumstances, i.e. when optimal tuning is assumed. Since the control parameters are optimized for a certain sea state, rather than for a particular frequency, the power absorption will be suboptimal, even in unconstrained conditions. Hence, for the current purpose, a measure is needed to express and compare the efficiency of different optimization strategies applied to a given array in suboptimal conditions. Therefore a gain factor \tilde{q} is defined as the ratio of the total power absorbed by the array to the power absorbed by the point absorbers in isolation, subjected to the same constraints.

Three strategies to determine the control parameters for multiple bodies will be compared: optimal control parameters from a single body, diagonal optimization and individual optimization.

Optimal control parameters from a single body

In the first strategy, the optimal control parameters from a single body (OPSB) are applied to all the bodies in the array. It should be kept in mind that ‘optimal parameters’ in this case means that these parameters lead to the maximum possible power absorption within the imposed constraints and with the described control and hence they do not necessarily give the absolute maximum power absorption capability of the array. With this method all bodies have the same control coefficients. However, the control forces, $M_{sup}\ddot{Z}$

and $B_{ext}\dot{Z}$, are not similar for the different buoys, since the buoy velocities and accelerations differ in amplitude and phase. If $m_{sup,SB}$ and $b_{ext,SB}$ are the single body optimal parameters for a specific sea state and a certain combination of restrictions, then the absorbed power for the array is obtained with the following control matrices:

$$\mathbf{M}_{sup} = m_{sup,SB} \mathbf{I} \text{ and } \mathbf{B}_{ext} = b_{ext,SB} \mathbf{I} \quad (5.10)$$

Diagonal optimization

With the second technique, all the buoys still get the same parameters, but they are optimized with a simplex search (SS) method for unconstrained conditions and a sequential quadratic programming (SQP) method for constrained conditions. The methods are validated with an exhaustive searching (ES) method. The latter method gives the same results as SS and SQP, however, SS and SQP are much faster, which is important if very accurate results need to be obtained. The supplementary mass matrix and external damping matrix are similar to those in Eq. (5.10), but $m_{sup,DO}$ and $b_{ext,DO}$ are determined so that the total absorbed power is maximal for the specific array (within the constraints). This technique is called diagonal optimization (DO). It is also referred to as scalar optimization [18].

$$\mathbf{M}_{sup} = m_{sup,DO} \mathbf{I} \text{ and } \mathbf{B}_{ext} = b_{ext,DO} \mathbf{I} \quad (5.11)$$

Individual optimization

With the last technique the floaters are individually optimized (IO), i.e. for every floater separate values of $m_{sup}^{(j)}$ and $b_{ext}^{(j)}$ are determined. Note that the control matrices are still diagonal matrices, however with non-identical elements on the diagonal:

$$\mathbf{M}_{sup} = \begin{bmatrix} m_{sup}^{(1)} & & & \\ & m_{sup}^{(2)} & & \\ & & \ddots & \\ & & & m_{sup}^{(N)} \end{bmatrix} \quad \mathbf{B}_{ext} = \begin{bmatrix} b_{ext}^{(1)} & & & \\ & b_{ext}^{(2)} & & \\ & & \ddots & \\ & & & b_{ext}^{(N)} \end{bmatrix} \quad (5.12)$$

IO has only been successfully applied in constrained conditions. The optimization is carried out with a SQP method only, since a simple exhaustive searching method would require too much CPU-time. If $n_{m_{sup}}$ and $n_{b_{ext}}$ values of $m_{sup}^{(j)}$ and $b_{ext}^{(j)}$, respectively, are to be evaluated, the calculation of the total power absorption needs to be performed $(n_{m_{sup}} \cdot n_{b_{ext}})^N$ times. If e.g. 40 values for each control parameter are to be assessed for a configuration of e.g. 12 floaters, the required number of power absorption calculations would be $2.8 \cdot 10^{38}$, which is not feasible. A drawback of the SQP algorithm for individual tuning is that it might converge to a local maximum, depending on the initial conditions. Hence, the choice of the initial conditions is very important. The control parameters from diagonal optimization have been used as initial values from which individual tuning parameters are obtained. It is advised to check the output with simulations based on different starting values. For instance, the control parameters obtained with individual optimization in a slightly less or more energetic sea state can also be used as begin values. If the number of buoys were small (preferably smaller than 6), the SQP algorithm could be executed with a set of initial conditions for $m_{sup}^{(j)}$ and $b_{ext}^{(j)}$ (multistart algorithm) to increase the chance of reaching the absolute maximum value. Unfortunately, a multistart application is much too time-consuming for the configurations that will be investigated in this Chapter, even if only two initial values per parameter are selected.

5.3 Case study specifications

5.3.1 Configuration

Two multiple body layouts are considered, an aligned grid configuration with 21 buoys, as presented by Fred Olsen and applied to the FO³ device [4], and a staggered grid configuration with 12 buoys. The layouts are shown in Figures 5.1 and 5.2, respectively. The buoys are placed in a square, fixed structure with four supporting columns at the edges. However, the effects of diffraction and reflection of waves on the columns will be further neglected in this study. The interdistance between two successive rows is 8.0 m and 6.5 m, respectively. The incoming waves propagate in the direction of the x -axis, as indicated on the Figures. The buoys are assumed to oscillate in heave mode only. In Figures 5.3 and 5.4 the buoy geometry is presented. A buoy consists of a cone

shape with top angle 90° and a cylindrical upper part with a diameter of 4 m for the configuration with 21 buoys and a diameter of 5 m for the array with 12 buoys. The equilibrium draft of the buoys is 2.5 and 3.0 m, respectively. The total submerged volume, which can be a measured for the material cost, is approximately the same for both configurations. However, it is expected that the total component cost of the array with 12 floaters will be less than for the grid with 21 buoys, since less power take-off units are required. Most results are presented for the configuration with 12 buoys.

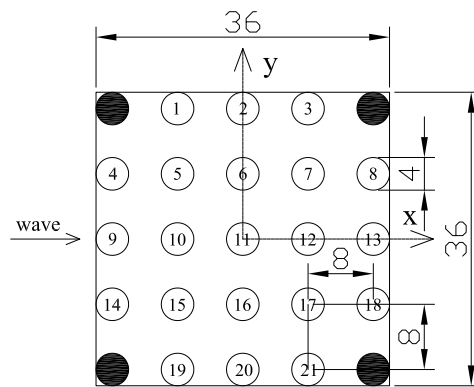


Figure 5.1: Configuration with 21 buoys in an aligned grid, dimensions in m.

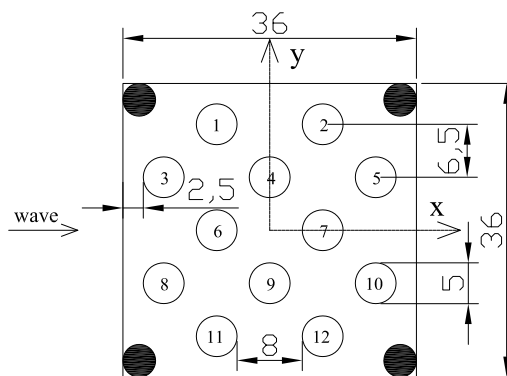


Figure 5.2: Configuration with 12 buoys in a staggered grid, dimensions in m.

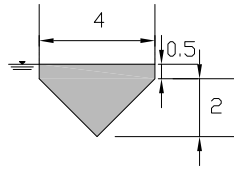


Figure 5.3: Point absorber layout for the configuration with 21 buoys, dimensions in m.

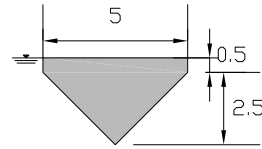


Figure 5.4: Point absorber layout for the configuration with 12 buoys, dimensions in m.

5.3.2 Wave climate

In Chapter 4, nine sea states were defined based on scatter diagrams from buoy measurements at Westhinder. The sea states with their corresponding occurrence probabilities (OP) are displayed in Table 5.1. The mean water depth at the Westhinder buoy is 28.8 m. The majority of calculations will be carried out for the fifth sea state, characterized by a significant wave height, $H_s = 2.25$ m and peak period, $T_p = 7.22$ s. The generated spectrum is based on a parameterized JONSWAP spectrum [20, 21].

Table 5.1: Sea states and occurrence probabilities at Westhinder based on measurements from 1-7-1990 until 30-6-2004 (Source of original scatter diagram: Flemish Ministry of Transport and Public Works (Agency for Maritime and Coastal Services, Coastal Division)).

Sea state	H_s [m]	T_p [s]	OP [%]
1	0.25	5.24	21.58
2	0.75	5.45	37.25
3	1.25	5.98	22.02
4	1.75	6.59	10.65
5	2.25	7.22	5.14
6	2.75	7.78	2.27
7	3.25	8.29	0.79
8	3.75	8.85	0.21
9	4.25	9.10	0.07

5.4 Results

5.4.1 Unconstrained

In this Section, simulations are presented for unconstrained point absorber motions and control forces on the configuration with 12 buoys. Figure 5.5(a) shows the time-averaged power absorption for each floater. As expected, the diagonal optimization (DO) method is more efficient than applying the optimal parameters of a single buoy to the array (OPSB). The power absorption is distributed very unequally between the buoys: the front buoys (in particular Nos 3 and 8) absorb about 2.7 times more energy than buoy No 7 in the back. Rather large buoy motions are observed in Figure 5.5(b), showing the significant amplitudes of the position of the buoys. Figures 5.6(c) and 5.6(d) present the external damping coefficients and supplementary mass coefficients, respectively.

If diagonal optimization is applied, the total power absorption is ca 400 kW. This corresponds to an increase with almost 50 kW compared to OPSB, as can be observed in Table 5.2. Although the power absorption of the array is large, the gain factor \tilde{q} is rather small (46 %), since the absorbed power of an isolated buoy is quite large. It must be stressed, however, that this unconstrained case leads to impractically large control forces (up to a value of $F_{tot,A,sign}$ of 400 kN) and floater motions, violating the assumptions behind linear theory. Consequently, these power absorption figures will most likely not be achieved in practical cases. Furthermore, as stated in the previous Chapters, the power absorption figures do not take into account losses due to mechanical friction, viscous losses, turbine and generator losses or any other losses in the conversion system and hence, they do not correspond to the produced electrical power.

In unconstrained conditions, an individual tuning (IO) did not lead to any realistic solutions. Some buoys may be totally tuned towards resonance, oscillating with very large amplitudes, while other buoys are kept still. This is of course not a desired situation at all. Moreover, in unconstrained conditions the optimization algorithm has a large chance to find a local maximum instead of the absolute maximum, sometimes even without finding a solution which is symmetric with respect to the x -axis. More realistic, constrained cases will be addressed in the next Section.

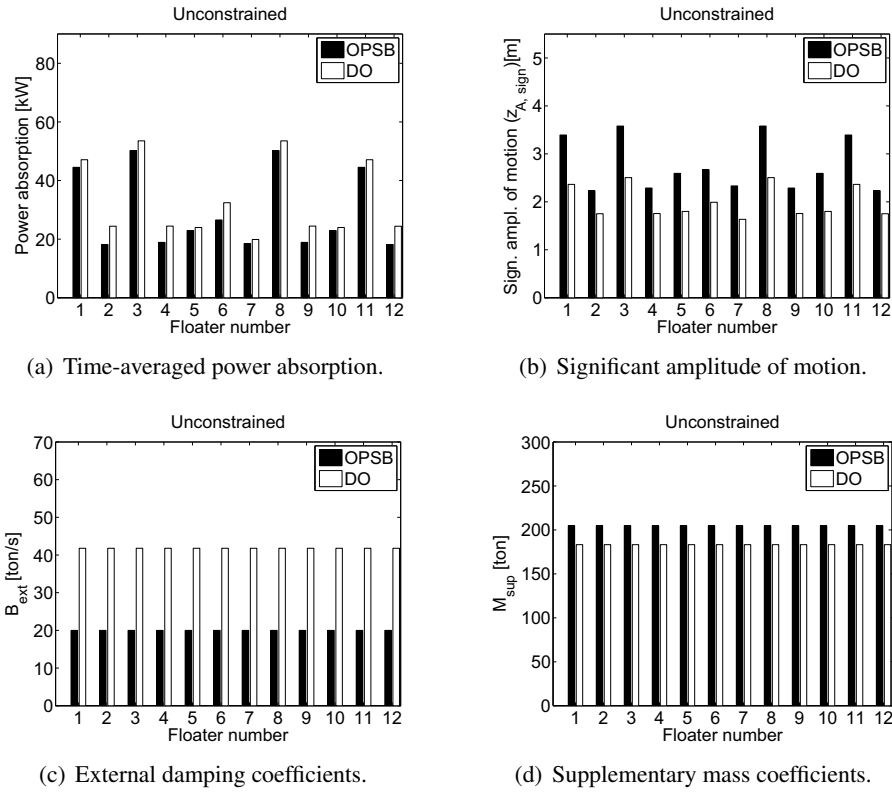


Figure 5.5: Simulation results in unconstrained conditions, with optimal control parameters for a single body and diagonal optimization, sea state: $H_s = 2.25$ m, $T_p = 7.22$ s.

5.4.2 Constrained

Slamming and Stroke constraint

The power absorption and gain factor are determined for the three optimization strategies, taking into account the slamming and stroke restrictions, as explained in Section 5.2.2. Table 5.2 shows that diagonal optimization performs slightly better than the optimal parameters of a single body: the total power absorption is 381 kW with OPBS and 389 kW with DO. A significant benefit can be made by individually optimizing the control parameters of the floaters. The power absorption becomes 443 kW with IO, which is an increase of about 14 % compared to DO or an increase of 54 kW. This figure corresponds

with the amount of power absorbed by an isolated buoy, and illustrates the large profit than can be made by individually tuning the buoys in case they are closely spaced. For the configurations evaluated in [18], the benefit of IO compared to DO was found to be less than one percent. This is most probably due to the fact that the floaters are wider spread from each other in [18]. The interdistance (centre-centre spacing) between two successive rows, for which the two methods were evaluated, varied between 3 and 4 times the diameter D , whereas in the present configuration the interdistance is about $1.3 D$. The larger the interdistance, the more the behaviour of the buoy resembles that of an isolated buoy and the less difference will be found between the optimization techniques. Also the number of floaters is much smaller in [18]: five floaters are considered compared to twelve floaters in the present configuration. Particularly, the buoys in the back benefit considerably from an individual tuning, as is shown in Figure 5.6(a), presenting the power absorption for each buoy. Figure 5.6(b) shows the significant amplitude of the buoy motions. The external damping and tuning parameters are shown in Figures 5.6(c) and 5.6(d), respectively.

With IO, the power absorption is much better distributed among the floaters. A maximum factor of 2.6 is found between the individual power absorption of the front buoys and the rear buoys if DO is used, whereas only a factor of 1.9 is observed when IO is utilized. With individual optimization the buoys in the front absorb less power than with OPSB or DO, however, the buoys in the back become more efficient. This is realized by detuning the front buoys (small value of m_{sup} in Figure 5.6(d)), whereas the rear buoys, on the other hand, are tuned very well to increase their velocity amplitude and power absorption. Consequently, the power that is not absorbed anymore by the front buoys can be absorbed by the buoys in the rows behind them. This makes the influence of restrictions less drastic for an array than for a single buoy. These conclusions will be even more pronounced when the constraints are more stringent, as they will be in the next Sections.

All the buoys reach the maximum stroke value when IO is used, so the stroke restriction is dominant (Figure 5.6(b)). The slamming constraint is generally not critical in the presented examples for the given buoy dimensions and sea state.

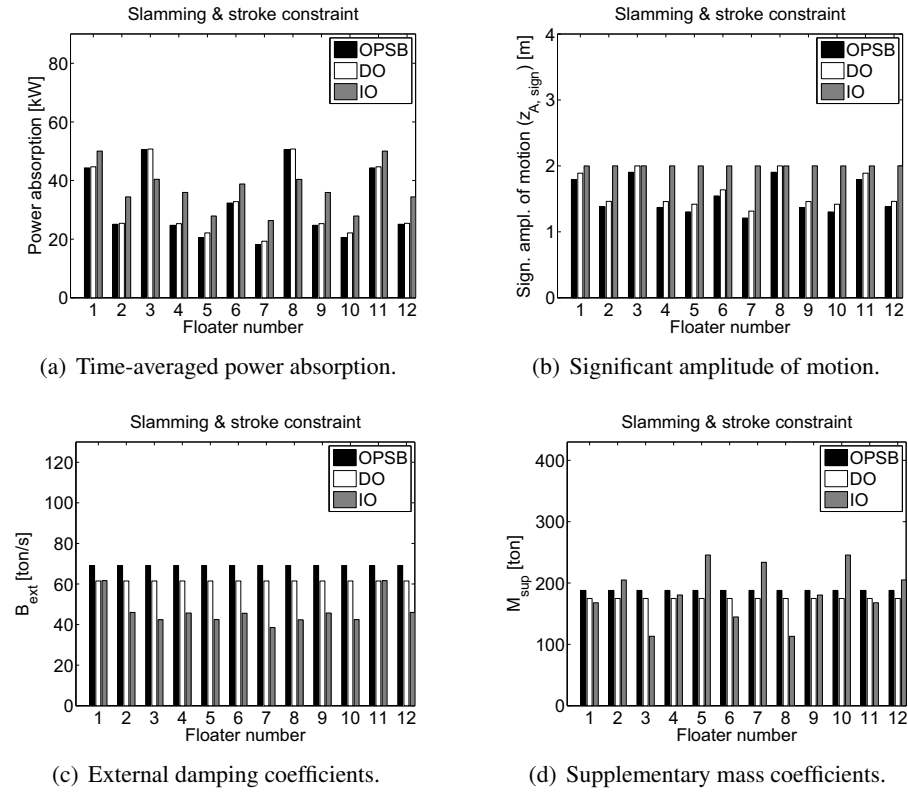


Figure 5.6: Simulation results in constrained conditions (slamming and stroke restriction), with optimal control parameters for a single body, diagonal and individual optimization, sea state: $H_s = 2.25$ m, $T_p = 7.22$ s.

Slamming, stroke and mild force constraint

In this Section the slamming and stroke restrictions are included together with a force constraint of 200 kN on the significant amplitude of the total control force. Figures 5.7(a)-5.7(d) give the power absorption, significant amplitude of the motion and the control parameters of each buoy. The significant amplitude of the damping force, tuning force and total force are presented in Figures 5.7(e)-5.7(g) for the three optimization methods. The force constraint is clearly the most critical constraint. The buoy motions are considerably smaller than the stroke limit. The force limit on the other hand, is reached by the front buoys with the OPSB and DO methods and by all the buoys with

IO. The front buoys even exceed the limit of 200 kN in case of OPSB. If certain control parameters meet the constraints for an isolated buoy, they do not necessarily satisfy the same restrictions applied to an array. This explains why more power is absorbed with OPSB (336 kW) than with the DO method (332 kW) in this case (see Table 5.2), although the DO method was found to be more efficient. Again, a large benefit can be made with the IO technique: the power absorption becomes 379 kW, corresponding with an increase of 46 kW compared to DO, which is even more than the power absorbed by an isolated buoy under the same constraints. Due to the extra force constraint, the power distribution among the floaters has been improved compared to the previous case; the buoys in the front absorb only about 50 % more than those in the back with IO, whereas with DO they absorb about double as much than the rear buoys.

The gain factors \tilde{q} have risen to 0.69 (DO) and 0.79 (IO) for this restriction case, although the total power absorption of the array has decreased due to the extra force constraint. This rise of \tilde{q} can be attributed to the considerable power drop by an isolated buoy under these restrictions. An isolated buoy loses about 25 % of the power absorption, whereas the array loses only 12 to 14 %, compared to the slamming and stroke restriction case. Since the array suffers a bit less from the constraints than the isolated buoy, it has an increased relative performance, although the absolute performance is decreased.

Slamming, stroke and stringent force constraint

In this case, the same slamming and stroke constraints are applied, but the force limit has been decreased till a maximum value of 100 kN. Figures 5.8(a)-5.8(g) show the simulation results of this test case. The power absorption seems to be considerably decreased with this restriction, but it is even more equally distributed among the floaters. The largest difference between the power absorption of the front and rear buoys is a only factor of 1.7 and 1.4 with DO and IO, respectively. In order to satisfy this stringent force restriction, phase control of the buoys is very limited. The tuning forces are considerably small in this case, even smaller than the damping forces.

Again, the restriction is not perfectly fulfilled with the OPSB method. With IO, all floaters have reached the maximum value of the total force, so it is very likely that the IO method has given the correct, most optimal solution. This strong force restriction has a harmful influence on the total power absorption,

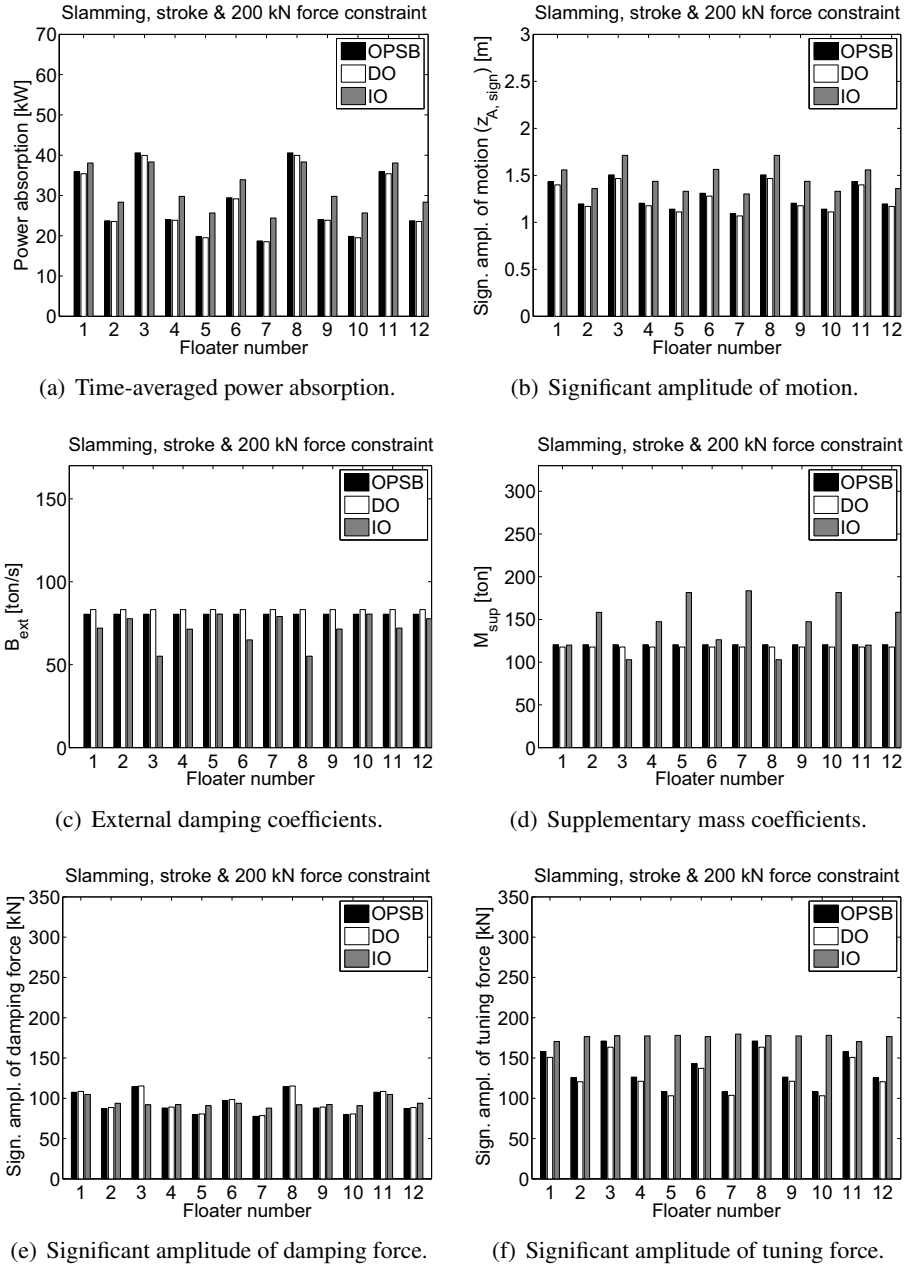
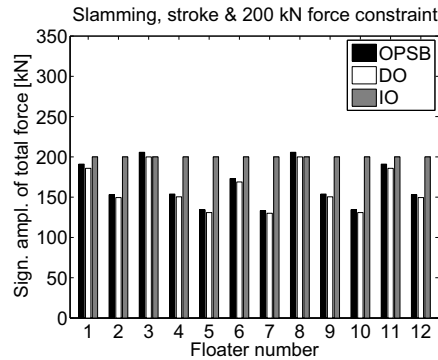


Figure 5.7: Figure continues on next page.



(g) Significant amplitude of total control force.

Figure 5.7: Simulation results in constrained conditions (slamming and stroke restriction, and mild force restriction: $F_{tot,A,sign}^{(j)} \leq 200$ kN), with optimal control parameters for a single body, diagonal and individual optimization, sea state: $H_s = 2.25$ m, $T_p = 7.22$ s.

as displayed in Table 5.2. Compared to the previous case with the mild force constraint, the absorbed power drops with more than 40 % for the single buoy and with 31 % to 33 % for the array.

The results in Table 5.2 for the different restriction combinations illustrate the benefits of phase control on power absorption. However, an economic optimum needs to be found between the power absorption profit of phase control and the costs to realise this tuning and to allow e.g. a larger stroke. Since the power absorption for an isolated buoy is very small, the gain factor reaches quite large values, up to 0.88. In other words the array has a good relative performance, since the rear buoys are still able to absorb an important share in the power, compared to an isolated buoy.

Angle of wave incidence and effects of mistuning

So far, irregular waves propagating along the x -axis have been considered. It might be of interest to investigate the array behaviour for a different angle of wave incidence β_i , e.g. $\beta_i = 45^\circ$. In that case, the configuration in Figure 5.2 can be considered as an aligned grid. The power absorption values and gain factors are presented in Table 5.2 for unconstrained motion as well as for the combination of slamming, stroke and mild force restrictions. It appears

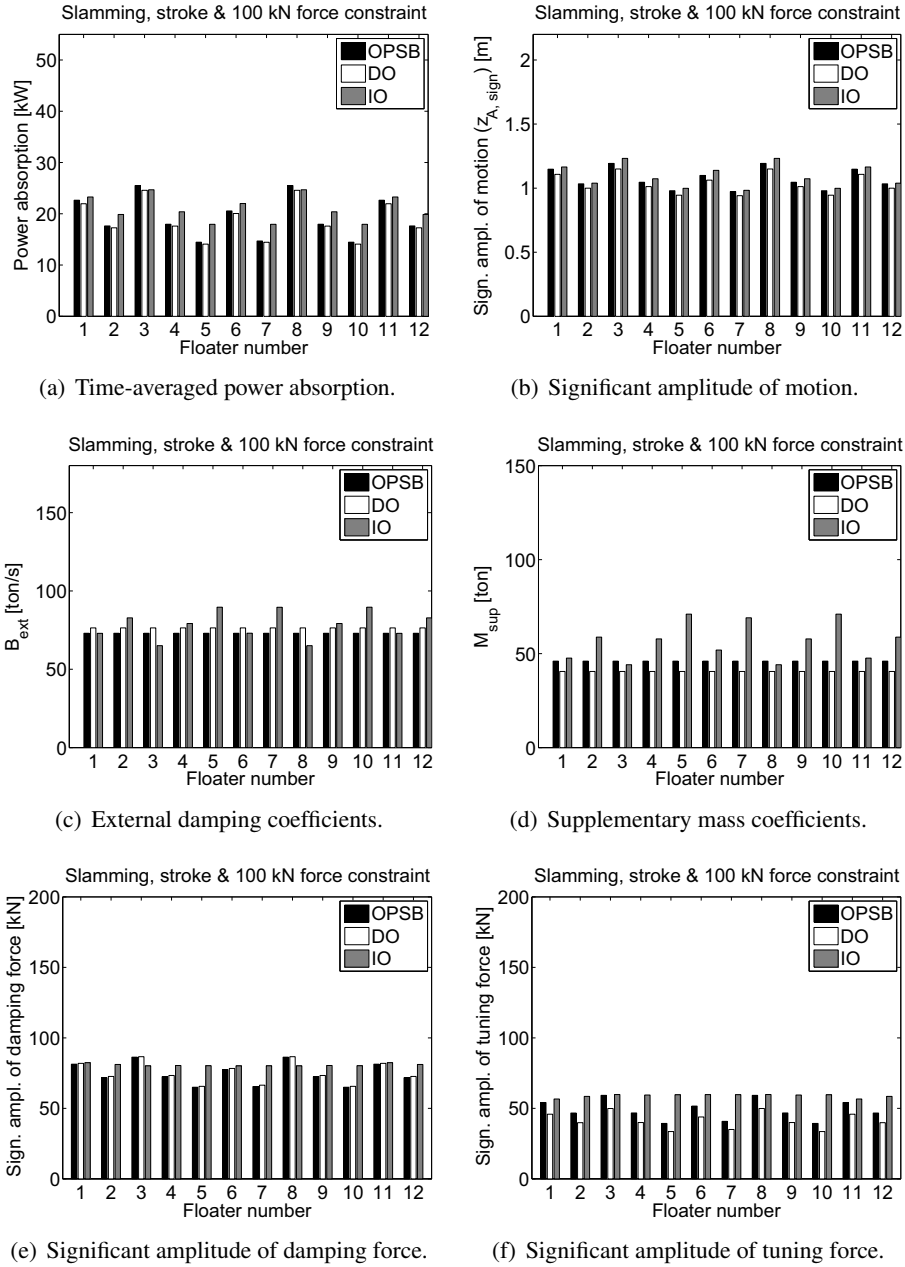
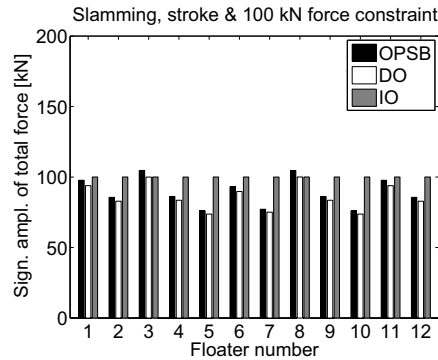


Figure 5.8: Figure continues on next page.



(g) Significant amplitude of total control force.

Figure 5.8: Simulation results in constrained conditions (slamming and stroke restriction, and stringent force restriction: $F_{tot,A,sign}^{(j)} \leq 100$ kN), with optimal control parameters for a single body, diagonal and individual optimization, sea state: $H_s = 2.25$ m, $T_p = 7.22$ s.

that the array performs slightly better when the incident waves propagate in the direction of the diagonal of the array (aligned grid), compared to normal incidence (staggered grid), however, the difference is not significant. The performance of an array is strongly dependent on the wave frequency and therefore the power absorption is calculated for the other sea states at Westhinder (as defined in Table 5.1). Figure 5.9 shows the gain factor \tilde{q} versus the sea state for DO and IO and for two different angles of wave incidence ($\beta_i = 0^\circ$ and, $\beta_i = 45^\circ$), obtained with the slamming, stroke and mild force constraints. A steep rise in \tilde{q} -factor can be noticed from sea state 4 onwards. This might give the impression that the gain factor rises for longer waves. However, the increase is most probably caused by the constraints, which become important for the more energetic wave classes. Since a single body is relatively more affected by the constraints, the gain factor rises in larger waves.

In Figure 5.9 the difference between an angle of incidence of 0° and 45° is very minor for all sea states and no final conclusion can be made about the best angle of incidence. The difference in optimization strategy, on the other hand is very clear: for all sea states and both angles of incidence, individual optimization outperforms diagonal optimization with on average 16%. For

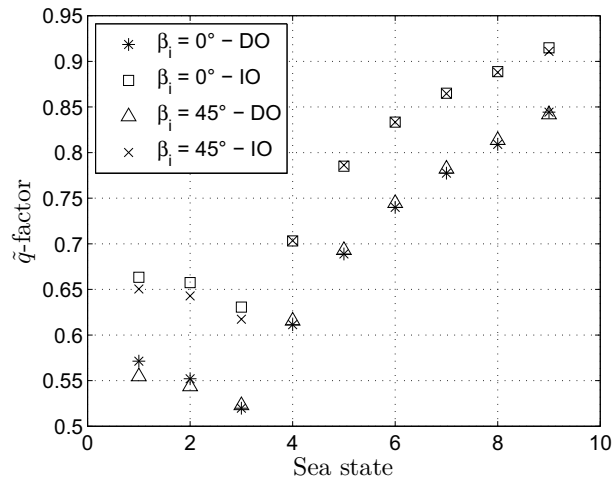


Figure 5.9: \tilde{q} -factors for diagonal and individual optimization as a function of the nine sea states on the Belgian Continental Shelf, configuration: 12 buoys, constraints: slamming, stroke and mild force restriction.

the layout with 21 buoys, the performance difference between DO and IO -on average over all sea states- is 18 %.

In practice, there will be uncertainties on the characteristics of the sea state and the real sea state might not perfectly correspond to the values used in the numerical calculations. For instance the real spectrum might differ from the JONSWAP spectrum that has been employed, the current angle of wave incidence might not be known exactly, etc. Hence, it is important to have an idea of the sensitivity of the optimization techniques to mistuning effects. An example is given in Table 5.3 for unconstrained motion and one case of constrained conditions. Simulation results are presented for an angle of incidence of 45° , but the optimal control parameters (CP) are taken from the simulations with normal wave incidence. It is expected that for the individually optimized parameters, the effect of mistuning will be more pronounced than for the diagonally optimized parameters. This appears to be correct, however, the effect of mistuning is extremely small. For DO the difference in power absorption is less than 0.50 % compared to the results with the correct control parameters for $\beta_i = 45^\circ$. For IO this difference is 1.76 % for the studied case. Obviously, the larger the mistuning, the larger will be the impact on the power

absorption, in particular for IO.

It needs to be mentioned that with the mistuned parameters, the force constraint is still fulfilled for DO, but not anymore for IO. The problem is caused by buoy No 12, exceeding the force limit by 20 %. The buoy is tuned as a rear buoy ($\beta_i = 0^\circ$), getting a high value of the supplementary mass, and becomes rather a front buoy when $\beta_i = 45^\circ$, where it is subjected to higher incident waves. The combination of an increased supplementary mass and large buoy motion parameters leads to larger control forces. When these control forces cannot be delivered, the power absorption figures will be less than expected and hence, the aforementioned losses due to mistuning effects will be larger. More serious problems might be expected when slamming or stroke restrictions are violated. In that case, not only the performance of the system will diminish, but also the lifetime of the device might be affected, due to heavily slamming of the floater on the water surface or e.g. on the fenders attached to the structure enclosing the point absorber.

Application to the Belgian Continental Shelf

Figure 5.10 gives the power absorption versus the sea states at Westhinder for the configuration with 12 and 21 floaters for individual optimization of the control parameters, considering the slamming, stroke and mild force constraints. It is observed from the graph that the power absorption rises swiftly as the sea states become more energetic. The order of magnitude of the power extraction figures corresponds to other wave energy converters, for instance the Pelamis. For a significant wave height ranging between 2 and 2.5 m and a peak period of 7.15 s, the power absorption of the Pelamis varies between 136 and 212 kW, whereas the considered point absorber configurations absorb between 379 kW (12 floaters) and 500 kW (21 floaters) ($H_s = 2.25$ m, $T_p = 7.22$ s). It must be emphasized that the values of Pelamis correspond to the produced power, since they take into account efficiency factors. This is not the case for the calculated power absorption values of the point absorbers, as mentioned before.

When combining the power absorption numbers of Figure 5.10 with the occurrence frequencies of the sea states at Westhinder (mentioned in Table 5.1), the annually absorbed energy can be determined. The results are presented in Table 5.4 and show that the energy absorption per year is around 1 GWh.

Table 5.2: Absorbed power and gain factor \tilde{q} for unconstrained and constrained cases, 12 buoys configuration.

Sea state: $H_s = 2.25$ m, $T_p = 7.22$ s	Single body (SB)		Multiple bodies (MB) - layout with 12 buoys					
	P_{abs} [kW]		P_{abs} [kW]	\tilde{q} [-]	P_{abs} [kW]	\tilde{q} [-]	IO P_{abs} [kW]	IO \tilde{q} [-]
Constraints								
$\beta_i = 0^\circ$								
Unconstrained	73		354	0.41	399	0.46	-	-
Slam, stroke 2.00 m	54		381	0.59	389	0.60	443	0.69
Slam, stroke 2.00 m, force 200 kN	40		336	0.70	332	0.69	379	0.79
Slam, stroke 2.00 m, force 100 kN	24		232	0.81	225	0.79	252	0.88
$\beta_i = 45^\circ$								
Unconstrained	73		360	0.41	403	0.46	-	-
Slam, stroke 2.00 m, force 200 kN	40		337	0.70	334	0.69	379	0.79

Table 5.3: Effects of mistuning - power absorption for the 12 buoy configuration, with $\beta_i = 45^\circ$, while the control parameters (CP) are those obtained for $\beta_i = 0^\circ$.

Sea state: $H_s = 2.25$ m, $T_p = 7.22$ s	DO		IO	
	P_{abs} [kW]	\tilde{q} [-]	P_{abs} [kW]	\tilde{q} [-]
Constraints				
$\beta_i = 45^\circ$, CP from $\beta_i = 0^\circ$				
Unconstrained	403	0.46	0.01	-
Slam, stroke 2.00 m, force 200 kN	333	0.69	0.45	0.77
			372	1.76

Table 5.4: Annually absorbed energy at Westhinder for the configurations with 12 and 21 buoys, both with DO and IO. Constraints: slamming, stroke and mild force constraint.

	12 buoys		21 buoys	
	DO	IO	DO	IO
Yearly energy absorption [GWh]	0.82	0.95	1.00	1.18
Truncated yearly energy absorption [GWh]	0.77	0.90	0.95	1.12

Figure 5.11 shows the contribution of each sea state to the power absorption for the two considered configurations with individual optimization. The share in the average power absorption of the larger sea states is huge compared to the smaller sea states. Note that the smallest sea state, which has an occurrence frequency of more than 20 %, has almost no contribution to the power absorption. It might be of interest to truncate the power absorption at a certain sea state, since the power levels corresponding with the most energetic sea states might be very large, resulting in a costly design. An example is presented in which the power absorption values of sea state 5 are considered as the upper limit, or alternatively, the power absorption of sea states 6 to 8 equals that of sea state 5. Note that the average power absorption values are truncated and that the instantaneous, rated power values are still larger. The yearly energy absorption values for the truncated case are also presented in Table 5.4. The effect of the truncation is rather small.

Based on these preliminary calculations, the benefit of exploiting a device with 21 floaters (of diameter 4 m) versus 12 floaters (of diameter 5 m) appears to be rather limited. The average power absorption is increased with only 23 to 25 % if 21 floaters with a 4 m diameter are installed compared to 12 floaters with a 5 m diameter. A device with 12 floaters is less complex and is therefore expected to be less expensive. Hence, further research is required to evaluate the performance of different configurations. It is important to combine results of the hydrodynamic performance with cost estimates before a definite pronouncement can be made on the entire performance of an array.

5.5 Conclusion

The behaviour of closely spaced point absorbers in unconstrained and constrained conditions has been analysed in irregular unidirectional waves. Two

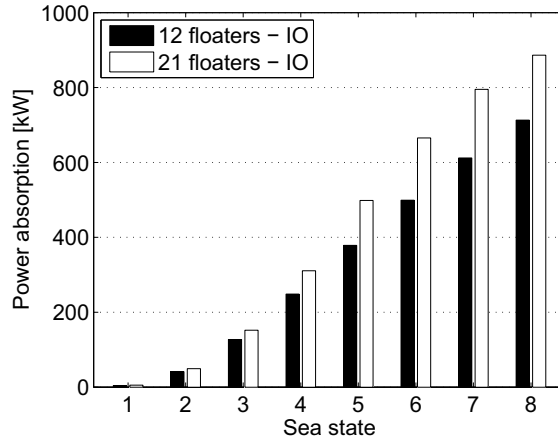


Figure 5.10: Power absorption per sea state for the configuration with 12 and 21 buoys. Constraints: slamming, stroke and mild force constraint.

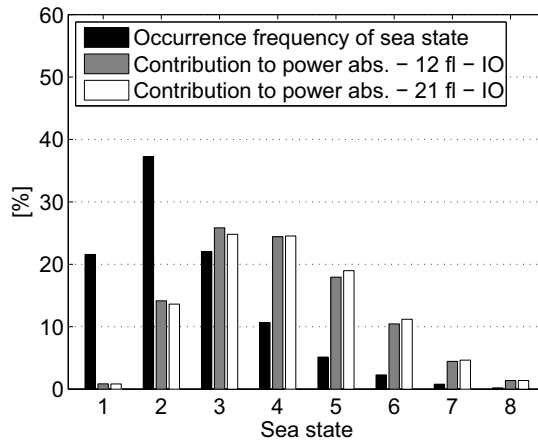


Figure 5.11: Occurrence frequency of sea states and the percentual contribution of each sea state to the power absorption for both array configurations. Constraints: slamming, stroke and mild force constraint.

configurations are considered, one with 12 buoys with a diameter of 5 m and another one with 21 buoys with a diameter of 4 m. The buoys are assumed to be equipped with a linear power take-off, consisting of a linear damping

and a linear tuning force. In unconstrained conditions the absorbed power is found to be very unequally distributed among the floaters. For the considered sea state and the 12 buoys configuration, the front buoys absorbed 2.7 times more power than the rear buoys in unconstrained conditions. For the most stringent constraints the difference was reduced to a factor of 1.4 to 1.7. The total power absorption of the array is negatively affected by the implementation of constraints. However, it is observed that the relative power loss of the array is less than for a single body, since mainly the front buoys are affected by the constraints and to a lesser extent the rear buoys. The power absorption of the arrays has been determined in three different ways. Firstly, the optimal parameters of a single body are applied to the array. This turns out not to be an efficient way. Moreover, the constraints were not always fulfilled for all the bodies in the array, although they were satisfied for the single body case. Secondly, diagonal optimization has been applied. With this method all buoys have the same control parameters, but they are optimized for the array. In the third method, the buoys get individually optimized control parameters. This strategy clearly outperforms the two other methods. On average over all sea states, the power absorption was increased by 16 % and 18 %, respectively, for the configurations with 12 and 21 buoys, by individually optimizing the control parameters, compared to diagonally optimizing them. The difference in performance between the two configurations is rather limited. It is found that the average power absorption at Westhinder for the 21 buoys with diameter 4 m is only one quarter larger than for the 12 buoys with diameter 5 m. The yearly energy absorption at the Westhinder area for the considered array configurations is estimated around 1 GWh. It is recommended for future work to investigate the behaviour of several array configurations in short-crested waves with varying directional spreading parameters, since real seas are multidirectional. Furthermore, it would be relevant to compare the performance of the different control strategies applied in short-crested waves with the presented findings based on long-crested waves.

Bibliography

- [1] De Backer G., Vantorre M., Beels C., De Rouck J., Frigaard P., Performance of closely spaced point absorbers with constrained floater motion. In: 8th European Wave and Tidal Energy Conference, Sweden, 2009.
- [2] Bjerrum A., The Wave Star Energy concept. In: 2nd International Conference on Ocean Energy, 2008.
- [3] <http://www.manchesterbobber.com/>.
- [4] Taghipour R., Arswendy A., Devergez M., Moan T., Efficient frequency-domain analysis of dynamic response for the multi-body wave energy converter in multi-directional waves. In: The 18th International Offshore and Polar Engineering Conference, 2008.
- [5] Budal K., Theory for absorption of wave power by a system of interacting bodies. *Journal of Ship Research* 1977;21:248–253.
- [6] Evans D., Some analytic results for two- and three-dimensional wave-energy absorbers. B. Count: Academic Press, 1980.
- [7] Falnes J., Radiation impedance matrix and optimum power absorption for interacting oscillators in surface waves. *Applied Ocean Research* 1980; 2:75–80.
- [8] Mavrakos S., Kalofonos A., Power absorption by arrays of interacting vertical axisymmetric wave-energy devices. *Journal of Offshore Mechanics and Arctic Engineering - Transactions of the ASME* 1997; 119:244–251.
- [9] Simon J., Multiple scattering in arrays of axisymmetric wave-energy devices. Part 1. A matrix method using a plane-wave approximation. *Journal of Fluid Mechanics* 1982;120:1–25.

-
- [10] McIver P., Evans D., Approximation of wave forces on cylinder arrays. *Applied Ocean Research* 1984;6:101–107.
- [11] McIver P., Wave forces on arrays of bodies. *Journal of Engineering and Mathematics* 1984;18:273–285.
- [12] Kagemoto H., Yue D., Interactions among multiple three-dimensional bodies in water waves: an exact algebraic method. *Journal of Fluid Mechanics* 1986;166:189–209.
- [13] McIver P., Some hydrodynamic aspects of arrays of wave-energy devices. *Applied Ocean Research* 1994;16:61–69.
- [14] McIver P., Mavrakos S.A., Singh G., Wave-power absorption by arrays of devices. In: 2nd European Wave Power Conference, Portugal, 1995, pp. 126–133.
- [15] Thomas S., Weller S., Stallard T., Comparison of numerical and experimental results for the response of heaving floats within an array. In: 2nd International Conference on Ocean Energy, France, 2008.
- [16] Mavrakos S.A., Hydrodynamic coefficients for groups of interacting vertical axisymmetric bodies. *Ocean Engineering* 1991;18:485–515.
- [17] Mavrakos S.A., McIver P., Comparison of methods for computing hydrodynamic characteristics of arrays of wave power devices. *Applied Ocean Research* 1997;19:283–291.
- [18] Ricci P., Saulnier J.B., Falcao A., Point-absorber arrays: a configuration study off the Portuguese west-coast. In: 7th European Wave and Tidal Energy Conference, Portugal, 2007.
- [19] WAMIT user manual: <http://www.wamit.com/manual.htm>.
- [20] Liu Z., Frigaard P., *Random seas*. Aalborg University, 1997.
- [21] Goda Y., *Random seas and design of maritime structures*. World Scientific Publishing Co, 2008.

CHAPTER 6

Water impact on axisymmetric bodies: laboratory drop tests

★ ★ ★

The results of an elaborate experimental investigation on bottom slamming of axisymmetric objects are presented. Drop tests have been performed on a hemisphere and two conical shapes with different deadrise angles. The test setup is designed so as to prevent small rotations of the test objects which cause scatter in the measurement data. The pressure distribution and evolution as well as the body motion parameters are measured during impact. By means of a high speed camera the water uprise is visualized and the wetting factor is determined for the cones. The results are compared with a three-dimensional asymptotic theory for axisymmetric rigid bodies with constant entry velocity. The ratio between the registered peak pressures and the asymptotic theory are in accordance with comparable experiments in the literature. The asymptotic theory, however, is found to be quite conservative, since the measured peak pressure levels appear to be approximately 50 % to 75 % of the theoretical levels.

This Chapter is largely based on: 'Experimental investigation of water impact on axisymmetric bodies' by G. De Backer et al. [1].

6.1 Introduction

An experimental test programme has been executed to investigate bottom slamming phenomena on point absorbers. As explained in Chapter 1, point absorbers are generally tuned to the characteristics of the incoming wave spectrum to increase the power absorption. However, this tuning might cause the buoys to rise out of the water which results in slamming back into the water surface on re-entry. It is important to know to which pressure magnitudes the buoy is exposed when slamming occurs. In this Chapter, bottom slamming on point absorbers is investigated by means of experimental drop tests at laboratory scale.

Figure 6.1 presents a schematic view of a conical point absorber subjected to water impact. The deadrise angle β is the angle between a meridian of the body surface and the horizontal free water surface. When the point absorber penetrates the water, the water surface is no longer plane, but rises along the body surface. If the fluid is assumed to be incompressible, the law of conservation of mass requires that the volume above $z = 0$ equals the displaced volume for $z \leq 0$. A jet flow is noticed which generally ends in a spray. The peak pressures occur in the ‘outer domain’, below to the spray roots. The spray roots are also denoted by the term ‘inner domain’. The pressure in the jet flow is very close to atmospheric pressure. For this reason the water uprise is very often modelled in a simplified way, focusing on the outer domain and neglecting the jet stream and spray roots (inner domain). Slamming pressures are typically very localized in space and time. They are higher and more peaked for larger drop heights and smaller (local) deadrise angles.

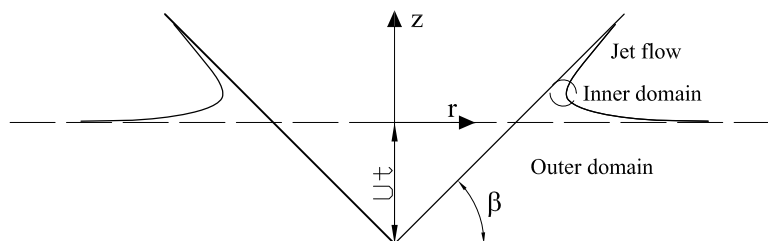


Figure 6.1: Definition sketch of impacting body.

Slamming phenomena have been studied over several decades especially

in naval hydrodynamics. Pioneering research has been carried out by von Karman [2] and Wagner [3]. Wagner studied the water impact on rigid two-dimensional bodies by approximating the bodies with a flat plate and taking into account the water uprise on the body in a simplified way. Because of the blunt body approach, the bodies are assumed to have small deadrise angles in the range of 4 up to 20 degrees [4]. Zhao and Faltinsen presented numerical solution results, based on the findings of Dobrovol'skaya [5], for two-dimensional bodies with deadrise angles between 4 and 81 degrees [6] [7]. Inspired by Zhao's work, Mei et al. [8] developed an analytical solution for the water impact problem of general two-dimensional bodies. The main difference with the Wagner method is that the exact body boundary conditions are fulfilled, instead of approximating the body by a flat plate. The advantage of Wagner's approximation is the ability to use analytical expressions for the velocity potential. However, with the generalized Wagner method, a broader range of (local) deadrise angles can be investigated in a more accurate way.

A substantial amount of experimental work has been performed to validate the analytical and numerical models. Lin and Shieh [9] experimentally investigated the pressure characteristics of a cylinder during water impact. They also visualized the flow pattern during penetration by making use of a digital imaging system and a high speed data acquisition system. Zhao and Faltinsen [7] performed drop tests to study two-dimensional flow situations of horizontal wedges dropped onto the free water surface. Experiments by Yettou [10] et al. consist of free fall drop tests on symmetrical wedges. They investigated the influence of the drop height, the deadrise angle and the mass of the wedge and compared the results with existing models from Mei et al. [8] and Zhao and Faltinsen [7].

Most studies have focused on two-dimensional impact problems since slamming on ships has been a major concern. However, there is a need for three-dimensional solutions because real impact phenomena are three-dimensional. In this work, vertical slamming of three-dimensional axisymmetric bodies is considered. Early studies in this area have been published by Shiffman and Spencer [11] [12]. They investigated vertical slamming phenomena on spheres and cones analytically by approximating the bodies as a lens and an ellipsoid and presented solutions for the impact force on these axisymmetric objects. Wagner's theory has been extended to axisymmetric

bodies by Chuang [13] and Faltinsen and Zhao [14]. In the case of axisymmetric objects, the body shape is approximated with a growing flat disc analogous to Wagner's flat plate approximation for two-dimensional shapes. Based on this principle, Chuang [13] developed an analytical expression for the pressure distribution on a cone with small deadrise angle. In 1997 Faltinsen and Zhao [14] presented an asymptotic theory for water entry of hemispheres and cones with small (local) deadrise angles based on the assumptions behind the Wagner theory. Scolan and Korobkin [15] presented analytical solutions for three-dimensional bodies obtained with the inverse Wagner method. Another important contributor to axisymmetric slamming problems is Miloh [16] [17] [18] who developed analytical expressions for the slamming forces on axisymmetric bodies. One of the main differences between his work and the classical Wagner's theory is that the body boundary conditions are satisfied exactly on the actual body surface instead of on a flat disc.

In 2003 Battistin and Iafrati [19] numerically studied impact loads and pressure distributions on two-dimensional and axisymmetric bodies. Two years later Faltinsen and Chezhian [20] presented a generalized Wagner method for three-dimensional slamming based on the approach presented by Zhao et al. [7] for two-dimensional water impact problems. To validate the numerical simulations, they performed drop tests on a three-dimensional shiplike composite structure from which they obtained several force measurements. Peseux, Gornet and Donguy [21] solved the three-dimensional Wagner problem numerically for both rigid and deformable bodies. The numerical model is validated with an interesting experimental investigation consisting of drop tests of conical shapes with small deadrise angles (6° - 10° - 14°). Kim and Hong [22] numerically studied the impact of arbitrary three-dimensional bodies with an extended von Karman and an extended Wagner approach, including the presence of incoming waves. They also presented experimental results on the impact loads during water entry of three-dimensional structures.

Very few experiments are available for validation of theoretical pressure predictions for axisymmetric bodies. In 1961 Nisewanger [23] performed drop tests on aluminium hemispheres and measured pressure distributions with self-made pressure transducers. For conical shapes, experimental research has been carried out by Chuang and Milne [24] in 1971 and more recently by Peseux et al. as mentioned above. In the former study impact pressures are measured on cone shapes with small deadrise angles varying from 1° to 15° . Point absorbers

with a conical shape are very likely to have larger deadrise angles ($\geq 20^\circ$). In this Chapter the results of new impact experiments on a hemisphere and on cone shapes with larger deadrise angles are presented.

6.2 Slamming pressures and forces

6.2.1 Pressures

Pressure distribution

The experimental results are compared with existing asymptotic solutions based on the classical Wagner method extended to axisymmetric bodies, as it was proposed by Chuang [13] and Faltinsen et al. [14]. Despite the interesting work that has already been carried out in the field of water impact, Wagner's method is even nowadays still very valuable, since it produces analytical formulas that are easy to handle and give a very good first insight into the problem. The fluid flow is described by potential theory and a constant entry velocity U is assumed. The initial time instant, $t_0 = 0$ s, is defined as the time where the body touches the calm water surface. At a time t , the penetration depth relative to the calm water surface ($z = 0$) equals Ut and the corresponding instantaneous radius at the wet section of the cone is $b_0(t)$, as shown in Figure 6.2. The instantaneous radius $b(t)$ at the intersection point between the body and the water is found by integrating the vertical velocity of the water particles at $z = 0$. For a cone shape this results in $b(t) = 4Ut / (\pi \tan \beta)$ [14]. It should be mentioned that Figure 6.2 gives a simplified representation of the water uprise, since in reality a jet flow occurs which might end in a spray, depending on the convexity of the object.

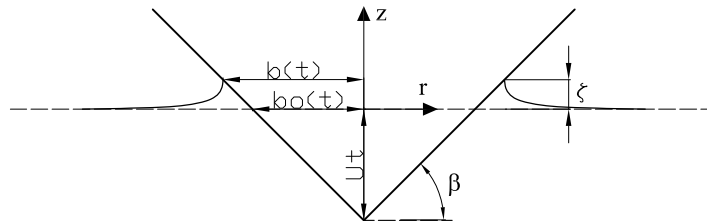


Figure 6.2: Simplified representation of water uprise as proposed by Wagner.

The pressure on a cone shape with deadrise angle β , at a certain distance r

from the symmetry axis, is expressed by:

$$p_{cone} = \frac{1}{2}\rho U^2 \left[1 - \frac{4\left(\frac{r}{Ut}\right)^2}{\pi^2\left(\frac{16}{\pi^2\tan^2\beta} - \left(\frac{r}{Ut}\right)^2\right)} + \frac{64}{\pi^3\tan^2\beta\sqrt{\frac{16}{\pi^2\tan^2\beta} - \left(\frac{r}{Ut}\right)^2}} \right] \quad (6.1)$$

Eq. (6.1) is composed of three terms. The first term expresses the stagnation pressure. The second term is a consequence of the permanent flow around the disc and the third term accounts for the expansion of the disc, representing the effect of the non-stationary behaviour of the flow around the disc. As mentioned before, the blunt body assumption in Wagner's method implies that bodies should have small local deadrise angles. In the literature, it is stated that the classical Wagner theory gives quite accurate results for wedges with deadrise angles in the range of 4 to 20 degrees [7]. When deadrise angles are smaller than 4 degrees, an air cushion is formed, which reduces the pressure on the structure and as a result, Wagner theory overestimates the pressure by a large margin.

For a hemisphere the relationship between the penetration depth and instant wet radius b is not as straightforward as it is for a cone shape. Faltinsen and Zhao [14] suggested a quadratic relation between Ut and b which is only valid for small submergences ($Ut/R < 1/5$): $b = \sqrt{3RUt}$. The pressure on an impacting hemisphere with radius R , at a distance r from the symmetry axis, is expressed as follows:

$$p_{hemisphere} = \frac{1}{2}\rho U^2 \left[1 - \frac{4\left(\frac{r}{Ut}\right)^2}{\pi^2\left(\frac{3R}{Ut} - \left(\frac{r}{Ut}\right)^2\right)} + \frac{6}{\pi\sqrt{\frac{3Ut}{R} - \left(\frac{r}{R}\right)^2}} \right] \quad (6.2)$$

Figure 6.3 shows the distribution of the slamming pressure coefficient as a function of the dimensionless radius for an impacting cone with different deadrise angles β . The slamming pressure coefficient can be expressed as: $C_p = p/(0.5\rho U^2)$. A more peaked pressure distribution and a significant pressure increase can be observed when the deadrise angle decreases. When β decreases from 30° to 15° , the dimensionless pressure peak rises from 6.3 up to 24.0, which is an increase by almost a factor of 4. Note that the pressure drops after the peak level occurred and even goes to minus infinity for r equal

to b , which is obviously unphysical. In order to know the correct pressure near $r = b$, an analysis near the spray roots is required.

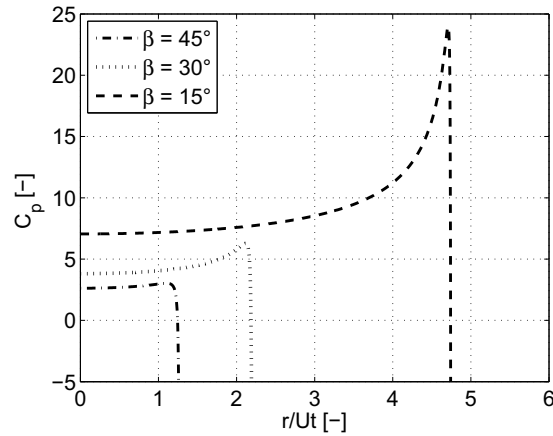


Figure 6.3: Pressure distribution on a cone as a function of the dimensionless radius r/Ut .

Figure 6.4 shows the pressure on a hemisphere with radius R and impact velocity U as a function of the dimensionless parameters r/Ut and R/Ut . The plot is restricted by the requirement that the coordinate r should be smaller than the instantaneous wetted radius b , which means: $r/Ut < \sqrt{3R/Ut}$. When a small fraction of the hemisphere is submerged (large R/Ut value), the material is exposed to very high pressure peaks, specifically in the area close to the wetted radius b (large r/Ut value).

Peak pressure

From Eqs. (6.1 - 6.2) the peak pressure levels for cones and hemispheres can be assessed. Figure 6.5 shows the maximum slamming pressure coefficient on a cone for deadrise angles varying between 10° and 45° . Figure 6.6 shows the maximum slamming pressure coefficient on a hemisphere as a function of the relative position r/R . At the bottom area of the hemisphere ($r/R < 0.1$) the local deadrise angles are very small and the peak pressure values are much overestimated for the same reason.

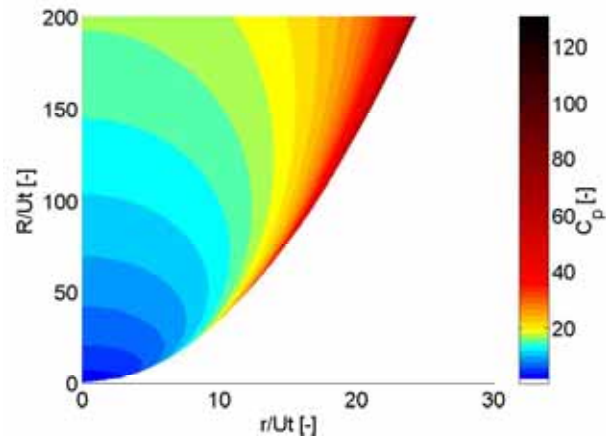


Figure 6.4: Slamming pressure coefficient C_p on a hemisphere as a function of the dimensionless parameters r/Ut and R/Ut .

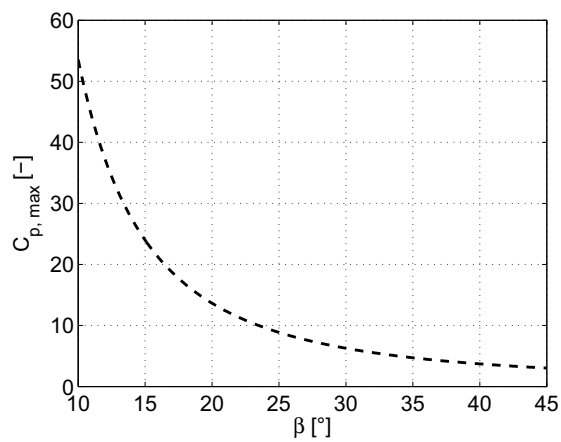


Figure 6.5: Maximum slamming pressure coefficient on a cone as a function of the deadrise angle β with asymptotic theory.

6.2.2 Vertical Slamming Forces

Besides slamming pressures, also the significant global loads acting on the point absorber structures might be of a concern. Hence, it is important to know to which vertical slamming forces, F_3 , the structure is subjected when bottom

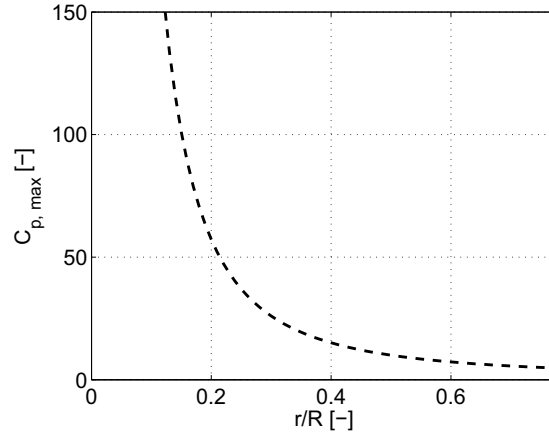


Figure 6.6: Maximum slamming pressure coefficient on a hemisphere as a function of the dimensionless parameter r/R with asymptotic theory.

slamming occurs. Slamming loads on impacting bodies have been extensively studied up to now. A brief overview of literature results will be given.

The hydrodynamic impact force can be expressed as:

$$F_3 = \frac{d(m_{a\infty}U)}{dt} = m_{a\infty} \frac{dU}{dt} + \frac{dm_{a\infty}}{dt}U \quad (6.3)$$

where $m_{a\infty}$ is the infinite frequency limit of the added mass. If a constant entry velocity is assumed, the first term in Eq. (6.3) vanishes. The slamming force obtained from the time derivative of the **added mass** is indicated with ‘AM’.

Shiffman and Spencer [12] developed a theoretical formula, as expressed in Eq. (6.4), for the impact force on a cone by approximating the cone shape by an ellipsoid:

$$F_{3cone} = \frac{3m_{a\infty}}{U t (1 + (m_{a\infty}/m))^3} U^2 \quad (6.4)$$

where m is the mass of the cone and U the initial entry velocity. The added mass for infinite frequency is expressed as:

$$m_{a\infty} = k_{ss}(\beta) \rho \left(U t \tan\left(\frac{\pi}{2} - \beta\right) \right)^3 \quad (6.5)$$

where k_{ss} is a non-dimensional value between 0 and 3 dependent on the deadrise angle. For a cone with deadrise angle $\beta = 20^\circ, 30^\circ$ and 45° , k_{ss} is 2.24, 1.6 and 1.4, respectively. Note that the expression for the added mass for infinite frequency is related to the mass of a hemisphere with a diameter equal to the waterline diameter $2Ut \tan(\frac{\pi}{2} - \beta)$, i.e. $m_{\text{hemisphere}} = 2/3\pi\rho (Ut \tan(\frac{\pi}{2} - \beta))^3$. Shiffman and Spencer stated that Eq. (6.4) is a good approximation up to the penetration depth where F_3 attains its maximum value. The theory is based on the similitude of the flow at different time instants and thus assumes an approximately constant entry velocity. This implies that the mass of the buoy should be much larger than the mass of the displaced water. Consequently Eq. (6.4) can be approximated with:

$$F_{3\text{cone}} = 3k_{ss}\rho \tan^3\left(\frac{\pi}{2} - \beta\right) U^4 t^2 \quad (6.6)$$

Battistin et al. [19] and Kleefsman et al. [25] found a good correspondence between their numerical results for a cone with constant entry velocity and Eq. (6.6) of Shiffman and Spencer.

Miloh [18] analysed the impact on a sphere satisfying the exact body boundary conditions. With a wetting coefficient, $C_w = 1 + \frac{\zeta}{U_t}$, of 1.327 he suggests a force F_3 for small entry depths and a constant entry velocity:

$$F_{3\text{hemisphere}} = 0.5\rho\pi R^2 U^2 \left(5.5 \left(\frac{Ut}{R}\right)^{(1/2)} - 4.19 \left(\frac{Ut}{R}\right) - 4.26 \left(\frac{Ut}{R}\right)^{(3/2)} \right) \quad (6.7)$$

The slamming impact force can also be obtained by pressure integration (PI) of the hydrodynamic pressures, for example by integrating the expressions in Eqs. (6.1) and (6.2) obtained with asymptotic theory.

The second term in Eq. (6.3) can also be computed by integration of the pressures given in Eqs. (6.1) and (6.2). This will be referred to as the pressure integration (PI) method. Faltinsen [14] presented analytical formulas for F_3 by integrating the third term of Eqs. (6.1) and (6.2), which is the predominant part of the pressure accounting for the non-permanent flow around the expanding disc. Since a constant entry velocity is assumed, the first term in Eq. (6.3) drops, resulting in Eqs. (6.8) and (6.9), for a cone and hemisphere, respectively

[14]:

$$F_{3cone} = 256\rho \frac{t^2 U^4}{(\pi \tan \beta)^3} \quad (6.8)$$

$$F_{3hemisphere} = 6\sqrt{3}\rho\sqrt{U^5 t R^3} \quad (6.9)$$

The same assumptions as for the pressure formulas apply here, i.e. small entry depths for the hemisphere and small deadrise angles for the cone shape. When F_3 is known, the acceleration at each time step is derived and the velocity and penetration depth are obtained by numerical integration of the acceleration.

Figure 6.7 shows several predictions of the slamming force coefficient $C_s = F_3/0.5\rho\pi R^2 U^2$ on a sphere. The black dashed line represents Eq. (6.9) by Faltinsen and the dotted line shows the slamming force coefficient obtained by pressure integration of the entire expression in Eq. (6.2). The formula derived by Miloh is given in a black solid line. The analytical expressions are compared with experimental results by Moghisi and Squire [26] (grey dash-dotted line) and numerical data by Faltinsen [14] (grey dashed line) and Battistin and Iafrati [19] (grey solid line). In the numerical approaches a constant entry velocity is assumed, the exact body boundary conditions are fulfilled and the uprise of the water is accounted for. The asymptotic theory clearly overestimates the force by a large margin after the very initial stage of submergence. The numerical results [14] [19] and the analytical formula from Miloh correspond quite well with the experimental values of Moghisi and Squire.

Figure 6.8 compares the impact force on a hemisphere ($R = 2.5$ m) and two cones with deadrise angle 30° and 45° for a drop height of 2 m. Note the large magnitude of the forces up to almost 500 kN for the hemisphere. Eq. (6.4) of Shiffman and Spencer corresponds well with the approximation in Eq. (6.6) during the initial impact phase. However, a gradual discrepancy occurs which becomes quite large at the maximum impact force. The maximum value of the hydrodynamic load on the hemisphere is reached very quickly after submergence (at $Ut = 0.41$ m). The maximum level for the 30° cone is attained at a submergence of 0.87 m and for the 45° cone at 1.75 m. Obviously the

deadrise angle of the cone has a huge influence on the magnitude and rise time of the impact force.

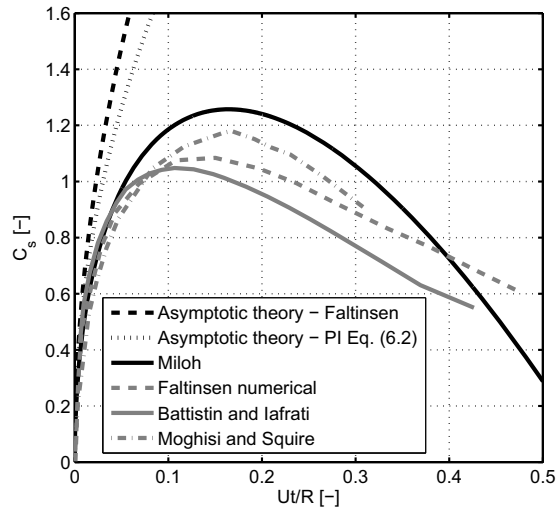


Figure 6.7: Force slamming coefficient C_s on a hemisphere versus the dimensionless time Ut/R .

6.3 Experimental design

6.3.1 Test setup and test objects

Table 6.1 shows the three different bodies that have been tested: a hemisphere and two cones with deadrise angles of 20° and 45° . The models are made from polyurethane and have a large thickness from 30 mm to 50 mm. As mentioned in Table 6.1 the diameter of the objects is 0.30 m, which is sufficient to reduce surface tension effects. The bodies are dropped in a water basin with horizontal dimensions of 1.20 m by 1.00 m and a height of 1.25 m. Twelve different drop heights between 0.05 m and 2.00 m have been evaluated, corresponding to impact velocities of 1.0 m/s and 6.3 m/s. A realistic stroke for a point absorber buoy is about 5 to 10 m. Dependent on the control parameters, a free fall of 2 m can be considered as an extreme case. Smaller drop heights will occur more frequently and are therefore relevant as well. Because of

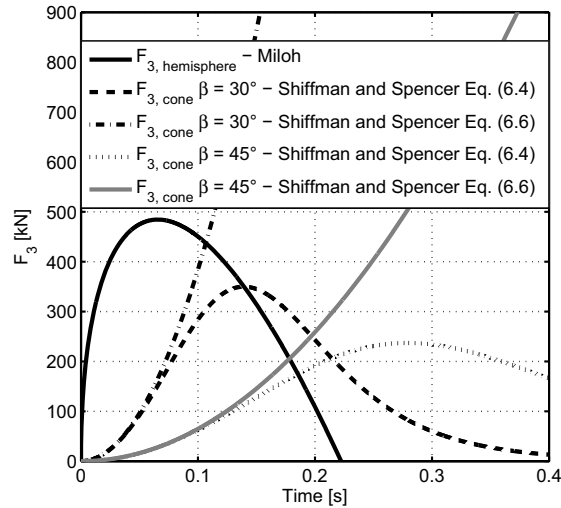
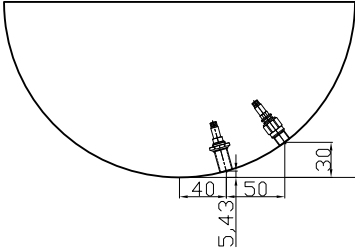
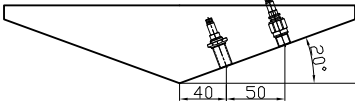
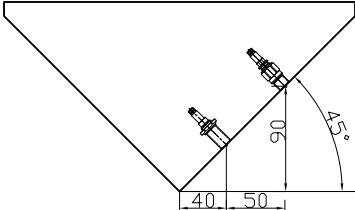


Figure 6.8: Force on a hemisphere and two cones ($\beta = 30^\circ$ and $\beta = 45^\circ$) with $R = 2.5$ m and a drop height of 2 m, i.e. $U = 6.3$ m/s; $m_{\text{hemisphere}} = 42.5$ ton, $m_{\text{cone}45^\circ} = 26.2$ ton, $m_{\text{cone}30^\circ} = 19.3$ ton.

reasons of similitude, the cone shape tests can be considered as full-scale tests, apart from the fact that the masses are not correctly scaled. In case of the hemisphere, the results from the smallest drop heights (0.05 m - 0.20 m) need to be upscaled to prototype values, according to the dimensions of a full-scale body. Expected scaling effects might arise from surface tension and viscous effects. For completeness, the tests with the hemisphere are also performed for larger drop heights. The majority of the drop tests have been performed by De Pré [27] in the framework of a master dissertation, supervised by the author of this PhD thesis.

The results of an improved test setup are presented. Initially the tests were carried out without any guiding structure. Although the test objects were balanced precisely, the scatter in the measured data appeared to be significant. In order to prevent small rotations of the floaters while falling down, the setup was equipped with a guiding system consisting of tightened steel wires [28]. The results discussed in this Chapter are obtained from a test setup with an improved guiding system. The tightened steel rods are replaced by a rail

Table 6.1: Test object characteristics.

Test objects (dimensions in mm)	Characteristics
	<p>Hemisphere Local deadrise angles: 7.7° and 18.4° Radius: 0.15 m Material thickness: 0.05 m Mass: 11.5 kg</p>
	<p>Cone Deadrise angle: 20° Max. radius: 0.15 m Material thickness: 0.03 m Mass: 9.8 kg</p>
	<p>Cone Deadrise angle: 45° Max. radius: 0.15 m Material thickness: 0.03 m Mass: 10.2 kg</p>

mounted on stiff aluminium profiles. The test bodies are attached to a profile structure equipped with wheels, rolling down the rail as shown in Figure 6.9. With this test setup the verticality of the impacting object is assured and the tests are very well reproducible.

The masses mentioned in Table 6.1 correspond to the total falling mass, i.e. the sum of the mass of the polyurethane bodies and the aluminium carriage. The drop height, h , is limited to 2 m, compared to 4 m for the original test setup. A 10 mm plexiglass sheet is installed in the side of the basin which allows to film the impact phenomena. A picture of the test setup is given in Figure 6.10.

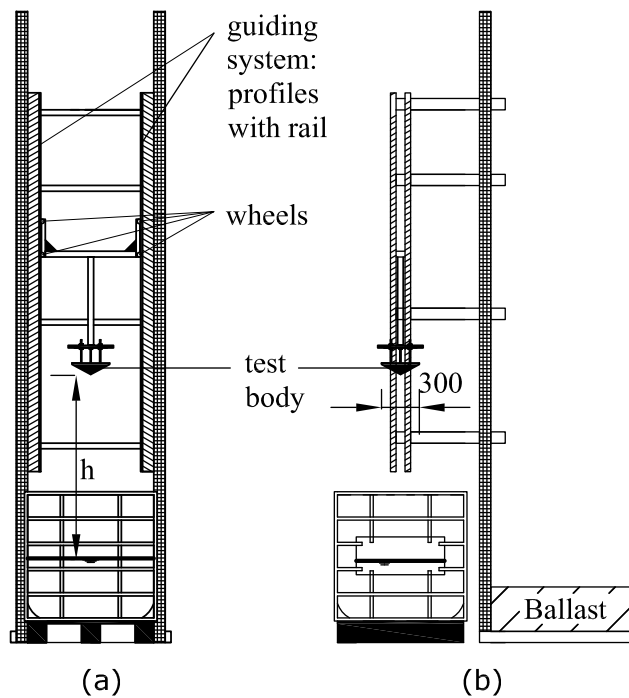


Figure 6.9: Schematic view of the experimental test setup [mm].



Figure 6.10: Picture of the experimental test setup.

6.3.2 Instrumentation

Pressure sensors and shock accelerometer

The pressure time history, the position and deceleration of the body were recorded during impact. Three high frequency piezoelectric pressure sensors were used. One ICP pressure sensor (A07) has a built-in microelectronic amplifier while two other high frequency pressure sensors (K30, K31) have external amplifiers. The measurement range for these devices is 3.45 bar and 2 bar, respectively. The pressure cells have a small diaphragm of 5.5 mm and a very high resonance frequency, see Table 6.2. Consequently the sensors are very well suited for measuring impact phenomena. The sensors are flush-mounted at a horizontal distance of 0.04 m and 0.09 m, respectively from the symmetry axis, as illustrated in Table 6.1. The deceleration of the object during impact was measured by a shock accelerometer with a measurement range up

Table 6.2: Sensor characteristics.

Sensor	Measurement range	Resonance frequency
A07	3.45 bar	≥ 250 kHz
K30, K31	2 bar	≥ 150 kHz
Shock accelerometer	500 g	≥ 54 kHz

to 500 g and a resonance frequency of 54 kHz.

Figure 6.11 shows the configuration of the pressure cells. The first three configurations (a-c) represent the sensor positions for the hemisphere. The sensors in Figure 6.11(a) are mounted on two opposite meridians in order to evaluate the verticality of the penetration. With the configuration in Figure 6.11(b) a comparison between the two local deadrise angles can be made and in Figure 6.11(c) the sampling frequency is increased up to 100 kHz for one pressure sensor and the shock accelerometer. In Figure 6.11(d) and (e) the configuration of the pressure sensors is given for the 20° cone. In each configuration two different pressure sensors are mounted on meridians close to each other, allowing for the assessment of the different sensors. Figure 6.11(f) shows the pressure sensor configuration in case of the 45° cone, which is similar to Figure 6.11(a) combined with (b). Each case has been tested at least three times for every drop height, varying between 0.05 m and 2 m.

A sampling frequency (SF) of at least 30 kHz was used for recording. Such high sampling frequencies are required, since the pressure peaks occur in a very small time interval (order of magnitude milliseconds). For the same reason the resonance frequency of the sensors should be high enough. A small pressure cell diaphragm area is necessary since the pressure peaks are also very much localized in space as well, as can be seen in Figure 6.12, showing the theoretically predicted pressure distribution according to asymptotic theory at $t = 0.002$ s for a cone with deadrise angle 20° and drop height 2 m.

In earlier investigations, sensors with larger diameters have sometimes been used, with values up to 19 mm in [10]. In that case the pressure peaks might have a smaller spatial extent than the sensor area. Even pressure cells with diameter 5.5 mm might measure a space-averaged pressure, which is slightly different from the peak pressure. The pressure distribution is particularly more peaked when the (local) deadrise angle is small and the impact velocity high. Assuming that a pressure cell registers the space-

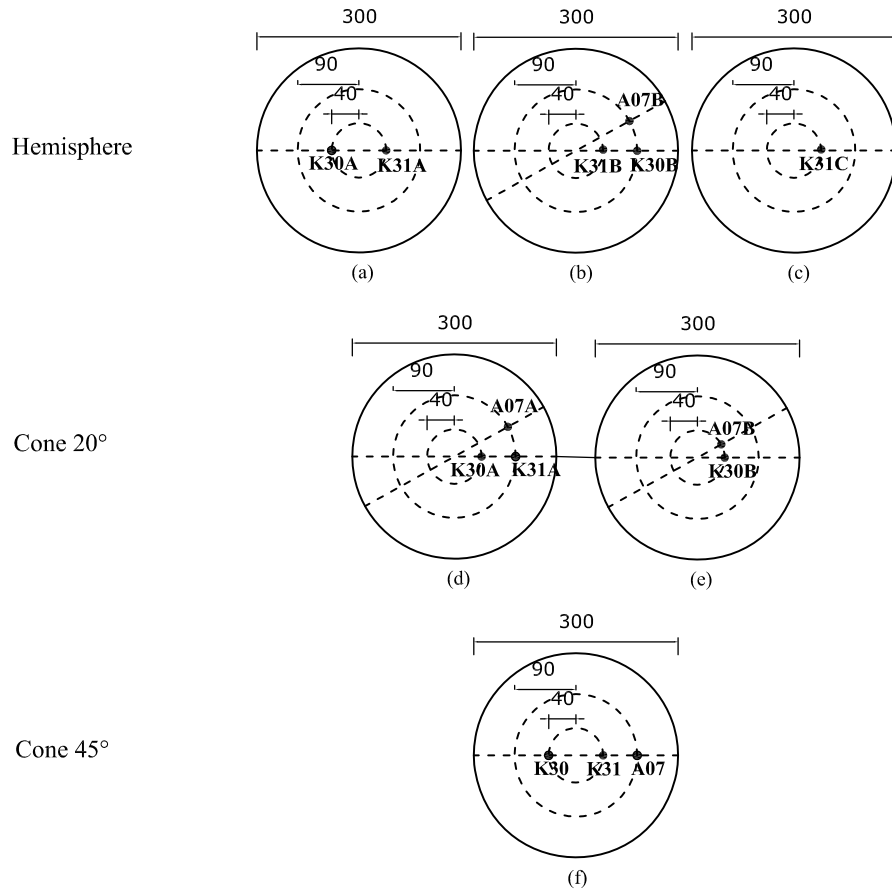


Figure 6.11: Pressure sensor positions [mm] for the hemisphere: (a) Sensors K30A and K31A - SF = 30 kHz, (b) Sensors K30B, K31B and A07B - SF= 30kHz, (c) Sensor K31C - SF = 100 kHz, for the 20° cone : (d) Sensors K30A, K31A and A07A - SF=30 kHz, (e) Sensors K30B and A07B - SF=30kHz, for the 45° cone: (f) Sensors K30, K31 and A07 - SF = 30 kHz.

averaged pressure when subject to a non-uniform pressure distribution, the deviation between the peak pressure and the sensor record can be determined. In [20], Faltinsen estimated that the theoretical peak pressure is at maximum 11 % higher than the space-averaged pressure, measured by a sensor with a diameter of 4 mm. Deviations of the same magnitude can be derived, based on the theoretically predicted pressure distribution by the 3D asymptotic theory. For pressure cells with diameter 5.5 mm it is estimated with the latter method

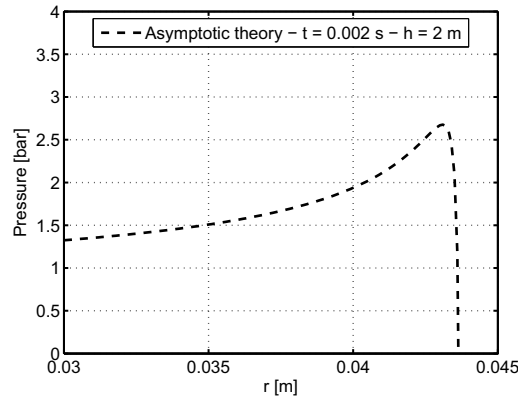


Figure 6.12: Theoretical pressure distribution as a function of r for a cone with deadrise angle 20° and drop height 2 m.

Table 6.3: Influence of pressure sensor diameter: estimated deviations from peak pressure for drop heights of 1 m and 4 m.

Sensor diameter	$h = 1 \text{ m}$	$h = 4 \text{ m}$
5.5 mm	10.8%	13.9%
19 mm	30.5%	34.2%

that the measured pressure on a cone with deadrise angle 20° deviates between 10 % and 14 % from the peak pressure for drop heights of 1 m and 4 m. In a similar way as above, it is expected that a pressure sensor with a diameter of 19 mm, would underestimate the peak pressure with more than 30 % for the same case of a cone with deadrise angle 20° , as shown in Table 6.3.

High speed camera

A high speed camera was used to record the penetration of the impacting bodies as a function of time. The camera provided information on the water uprise along the body and on the position and velocity of the impacting body. For this purpose a marker tracking technique has been applied. The high speed camera is able to deliver images up to 250 000 frames per second (fps) and has full mega pixel resolution at 3000 fps. In this test case, it has been used at 5000 up to 18000 fps, dependent on the desired pixel resolution. Because

of the high frame rate, the camera shutter time is extremely short. In order to overcome low illumination and to avoid interference with the grid frequency, special flicker free lights have been used. Two lasers are mounted on top of the basin and serve as a trigger for the data acquisition system. When the dropped objects intersect the laser beams, the recording of the pressure sensors, accelerometer and camera signal starts automatically.

6.4 Experimental test results

6.4.1 Water uprise and impact velocity

Figure 6.13 shows a selected number of images of a hemisphere penetrating the free water surface, dropped from 1 m. A software program recognizes the pattern of the marker and determines its coordinates at each time step. Consequently the position of the body is known as a function of time and the velocity can be determined. The pictures clearly show the water uprise along the hemisphere. The jet flow is quickly detached from the body surface ending up in a spray. This phenomenon has also been observed for cylinders by Greenhow and Lin in [29] and [30]. Figures 6.14 and 6.15 show camera images of the impacting cones for a drop height of 1 m. The creation and propagation of a jet along the cone surface can be clearly seen and measured.

From the photographs of the cones the ratio C_w can be determined and compared with theoretical values. The C_w factor is defined as the ratio between the heights of the immediate and undisturbed free water surfaces measured from the bottom point of the falling object:

$$C_w = 1 + \frac{\zeta(b, t)}{Ut} \quad (6.10)$$

with ζ the z-coordinate of the intersection point between the object and the free water surface, see Figure 6.2. When flow separation occurs above ζ , as in the case of the hemisphere, C_w has the physical meaning of a wetting factor. However, in the case of a cone a thin jet flow might occur above this intersection point as observed in Figures 6.14 and 6.15. The wetting factor C_w for a cone with attached jet flow can then be defined as:

$$C_w = 1 + \frac{\zeta(b, t) + l_{jet}}{Ut} = \frac{b}{b_0} + \frac{l_{jet}}{Ut} \quad (6.11)$$

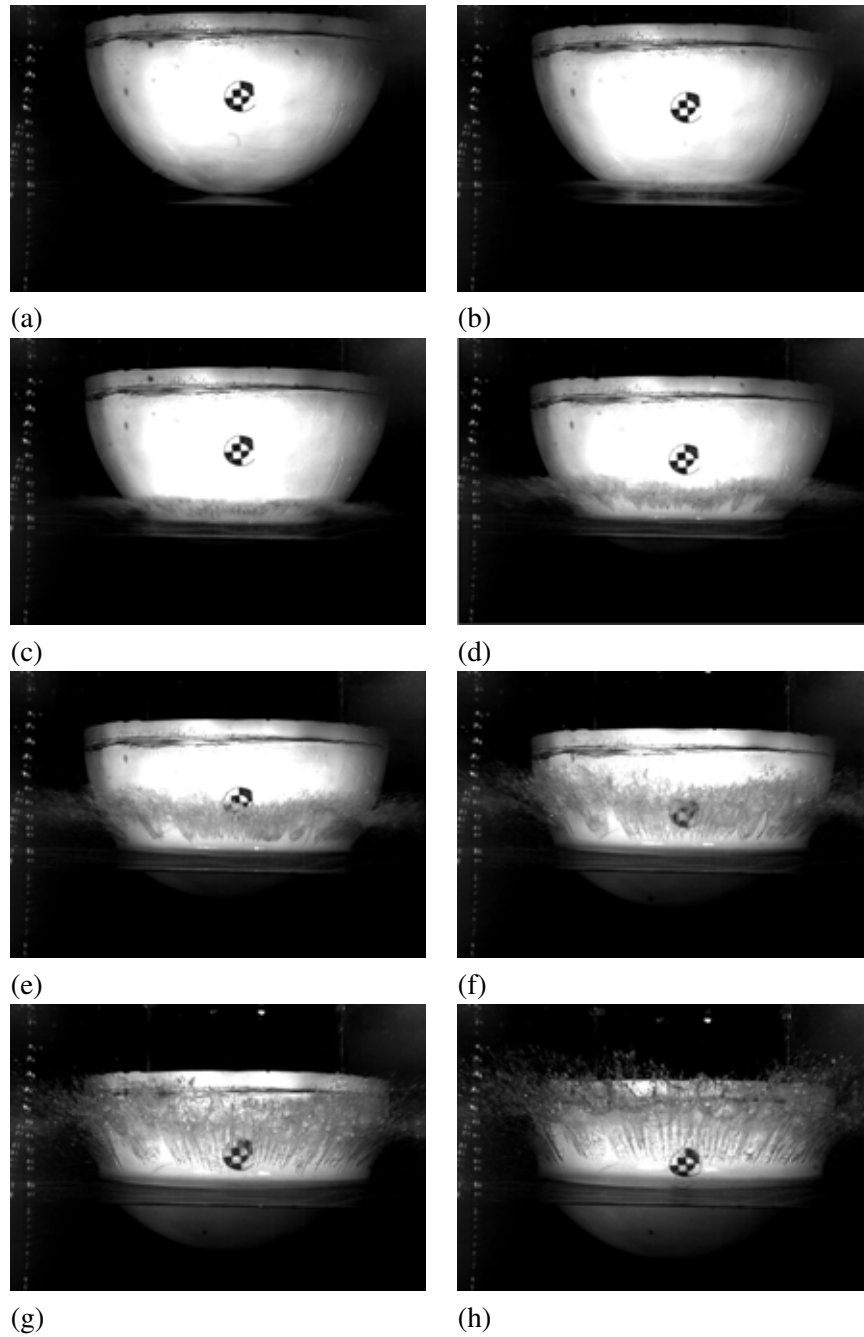


Figure 6.13: Hemisphere penetrating the water - (a) $t = 0.0000$ s, (b) $t = 0.0022$ s, (c) $t = 0.0044$ s, (d) $t = 0.0066$ s, (e) $t = 0.0088$ s, (f) $t = 0.0110$ s, (g) $t = 0.0132$ s.

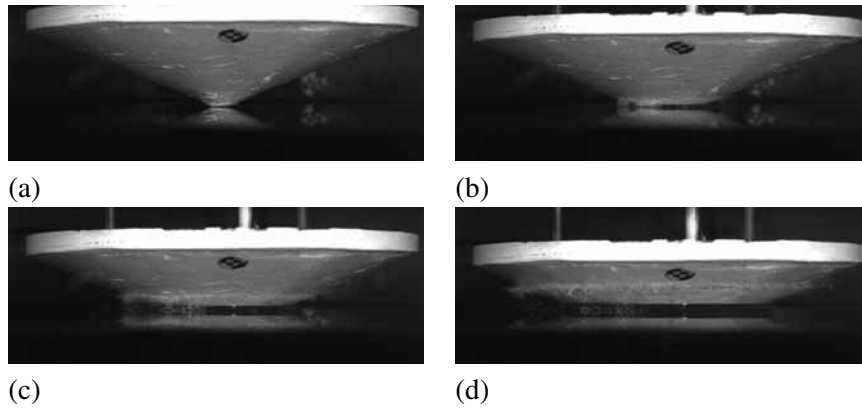


Figure 6.14: Cone ($\beta=20^\circ$) penetrating the water - (a) $t = 0.0000$ s, (b) $t = 0.0044$ s, (c) $t = 0.0088$ s, (d) $t = 0.0132$ s.

where l_{jet} is the height of the jet. Considering the outer flow domain, Faltinsen et al. [14] found a ratio b/b_0 equal to $4/\pi$ for cones based on Wagner's blunt body approach. By matching the outer 3D solution for axisymmetric flow with the inner 2D jet flow solution by Wagner, Faltinsen described the jet flow during water entry of a cone. Based on Faltinsen's considerations, the height of the jet is found to be $\frac{4Ut}{\pi}\cos\beta$, resulting in a wetting factor C_w equal to $\frac{4}{\pi}(1 + \cos\beta)$ for a cone with attached jet flow. The formula by Faltinsen et al. [14] is slightly different¹ from the latter, probably due to a typing error in [14]. In numerical models that satisfy the real body boundary conditions, the description of the jet flow can be very complex. Zhao and Faltinsen [6] developed a numerical model that significantly simplifies the description of the jet flow. This approach has been adopted by Battistin and Iafrati [19] who determined the water surface elevation numerically for axisymmetric bodies, among them a cone with deadrise angle 30° . However, the jets are truncated at the top, which makes it impossible to derive the correct wetting factor. Figures 6.16 and 6.17 illustrate the wetting factor versus the penetration depth for three different drop heights for the 45° cone and the 20° cone, respectively. The value of C_w is relatively constant during penetration, although in both cases slightly higher values are measured for small penetration depths. Furthermore the influence of the drop height appears

¹ $C_{w,Faltinsen} = \frac{4}{\pi}(1 + 1/\cos\beta)$

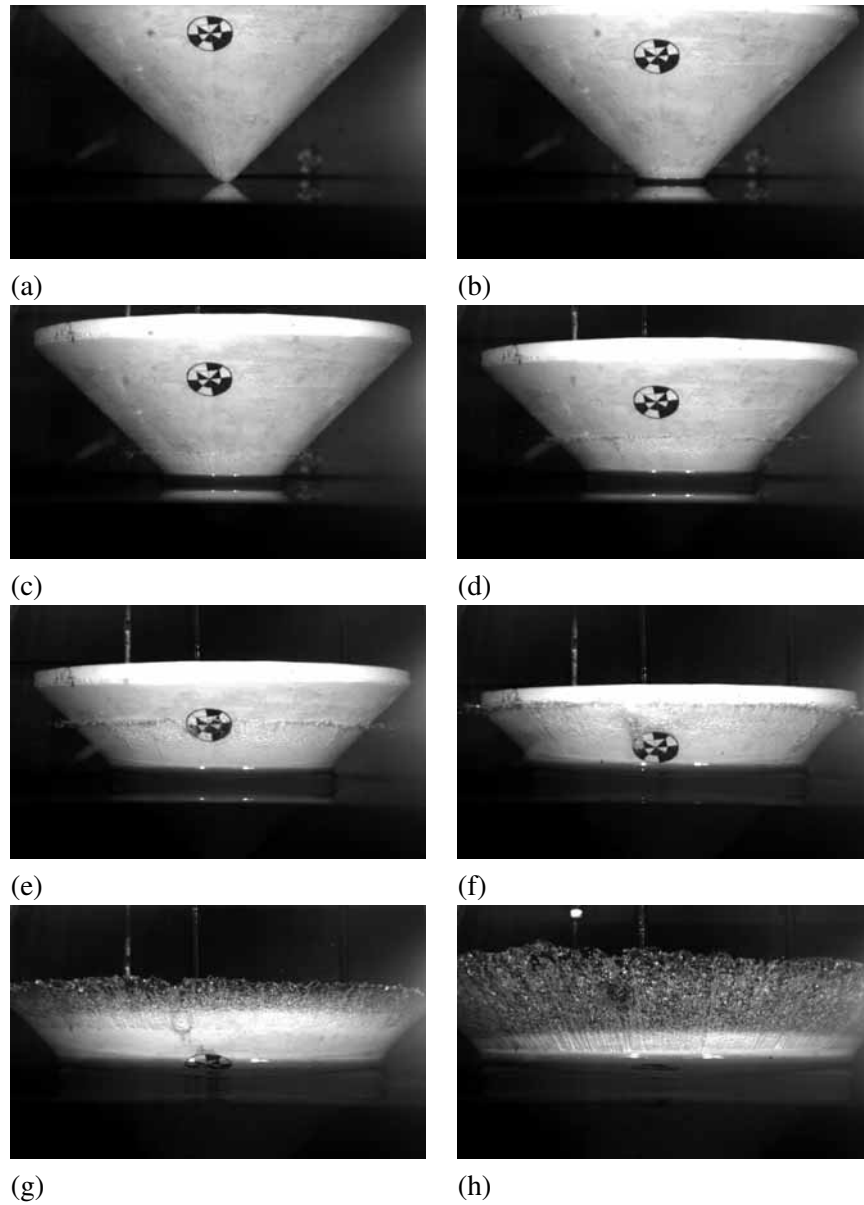


Figure 6.15: Cone ($\beta=45^\circ$) penetrating the water - (a) $t = 0.000$ s, (b) $t = 0.004$ s, (c) $t = 0.008$ s, (d) $t = 0.012$ s, (e) $t = 0.016$ s, (f) $t = 0.020$ s, (g) $t = 0.024$ s, (h) $t = 0.028$ s.

to be not very significant and a smaller wetting factor is found for the highest deadrise angle. On average the measured values are 19 % and 23 % smaller than the values found by Faltinsen et al. for the 45° and 20° cone, respectively. The wetting factor of the hemisphere cannot be derived from the camera images, since it is difficult to determine the intersection point between the free water surface and the body, due to the disturbing effect of the 3D spray. In order to better visualize the flow separation at the hemisphere, it would be necessary to create a light sheet through the symmetry axis of the hemisphere with a strong laser. In that case the water spray particles in front of the hemisphere are not illuminated and do not disturb the measurement.

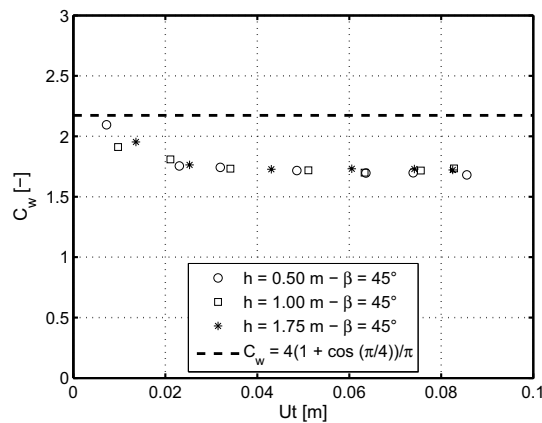


Figure 6.16: Wetting factor as a function of penetration depth on the 45° cone.

Figure 6.18 illustrates the velocity during the initial impact stage determined by the high speed camera as a function of the entry depth. For each shape three initial velocities, U_0 , are considered: $U_0 < 3$ m/s, $U_0 \approx 4$ m/s and $U_0 > 4.6$ m/s. Although the mass of the hemisphere is the largest of the three tested objects, the velocity decrease during the initial stage of the impact is most pronounced for this shape. This is especially the case for higher drop heights, corresponding to larger values of U_0 and consequently higher impact forces.

For the 45° cone the slamming force is so small that the impact velocity remains quite constant. Note that the velocity increases for both cone shapes in particular for small values of U_0 . Immediately after contacting the water

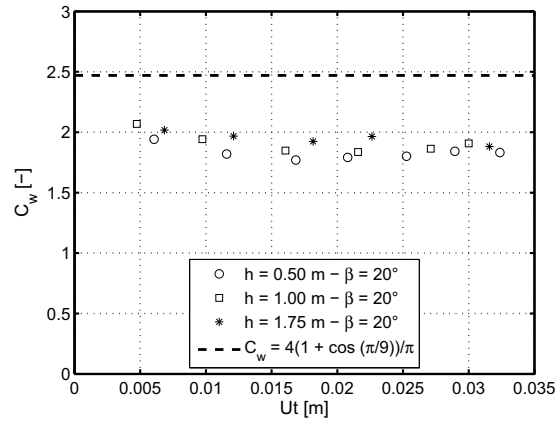


Figure 6.17: Wetting factor as a function of penetration depth on the 20° cone.

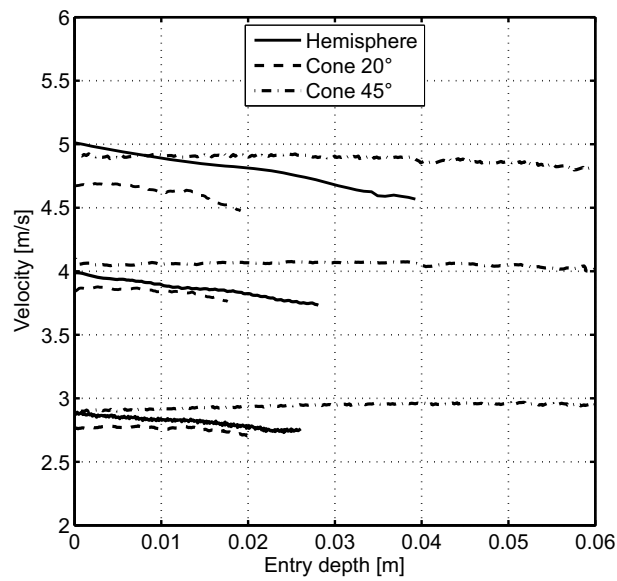


Figure 6.18: Velocity measured by the high speed camera for three different initial impact velocities for each shape.

surface, the impact forces on the cones are still rather small compared to the gravity force. For this reason the impact velocity first builds up for a very short period of time before starting to decrease. The graph illustrates that the assumption of a constant entry velocity can be better justified for smaller initial velocities U_0 . The recorded velocity time history is short for the 20° cone, because the marker pattern becomes quickly unclear due to the water uprise. Longer velocity time histories are obtained with the accelerometer, as will be illustrated in Section 6.4.2.

6.4.2 Pressure distribution, impact velocity and deceleration

Hemisphere

Figures 6.19 and 6.20 show the pressure coefficient $C_p = p/(0.5\rho U_0^2)$ on the hemisphere as a function of time for a drop height of 1 m at $r = 0.04$ m and $r = 0.09$ m, respectively. The initial time is defined as the moment where the bottom of the hemisphere touches the water surface. The pressure measurements are compared with the asymptotic solutions, assuming a constant entry velocity. The figure indicates that the asymptotic theory overestimates the pressures significantly, particularly for small local deadrise angles. This was also observed in the experiments of Lin and Shieh [9] for a cylinder.

The pressure profiles indicate that smaller local deadrise angles lead to higher pressures which have a shorter duration in time. The rising time of the first pressure peak (Figure 6.19) is only 0.2 ms. Due to the decrease in velocity, the time interval between the measured pressure peaks is larger than between the theoretically predicted peaks. Furthermore it can be noted that the pressure distribution of the four sensors at $r = 0.04$ m obtained from the three different test configurations in Figure 6.11 (a-c) coincide very well. This implies firstly that the hemisphere penetrated perfectly along a vertical line and secondly that a sampling frequency of 30 kHz is sufficiently large since no higher peak has been registered at 100 kHz.

Figures 6.21, 6.22 and 6.23 show the measured and theoretical acceleration, velocity and entry depth, respectively. The theoretical values are based on the pressure integration method (PI) and added mass method (AM) as explained in Section 6.2.2. The presented velocity and position data from the high speed camera are measured at 18000 fps for the three shapes. The

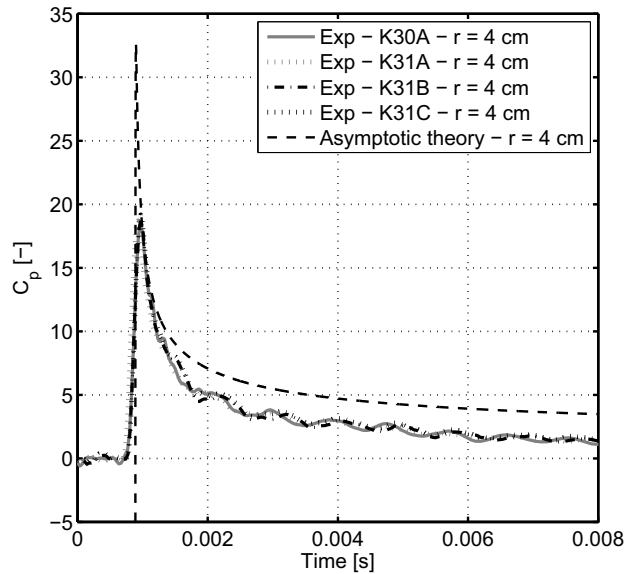


Figure 6.19: Measured and calculated pressure distribution on the hemisphere at $r = 0.04$ m for $U_0 = 4.0$ m/s.

acceleration signal in Figure 6.21 is disturbed by a high frequency noise, probably originating from oscillations of the horizontal aluminium beam since the noise was not registered in the original setup. Nevertheless the accelerometer signal is still valuable, as can be seen in Figure 6.22. The velocity, based on numerical integration of the accelerometer signal coincides very well with the velocity derived from the high speed camera images. The theoretical velocities drop more quickly, which is due to the fact that the forces and consequently the accelerations are overestimated by both methods. The measured initial velocity is 4.0 m/s, whereas the calculated speed $U_0 = \sqrt{2gh}$ would be 4.4 m/s. This difference can be attributed mainly to friction in the guiding system. For this reason all theoretical values are calculated based on the measured initial speed. Note the very short time span of 12 ms in the plots. In this time span the hemisphere has reached a submergence of about $R/3$ (see Figure 6.23) and the relevant impact phenomena have occurred.

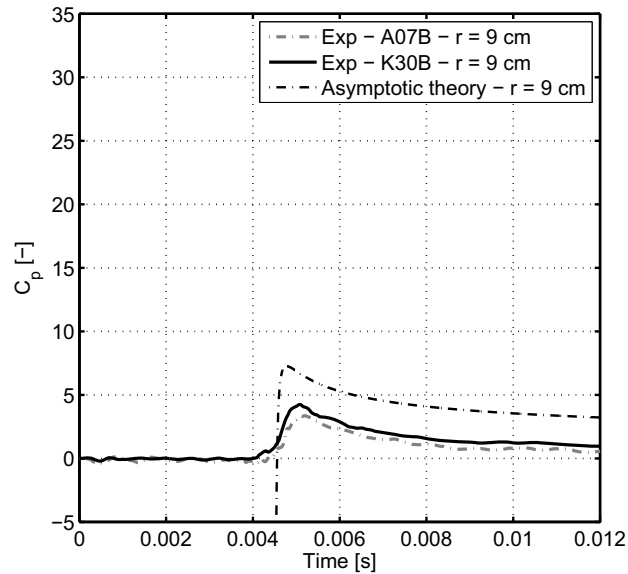


Figure 6.20: Measured and calculated pressure distribution on the hemisphere at $r = 0.09$ m for $U_0 = 4.0$ m/s.

Cone 20°

Figure 6.24 shows the measured and calculated pressure distribution on the 20° cone for a measured impact velocity $U_0 = 3.85$ m/s. It can be noticed that the pressures measured with the different sensor types correspond very well in both sensor positions $r = 0.04$ m and $r = 0.09$ m. According to the asymptotic theory, the peak pressure level does not change along the object. In the experiments the second pressure peak is slightly larger than the first one. On average over all the tests, the difference in peak pressure between the two positions is 3.8 %. This phenomenon was also observed by Peseux et al. [21] with even more pronounced differences for cones with smaller deadrise angles (14° - 10° - 6°). The reason for this trend is not entirely clear. It could possibly be attributed to mounting problems due to the small radius of curvature at $r = 0.04$ m compared to $r = 0.09$ m. The sensors, having a flat membrane area, disturb the geometry of the cone more at a smaller radius of curvature and this might slightly influence the pressure measurement.

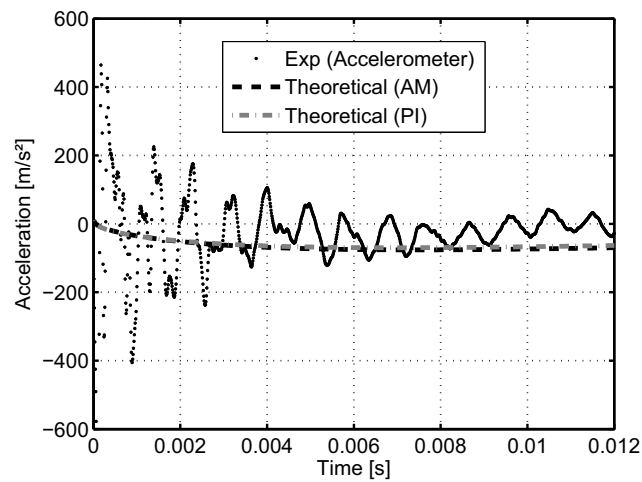


Figure 6.21: Measured and calculated acceleration on the hemisphere.

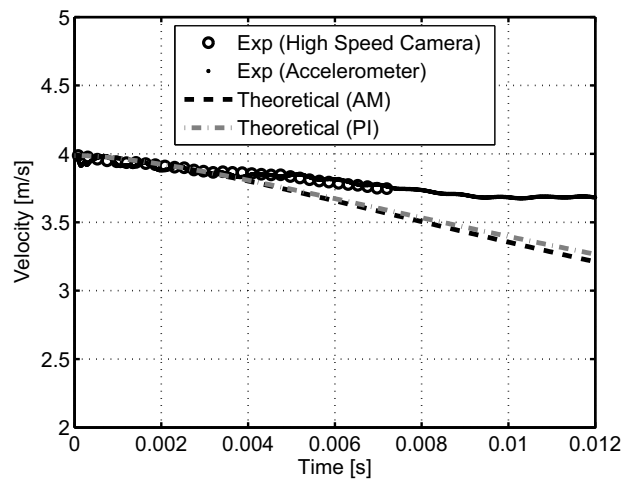


Figure 6.22: Measured and calculated velocity on the hemisphere.

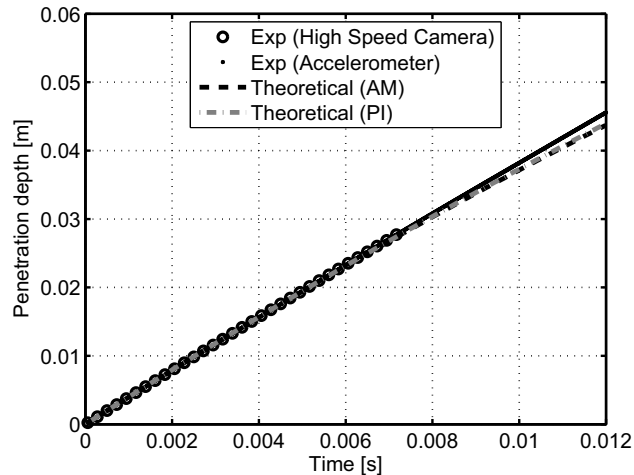


Figure 6.23: Measured and calculated position on the hemisphere.

In Figure 6.25 a quite high deceleration peak of about -100 m/s^2 can be noticed, which results in a non-negligible velocity decrease (Figure 6.26). As in the case of the hemisphere, the theory is rather conservative, especially the added mass method. The height of the tested cone shape is 0.055 m, which means it is almost completely submerged after 12 ms (Figure 6.27).

Cone 45°

Figures 6.28-6.31 show the pressure distribution, acceleration, velocity and entry depth for the 45° cone with an impact velocity of 4.05 m/s. Although the classical Wagner principle assumes small deadrise angles, a quite good correspondence is found between theory and experiments for the first sensor position. However, the peak at the second sensor position seems to be significantly smaller than the first peak, whereas the theory predicts the same values because of the similarity of the problem. The discrepancy between the two sensor positions has been observed for all impact velocities and is on average 35 %. This pressure drop cannot be explained by a smaller instantaneous velocity, since the velocity during the second peak is about the same value as during the first peak. However, the accelerometer measures a small acceleration (during the first 10 ms) followed by a deceleration. The

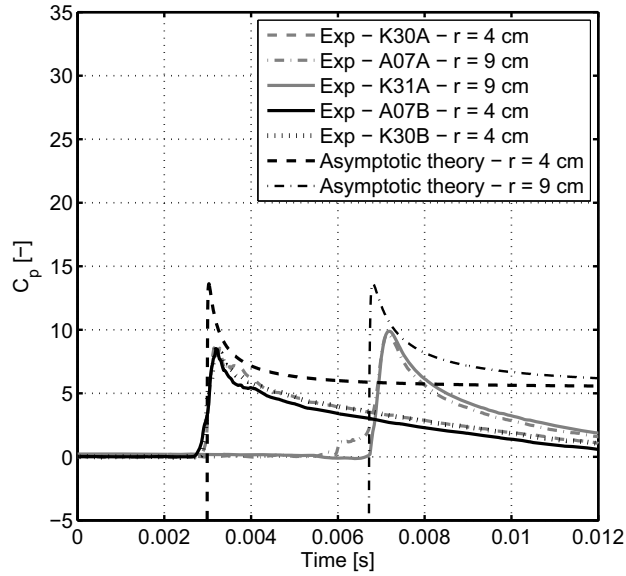


Figure 6.24: Measured and calculated pressure distribution on cone ($\beta = 20^\circ$) for $V_0 = 3.85$ m/s.

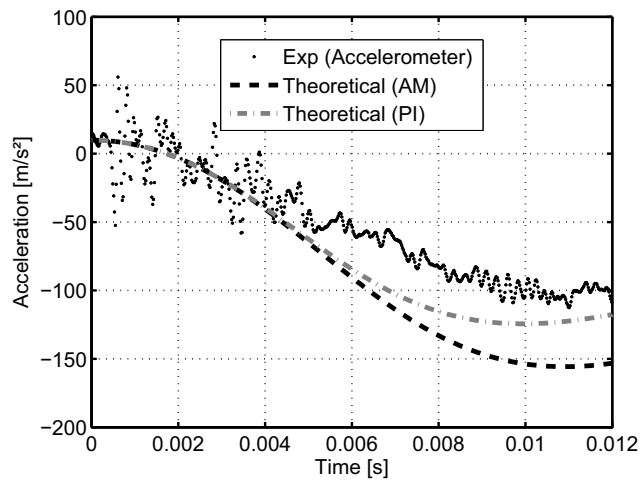


Figure 6.25: Measured and calculated acceleration on cone ($\beta = 20^\circ$).

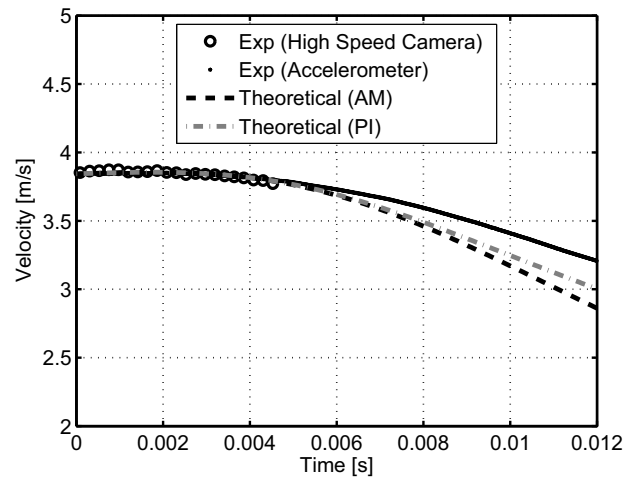


Figure 6.26: Measured and calculated velocity on cone ($\beta = 20^\circ$).

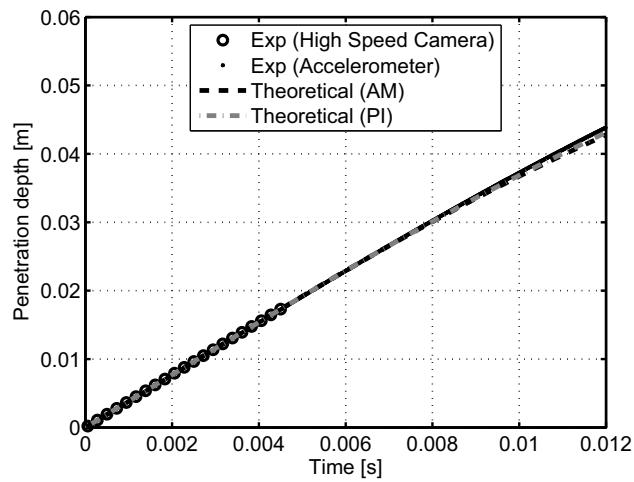


Figure 6.27: Measured and calculated position on cone ($\beta = 20^\circ$).

influence of this acceleration and deceleration on the pressure is not taken into account by the asymptotic theory. Assuming a uniform pressure distribution originating from the part of the impact force proportional to the acceleration ($M_{a33} \frac{d^2z}{dt^2}$), it is estimated that this contribution to the pressure is between 5% and 15% of the measured pressure, which is rather small and does not explain the pressure drop. A small time shift of 0.5 ms is observed between the pressure signals of sensor K30 and K31. As this corresponds to a vertical distance of 2.0 mm, which is a fraction of the sensor diameter of 5.5 mm, this shift might be caused by imperfections in the sensor mounting.

The deceleration, velocity and penetration are well predicted by the analytical approaches for small entry depths, since the pressures correspond well with the experiments in this case. The deceleration peak is -25 m/s^2 , which is only one quarter of the peak measured for the cone 20° .

For this range of impact velocities the theoretical assumption of a constant impact velocity is acceptable for the 45° cone and the hemisphere. The 20° cone experiences the largest velocity drop, which is still smaller than 20 % after almost complete submergence.

6.4.3 Comparison between shapes

Figures 6.32-6.33 show the slamming pressure coefficient as a function of the dimensionless entry depth $U_0 t/R$ at $r/R = 0.267$, respectively $r/R = 0.300$. Although the analytical solution is quite conservative in predicting the peak levels, the global pressure distribution fits the experiments quite well. In the bottom area, the hemisphere is subject to much higher slamming coefficients than the cones. For very small r -values, the local deadrise angle of the hemisphere tends to zero and very high impact pressures may occur. Structural designers should pay special attention to this zone. For larger values of r/R the slamming coefficient on the hemisphere drops rapidly, which is not the case for the cones. Note in Figure 6.33 that the peak value of the hemisphere is smaller than for the 20° cone, whereas the local deadrise angle of the former is only 18.4° .

6.4.4 Peak pressure

Structural designers are often interested in maximum pressures. Figures 6.34-6.37 give the maximum pressures as a function of the equivalent drop height,

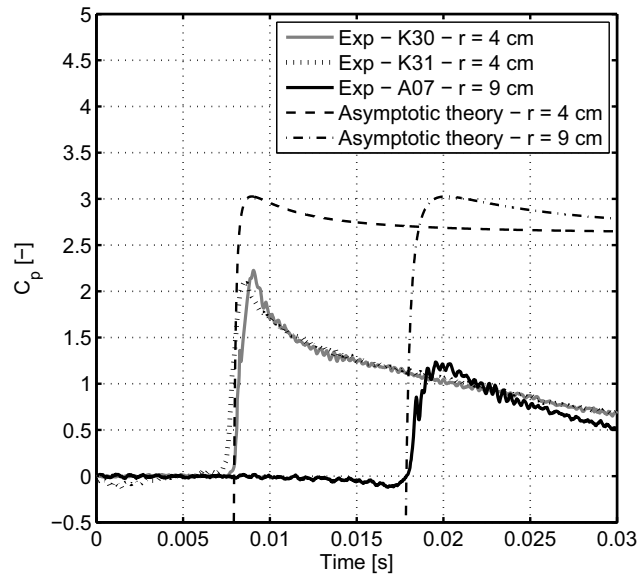


Figure 6.28: Measured and calculated pressure distribution on cone ($\beta = 45^\circ$) for $V_0 = 4.05$ m/s.

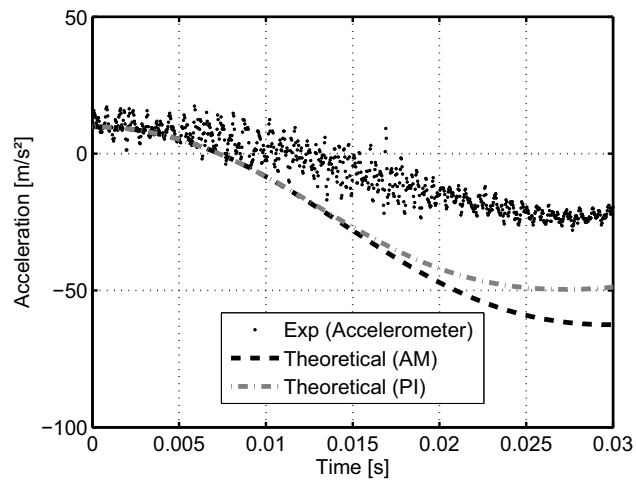


Figure 6.29: Measured and calculated acceleration on cone ($\beta = 45^\circ$).

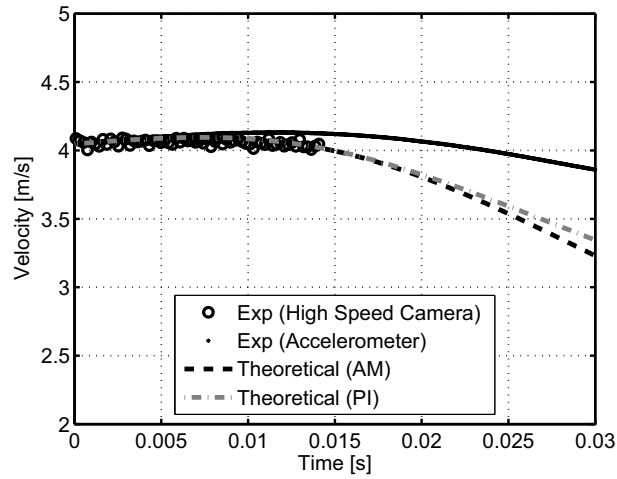


Figure 6.30: Measured and calculated velocity on cone ($\beta = 45^\circ$).

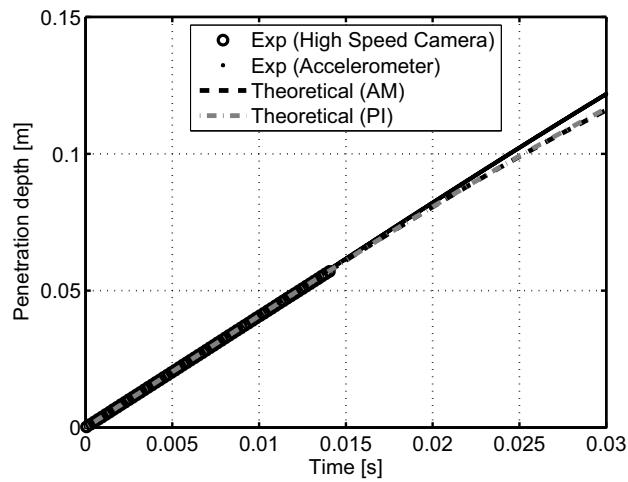


Figure 6.31: Measured and calculated position on cone ($\beta = 45^\circ$).

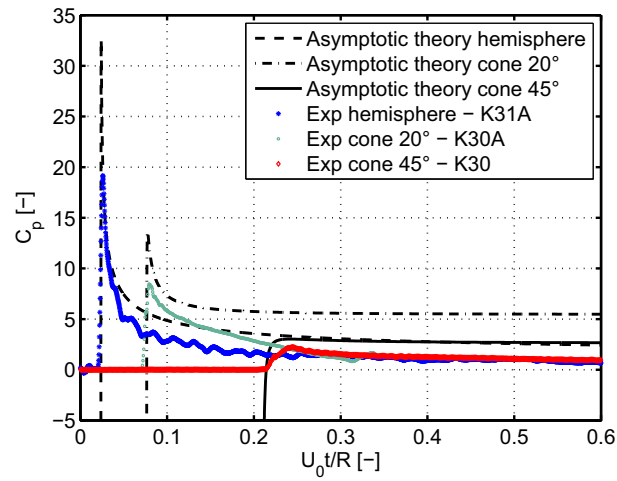


Figure 6.32: Slamming pressure coefficient at $r/R = 0.267$.

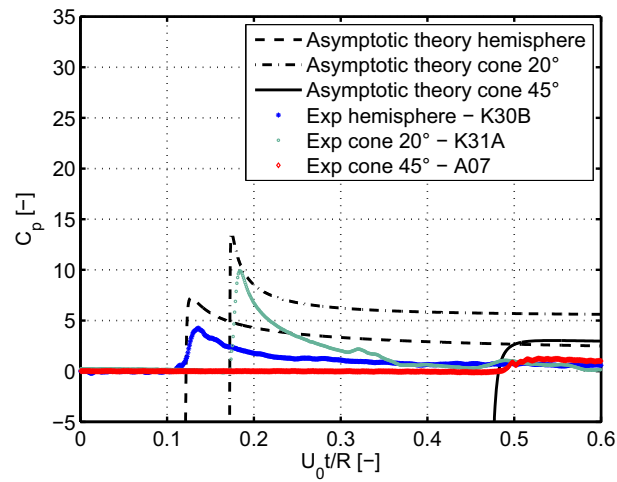


Figure 6.33: Slamming pressure coefficient at $r/R = 0.300$.

h^* , which corresponds to the drop height calculated from the measured impact velocity. The use of this equivalent drop height makes it possible to compare the measurement results with other research results. Since the maximum pressure is proportional to the drop height, a linear least squares fitting (LSF) has been adopted. The value of the squared Pearson correlation coefficient, R_*^2 , is always very close to one, indicating a high linear correlation between the different data points of each test series. The average deviation between the measured and analytical peak pressure levels can be easily assessed from the graphs. For the hemisphere, the measured peak values are respectively 58 % and 55 % of the Wagner peak values, for the first and second sensor position. For the 20° cone the ratios are 66 % and 68 % respectively and for the 45° cone 73 % and 48 %. The ratio between Chuang's experiments [24] and asymptotic theory is 27 % and 86 % for a cone with deadrise angle 3° and 15°, respectively. In [21] a numerical solution of the Wagner 3D problem is suggested and evaluated by experiments on cone shapes with deadrise angles 6°, 10° and 14°. The ratios between the experiments and numerical solution are on average 53 %, 67 % and 76 %, respectively and consequently comparable to the ratios found in this study. Nisewanger [23] found pressure peaks on hemispheres that are closer to the asymptotic theory levels using pressure transducers with a diaphragm of 6.4 mm. Generally the blunt body approach is found to be conservative. This is considered as the main reason for the discrepancies between experiments and theory. Minor differences are attributed to the cell membrane diameter, which should be as small as possible. The assumption of a constant entry velocity might also have a small influence, depending on the shape and mass of the body. Furthermore the theory assumes rigid bodies, a condition which is seldom fulfilled in practice. Deformable bodies might experience significantly smaller pressure as demonstrated in [21].

In order to evaluate the reproducibility of the tests, the hemisphere and the 20° cone were each dropped ten times from a drop height of 1 m. The sensor positions correspond to the configurations in Figure 6.11(b) and (d) for the hemisphere and cone, respectively. Table 6.4 shows the coefficient of variation C_v -the ratio of the standard deviation to the mean- of the measured peak pressures. For sensor A07 and K31 the relative spreading of the peak levels to the mean is extremely small. This indicates that these sensors measure very accurately and the tests are well reproducible. The larger spreading found for sensor K30 should be attributed to inaccuracies of the sensor itself.

Table 6.4: Coefficient of variation for the hemisphere and cone 20°, drop height = 1 m.

Coefficient of variation	A07	K30	K31
Hemisphere	0.66%	8.48%	0.44%
Cone 20	0.93%	12.22%	1.25%

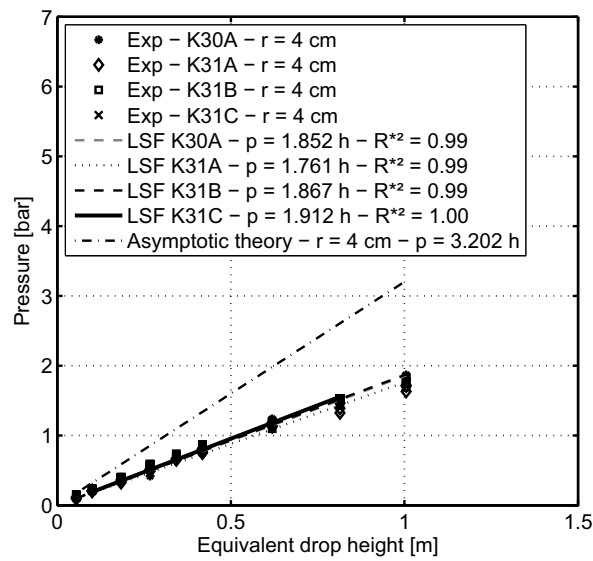


Figure 6.34: Peak pressure versus drop height on the hemisphere at $r = 0.04$ m.

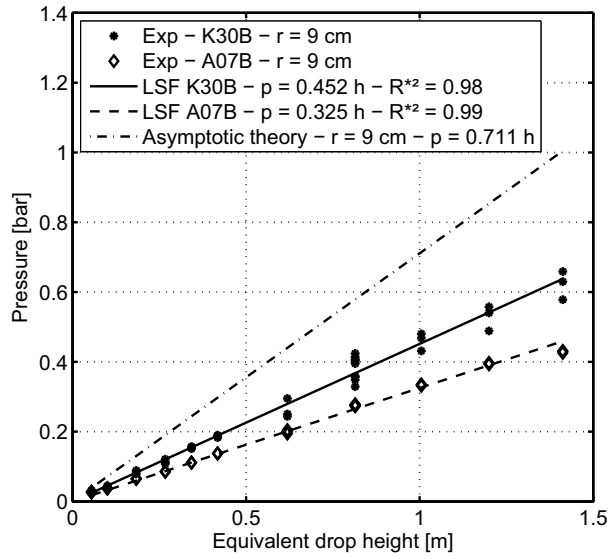


Figure 6.35: Peak pressure versus drop height on the hemisphere at $r = 0.09$ m.

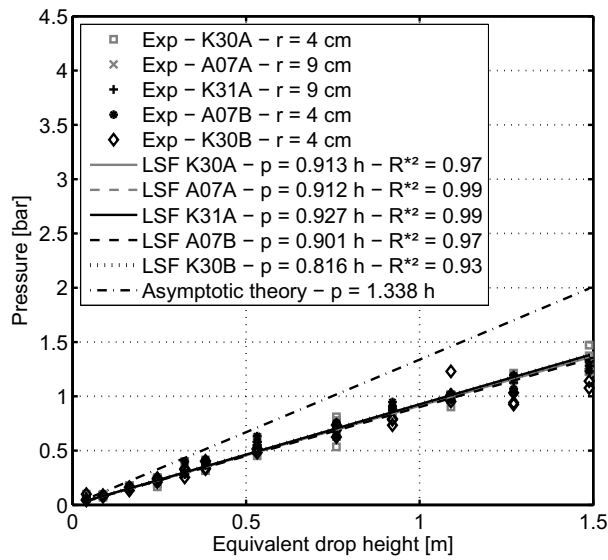


Figure 6.36: Peak pressure versus drop height on cone ($\beta = 20^\circ$).

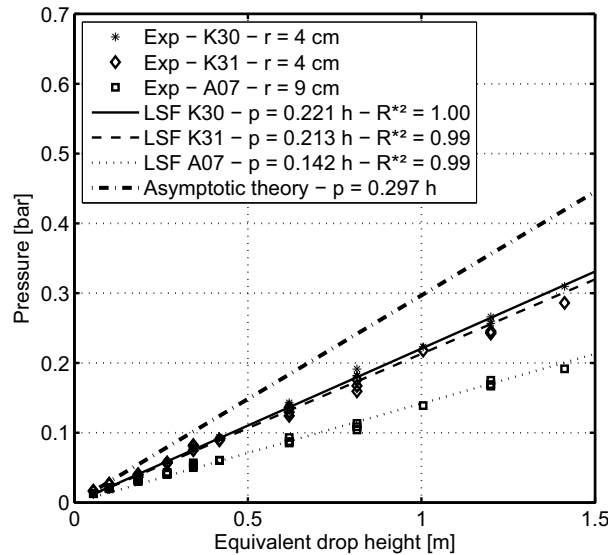


Figure 6.37: Peak pressure versus drop height on cone ($\beta = 45^\circ$).

6.5 Conclusion

Slamming phenomena on axisymmetric bodies have been experimentally studied by means of drop tests. A hemisphere and two cone shapes with deadrise angle 20° and 45° are dropped onto initially calm water. The water surface elevation is visualized with a high speed camera. Along the hemisphere the water uprise quickly ends in a spray, whereas a jet is attached to the body of the cone shapes. The wetting factor is determined for the cones and is about one fifth smaller than the value predicted by matching the outer 3D flow with Wagner's 2D jet flow model as described by Faltinsen in [14]. The pressure time history, impact velocity and deceleration are measured during impact. The velocity decrease during impact is found to be rather small, particularly for the 45° cone. In fact, for small entry velocities the 45° cone first experiences a very small velocity increase after making contact with the water surface. The measurements are compared with asymptotic theory for rigid axisymmetric bodies with constant entry velocity. Axisymmetric theory gives a good first idea of the slamming pressure distributions, however, it is

found to be quite conservative. The ratio between measured and theoretical peak levels is roughly between $1/2$ and $3/4$, which is in accordance with the findings of Peseux et al. [21] on cone shapes with smaller deadrise angles. To achieve better theoretical predictions, more advanced models should be applied in which e.g. the real body boundary conditions are satisfied, the variation of impact velocity is accounted for and possibly also the deformation of the body. At the Department of Flow, Heat and Combustion Mechanics of Ghent University, water impact problems of point absorbers have recently been studied with the CFD package Fluent [31], resulting in two master dissertations [32, 33].

The experience gained with the small scale laboratory tests has been used to perform free fall outdoor drop tests with composite point absorbers at large scale. The results of these tests are described in Chapter 7.

Bibliography

- [1] De Backer G., Vantorre M., Beels C., De Pré J., Victor S., De Rouck J., Blommaert C., Van Paepegem W., Experimental investigation of water impact on axisymmetric bodies. accepted for publication in Applied Ocean Research ;.
- [2] von Karman T., The impact of seaplane floats during landing. Technical Report 321, National Advisory Committee for Aeronautics, 1929.
- [3] Wagner H., Über Stoss- und Gleitvorgänge an der Oberfläche von Flüssigkeiten. Z Angew Math Mech 1932;12:193–215.
- [4] Malleron N., Scolan Y.M., Korobkin A., Some aspects of a generalized Wagner model. In: 22nd IWWF, Croatia, 2007, pp. 137–140.
- [5] Dobrovolskaya Z., On some problems of similarity flow of fluid with a free surface. Journal of Fluid Mechanics 1969;36(4):805–825.
- [6] Zhao R., Faltinsen O., Water entry of two-dimensional bodies. Journal of Fluid Mechanics 1993;246:593–612.
- [7] Zhao R., Faltinsen O., Aarsnes J., Water entry of arbitrary two-dimensional sections with and without flow separation. In: ONR, Norway, 1996, pp. 408–423.
- [8] Mei X., Liu Y., Yue D., On the water impact of general two-dimensional sections. Applied Ocean Reserach 1999;21(1):1–15.
- [9] Lin M.C., Shieh L.D., Flow visualization and pressure characteristics of a cylinder for water impact. Applied Ocean Reserach 1997;19(2):101–112.
- [10] Yettou E.M., A. A.D., Champoux Y., Experimental study on the water impact of a symmetrical wedge. Fluid Dynamics Research 2006; 38(1):47–66.

-
- [11] Shiffman M., Spencer D., The force of impact on a sphere striking a water surface. *Appl. Math. Panel Rep.* 42 IR AMG-NYU No. 105, 1945.
- [12] Shiffman M., Spencer D., The force of impact on a cone striking a water surface. *Comm Pure Appl Math* 1951;4:379–417.
- [13] Chuang S., Theoretical investigations on slamming of cone-shaped bodies. *Journal of Ship Research* 1969;13:276–283.
- [14] Faltinsen O., Zhao R., Water entry of ship sections and axisymmetric bodies. Technical Report 818, AGARD FDP and Ukraine Institute of Hydromechanics Workshop on HighSpeed Body Motion in Water, Kiev, Ukraine, 1997.
- [15] Scolan Y.M., Korobkin A., Three-dimensional theory of water impact. Part 1. Inverse Wagner problem. *Journal of Fluid Mechanics* 2001; 440:293–326.
- [16] Miloh T., Wave slam on a sphere penetrating a free surface. *Journal of Engineering Mathematics* 1981;15(3):221–240.
- [17] Miloh T., On the oblique water-entry problem of a rigid sphere. *Journal of Engineering Mathematics* 1991;25(1):77–92.
- [18] Miloh T., On the initial-stage slamming of a rigid sphere in a vertical water entry. *Applied Ocean Research* 1991;13(1):34–48.
- [19] Battistin D., Iafrati A., Hydrodynamic loads during water entry of two-dimensional and axisymmetric bodies. *Journal of Fluids and Structures* 2003;17(5):643–664.
- [20] Faltinsen O., Chezhian M., A generalized Wagner method for three-dimensional slamming. *Journal of Ship Research* 2005;24(4):279–287.
- [21] Peseux B., Gornet L., Donguy B., Hydrodynamic impact: Numerical and experimental investigations. *Journal of Fluids and Structures* 2005; 21(3):277–303.
- [22] Kim Y., Hong S., Theoretical and numerical studies on three-dimensional water entry. In: 27th Symposium on Naval Hydrodynamics, Korea, 2008.

-
- [23] Nisewanger C., Experimental determination of pressure distribution on a sphere during water entry. Technical Report 7808, NAVWEPS, 1961.
- [24] Chuang S., Milne D., Drop tests of cones to investigate the three-dimensional effects of slamming. Technical Report 3543, NSDRDC, 1971.
- [25] Kleefsman K., Fekken G., Veldman A., Iwanowski B., Buchner B., A Volume-of-Fluid based simulation method for wave impact problems. *Journal of Computational Physics* 2005;206(1):363–393.
- [26] Moghisi M., Squire P., An experimental investigation of the initial force of impact on a sphere striking a liquid surface. *Journal of Fluid Mechanics* 1981;108:133–146.
- [27] De Pré J., Experimental study of slamming phenomena on point absorbers. Master dissertation. (in Dutch). Ghent University, Belgium, 2008.
- [28] De Backer G., Vantorre M., Victor S., De Rouck J., Beels C., Investigation of vertical slamming on point absorbers. In: *27th International Conference on Offshore Mechanics and Arctic Engineering*, Portugal, 2008.
- [29] Greenhow M., Lin W.M., Nonlinear free surface effects: experiments and theory. Technical Report 83-19, MIT, 1983.
- [30] Greenhow M., Water-entry and -exit of a horizontal circular cylinder. *Applied Ocean Research* 1988;10(4):191–198.
- [31] <http://www.fluent.com/>.
- [32] Stoop K., Vermeulen S., Numerical simulation of fluid structure interaction on hydrodynamic impact. Master dissertation (in Dutch). Ghent University, Belgium, 2008.
- [33] de Diego J., Numerical study of water impact on axisymmetrical bodies. Master dissertation. Ghent University, Belgium, 2009.

CHAPTER 7

Large scale outdoor bottom slamming tests

★ ★ ★

Experimental results of outdoor drop tests to investigate bottom slamming are presented. The tests are performed on two large buoys made of composite material. One buoy has an additional foam layer between the filament wound layers. The bodies consist of two conical parts (with deadrise angle 45°), connected by a cylindrical centre part. They are instrumented with pressure sensors, a shock accelerometer and strain gauges. The peak pressures on the conical bottom part are found to be much smaller than those measured on the 45° cone during the laboratory tests. One of the reasons for the small pressures is the large deceleration the bodies experience, shortly after having touched the water surface. This deceleration is most probably due to the presence of the flange, at the bottom of the cone. The deformability of the large-scale bodies may also be partly responsible for the smaller pressures, although the measured strain peaks are in the order of magnitude of only 70 microstrain. The measurement results indicate that the tested shape is favourable from the point of view of bottom slamming.

7.1 Introduction

Large scale outdoor drop tests have been performed at the Watersportbaan in Ghent, Belgium in cooperation with the Department of Materials Science

and Engineering at Ghent University. Two large floaters made of composite material were dropped from 1.00 m to 5.35 m in a canal. The bodies have a diameter of about 1.75 m and consist of two conical parts with an apex angle of 90° and a cylindrical middle part. The floaters are designed by the Department of Materials Science and Engineering and manufactured by the company Spiromatic (Nazareth) with the filament winding technique. For practical reasons, the conical parts are truncated by the presence of flanges and hence, the composite bodies are different from the conical body with a deadrise angle of 45° used in the laboratory tests. One of the large floaters has a foam layer between the composite layers (BWF = buoy with foam), the other one has no intermediate foam layer and is consequently slightly more deformable (BWOFF = buoy without foam). Not only bottom tests, but also lateral tests have been performed at the Watersportbaan. In that case the floater is dropped with its axis of rotation in the horizontal direction in order to simulate a breaking wave on the cylindrical part. More details about the design and manufacturing are given by Blommaert in [1] and Blommaert et al. in [2]. The results obtained from the lateral tests are also discussed in [1, 2].

7.2 Test setup

Figure 7.1-Figure 7.4 give an impression of the free fall outdoor drop tests. A crane lifted the floaters at the desired drop height between 1.00 and 5.35 m. The drop height was gradually increased in steps of 1 m. The tests at the largest drop height (i.e. 5.35 m for the BWF and 5.00 m for the BWOFF) have been repeated 10 times. For the other drop heights, one to four tests have been performed per drop height. In total, 44 bottom drop tests have been effectuated. A mechanical system was used to release the floaters, see Figure 7.2. By pulling a lever, the hook turns around the hinge point and the hoist cables are released together with the test body. The floaters fell down freely.

The drop height has been determined either by a measurement rope with affixed markers indicating the height (BWF), or by the measurement instrumentation of the crane (BWOFF). A 'pull rope' was attached to the test bodies, to pull them back to the bank where the hoist cables were reattached to the release mechanism. The different ropes and cables are indicated in Figure 7.3.

The floater shape and its dimensions are given in Figure 7.5. Due to the



Figure 7.1: Test setup at the Watersportbaan: a crane lifts up the floater.



Figure 7.2: Mechanical release system.

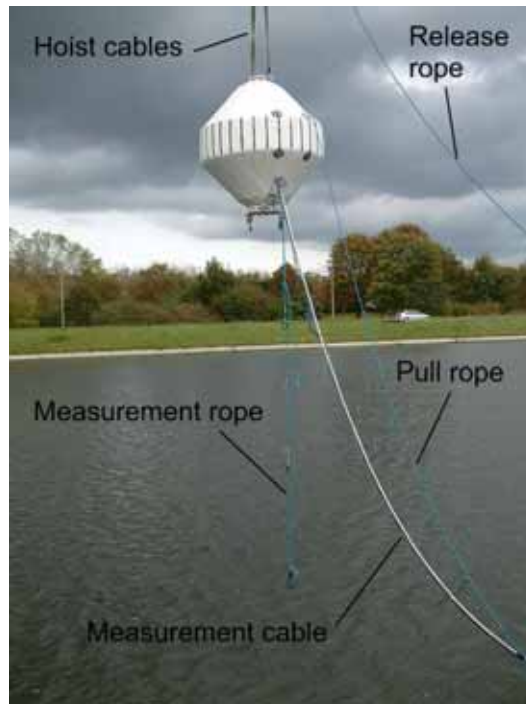


Figure 7.3: Drop test with composite body at Watersportbaan, Ghent - drop height 5.35 m.



Figure 7.4: Spray during impact.

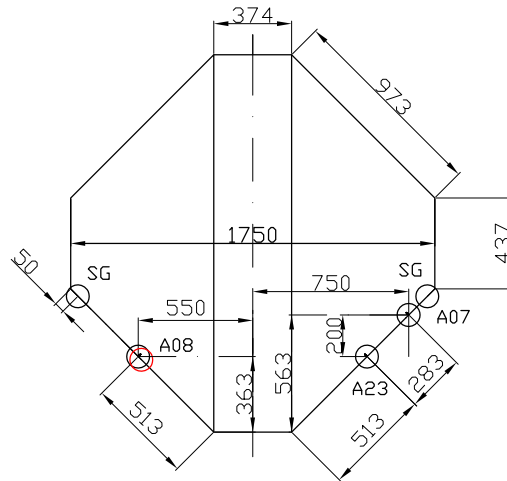


Figure 7.5: Dimensions of the large scale test bodies [mm] with indication of the pressure sensor and strain gauge positions.

filament winding technique, the thickness of the structures is not constant; the thickness increases at the edges of the cone. Figure 7.6 and Figure 7.7 give the thicknesses at a position near the pressure sensors for the buoy with and without foam, respectively. The position is indicated by a red circle in Figure 7.5. The first layer attached to the mould, is an isotropic fibre layer. It consists of mats with chopped fibres, randomly spread in all directions, improving the attachment with the other layers. Next, the buoy with foam has twice 4 filament wound layers, with in between a thick foam layer. The buoy without foam has 7 filament wound layers and no foam layer. On top of the last wound layer, a protective coating has been applied.

7.3 Instrumentation

7.3.1 Pressure sensor and accelerometer

The time history of the pressure and the position and deceleration of the body have been measured during impact, as well as the deformation of the structure. Three piezoelectric pressure sensors have been used: sensors A07, A08 and A23. Their position is indicated in Figure 7.5.

Sensor A07 has been used also for the laboratory tests in Chapter 6, sensors

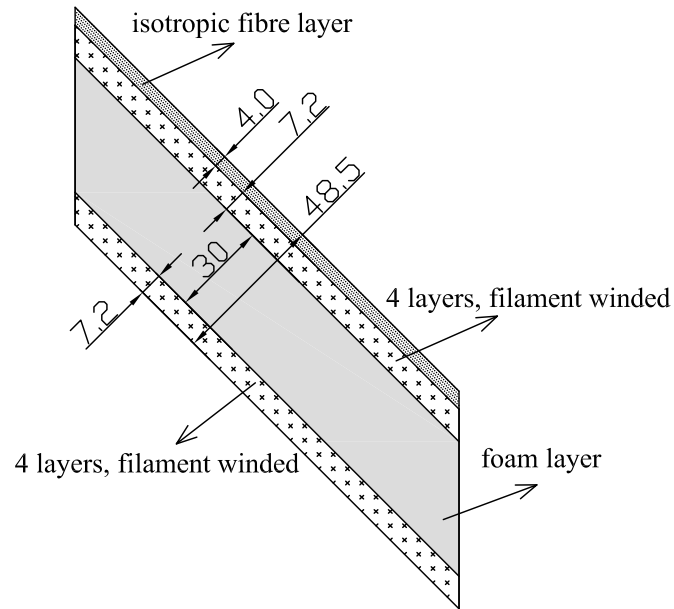


Figure 7.6: Layer construction and thickness - buoy with foam layer, dimensions in mm.

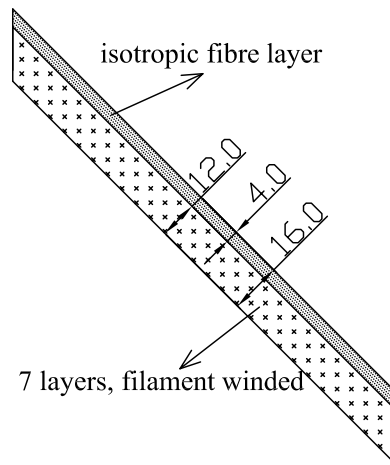


Figure 7.7: Layer construction and thickness - buoy without foam layer, dimensions in mm.

A08 and A23 are comparable ICP sensors, having built-in microelectronic amplifiers. All three sensors have a measurement range of 3.45 bar and a high resonance frequency (> 250 kHz). The cell membrane diameter is 5.5 mm. Unfortunately, sensor A23 has been broken in the beginning, as it has not given any realistic output. The same shock accelerometer as for the laboratory tests, with a measurement range of 500 g , has been used to register the deceleration during impact (resonance frequency > 54 kHz). The deformation is measured with strain gauges (SG) which are mounted at 4 different locations at the same cross section, i.e. 5 cm from the transition of the conical part to the cylinder (see Figure 7.5). In every location, one strain gauge is placed parallel to the water surface and a second is installed perpendicular to the first strain gauge. For the bottom tests, the strain gauges are intended to give information on the rigidity of the body.

7.3.2 High speed camera

The high speed camera (HSC) filmed the slamming phenomena at 1000 frames per second (fps). For the laboratory tests, a frame rate of 5000 up to 18000 fps had been chosen. Such high frame rates are more difficult to achieve in the outdoor large scale drop tests. For the latter tests the recording time had to be rather long (6.144 s) to make sure that the drops were registered within the recording time frame. In addition to this, the selected frame size had to be large enough, since the entire floater and a part of the water spray had to be recorded. As the buffer of the camera is limited, the combination of a large recording time and a large frame directly constrained the frame rate. Eventually, a frame rate of 1000 fps has been selected.

7.3.3 Data acquisition and synchronization

A single data acquisition (DAQ) card is used for the pressure sensors and shock accelerometer. The data is sampled at 75 000 Hz, which is a very high sampling frequency, allowing the measurement of sharp high frequent signals. The DAQ card is connected to a laptop for data registration. A separate computer controls the high speed camera and collects its data. This means that the data from the pressure sensors and accelerometer on the one hand and the data from the high speed camera on the other hand need to be synchronized. To make this possible, the high speed camera sends a block signal to the DAQ card.

The flanks of the signal correspond to the exact switch-on and switch-off time instants of the high speed camera. With this block signal, the pressure time history, acceleration and position of the buoy measured by the camera can be combined with the same time axis.

All the data acquisition material was installed on the river bank. Strong measurement cables, consisting of 5 protective layers have been used. Since the cables have a rather large length of 20 m, it is advantageous to use pressure sensors with built-in microelectronic amplifier to reduce additional noise.

7.4 Test results

7.4.1 Visualization of impact phenomena

Figure 7.8 shows a filmstrip of the impact phenomena for the buoy with foam with a drop height of 5.35 m. The time step between the frames is 0.008 s. As observed in Figure 7.4, an impressive water uprise can also be noticed on the snapshots of Figure 7.8. With the high speed camera images it can be seen very well whether the floaters fell down perfectly vertically. This is important, since small rotations have a significant influence on the pressure measurement. Consequently, the images made it possible to exclude data from poor measurement tests where the floater was inclined. An overview of all tests is given in Appendix G.1, with comments on the verticality and quality of the pressure and accelerometer signal, based on visual judgement. The high speed camera images were also used to determine the position and velocity of the buoy as a function of time, by applying a marker tracking technique.

7.4.2 Pressure distribution, impact velocity and deceleration

Figure 7.9(a) gives the pressure time history of the buoy with foam (BWF), measured by the sensors A07 and A08 for a drop height of 5.35 m. The initial time instant $t = 0$ is defined as the time where the flange of the body touches the calm water surface. This moment has been manually determined from the high speed camera images and might have a deviation of 1 to 2 ms. As soon as the body touches the water, large oscillations appear in the pressure signal. The first pressure peak (A08) shows a steep rise followed by a more gradual decrease. The second pressure sensor (A07) experiences at first a remarkably deep trough. This has been observed in other tests as well, for

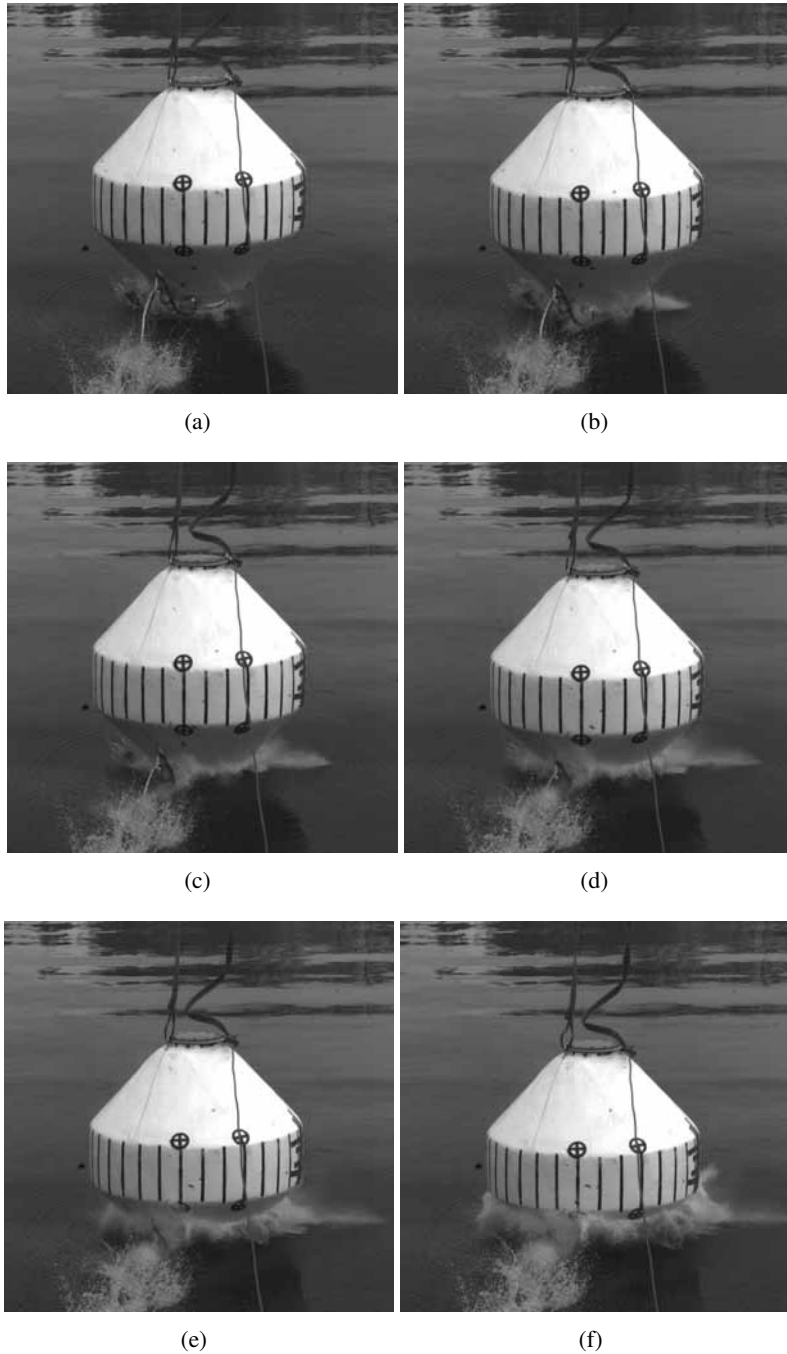
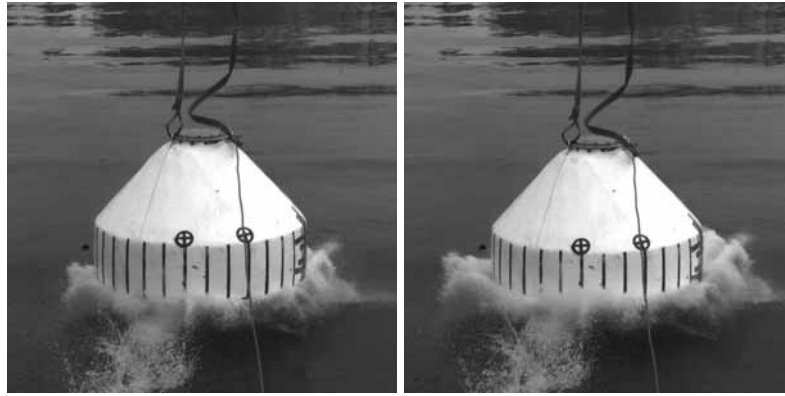
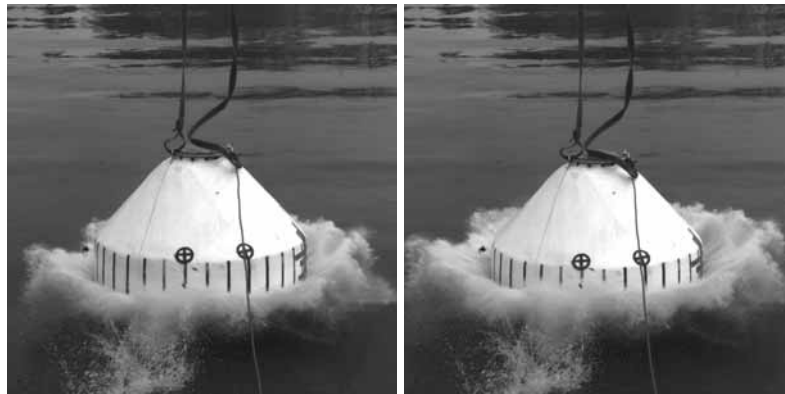


Figure 7.8: Figure continues on next page.



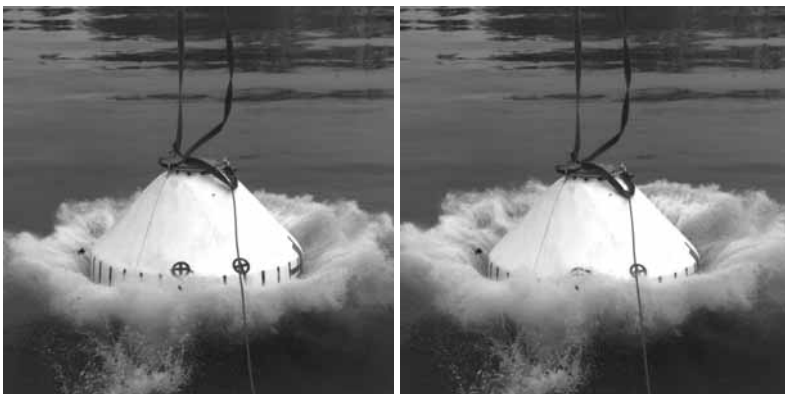
(g)

(h)



(i)

(j)



(k)

(l)

Figure 7.8: Figure continues on next page.



(m)

Figure 7.8: Snapshots of impact of a composite floater with foam with a drop height of 5.35 m. (a) = 0.000 s, (b) = 0.008 s, (c) = 0.016 s, (d) = 0.024 s, (e) = 0.032 s, (f) = 0.040 s, (g) = 0.048 s, (h) = 0.056 s, (i) = 0.064 s, (j) = 0.072 s, (k) = 0.080 s, (l) = 0.088 s, (m) = 0.096 s.

both sensors and both bodies, however, in particular for the buoy with foam. It is not clear which phenomenon causes the large underpressures. It is advised to further investigate whether these underpressures may influence the ‘damage-behaviour’ of the floater.

Figures 7.9(b) - 7.9(d) show the acceleration, velocity and penetration versus time, measured by the shock accelerometer for the BWF. The depth and velocity as a function of time is also given by the high speed camera. Very large oscillations appear in the accelerometer signal, making it impossible to determine the peak deceleration during impact. However, the signal is still valuable to calculate the velocity and penetration depth of the point absorber and a quite good correspondence is found with the results from the high speed camera. The velocity drops quite significantly, especially in the first 40 to 60 ms. Thereafter it decreases more gradually. The quick velocity reduction after the floater has made contact with the water is caused by the presence of the flange. This velocity decrease might be one of the reasons why the second sensor (A07) gives a smaller peak pressure than the first sensor (A08). In the laboratory tests, where a pure cone shape with apex angle 90° was tested, the measured velocity first showed a very small rise after the apex touched the water surface, followed by a gradual decrease in velocity. Consequently,

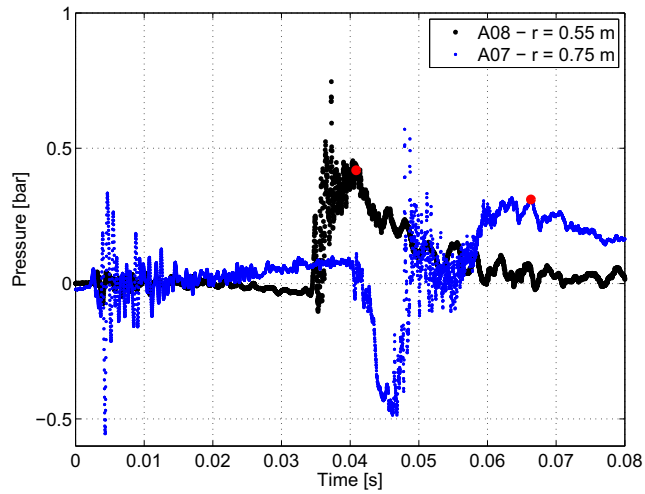
the pressure peaks on the large scale composite bodies are expected to be much smaller than those measured on the pure cone shape in the laboratory. Furthermore, it can be noted that the body has achieved a submergence of almost 0.7 m in only 80 ms.

Figure 7.10(a) shows the pressure time history of the buoy without foam (BWO), dropped from a height of 5.00 m. In Figures 7.10(b)- 7.10(d) the acceleration, velocity and position are shown as a function of time for the BWO. The results are in line with those from the BWF. Note that the initial velocity is slightly smaller than the value in Figure 7.10(c) for the BWF, since the drop height is smaller as well. More results for both buoys dropped from different heights are shown in Appendix G.2.

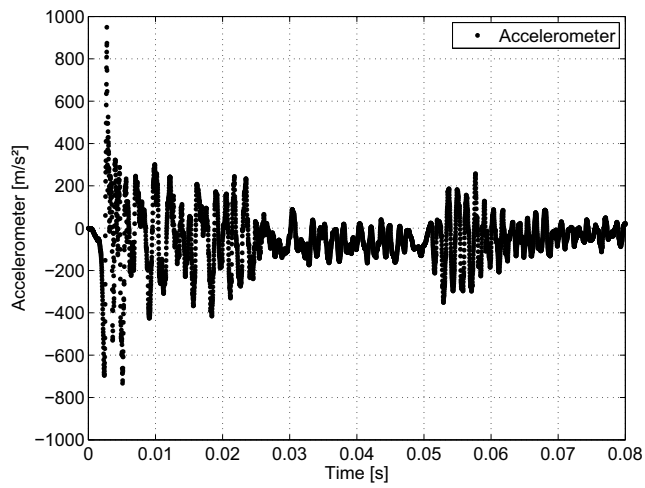
7.4.3 Peak Pressures

In Figure 7.11 and Figure 7.12 the recorded peak pressures are shown for the floaters with and without foam layer respectively. The values are shown as a function of the first equivalent drop height, i.e. the drop height derived from the initial impact velocity measured by the high speed camera. The relationship between the first equivalent drop height h^* and the initial measured impact velocity U_{0m} is given by: $h^* = U_{0m}^2/2g$. The presented data only contains the measurements of the well succeeded drop tests. In Appendix G.1, comments on the quality are added to each test, based on the measurements of the high speed camera, the pressure sensors and accelerometer. The omitted tests are indicated as well.

Since the pressure time histories contain some high frequency oscillations, a smoothing function has been applied on the data. The function averages the figures progressively over a number of data points so that the presented maximum pressures do not contain the exceptionally high values in the pressure time histories. The number of data points in the smoothing function could be derived from the period of the oscillations. In this case, however, this would require a smoothing function with 45 up to 130 data points. In order to avoid truncating the real pressure peak, the number of data points was set to 40 in general and to 10 in some particular cases with steep peaks. In Appendix G.1, the numbers of the maximum values without smoothing are presented as well. Even if the effect of the noise is not reduced, the pressure values are very small. The relationship between p and h as predicted by asymptotic theory, i.e. $p = 0.297 h$, is given by a dash-dotted

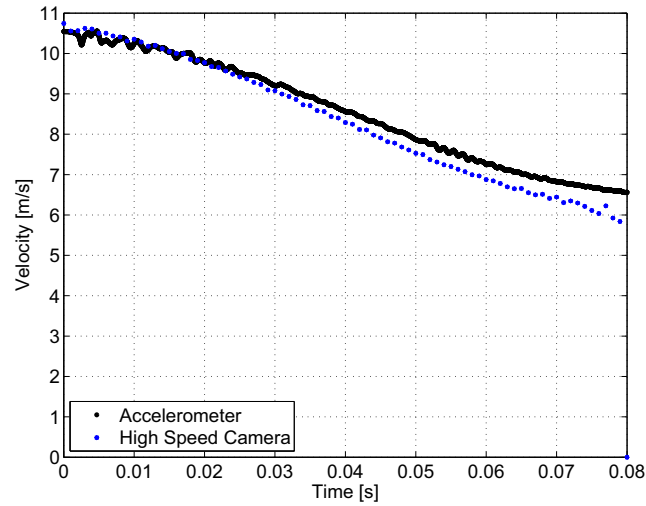


(a) Pressure time history.

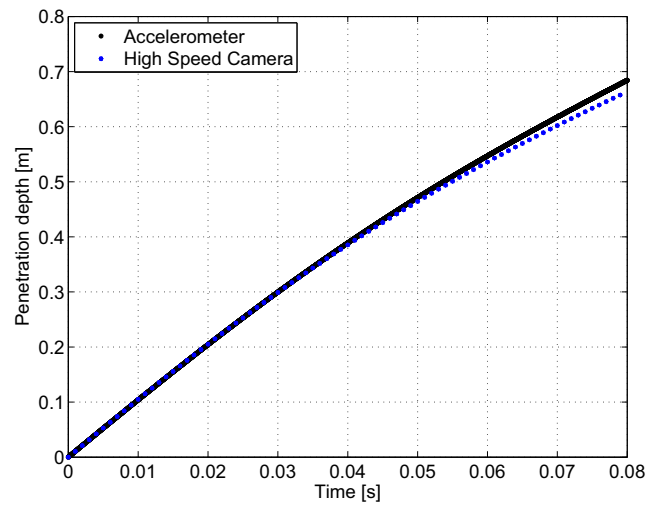


(b) Acceleration as a function of time.

Figure 7.9: Figure continues on next page.

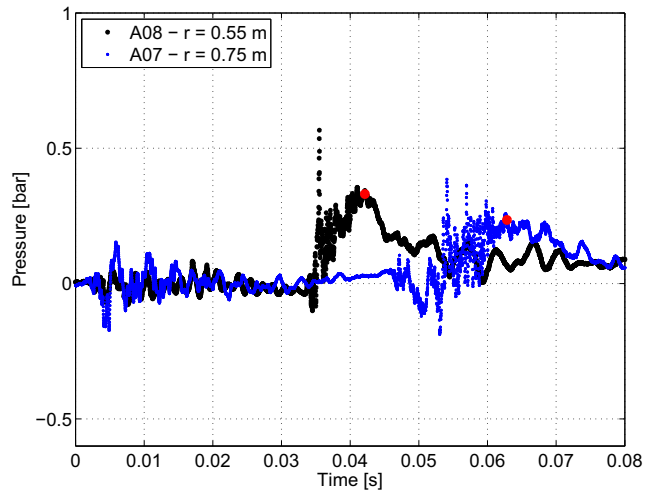


(c) Velocity as a function of time.

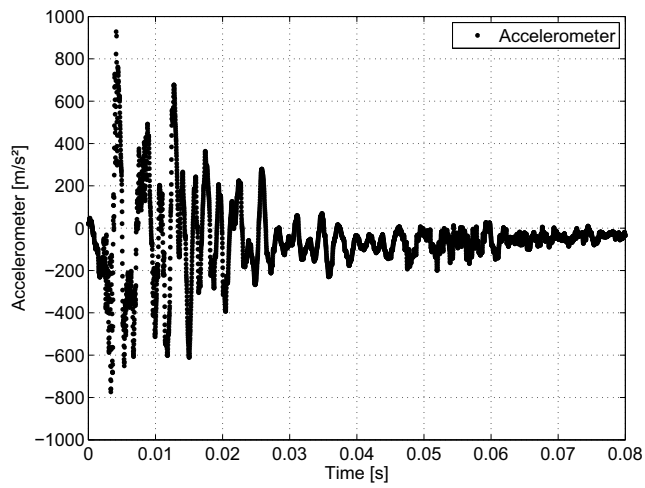


(d) Position as a function of time.

Figure 7.9: Measured data on BWF, drop height 5.35 m.

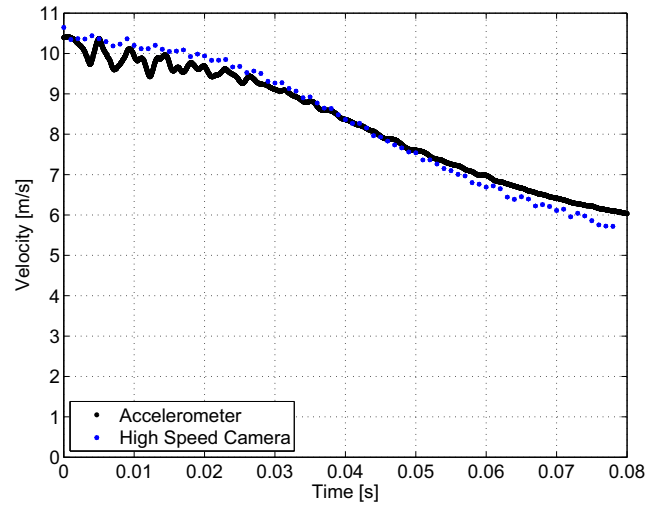


(a) Pressure time history.

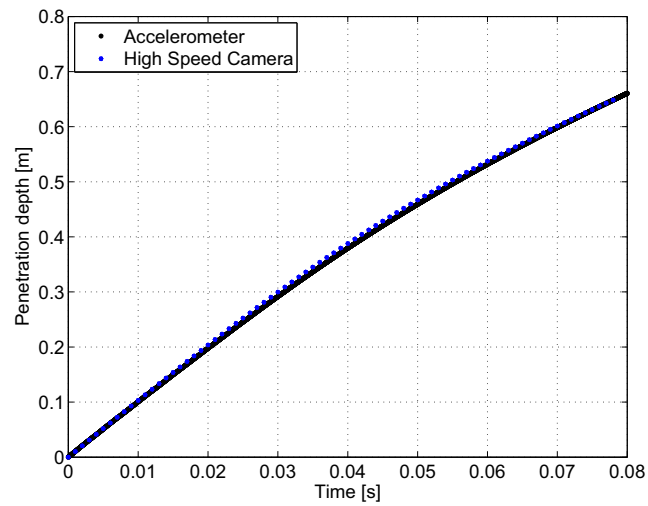


(b) Acceleration as a function of time.

Figure 7.10: Figure continues on next page.



(c) Velocity as a function of time.



(d) Position as a function of time.

Figure 7.10: Measured data on BWO, drop height 5.00 m.

gray line. The asymptotic theory for rigid cones clearly overestimates the pressure measurements in this case. The scattering in the data is rather large, particularly for sensor A08 of the buoy with foam. This is also expressed by the quite small value of the squared Pearson correlation coefficient, R^{*2} for sensor A08.

Furthermore, it can be seen that the peak pressures are slightly smaller for the BWOF case than for the BWF, which could possibly be explained by the fact that the latter is less deformable. In general, the pressure values are very small. Based on all the pressure measurements on the buoys with and without foam, the following average relationship between the pressure and first equivalent drop height is found: $p = 0.060 h^*$, with h^* the first equivalent drop height, based on the impact velocity at time instant $t = 0$. According to this relationship, the measured peak pressures are almost a factor of five smaller than the values that are predicted by the asymptotic theory for rigid cone shaped bodies with an apex angle of 90° . A factor of 2.4 and 3.6 is found between the peak values measured in the laboratory on the polyurethane 90° cone and the measured peak pressures of the outdoor drop tests. (The average relationships between the peak pressures and drop heights derived from the laboratory tests are: $p = 0.142 h$ and $p = 0.217 h$ for the two different sensor positions (Figure 6.37 of Chapter 6)). The results are summarized in Table 7.1. It must be stressed that the asymptotic theory assumes a constant entry velocity and also the measured velocity for the 45° cone in the lab tests remained almost constant, which is absolutely not the case for the outdoor experiments. Serious velocity drops were recorded at the positions of the sensors in the Watersportbaan tests. The presence of the horizontal flange influences the fluid flow considerably and decreases the penetration velocity significantly, resulting in smaller impact pressures.

For both test bodies, sensor A08, which is mounted closer to the bottom, gives on average somewhat higher peak levels than sensor A07. This might be explained by the value of the instantaneous body velocity, which is considerably smaller when the peak of sensor A07 occurs, compared to the peak of A08. Therefore, it would be interesting to compare the peak pressure values versus the instantaneous velocity, U_{tp} , at the time instant where the peak pressure, t_p , occurs. The difference with the laboratory tests and asymptotic theory will also become smaller, if the instantaneous velocity is taken into account. In order to effectuate this, a second equivalent drop

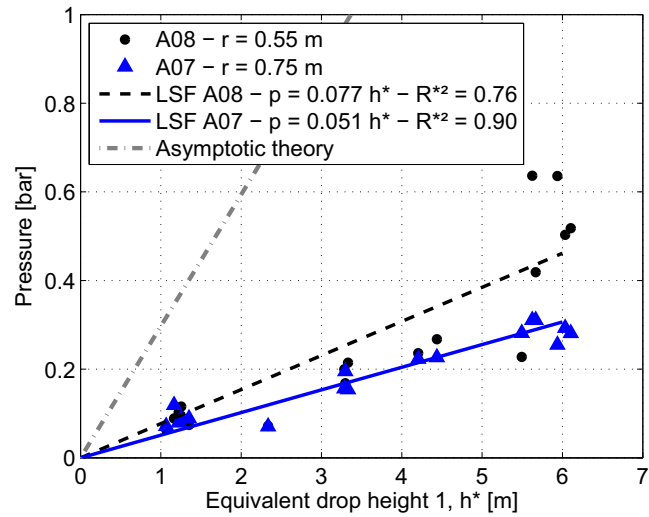


Figure 7.11: Maximum pressure [bar] as a function of the first equivalent drop height [m] for the buoy with foam layer (BWF).

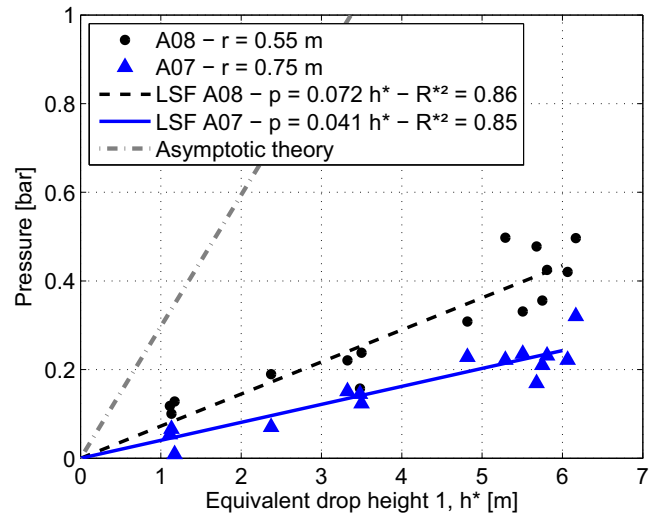


Figure 7.12: Maximum pressure [bar] as a function of the first equivalent drop height [m] for the buoy without foam layer (BWO).

Table 7.1: Ratio of average peak pressures from the outdoor tests (indicated by *ot*) to the asymptotic theory (*at*) and the laboratory test results (*lt*). The superscripts * and ** refer to the first and second equivalent drop height, respectively.

p_{at}/p_{ot}^*	$p_{lt,r=4cm}/p_{ot}^*$	$p_{lt,r=9cm}/p_{ot}^*$
4.9	3.6	2.4
p_{at}/p_{ot}^{**}	$p_{lt,r=4cm}/p_{ot}^{**}$	$p_{lt,r=9cm}/p_{ot}^{**}$
2.7	2.0	1.3

height is introduced, h^{**} , defined by the relationship: $h^{**} = U_{tp}^2/2g$. The peak pressure values as a function of this second equivalent drop height are presented in Figure 7.13 and Figure 7.14 for the buoy with foam and without foam, respectively. As expected, the difference between the data points from sensor A07 and sensor A08 is significantly diminished and their least squares fitting lines lie much closer to each other. This means that the pressure difference between the two sensors can be mainly explained by the difference in immediate velocity. Note that the slope of the relationships between the pressure and the equivalent drop height is increased, compared to Figure 7.11 and Figure 7.12. The gap between the measured values and the estimated values derived from the asymptotic approach is smaller, though still significant.

Based on all the pressure measurements on both buoys, the average relationship between the pressure and second equivalent drop height becomes: $p = 0.109 h^{**}$. When considering this relationship, the theory -based on a constant entry velocity- gives values that are on average a factor of 2.7 higher than the experiments, and the laboratory tests on a pure cone (Chapter 6) give values that are a factor of 1.3 and 2.0 higher (Table 7.1). Consequently, when taking into account the instantaneous impact velocity at the time instant where the peak pressures occur, the measured outdoor results are much closer to the lab tests and theoretical values. However, still a significant difference is noticeable. This difference might be attributed to the effect of the deceleration of the object in the water. Since a significant velocity drop is observed, the deceleration is non negligible. The influence of this acceleration and deceleration on the pressure is not taken into account by the asymptotic theory and turned out to be small - between 5 % and 15 %- for the lab tests on the 45° cone. The pressure originating from the part of the impact

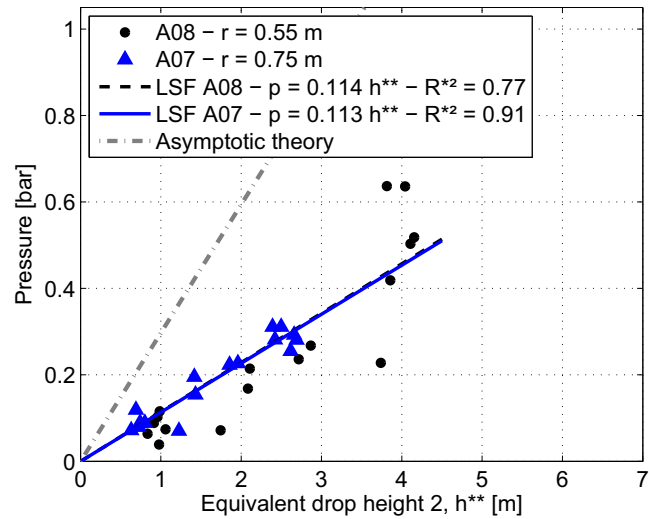


Figure 7.13: Maximum pressure [bar] as a function of the second equivalent drop height [m] for the buoy with foam layer (BWF).

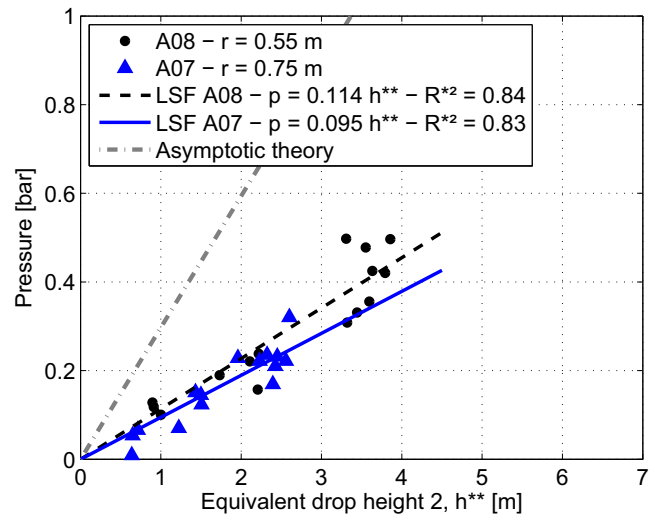


Figure 7.14: Maximum pressure [bar] as a function of the second equivalent drop height [m] for the buoy without foam layer (BWO).

force proportional to the acceleration ($m_{a,\infty} d^2z/dt$) is assumed uniformly distributed. Because of the huge oscillations in the measured accelerometer signal, the decelerations at the time instants where the peak pressures occur, are determined from the derivative of a fifth order polynomial approximation of the velocity signal. The contribution of this pressure is estimated between 11 % and 28 % of the measured values for pressure sensor A08 and between 38 % and 66 % of the measured values for pressure sensor A07. Consequently, the effect of this pressure is quite important in this case and explains partly the smaller values that were found at the Watersportbaan tests.

In addition, the smaller values could be attributed to the fact that the composite floaters cannot be considered as rigid bodies, although the measured strains are not very large. The average peak strains that were recorded during impact are in the order of magnitude of 70 microstrain. This figure does not differ a lot from the results of previous experiments on bodies considered as rigid. However, this can be explained due to the fact that the floaters were produced by means of filament winding. In other words the conical part, where the strain gauges were placed, has a rather large thickness compared to the cylindrical part. Since the measured pressures are quite small on these floaters, this shape - i.e. a cone with deadrise angle of 45° - is considered as a good choice in order to minimize the effects of bottom slamming.

7.5 Conclusion

Drop tests with two large composite point absorbers have been performed in the Watersportbaan canal in Ghent. The drop height varied from 1.00 to 5.35 m. The slamming pressure on the bodies has been measured, as well as the deceleration and strain of the material. The impact phenomenon has been filmed with a high speed camera, showing an enormous water spray during impact. A significant velocity decrease was measured during impact, most probably due to the presence of the flange. Generally the measured peak pressure values are rather small. For a large drop height of 5.35 m, the measured peak levels vary between 0.23 and 0.64 bar. A least squares fitting has been applied through the maximum pressures as a function of two equivalent drop heights. When taking into account the instantaneous velocity and comparing the fitting to the least squares fittings from the peak levels measured on the small polyurethane 90° cone, it was found that the

peak pressures on the composite bodies are on average a factor of 1.3 to 2.0 smaller than those from the lab tests. Moreover they are a factor of 2.7 smaller than the peak levels predicted by the asymptotic theory based on Wagner's assumptions. Reasons for this deviation might be the presence of the flange, which influences the fluid flow considerably, the influence of the impact pressure part that is proportional to the acceleration and the non-rigidness of the large scale bodies. It is concluded that a conical body with an apex angle of 90° is a very good shape to reduce problems with bottom slamming, as it experiences small impact pressures compared to a hemisphere and a cone with smaller deadrise angle.

Bibliography

- [1] Blommaert C., Composite floating 'point absorbers' for wave energy converters: survivability, design, production method and large-scale testing. Ph.D. thesis, Ghent University, Belgium, 2009.
- [2] Blommaert C., Van Paepegem W., Dhondt P., De Backer G., Degrieck J., De Rouck J., Vantorre M., Van Slycken J., De Baere I., De Backer H., Vierendeels J., De Pauw P., Matthys S., Taerwe L., Large scale slamming tests on composite buoys for wave energy applications. In: 17th International Conference on Composite Materials, United Kingdom, 2009.

CHAPTER 8

Influence of constraints to reduce bottom slamming



Whereas the focus of the previous two Chapters laid on the impact pressures and loads, the emphasis of this Chapter will be on the occurrence probabilities of emergence events. Numerical simulations are performed for three different sea states and three buoy shapes: a hemisphere and two conical shapes with deadrise angles of 30° and 45°, with a waterline diameter of 5 m. The simulations indicate that the risk of rising out of the water is largely dependent on the buoy draft and sea state. Emergence occurrence probabilities can be significantly reduced by adapting the control parameters of the point absorber; however, this is associated with power losses. For various levels of slamming constraints, the impact velocities and corresponding slamming forces on the bodies are estimated. The buoy shape severely influences the slamming loads. The ratio between the peak impact loads on the hemisphere and the 45° cone is approximately a factor of 2, whereas the power absorption is only 4 to 8 % higher for the 45° cone in the selected sea states. This Chapter illustrates the necessity to include slamming considerations apart from power absorption criteria in the buoy shape design process as well as in the control strategy. This Chapter is based on 'Bottom slamming on heaving point absorber wave energy converters' by G. De Backer et al. [1]

8.1 Introduction

Point absorber buoys generally have a larger natural frequency than the incident wave frequencies and are therefore often tuned to the characteristics of the incident waves to augment power absorption (Chapter 1). This tuning increases the body motions and consequently also the probability of rising out of the water. When re-entering in the water, the buoys might be subjected to bottom slamming, which can be associated with large impact pressures and forces (Chapter 6). So far, research on point absorbers has mainly focused on power absorption maximization, for example, by optimizing the buoy shape and improving the control strategy. In order to determine an efficient practical tuning strategy and an optimal shape, however, slamming considerations need to be taken into account as well. Not only the extreme load cases are important, but also the operational conditions where regular bottom slamming occurs, resulting in fatigue of the material. Hence, it is important to assess the occurrence probability of slamming dependent on the wave climate, power take-off (PTO) and control system.

For completeness, it is worth mentioning that not only bottom slamming is of importance in point absorber design but also lateral slamming (wave slamming) on the buoys. The work of Wienke and Oumeraci [2], who experimentally investigated impact forces on slender cylinders due to plunging breaking waves, can be used as a first approximation of wave slamming forces on point absorbers. Furthermore, drop tests on the flanks of composite point absorbers to simulate breaking wave impacts have been carried out by Blommaert [3].

First, the influence of varying slamming restrictions on the power absorption will be illustrated in this Chapter. Next, the occurrence probabilities of emergence events and the distribution of the impact velocities and forces will be given for several examples.

8.2 Different levels of slamming restrictions

The occurrence probability of slamming and the associated impact loads can be decreased by influencing the control parameters of the buoy, as illustrated in Chapter 2. Either the external damping applied on the buoy to extract power can be increased, or the buoy can be detuned or a combination of both can be

applied. In Chapter 2 only one slamming restriction level has been applied. In this Chapter the stringency of the slamming constraint is varied and the effect on the probability of emergences is investigated with a time domain model. Three shapes are considered in this Chapter: two cones with deadrise angle 45° and 30° , respectively, and a hemisphere. All bodies have a cylindrical upper part that is submerged by 0.50 m in equilibrium position. The waterline diameter, D , is 5.00 m, as indicated in Figure 8.1. The equilibrium draft is 3.00 m for the 45° cone and the hemisphere and is 1.94 m for the 30° cone. The shapes and their corresponding masses are presented in Figure 8.1. In practice the edges at the transition between the conical and cylindrical part are preferably rounded to reduce turbulence effects.

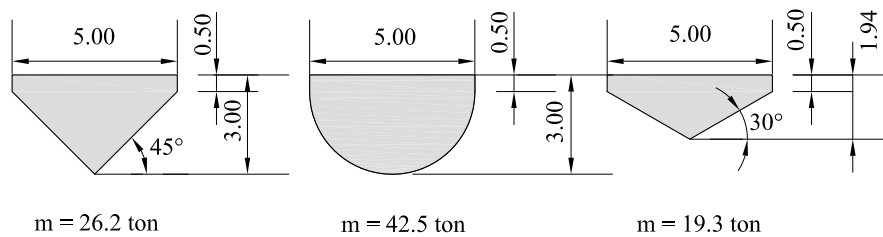


Figure 8.1: Test shapes - submerged part in equilibrium: Cone with deadrise angle 45° , cone with deadrise angle 30° and hemisphere, dimensions in [m].

Three sea states have been defined: (1) $H_s = 1.25$ m - $T_p = 5.98$ s, (2) $H_s = 2.75$ m - $T_p = 7.78$ s, (3) $H_s = 4.25$ m - $T_p = 9.10$ s. The first sea state represents a rather small wave, that can be regarded as the minimum threshold to produce electricity. In the second sea state the significant wave height rather has the order of magnitude of a design wave, and has most likely a high probability of occurrence in the areas developers are currently focussing on. It is assumed that the point absorbers are still in operation in the third, more energetic sea state. In storm conditions, however, point absorber devices generally stop producing electricity and switch to a safety mode in which the floaters are protected against bottom slamming or breaking wave slamming. This can be realized by completely submerging the buoys or by lifting them up to a certain level above the water surface [4]. The wave spectrum is determined with the parameterized JONSWAP spectrum [5, 6], also given in Chapter 2.

In order to avoid excessive slamming, a slamming constraint has been formulated in Chapter 2, requiring that the significant amplitude of the position

of the buoy relative to the free water surface, ζ , is limited to a fraction α of the buoy draft d :

$$(z - \zeta)_{A,sign} < \alpha d \quad (8.1)$$

The choice of the slamming restriction factor α in Eq. (8.1) has a direct impact on the occurrence probability of emergence. In Chapter 2 α is chosen equal to 1, meaning that emergence events are still allowed for the 13.5 % highest waves, assuming the wave and body displacement amplitudes are Rayleigh distributed. In small waves, the slamming criterion does not influence the optimal values of the control parameters. However, for higher waves less optimal values of the control parameters b_{ext} and m_{sup} have to be chosen in order to fulfill the slamming criterion. This is illustrated for the 45° cone in Figures 8.2 - 8.4 showing the time-averaged absorbed power as a function of the control parameters b_{ext} and m_{sup} . In Figure 8.2 the power absorption is given for the second sea state ($H_s = 2.75$ m - $T_p = 7.78$ s), together with three slamming contour lines, with α -values of 0.75, 1.00 and 1.50, respectively. The area enclosed by the contour lines has to be avoided to fulfill the slamming restriction, resulting in less power absorption for stricter slamming constraints. For the least stringent constraint ($\alpha = 1.50$), the power absorption in the remaining area is 115 kW, for the intermediate constraint ($\alpha = 1.00$), it drops to 96 kW and for the most stringent constraint ($\alpha = 0.75$), the maximum absorbed power equals 79 kW. The maximum values are indicated with a black circle.

Two velocity contour lines of 2 m/s and 4 m/s are shown as well in Figure 8.2. They represent lines of equal significant values of the vertical buoy velocity relative to the vertical velocity of the water surface. The significant amplitude of the relative velocity could also be used to formulate a slamming constraint instead of the relative displacement amplitude. The latter restriction has a direct link with the slamming occurrence probabilities, whereas the relative velocity constraint is rather related to the pressures and forces.

It can be observed from the graph that the slamming restrictions are mainly fulfilled by increasing the damping and only to a lower extent by decreasing the supplementary mass. Table 8.1 presents the time-averaged power absorption values for the three shapes per sea state and for different levels of the slamming restriction factor α . The presented power absorption numbers are the maximum values that can be obtained when satisfying the slamming

restriction, according to Eq. (8.1). The values that could be theoretically absorbed if no restrictions are included ($\alpha = \infty$) are shown as well. However, these values and those associated with weak slamming constraints do not always represent practically achievable solutions. As stated in the previous Chapters, the power absorption values do not correspond to the produced power, since they do not take into account any losses.

Table 8.1: Power absorption [kW] by the three shapes for different levels of slamming restrictions.

$\alpha \setminus$ Sea state	45° cone			hemisphere			30° cone		
	1	2	3	1	2	3	1	2	3
0.75	17	79	125	16	75	119	18	55	83
1.00	17	96	162	16	91	155	18	72	110
1.50	17	115	221	16	108	211	18	96	161
∞	17	118	317	16	111	302	18	121	326

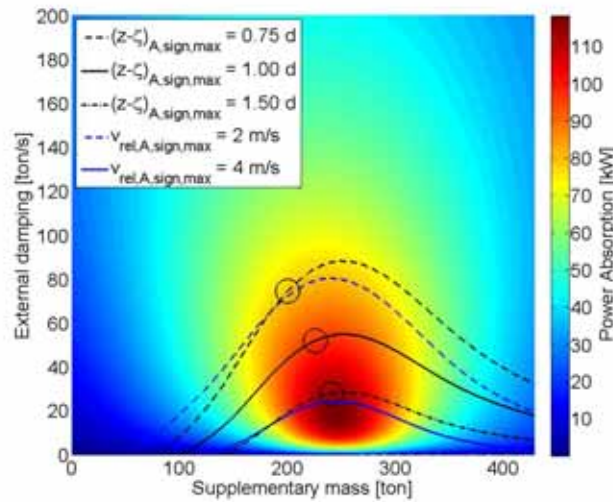


Figure 8.2: Power absorption [kW] versus b_{ext} and m_{sup} , by the 45° cone for sea state 2 ($H_s = 2.75$ m - $T_p = 7.78$ s) with slamming restriction contour lines.

Figure 8.3 shows the power absorption for the first sea state ($H_s = 1.25$ m

- $T_p = 5.98$ s). None of the slamming constraints has an influence on the optimal tuning and damping parameters. The maximum power absorption value (17 kW) can be achieved while slamming phenomena will seldom occur.

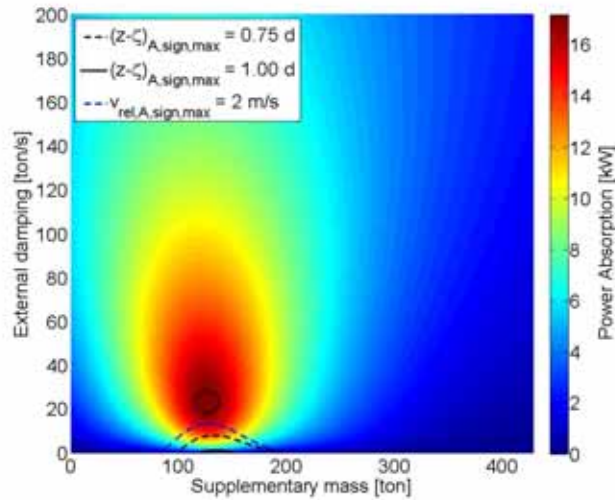


Figure 8.3: Power absorption [kW] versus b_{ext} and m_{sup} , by the 45° cone for sea state 1 ($H_s = 1.25$ m - $T_p = 5.98$ s) with slamming restriction contour lines.

Figure 8.4 presents the power absorption and slamming contour lines for the most energetic sea state ($H_s = 4.25$ m - $T_p = 9.10$ s). Theoretically, the dark red coloured area, the resonance zone, leads to the highest power absorption. However, this zone requires very large tuning forces on the one hand and it is associated with extremely high buoy displacement and velocity amplitudes on the other hand. Therefore, for practical cases, this zone is not the target area in large waves. In order to satisfy the restrictions, not only the damping has to be increased but also the tuning forces need to be considerably decreased. The absorbed power is largely dependent on the level of slamming that is allowed. The optimal power values drop from 221 kW to 162 kW and 125 kW, respectively, for the weakest, to the intermediate and most stringent restriction.

For comparison, the power absorption in the intermediate sea state ($H_s = 2.75$ m - $T_p = 7.78$ s) is shown in Figures 8.5 and 8.6 for the hemisphere and the 30° cone, respectively. The results for the hemisphere are very similar

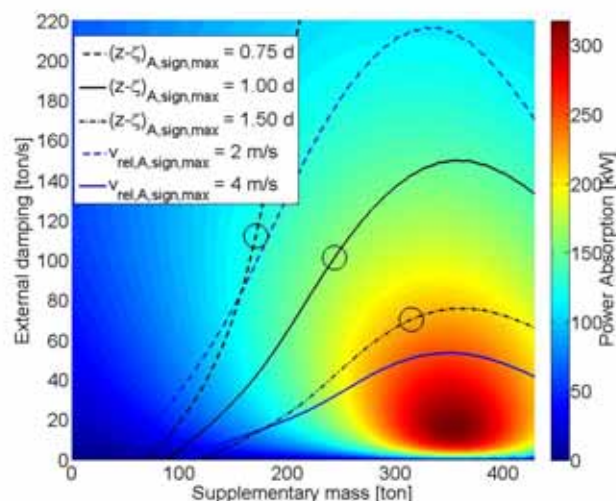


Figure 8.4: Power absorption [kW] versus b_{ext} and m_{sup} , by the 45° cone for sea state 3 ($H_s = 4.25$ m - $T_p = 9.10$ s) with slamming restriction contour lines.

to those for the 45° cone, although there is a slight advantage for the 45° cone. The performance of the latter is between 4 and 8 % better than that of the hemisphere for the same slamming conditions, as illustrated by the power absorption figures in Table 8.1. Much larger differences (between 15 % and 30 %) are observed for the 30° cone. For α equal to 1.50, the power absorption is 96 kW, for α -values of 1.00 and 0.75, the power absorption drops to 72 kW and 55 kW, respectively (see Table 8.1). For the same α -values as for the other shapes, the constraints are much more stringent for the 30° cone shape, since the draft d is smaller. Because of its small draft, the buoy will easily loose contact with the water surface and slam.

This is why the slamming constraint needs to be stricter in this case to allow the same level of slamming as for the other shapes, which is equivalent to using the same value of α . Alternatively, if the same absolute restriction is imposed on the relative significant position of the buoy, i.e. the same value of $\alpha \cdot d$, the 30° cone will emerge much more frequently than the other shapes. However, the power absorption will be in the same order of magnitude or even slightly higher, since it benefits from large exciting forces due to its small draft. An example is given for $\alpha = 2.30$ for the 30° cone. This number

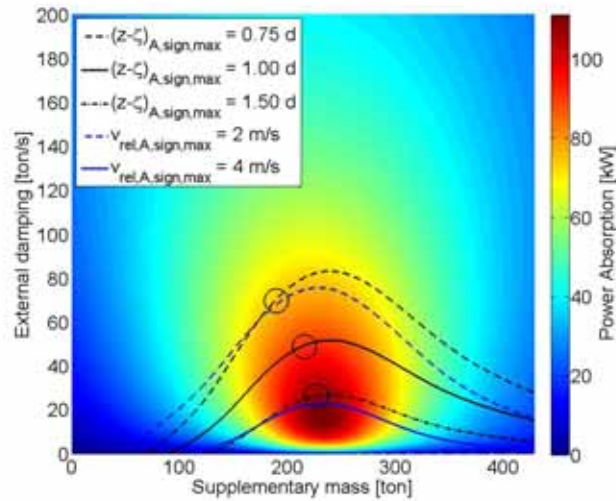


Figure 8.5: Power absorption [kW] versus b_{ext} and m_{sup} , by the hemisphere for sea state 2 ($H_s = 2.75$ m - $T_p = 7.78$ s) with slamming restriction contour lines.

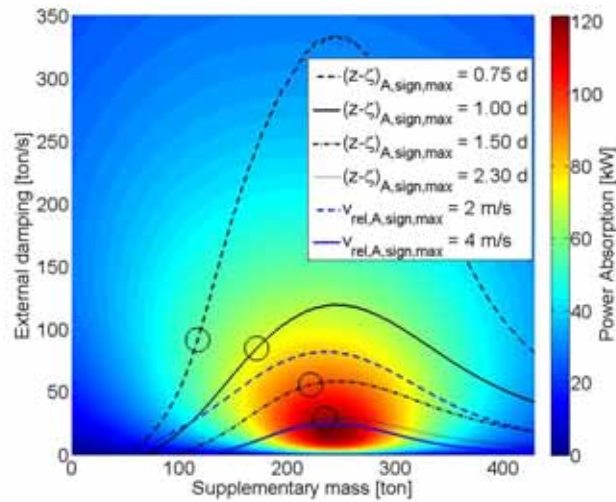


Figure 8.6: Power absorption [kW] versus b_{ext} and m_{sup} , by the 30° cone for sea state 2 ($H_s = 2.75$ m - $T_p = 7.78$ s) with slamming restriction contour lines.

of α implies a restriction of approximately 4.5 m on the maximum relative significant amplitude of the buoy position and corresponds with an α -value of 1.50 for the 45° cone and hemisphere. The power absorption in this case is 117 kW for the 30° cone, compared to 115 kW and 106 kW for the 45° cone and hemisphere, respectively. These numbers have to be treated with caution, since this example represents a case where extreme high slamming rates and buoy motions occur, as will be shown later, violating the assumptions behind linear theory. Contrary to Figures 8.2 and 8.5 for the 45° cone and hemisphere, respectively, the two velocity contour lines in Figure 8.6 enclose a relatively limited area compared to the displacement contour lines for the 30° cone. Hence, when slamming constraints are formulated, based on the same velocity contour lines for the three shapes, this might result in a relatively weaker restriction for the 30° cone compared to constraints based on the same contour lines of relative displacement.

The control strategy used in this work optimizes the tuning and damping coefficients (m_{sup} and b_{ext}) for a certain sea state and keeps them fixed during that sea state. This offers the practical benefit of a relatively simple control strategy. With a more complex (wave to wave) strategy, the control can be adapted to the instantaneous water elevation at the position of the buoy and/or the motion parameters of the buoy. Slamming phenomena can then be reduced e.g. by decreasing the immediate floater displacement and velocity at time instants where they might become very large. In that way, slamming can be diminished without too much penalizing the power absorption in instantaneous small and intermediate waves within a certain sea state. Compared to this method, the slamming restrictions of the fixed coefficients control strategy are rather conservative and consequently so are the estimated drops in power absorption. However, a wave to wave control strategy is a lot more difficult to realize in practice: a particularly reliable control system is required as well as a very reliable prediction of the immediate water elevation at the position of the buoy and of the motion parameters of the buoy. The decision on how stringent a slamming constraint needs to be, depends on the impact loads to which the buoys can be subjected and the number of slamming occurrences that are tolerable for the buoys (fatigue).

8.3 Probability of emergence

The occurrence probabilities of the emergence events are investigated with the time domain model described in Chapter 3. The model has been slightly extended with the possibility to store the information on each slamming event in regular and irregular waves. For the three sea states and the point absorber shapes as defined in Section 8.2, simulations are run with this linear time domain model.

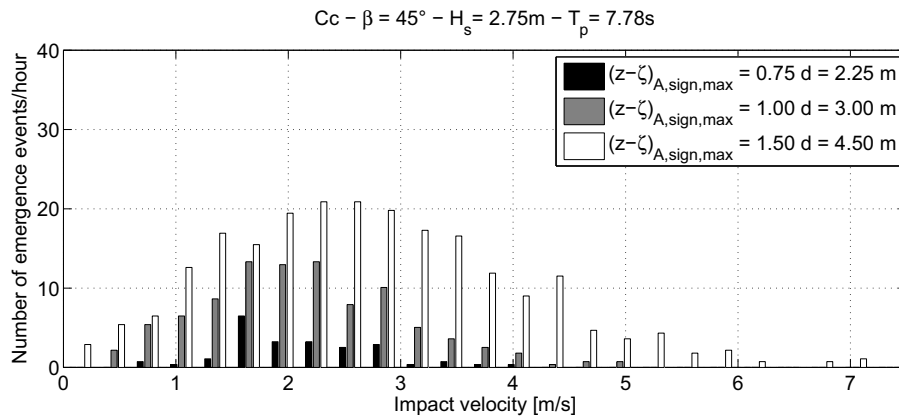
Long crested waves are generated with a duration of 10 000 s. This duration is considered to be long enough to study slamming phenomena. It contains 2011 waves for the first sea state, 1510 waves for the second sea state and 1333 waves for the third sea state. The impact velocity, when the body re-enters the water surface, has been determined as well as the number of emergences per hour. In marine hydrodynamics it is convenient to consider a minimum relative impact velocity to determine slamming occurrence probabilities. This threshold velocity is based on the impact pressures and forces. A general threshold velocity has not been considered in this case, since the impact loads are very dependent on the point absorber shapes. Therefore, the probability of emergence has been determined, i.e. the chance on rising out of the water, rather than the slamming probability.

The peak load is derived for each shape from the impact velocity based on the expressions in Section 6.2.2 of Chapter 6. Eq. (6.4) by Shiffman and Spencer [7] has been used for the conical shape and Eq. (6.7) by Miloh for the hemisphere [8].

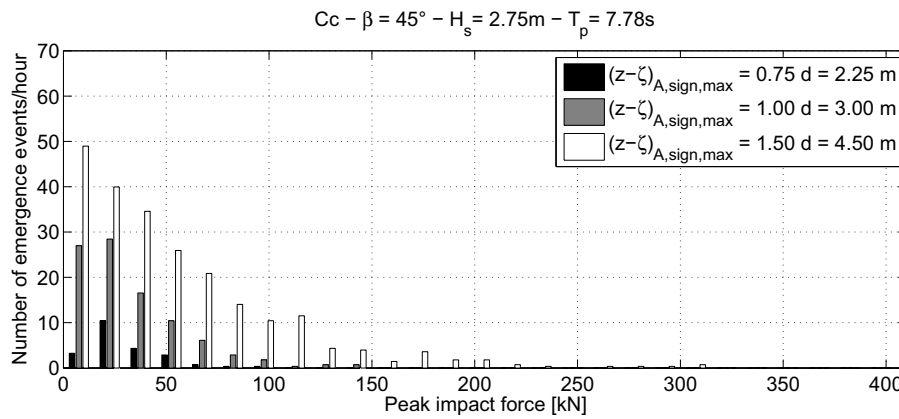
Attention should be drawn to the fact that the assumptions behind linear theory (small waves and small body motions) are violated in cases where the buoy leaves the water. However, in irregular waves, the correspondence between linear theory and experiments is still satisfactory when the buoy is operating outside the resonance zone (Chapter 4 and [9]). Since this is generally the case, the linear model can be used in an acceptable way to predict the occurrence probability of emergence and to estimate the impact velocities of the buoy. To obtain more accurate results on the impact velocities, the use of a non-linear time domain model is advised for future work, especially from the point of the body mechanics rather than for the wave mechanics.

Figure 8.7(a) shows the number of emergence events per hour for the three slamming restrictions as a function of the impact velocity. These results are obtained from simulations with the 45° cone-cylinder shape ($cc - \beta = 45^\circ$)

in the second sea state ($H_s = 2.75 \text{ m} - T_p = 7.78 \text{ s}$). The contribution of the velocity of the surface elevation to the impact velocity is neglected in these calculations. Hence, the impact velocity is approximated with the buoy velocity at re-entry. An enormous difference between the restrictions



(a) Number of emergence events per hour as a function of the impact velocity.



(b) Number of emergence events per hour as a function of the peak impact force.

Figure 8.7: Shape: 45° cone, sea state: $H_s = 2.75 \text{ m}$, $T_p = 7.78 \text{ s}$.

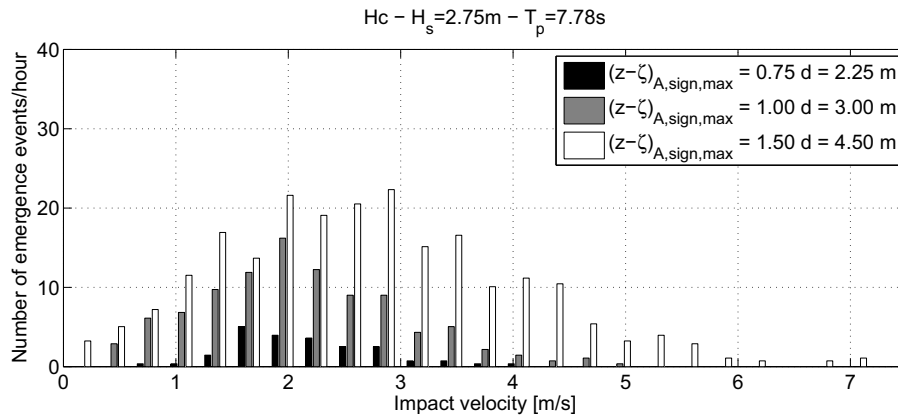
is observed both in the number of emergences and in the magnitude of the impact velocity. The emergence occurrence probability is defined as the number of emergence events divided by the number of waves in the wavetrain. Figure 8.7(b) gives the hourly number of emergences as a function of the peak

impact force corresponding with the estimated impact velocities, according to Eq. (6.4). The influence of the slamming restrictions is even more pronounced for the impact forces, since a quadratic relationship exists between the impact velocity and peak impact force. However, most of the emergences occur still with relatively small peak impact forces for the 45° cone.

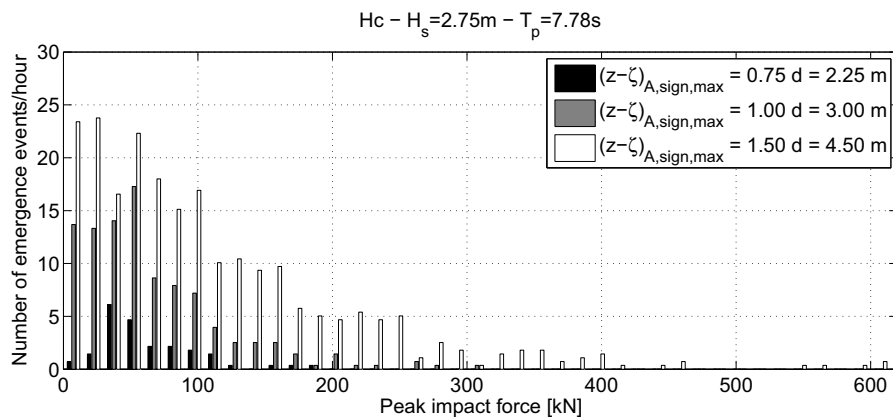
The results for the third sea state are similar as those for the second sea state, since the same level of slamming is allowed by applying the same restrictions. However, the power losses involved to fulfill these restrictions are much larger for the third sea state than for the second sea state, as can be seen by comparing the power plots of Figure 8.2 and Figure 8.4.

In Figures 8.8(a) and 8.8(b) the distribution of the impact velocity and peak impact load, according to Eq. (6.7), is given for the hemisphere-cylinder shape (hc) in the second sea state ($H_s = 2.75$ m - $T_p = 7.78$ s). As expected, Figure 8.8(a), showing the velocity distribution of the hemisphere resembles very much Figure 8.7(a), presenting the impact velocities of the 45° cone. Consequently, also the total number of emergences per hour is almost the same in the two cases for the same α -factors. However, the distribution of the peak loads is very different. For the 45° cone, most of the emergence events occur at small forces, whereas for the hemisphere the number of emergences at small impact forces is minor, compensated by a significant amount of emergences with higher impact forces. This is not surprising, since the ratio of the peak loads on the hemisphere and the 45° cone is 2.0 in this example. This kind of graphs can be used as an input for material design processes. Extreme operational load cases in energetic waves need to be simulated as well as fatigue tests in -most presumably- smaller waves with a high occurrence probability. If the occurrence probabilities of several sea states are known, e.g. derived from a scatter diagram, the yearly number of emergences and their corresponding impact forces can be calculated for the specific target location. The graphs are also useful to evaluate the control strategy with respect to slamming and adapt or optimize it where necessary taking into account the requirements from the structural designers. If the control is adapted to reduce slamming, power will be lost, but the manufacturing cost of the buoys will benefit from it and vice versa.

Figures 8.9(a) and 8.9(b) give the hourly number of emergence events as a function of the impact velocity and peak impact force, respectively, for the 30° cone in the second sea state, i.e. $H_s = 2.75$ m, $T_p = 7.78$ s. For the same α -



(a) Number of emergence events per hour as a function of the impact velocity.



(b) Number of emergence events per hour as a function of the peak impact force.

Figure 8.8: Shape: hemisphere, sea state: $H_s = 2.75\text{ m}$, $T_p = 7.78\text{ s}$.

values as before, the impact velocities are found to be a bit smaller than those of the 45° cone. This is compensated by the larger peak forces on the 30° cone, which are approximately a factor of 1.5 larger than those on the 45° cone for the same values of the impact velocity, according to Eq. (6.4) of Shiffman and Spencer.

It should be reminded that applying the same α -values in the formulation of the constraints, implies much stricter slamming constraints for the 30° cone, because its draft is considerably smaller. When the relative significant

amplitude of the 30° cone is limited to the same values as the 45° cone and hemisphere, then emergence will obviously occur a lot more for the 30° cone due to its small submergence. This is illustrated in Figures 8.9(a) and 8.9(b) with the extra bars coloured in pale gray. They represent a restriction on the relative significant buoy amplitude of $2.30 d = 4.47$ m. This limitation corresponds approximately with the constraint of the white bars in Figures 8.7(a) - 8.8(b). Similarly, the white bars of Figures 8.9(a) and 8.9(b) can be compared with the dark gray bars of Figures 8.7(a) - 8.8(b), as the restriction on the relative significant amplitude is 2.92 m and 3.00 m, respectively. The difference is huge between the response of the 30° cone and the two other shapes, both concerning number of emergences and impact velocity. For the least restrictive constraint on the 30° cone, i.e. $((z - \zeta)_{A,sign} \leq 2.30 d)$, the number of emergence events per hour has risen to an enormous value of 342, which is equivalent to an emergence occurrence probability of 63.0 %. Suchlike situations should be avoided by tuning the buoy away from resonance, i.e. by decreasing the supplementary mass and increasing the external damping. For comparison, with the most stringent constraint ($\alpha = 0.75$) the buoy rises out of the water only 17 times per hour, corresponding to an occurrence probability of 3.1 %. With the intermediate constraint ($\alpha = 1.00$) the buoy loses contact with the water surface approximately 86 times per hour, corresponding to an occurrence probability of almost 15.8 %. In both cases the impact velocities are relatively small compared to the weaker constraints, as illustrated in Figure 8.9(a). For $\alpha = 1.50$, the buoy releases the water about 230 times per hour, which gives a high occurrence probability of 42.2 %. Assuming the buoy responses are Rayleigh distributed, the occurrence probabilities would be 2.9 %, 13.5 % and 41.1 %, respectively, which is close to the calculated figures.

These numbers show that the implementation of slamming constraints can significantly reduce the occurrence probability of slamming. For a constraint with $\alpha = 0.75$ compared to $\alpha = 1.50$, the number of emergences is reduced by a factor of 14, whereas the power absorption by the 30° cone is only decreased with 43 % and 48 % for the intermediate and energetic sea states, respectively. For the same constraints applied to the hemisphere and 45° cone, the power absorption is even only reduced with 30 % and 43 % for the same respective sea states.

It has been shown that a buoy which is controlled according to very weak

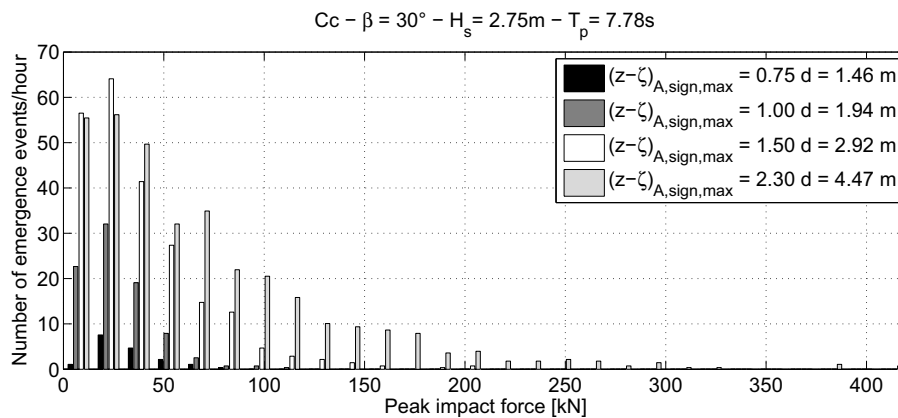
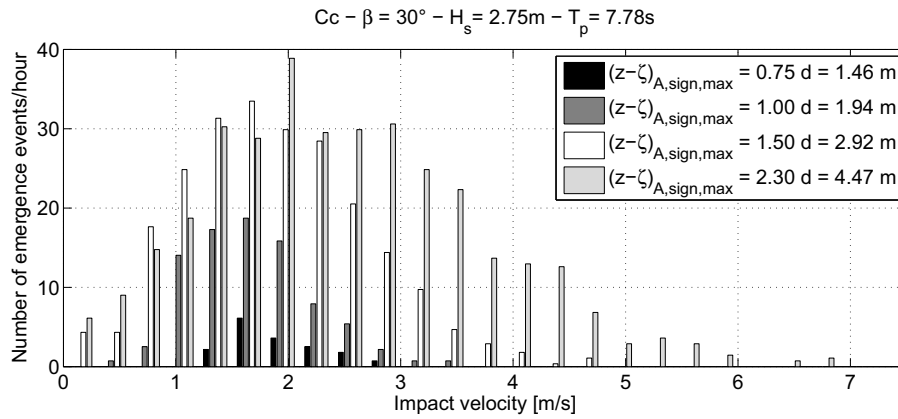


Figure 8.9: Shape: 30° cone, sea state: $H_s = 2.75$ m, $T_p = 7.78$ s.

constraints (e.g. $\alpha = 2.30$) is subjected to excessive slamming. Apart from slamming, there are other reasons why these control situations should be avoided. One of these reasons is the large buoy motions that are associated with this case. In fact, for practicality, many devices have limitations on the maximum stroke of the buoy. For $\alpha = 2.30$, the significant amplitude of the buoy motion is 4.9 m, which is very large, especially compared to the incident wave height ($H_s = 2.75$ m). Another problem is the very large tuning forces that are required to obtain this tuning. The significant amplitude of the required

tuning force is 775 kN compared to 117 kN for the damping force to enable power extraction. Depending on how this tuning force needs to be effectuated, e.g. by the generator, it might lead to a very uneconomic solution, as discussed before.

Note again that the reliability of the model can be questioned for the case, where the buoy operates very close to resonance. Nevertheless, the conclusion remains that a suchlike situation is unrealistic and will never be aimed for. Also the restriction where α equals 1.50, giving rise to an undesired high emergence occurrence probability of above 40 %, must be avoided in practice. Within this context it is concluded that the theoretical power absorption values for $\alpha = 1.50 - \infty$, as mentioned in Table 8.1, are not practically achievable, except for the smaller sea states where slamming seldom occurs. The most realistic constraints are the stricter constraints with α -values smaller than or equal to 1. Moreover, smaller control forces and buoy strokes need to be involved. For an α -value of 1 and sea state 2 ($H_s = 2.75$ m, $T_p = 7.78$ s), the significant amplitude of the buoy motion is 3.3 m and the significant amplitudes of the tuning and damping forces are 515 kN and 142 kN, respectively. If the α -value equals 0.75, the significant motion amplitude is 2.47 m and the significant amplitudes of the tuning and damping forces are equal to 354 kN and 154 kN, respectively. Note that the force constraints introduced in Chapter 2, required a maximum significant amplitude of the total control force of 200 kN and 100 kN, respectively. In order to reduce the power absorption penalty of the slamming constraints, it is advisable to increase the draft of the buoy, particularly if slamming is -almost- not tolerable.

8.4 Conclusion

Slamming effects are investigated for three sea states and three buoy shapes: two cones with deadrise angles of 45° and 30° and a hemisphere with a waterline diameter of 5 m. For a tuned buoy, the probability of emergence increases dramatically with increasing wave height. In very small waves the buoys may absorb the theoretically maximum power, while slamming phenomena rarely occur. In more energetic waves the floater motions become larger and the buoys rise out of the water very frequently, if they are tuned towards the dominant incident wave frequencies. The risk of slamming can be reduced by adjusting the control parameters of the buoy, i.e. the tuning

and damping force. Several levels of slamming restrictions are introduced, diminishing the occurrence probability of emergence to approximately 42 %, 16 % and 3 %. Going from the most stringent to the mildest constraint, the risk of emergence is reduced by a factor of almost 14, while the power absorption for the hemisphere and 45° cone is only reduced by 30 % to 43 % for the intermediate and energetic sea states, respectively. The probability of emergence is largely affected by the buoy draft. The same constraints reduce the power more severely for the 30° cone, having a draft of less than 2 m. Slamming constraints do not only limit the number of emergences, they also have the benefit of reducing the required buoy strokes and control forces.

High peak loads can be associated with slamming. Depending on the slamming constraints, the order of magnitude of the impact forces ranges from small values up to more than 300 kN for the considered buoys with a diameter of 5 m. These forces might ultimately lead to fatigue problems for the structures, if no measures are taken. The magnitude of these forces is significantly influenced by the buoy shape. According to the formulas by Shiffman and Spencer [10] and Miloh [8], the difference in peak loads between the 45° cone and the hemisphere is a factor of 2, whereas the difference in power absorption is only 4 to 8 %. A ratio of approximately 1.5 is found between the peak loads of the 30° and 45° cone. This illustrates the importance of considering slamming phenomena in the shape design process, apart from power absorption considerations.

To avoid problems with slamming, attention should be paid to the buoy geometry: too small drafts should be avoided as well as too small (local) deadrise angles, since small deadrise angles imply large impact pressures and forces. Further, optimal control strategies should not focus solely on power absorption, but also on emergence risks and consequences. The implementation of slamming constraints in the control strategy might be essential to reduce slamming. Slamming constraints can also be related to the buoy velocities or impact loads, instead of being based on emergence probabilities. In any case, slamming constraints are associated with power losses, and hence, the tolerable level of slamming is an economic equilibrium between power absorption profits and material costs.

Bibliography

- [1] De Backer G., Vantorre M., Frigaard P., Beels C., De Rouck J., Bottom slamming on heaving point absorber wave energy converters. submitted for publication in *Journal of Marine Science and Technology* 2009;.
- [2] Wienke J., Oumeraci H., Breaking wave impact force on a vertical and inclined slender pile - theoretical and large-scale model investigations. *Coastal Engineering* 2005;52(5):435–462.
- [3] Blommaert C., Composite floating ‘point absorbers’ for wave energy converters: survivability, design, production method and large-scale testing. Ph.D. thesis, Ghent University, Belgium, 2009.
- [4] Bjerrum A., The Wave Star Energy concept. In: 2nd International Conference on Ocean Energy, 2008.
- [5] Liu Z., Frigaard P., *Random seas*. Aalborg University, 1997.
- [6] Goda Y., *Random seas and design of maritime structures*. World Scientific Publishing Co, 2008.
- [7] Shiffman M., Spencer D., The force of impact on a cone striking a water surface. *Comm Pure Appl Math* 1951;4:379–417.
- [8] Miloh T., On the initial-stage slamming of a rigid sphere in a vertical water entry. *Applied Ocean Research* 1991;13(1):34–48.
- [9] De Backer G., Vantorre M., De Beule K., Beels C., De Rouck J., Experimental investigation of the validity of linear theory to assess the behaviour of a heaving point absorber at the Belgian Continental Shelf. In: 28th International Conference on Ocean, Offshore and Arctic Engineering, Hawaii, 2009.
- [10] Shiffman M., Spencer D., The force of impact on a sphere striking a water surface. *Appl. Math. Panel Rep.* 42 IR AMG-NYU No. 105, 1945.

CHAPTER 9

Conclusion and future research

In this thesis, several design aspects of heaving point absorbers have been investigated. The performance of single and multiple point absorbers is optimized, taking into account realistic constraints. In this Chapter, the most important findings are emphasized and possibilities for future research are suggested.

9.1 Discussion and conclusion

The behaviour of a heaving point absorber is simulated with a linear frequency and time domain model, fed by the BEM package WAMIT. The point absorber is externally controlled with a linear damping force and tuning force. The numerical models have been validated by means of experimental tests in the wave flume of Flanders Hydraulics Research. A conical and hemispherical buoy shape have been tested, both with a cylindrical upper part. The correspondence between the numerical and experimental results was good for the evaluated sea states, representing rather small waves on the Belgian Continental Shelf. The numerical results generally overestimated the experimental results with 10 % to 20 % for the conical and hemispherical shape, respectively. It is expected that this difference can be attributed to non linear effects, such as viscous losses and the non-linear behaviour of the hydrostatic restoring force, which are not included in the numerical model.

Power absorption optimization runs have been performed in irregular

waves for different geometrical parameters and several constraints, i.e. slamming, stroke and force constraints. The difference in power absorption between the two evaluated shapes is very small: the conical shape absorbs only between 4 % to 8 % more energy than the hemispherical shape. Hence, the choice between a hemispherical, a conical or an intermediate shape, with the same dimensions and inducing small viscous losses, will probably be more influenced by other aspects than its hydrodynamic performance, e.g. by the material cost, fabrication cost and the ability to withstand bottom and breaking-wave slamming.

Whereas the shape has a minor influence, the dimensions of the buoy significantly affect the power absorption. A larger diameter as well as a smaller draft result in an increased power absorption value. However, the draft of the buoy needs to be sufficiently large to avoid problems with bottom slamming. Slamming can also be avoided by implementing slamming constraints. These constraints might require to increase the buoy damping and to tune the buoy further away from resonance. Those measures reduce the probability of emergence, but have a negative impact on the power absorption. Hence, it is preferred to effectuate tuning and to provide a sufficiently large draft. The optimal buoy size is case specific, since it is determined by the wave climate and by cost considerations. For instance, the profits of increasing the diameter must be balanced against the corresponding rising costs for production as well as installation and maintenance.

If the buoy has a sufficiently large draft, stroke restrictions are found to be more stringent than slamming restrictions. They have a particular negative influence on the power absorption in more energetic sea states. Increasing the maximum stroke is, however, often practically not feasible, due to technical constraints imposed by e.g. the limited height of the frame enclosing the point absorbers or the limited height of hydraulic rams, etc. Restrictions on the control force might be relevant to consider, in case the tuning needs to be delivered by the PTO. In more energetic sea states with large periods, the tuning forces might become a multiple of the required damping forces. If these large tuning forces need to be provided by the PTO system, the design of the PTO might become uneconomic. Force restrictions can reduce the tuning force substantially, resulting in a severe drop in power absorption. Moreover, small inaccuracies in the timing of this tuning force may have drastic implications on the power absorption. It is therefore advised to consider other options to realize

the tuning yet from the initial design onward, e.g. by means of latching.

Bottom slamming phenomena have been studied in more detail by means of drop tests with small and large bodies. Impact pressures and decelerations have been measured. The pressure evolution is compared with an analytical theory based on Wagner's method, applied to axisymmetric bodies. The ratio between measured and theoretical peak levels is roughly between 1/2 and 3/4 for the small bodies made from polyurethane and is slightly larger than 1/3 for the large composite bodies. Smaller (local) deadrise angles are associated with larger peak pressures. The maximum impact pressures are significantly larger near the bottom of the hemisphere, compared to the pressures of cones with deadrise angles of 20° and 45° . Hence, the cone with apex angle 90° , corresponding to a deadrise angle of 45° , seems to be a good choice from the perspective of bottom slamming.

In practical applications, point absorbers are installed in arrays. The effect of interacting point absorbers on the design characteristics and power absorption is investigated in unidirectional, irregular waves. Due to the shadowing effect, the power absorption of an array of N closely spaced buoys is smaller than the power absorption of N isolated buoys. It has been found that the implementation of restrictions has a less drastic influence on the power absorption of an array than for a single body. The restrictions cause the front buoys to absorb less power, so more power is left for the rear buoys. The constraints have a so-called 'smoothing' effect on the power absorption, which means that the difference in absorbed power between the front and rear buoys is smaller when the restrictions are more stringent. The control parameters of the point absorbers in an array have been determined in three different ways. Applying the optimal control characteristics of a single body to an array, results clearly in a suboptimal performance of the array. This is not surprising, since the purpose is not to optimize the power absorption of a single body, but to optimize the performance of the entire array. Diagonal optimization of the control parameters is generally better, however, the best results are obtained when the control parameters of the buoys are individually optimized. On average over the considered sea states, this individual optimization leads to an increase in power absorption between 16 % and 18 % compared to diagonal optimization, for the configurations with 12 and 21 buoys, respectively. With individual tuning, the annual energy absorption at Westhinder for both configurations (with buoy diameters of 5 m

and 4 m, respectively) is estimated roughly around 1 GWh.

9.2 Recommendations for future research

9.2.1 Further improvements on the control and optimization process

In this thesis, the implemented control technique consists of a damping force proportional to the velocity and a tuning force proportional to the acceleration of the buoy. An optimal frequency-invariant damping coefficient and supplementary mass is selected for each sea state. Hence, the optimization in irregular waves leads to a somehow suboptimal result. It could be advantageous to perform the power absorption optimization for frequency-dependent functions of external damping and supplementary mass. It is expected that this would increase the power absorption, particularly in small waves where the restrictions do not affect the power absorption.

In a next step, when a particular device is to be modelled, the real power take-off behaviour of the device should be implemented, which is very likely to be non-linear. Also, the practical possibilities of control should be examined. As already briefly mentioned in Chapter 2 it could be very beneficial if the control mechanism can handle instantaneous motion restrictions. For instance, it would be meriting if the control mechanism is able to efficiently brake the floater, just before it is reaching its maximum stroke. It is very important that the control system can determine the right starting time and magnitude of the braking force, based on the motion parameters of the buoy, to avoid damage to the system. If such a control can be realized, it is expected that the negative influence of the motion restrictions could be considerably reduced. A cooperation with the electrical and control engineering sector seems to be indispensable to implement a real power take-off system and a more sophisticated control in the hydrodynamic model. Also the mooring design and its influence on the point absorber behaviour -if the point absorber system is floating- is an issue that needs to be further addressed. Involvement of the mechanical engineering sector is required as well for the structural design of the components. Hence, a multidisciplinary approach is crucial for future developments.

Furthermore, it is important to include economic considerations in the design process. Optimal design parameters, such as buoy shape, buoy

dimensions and array layout are dependent on the costs involved and hence, it is essential to take this aspect into account.

9.2.2 Further research on multiple point absorbers

The focus of multiple body studies has often been on a farm of widely spaced point absorbers. Currently, some developers have proposed devices with multiple, closely spaced point absorbers. It would be useful to study in depth the influence of the design parameters that may affect the performance of the array: i.e number of bodies, grid layout (e.g. staggered or aligned grid), interdistance between the buoys, buoy draft, shape and diameter, sea state, angle of incidence, etc. Not only unidirectional irregular waves have to be investigated, but also multidirectional waves (short-crested waves) with different spreading parameters. In a next step, it would be relevant to develop a time domain model for multiple bodies, to be able to implement real power take-off characteristics.

APPENDICES

APPENDIX A

Steady-state solution of a mass-spring-damper system

The equation of motion of a mass-spring-damper system, subjected to an external harmonic force in the direction of the degree of freedom is given by:

$$m \frac{d^2 z}{dt^2} + b_d \frac{dz}{dt} + kz = F_A \sin \omega t \quad (\text{A.1})$$

The homogeneous or transient solution was expressed as:

$$z = z_{Af} e^{-\zeta_d \omega_n t} \sin(\sqrt{1 - \zeta_d^2} \omega_n t + \beta_f) \quad (\text{A.2})$$

The particular or steady-state solution of Eq. (1.31) is of the form:

$$z = z_{As} \sin(\omega t + \beta_s) \quad (\text{A.3})$$

The amplitude z_{As} of the position and phase β_s can be found as follows: Replacing this expression for z and its derivatives with respect to time in Eq. (1.31) gives Eq. (A.4), which is valid for all values of t :

$$-m\omega^2 z_{As} \sin(\omega t + \beta_s) + b_d \omega z_{As} \cos(\omega t + \beta_s) + k z_{As} \sin(\omega t + \beta_s) = F_A \sin(\omega t) \quad (\text{A.4})$$

This equation can be rewritten as:

$$\begin{aligned}
 & -m\omega^2 z_{As} (\sin\omega t \cos\beta_s + \cos\omega t \sin\beta_s) \\
 & + b\omega z_{As} (\cos\omega t \cos\beta_s - \sin\omega t \sin\beta_s) \\
 & + k z_{As} (\sin\omega t \cos\beta_s + \cos\omega t \sin\beta_s) = F_A \sin\omega t
 \end{aligned} \tag{A.5}$$

Substituting t by $\pi/(2\omega)$ and 0 successively gives:

$$\begin{cases} -m\omega^2 z_{As} \cos\beta - b_d\omega z_{As} \sin\beta_s + k z_{As} \cos\beta_s = F_A \\ -m\omega^2 z_{As} \sin\beta_s + b_d\omega z_{As} \cos\beta_s + k z_{As} \sin\beta_s = 0 \end{cases} \tag{A.6}$$

From these equations the motion amplitude z_{As} and the phase angle β_s can be obtained:

$$z_{As} = \frac{F_A}{\left[(k - m\omega^2)^2 + (b_d\omega)^2 \right]^{1/2}} \tag{A.7}$$

and

$$\tan\beta_s = \frac{-b_d\omega}{k - m\omega^2} \tag{A.8}$$

In complex notation, the equation of motion can be formulated as:

$$-\omega^2 m \hat{z} + j\omega b_d \hat{z} + k \hat{z} = \hat{F}_{ex} \tag{A.9}$$

where \hat{z} is the complex amplitude of z , i.e. $\hat{z} = z_{As} \cdot e^{j\omega\beta_s}$.

Eq. (A.9) can be rearranged as:

$$\hat{z} = \frac{\hat{F}_{ex}}{-\omega^2 m + j\omega b_d + k} \tag{A.10}$$

which is equivalent with:

$$\hat{z} = \frac{\hat{F}_{ex}(k - \omega^2 m - j b_d \omega)}{(k - \omega^2 m)^2 + (b_d \omega)^2} \tag{A.11}$$

This is a complex number of the form $A + jB$. Determination of the amplitude and phase angle of this complex number gives the relationships in Eq. (A.7)

and (A.8), respectively.

APPENDIX B

Formulas for a floating reference case

B.1 Equation of motion

This case is simplified to one heaving point absorber located at the centre of the floating platform. Hence, only the heave motion of the platform is considered. A schematic representation is given in Figure B.1.

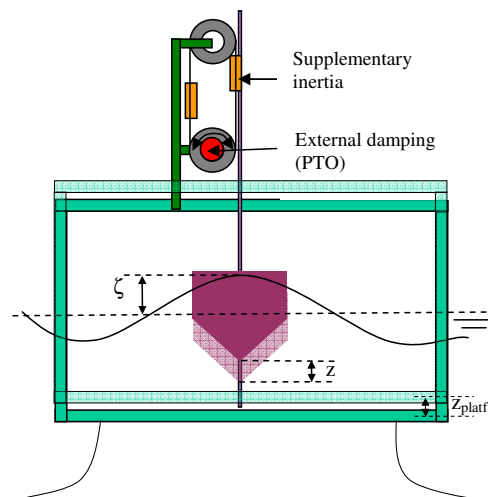


Figure B.1: Semi-submerged floating platform with a heaving point absorber.

When the point absorber oscillates with respect to a floating platform, Eq. (1.56)

describing the motion of the point absorber has to be adapted. Because the generator and the supplementary mass move together with the platform, the forces associated with the control parameters, b_{ext} and m_{sup} , are dependent on the buoy velocity relative to the platform velocity, respectively the acceleration relative to the platform acceleration. With z_{pl} denoting the position of the platform, the equation of motion can be written as:

$$(m+m_a(\omega)) \frac{d^2 z}{dt^2} + m_{sup} \left(\frac{d^2 z}{dt^2} - \frac{d^2 z_{pl}}{dt^2} \right) + b(\omega) \frac{dz}{dt} + b_{ext} \left(\frac{dz}{dt} - \frac{dz_{pl}}{dt} \right) + kz = F_{ex}(\omega) \quad (\text{B.1})$$

Rearranging of Eq. (B.1) gives:

$$(m + m_{sup} + m_a(\omega)) \frac{d^2 z}{dt^2} + (b(\omega) + b_{ext}) \frac{dz}{dt} + kz = F'_{ex}(\omega) \quad (\text{B.2})$$

with $F'_{ex} = F_{ex} + m_{sup} \cdot \frac{d^2 z_{pl}}{dt^2} + b_{ext} \cdot \frac{dz_{pl}}{dt}$

In order to find the steady state solution of the buoy motion, the amplitude, $F'_{ex,A}$, and phase shift, $\beta'_{F_{ex}}$, of F'_{ex} should be determined.

With $z_{pl} = z_{A,pl} e^{j(\omega t + \beta_{pl})}$, $F'_{ex} = F'_{ex,A} e^{j(\omega t + \beta'_{F_{ex}})}$, the complex amplitude of F'_{ex} can be expressed as:

$$\begin{aligned} \hat{F}'_{ex} &= F'_{ex,A} e^{j\beta'_{F_{ex}}} \\ &= F_{ex,A} e^{j\beta_{F_{ex}}} + j \omega b_{ext} z_{A,pl} e^{j\beta_{pl}} - \omega^2 m_{sup} z_{A,pl} e^{j\beta_{pl}} \\ &= F_{ex,A} \cos\beta_{F_{ex}} - \omega b_{ext} z_{A,pl} \sin\beta_{pl} - m_{sup} \omega^2 z_{A,pl} \cos\beta_{pl} \\ &\quad + j [F_{ex,A} \sin\beta_{F_{ex}} + \omega b_{ext} z_{A,pl} \cos\beta_{pl} - m_{sup} \omega^2 z_{A,pl} \sin\beta_{pl}] \\ &= \text{Re}(\hat{F}'_{ex}) + j \text{Im}(\hat{F}'_{ex}) \end{aligned} \quad (\text{B.3})$$

where the hat indicates the complex amplitude. The amplitude of the adjusted exciting force F'_{ex} becomes:

$$\begin{aligned}
F'_{ex,A} &= \sqrt{(\text{Re}(\hat{F}'_{ex}))^2 + (\text{Im}(\hat{F}'_{ex}))^2} \\
&= [F_{ex,A}^2 + \omega^2 z_{pl,A}^2 b_{ext}^2 \\
&\quad + \omega^4 z_{pl,A}^2 m_{sup}^2 + 2 \omega z_{pl,A} b_{ext} F_{ex,A} \sin(\beta_{F_{ex}} - \beta_{pl}) \\
&\quad - 2 \omega^2 z_{pl,A} m_{sup} F_{ex,A} \cos(\beta_{F_{ex}} - \beta_{pl})]^{\frac{1}{2}} \quad (\text{B.4})
\end{aligned}$$

and the phase angle $\beta'_{F_{ex}}$ can be computed by:

$$\beta'_{F_{ex}} = \arctan \left[\frac{F_{ex,A} \sin \beta_{F_{ex}} + \omega b_{ext} z_{A,pl} \cos \beta_{pl} - m_{sup} \omega^2 z_{A,pl} \sin \beta_{pl}}{F_{ex,A} \cos \beta_{F_{ex}} - \omega b_{ext} z_{A,pl} \sin \beta_{pl} - m_{sup} \omega^2 z_{A,pl} \cos \beta_{pl}} \right] \quad (\text{B.5})$$

In this way, the steady state solution for the buoy motion, relative to the platform becomes:

$$z_A(\omega) = \frac{F'_{ex,A}(\omega)}{\sqrt{[(k - (m + m_{sup} + m_a(\omega))) \cdot \omega^2]^2 + [(b(\omega) + b_{ext})\omega]^2}} \quad (\text{B.6})$$

$$\beta_{mot} = \beta'_{F_{ex}} - \arctan \left[\frac{(b(\omega) + b_{ext})\omega}{k - (m + m_{sup} + m_a(\omega))\omega^2} \right] \quad (\text{B.7})$$

In the same way as for a fixed platform, the significant wave amplitude can be determined.

B.2 Restrictions

B.2.1 Slamming restriction

The slamming constraint is not subjected to changes when a floating platform is considered, since it concerns a limitation on the relative motion between the floater and the free water surface. Therefore the required restriction expressed by Eq. (2.16) is still valid. The amplitude of the buoy motion relative to wave can be computed similarly as in Eq. (2.19):

$$z_{A,rel,wave} = \sqrt{(z_A \cos \beta_{mot} - A)^2 + z_A^2 \sin^2 \beta_{mot}} \quad (\text{B.8})$$

B.2.2 Stroke restriction

In case of a floating platform, the stroke restriction reduces the probability that the oscillating point absorber hits the platform. In contrast with formula (2.22), the restriction is now dependent on the platform motion. Formula (B.9) expresses that the significant value of the amplitude of the buoy motion relative to the platform motion is limited to a certain maximum value:

$$(z - z_{pl})_{A,sign} < (z - z_{pl})_{A,sign,max} \quad (\text{B.9})$$

The motion of the buoy relative to the platform is:

$$\begin{aligned} z - z_{pl} &= z_A \cos(\omega t + \beta_{mot}) - z_{pl} \cos(\omega t + \beta_{pl}) \\ (z - z_{pl})_A &= \sqrt{(z_A \cos\beta_{mot} - z_{A,pl} \cos\beta_{pl})^2 + (z_A \sin\beta_{mot} - z_{A,pl} \sin\beta_{pl})^2} \\ &= \sqrt{z_A^2 + z_{A,pl}^2 - 2 z_A z_{A,pl} \cos(\beta_{pl} - \beta_{mot})} \end{aligned} \quad (\text{B.10})$$

B.2.3 Force restriction

Both the control force and the force due to power absorption are dependent on the platform motions. The significant values of the amplitude of these forces can be calculated with:

$$F_{b_{ext},A,sign} = 2 \sqrt{\int_0^\infty b_{ext}^2 \omega^2 \left(\frac{(z - z_{pl})_A}{\zeta_A} \right)^2 S_\zeta(\omega) d\omega} \quad (\text{B.11})$$

$$F_{m_{sup},A,sign} = 2 \sqrt{\int_0^\infty m_{sup}^2 \omega^4 \left(\frac{(z - z_{pl})_A}{\zeta_A} \right)^2 S_\zeta(\omega) d\omega} \quad (\text{B.12})$$

APPENDIX C

Simulation results

Simulation results are presented for several restriction cases:

- **Constraint case 1:** Slamming constraint, no stroke nor force constraint.
- **Constraint case 2:** Slamming constraint, stroke constraint: $z_{A,sign,max} = 2.00$ m, no force constraint.
- **Constraint case 3:** Slamming constraint, stroke constraint: $z_{A,sign,max} = 2.00$ m, force constraint: $F_{tot,A,sign,max} = 200$ kN.

The graphs show the power absorption, the absorption efficiency, the significant amplitude of the buoy position, the significant amplitude of the buoy position relative to the waves divided by the buoy draft, the significant amplitude of the damping force, the significant amplitude of the tuning force and the significant amplitude of the total control force. The cone-cylinder and hemisphere-cylinder shapes are abbreviated to ‘cc’ and ‘hc’, respectively. The draft is indicated with the symbol d , followed by the magnitude of the draft expressed in meter.

C.1 Constraint case 1

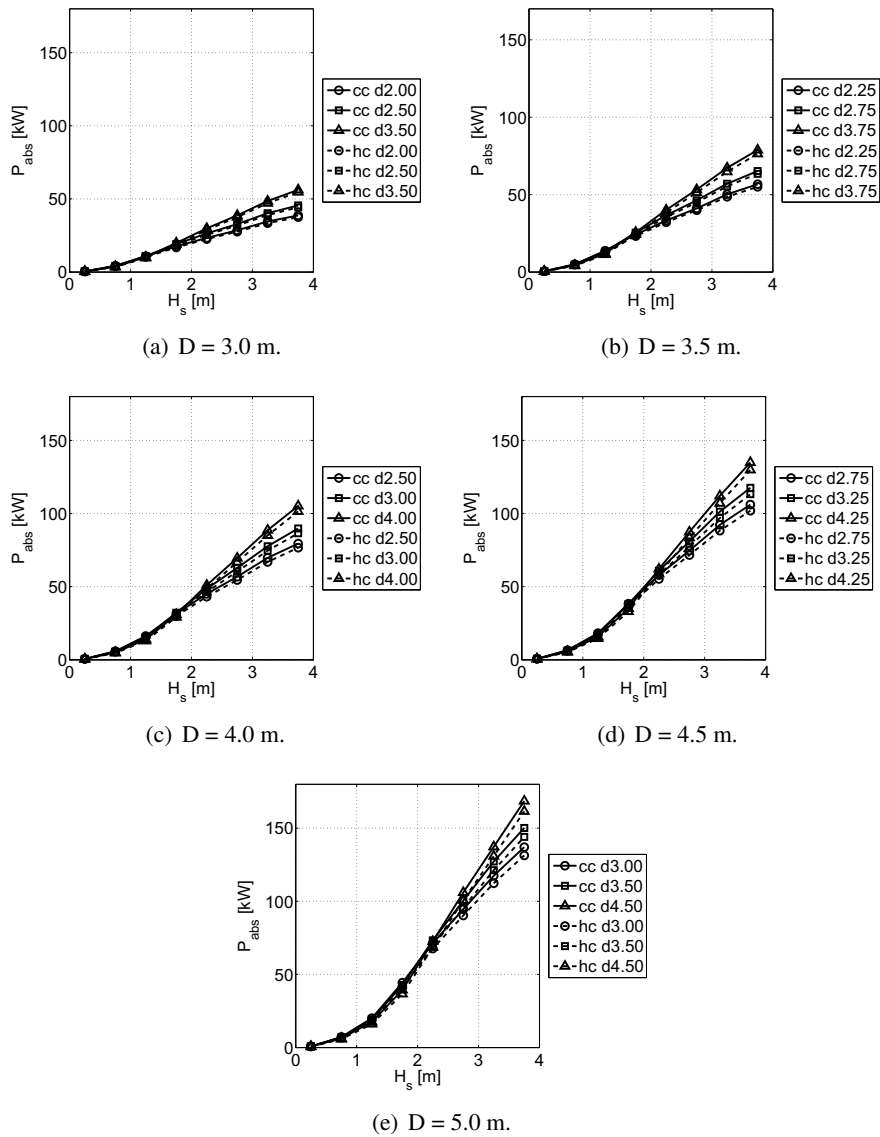


Figure C.1: Power absorption as a function of the H_s -classes defined in Table 2.1. Constraints: slamming restriction; no stroke nor force restriction.

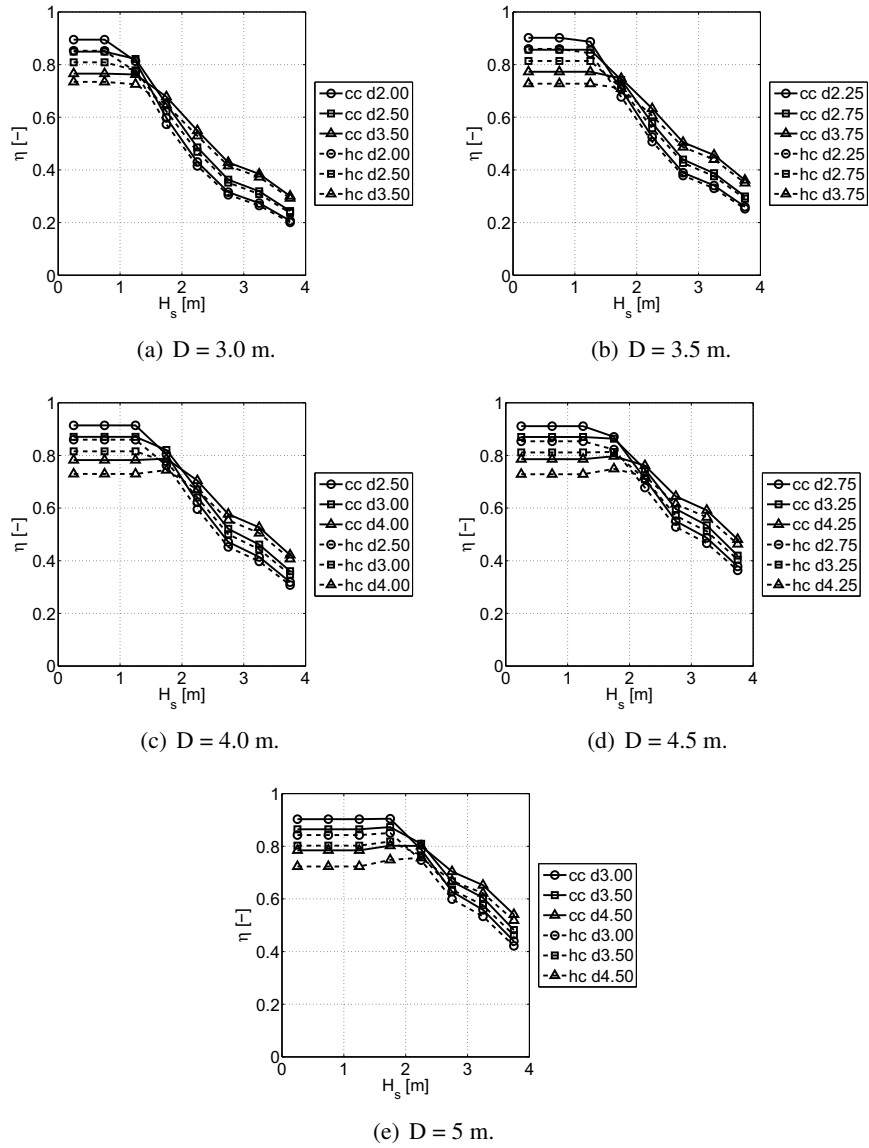


Figure C.2: Absorption efficiency as a function of the H_s -classes defined in Table 2.1. Constraints: slamming restriction; no stroke nor force restriction.

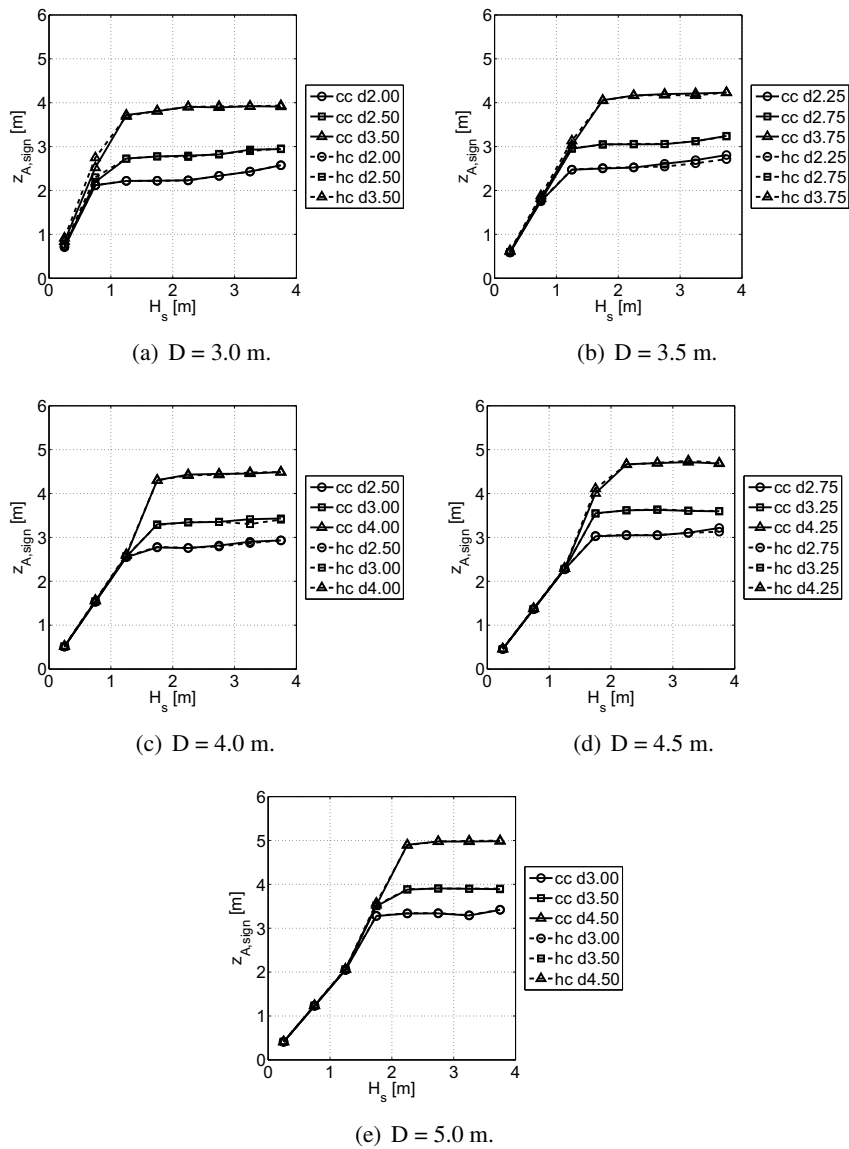


Figure C.3: Significant amplitude of the buoy position as a function of the H_s -classes defined in Table 2.1. Constraints: slamming restriction; no stroke nor force restriction.

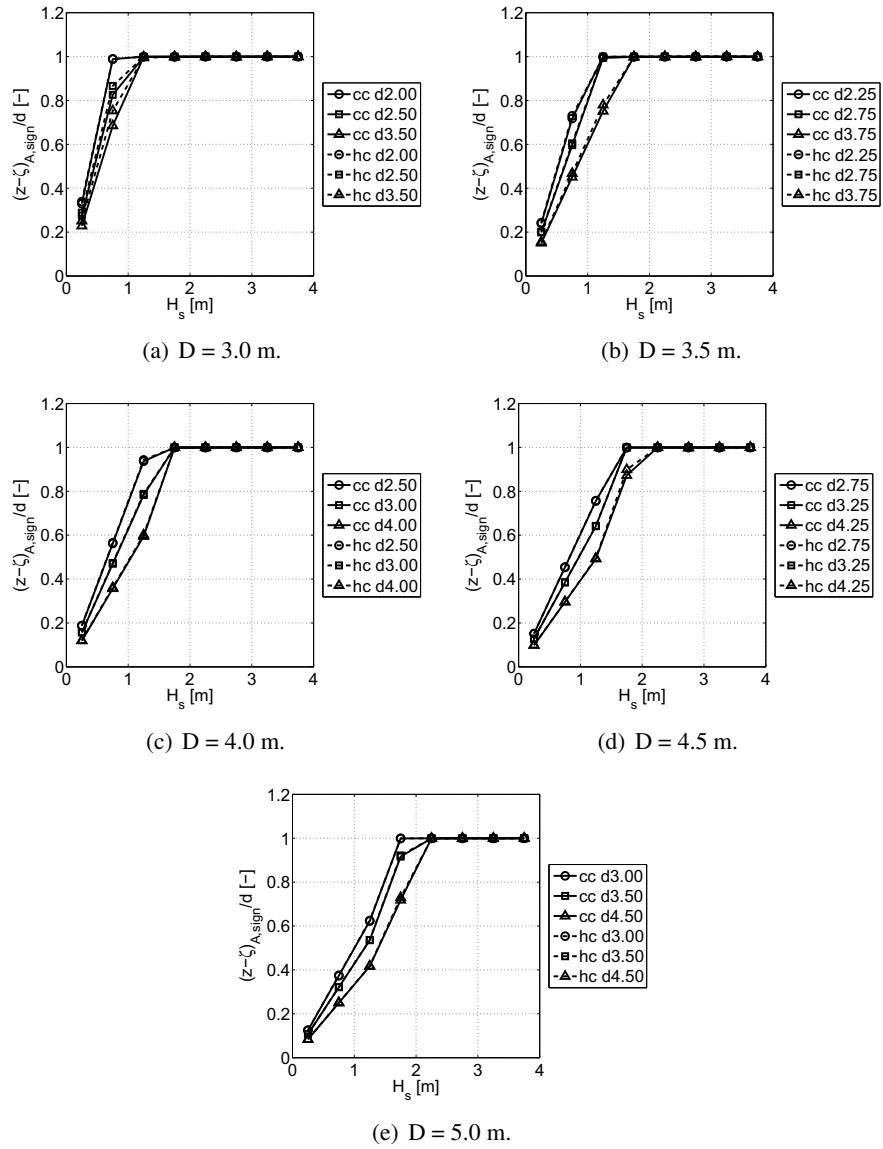


Figure C.4: Significant amplitude of the relative buoy position divided by the draft as a function of the H_s -classes defined in Table 2.1. Constraints: slamming restriction; no stroke nor force restriction.

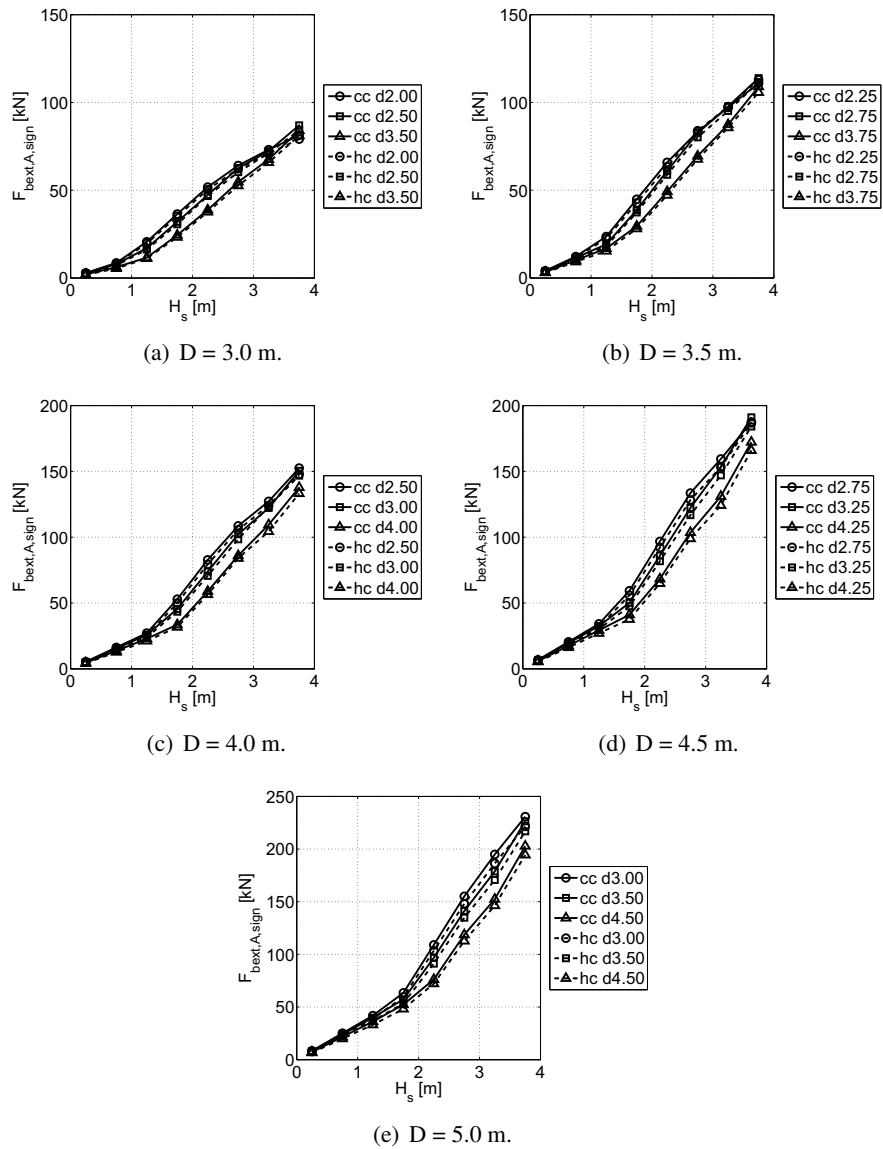


Figure C.5: Significant amplitude of the damping force as a function of the H_s -classes defined in Table 2.1. Constraints: slamming restriction; no stroke nor force restriction.

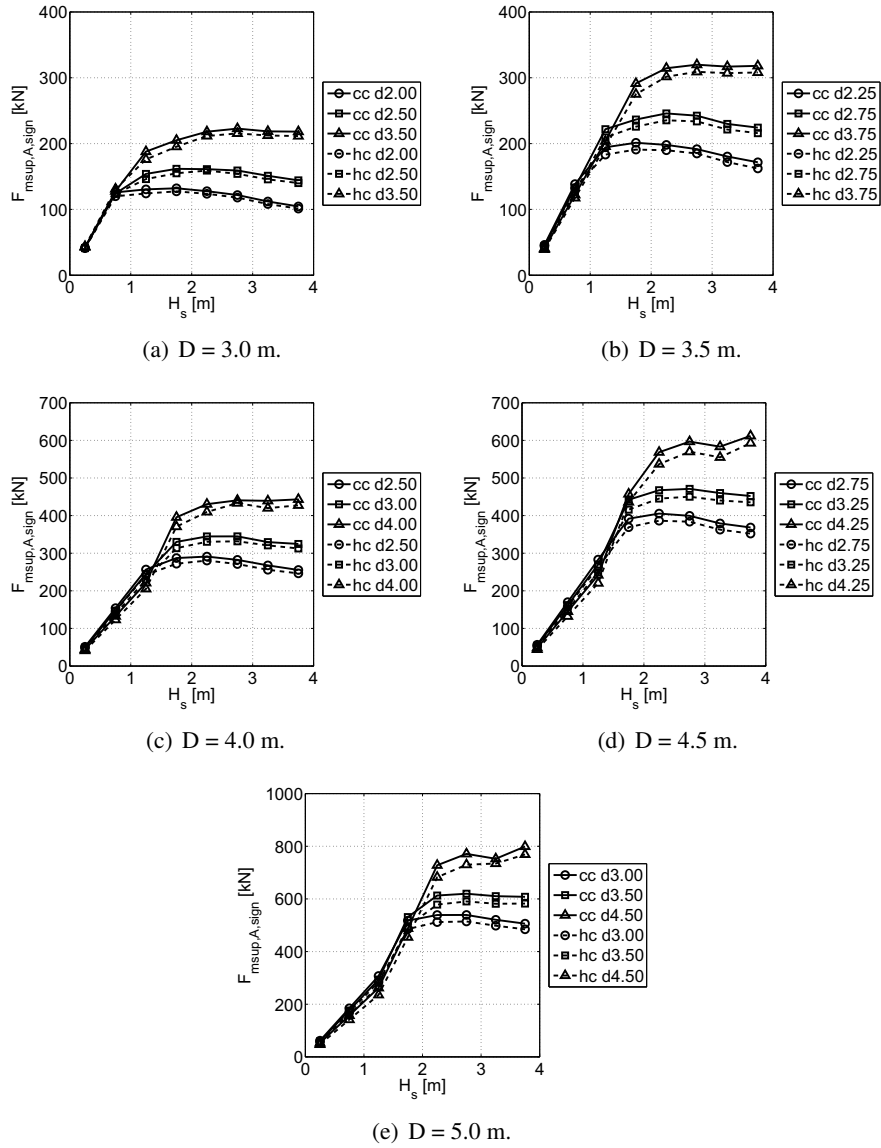


Figure C.6: Significant amplitude of tuning force as a function of the H_s -classes defined in Table 2.1. Constraints: slamming restriction; no stroke nor force restriction.

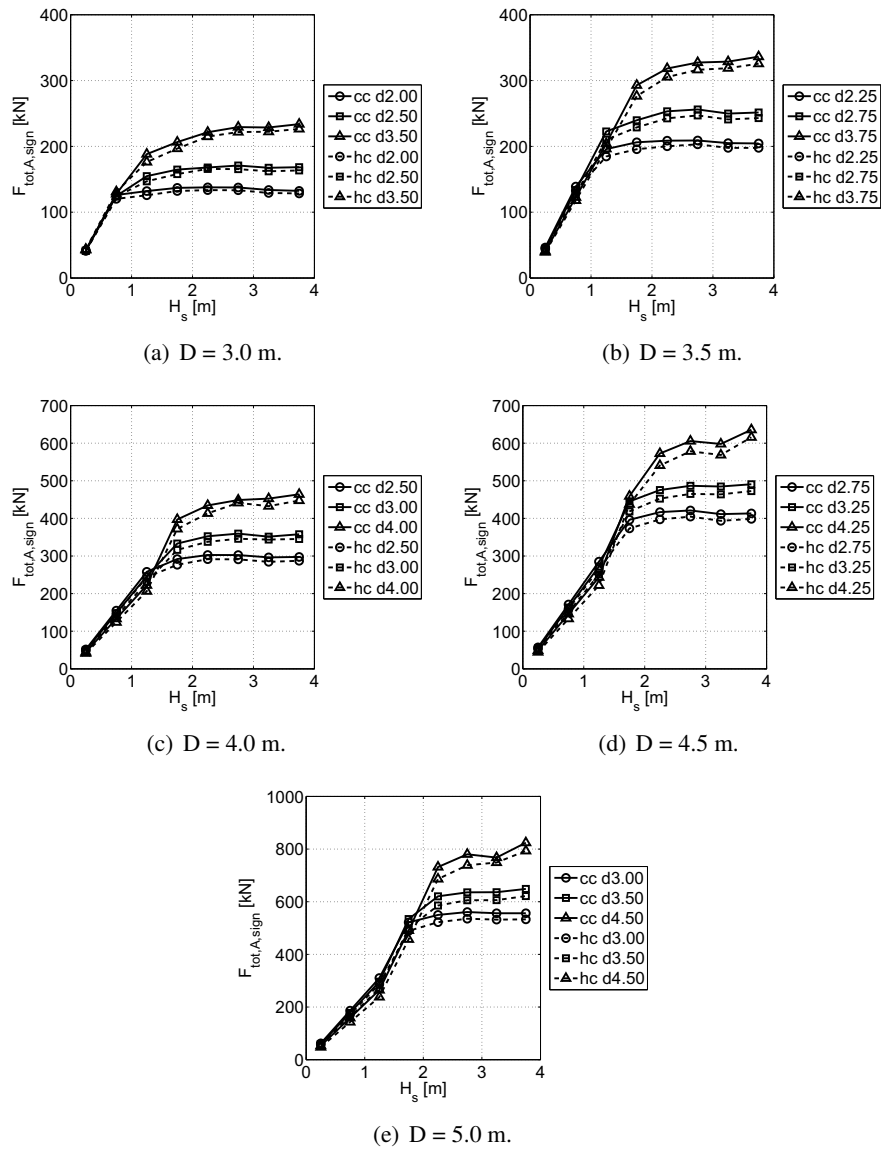


Figure C.7: Significant amplitude of the total control force as a function of the H_s -classes defined in Table 2.1. Constraints: slamming restriction; no stroke nor force restriction.

C.2 Constraint case 2

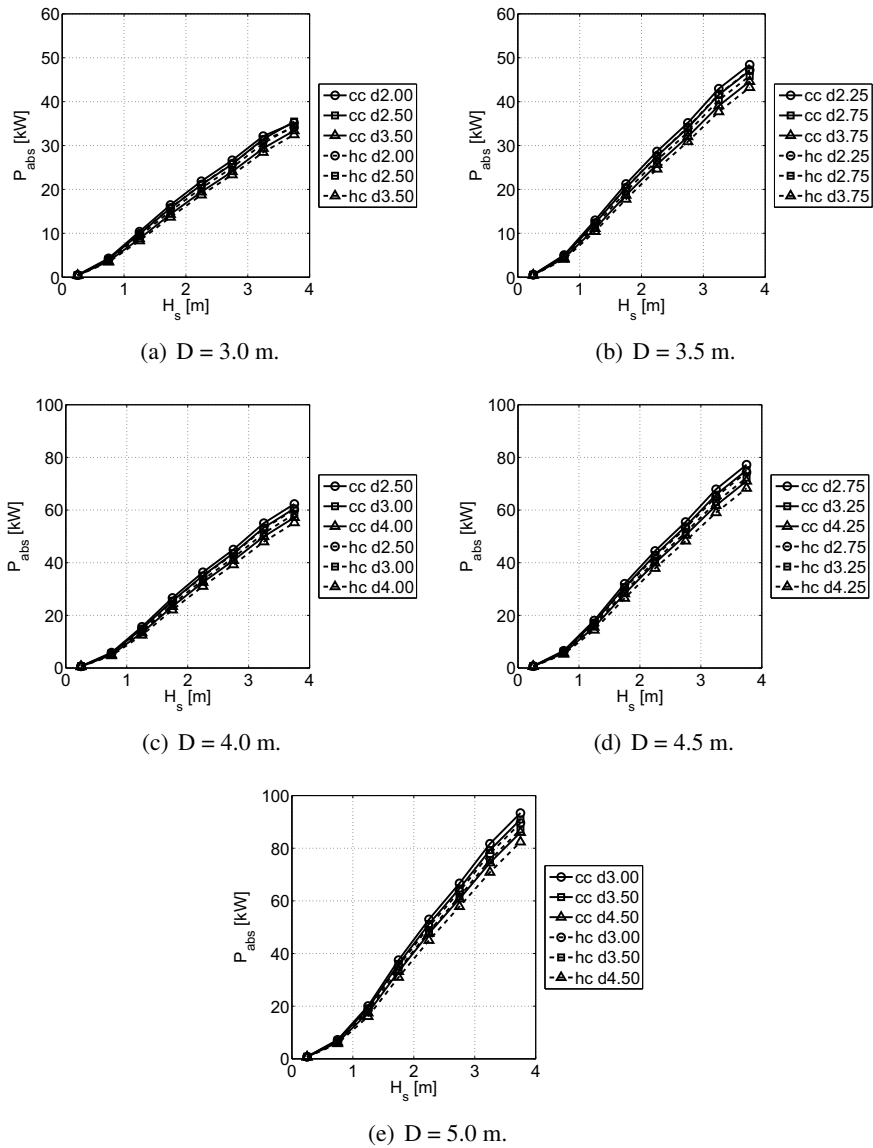


Figure C.8: Power absorption as a function of the H_s -classes defined in Table 2.1. Constraints: slamming restriction; stroke restriction: $z_{A,sign,max} = 2.00$ m; no force restriction.

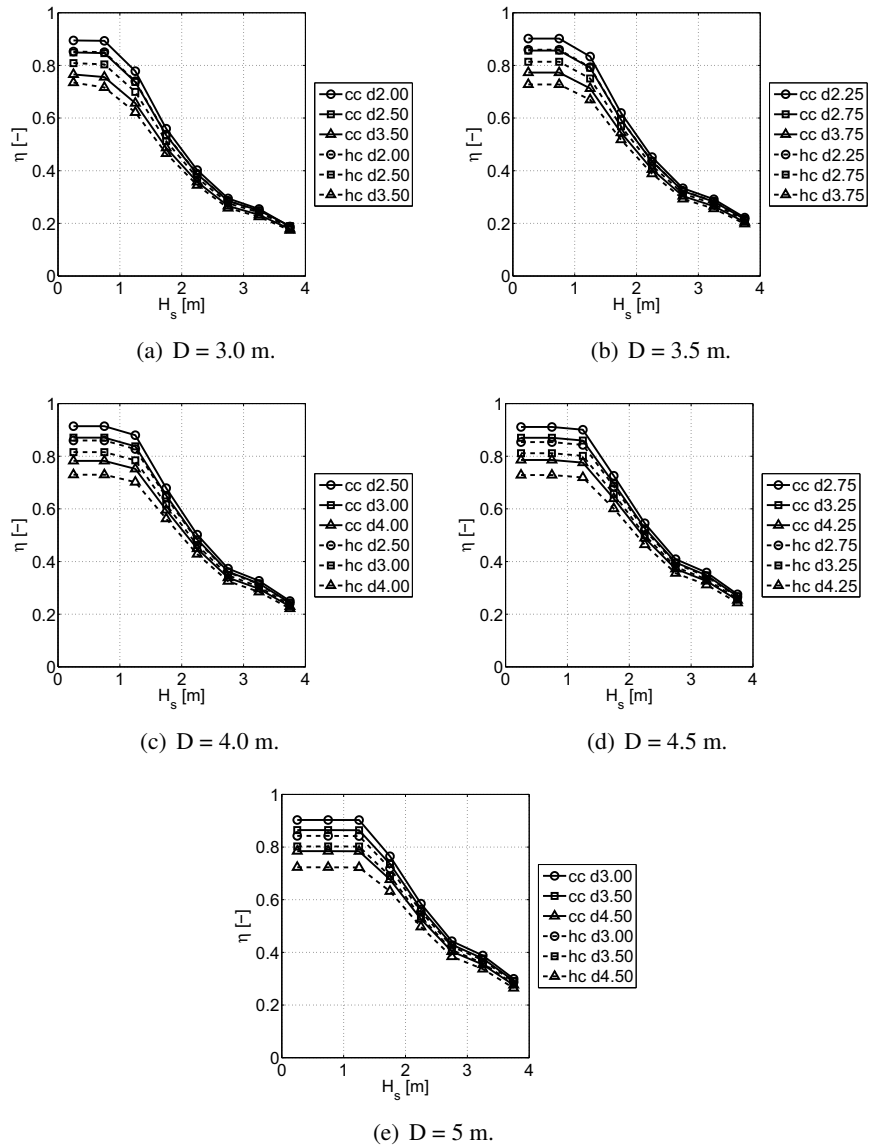


Figure C.9: Absorption efficiency as a function of the H_s -classes defined in Table 2.1. Constraints: slamming restriction; stroke restriction: $z_{A,sign,max} = 2.00$ m; no force restriction.

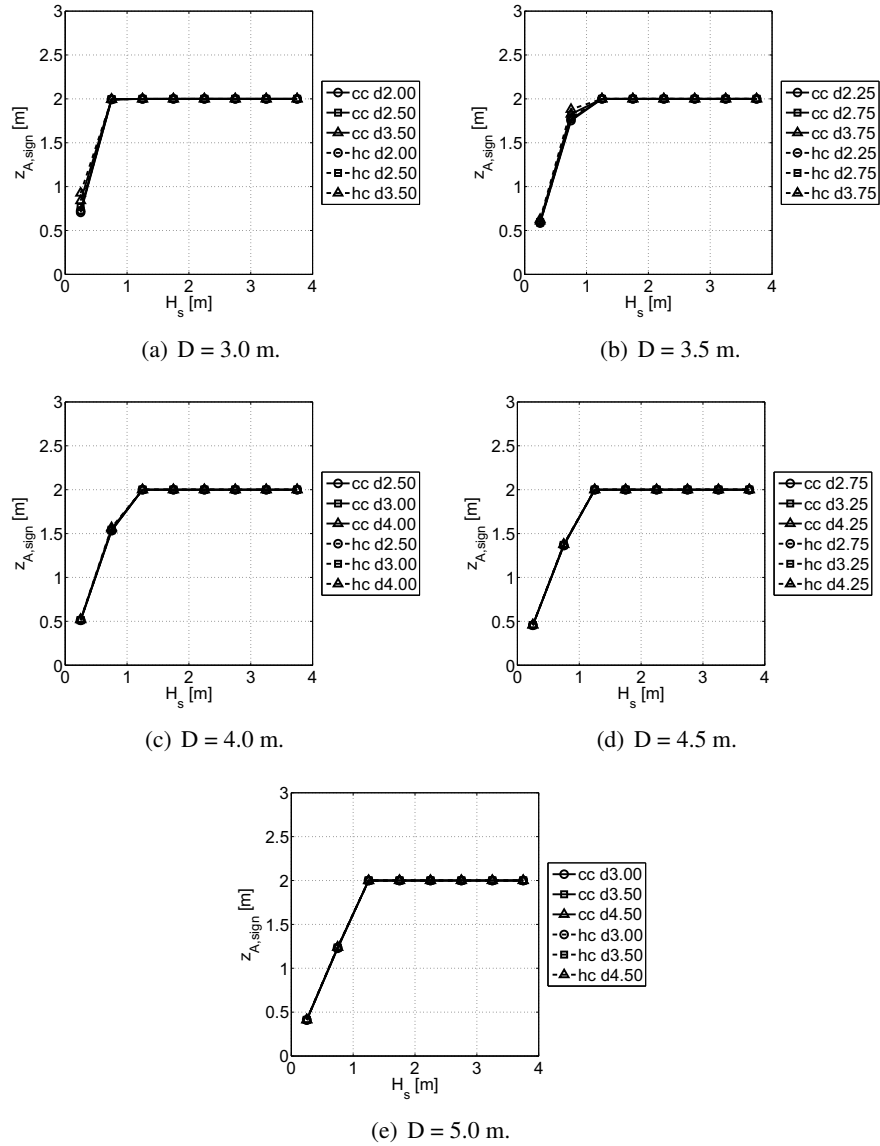


Figure C.10: Significant amplitude of the buoy position as a function of the H_s -classes defined in Table 2.1. Constraints: slamming restriction; stroke restriction: $z_{A,sign,max} = 2.00$ m; no force restriction.

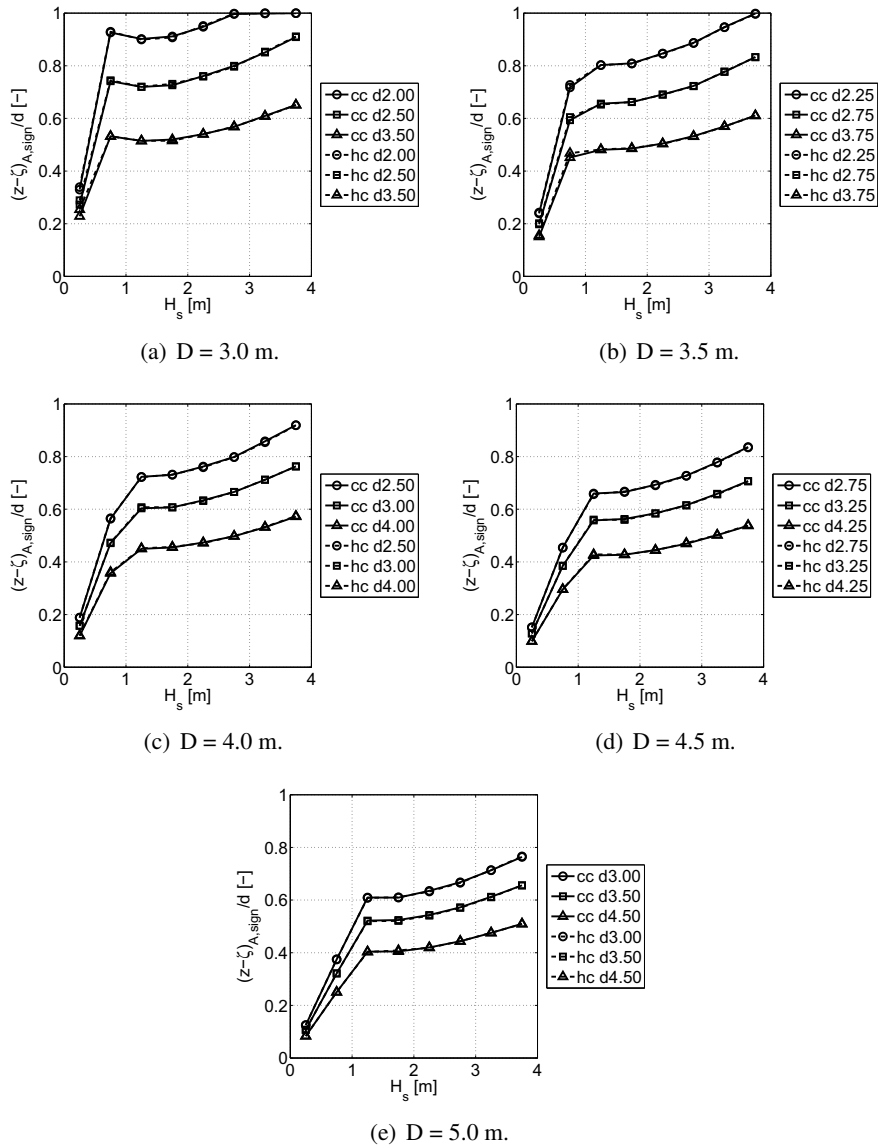


Figure C.11: Significant amplitude of the relative buoy position divided by the draft as a function of the H_s -classes defined in Table 2.1. Constraints: slamming restriction; stroke restriction: $z_{A,sign,max} = 2.00$ m; no force restriction.

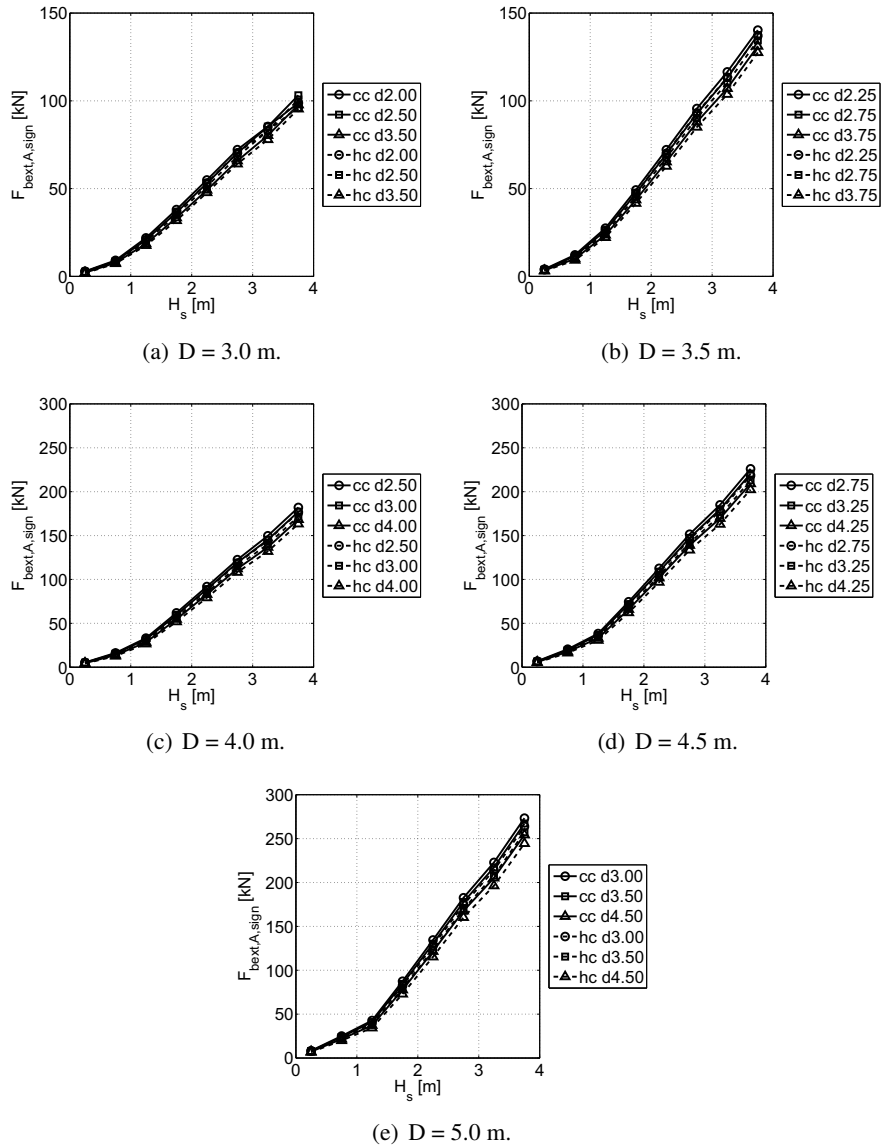


Figure C.12: Significant amplitude of the damping force as a function of the H_s -classes defined in Table 2.1. Constraints: slamming restriction; stroke restriction: $z_{A,sign,max} = 2.00$ m; no force restriction.

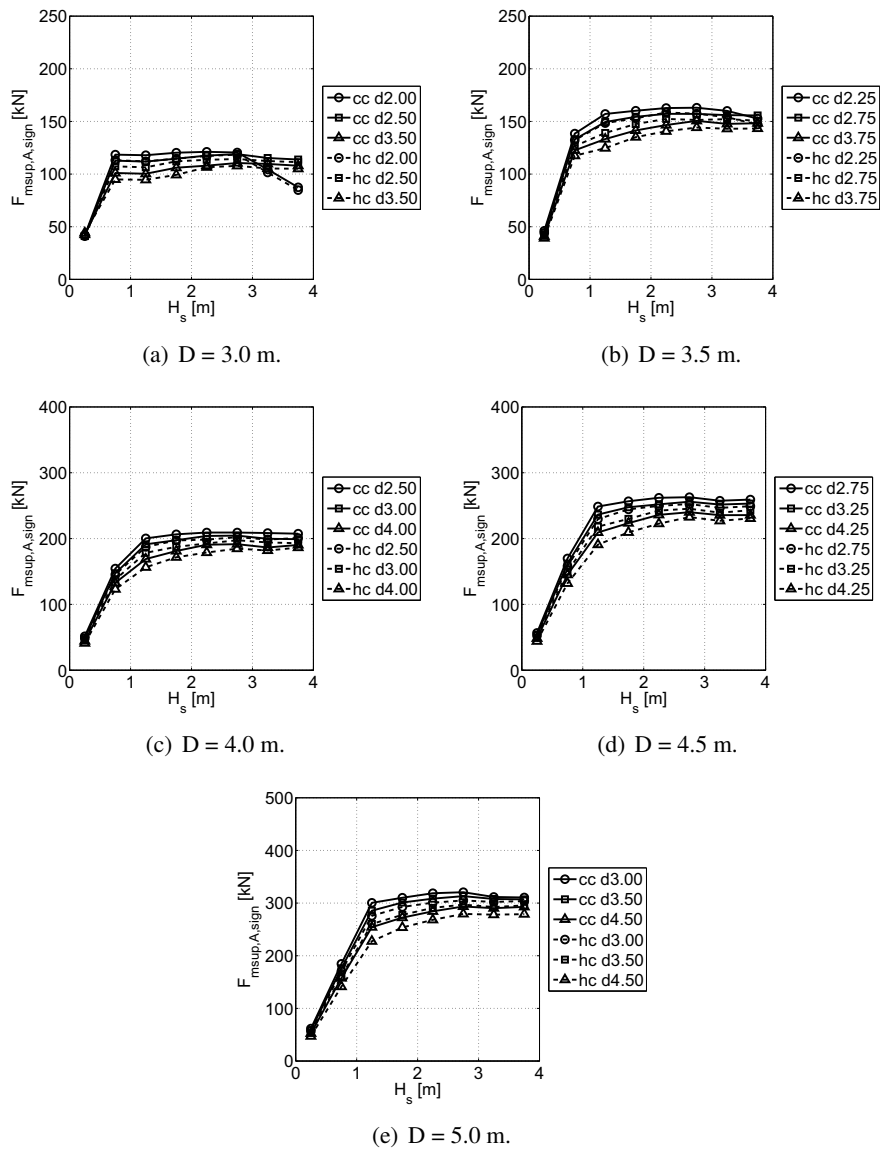


Figure C.13: Significant amplitude of tuning force as a function of the H_s -classes defined in Table 2.1. Constraints: slamming restriction; stroke restriction: $z_{A,sign,max} = 2.00$ m; no force restriction.

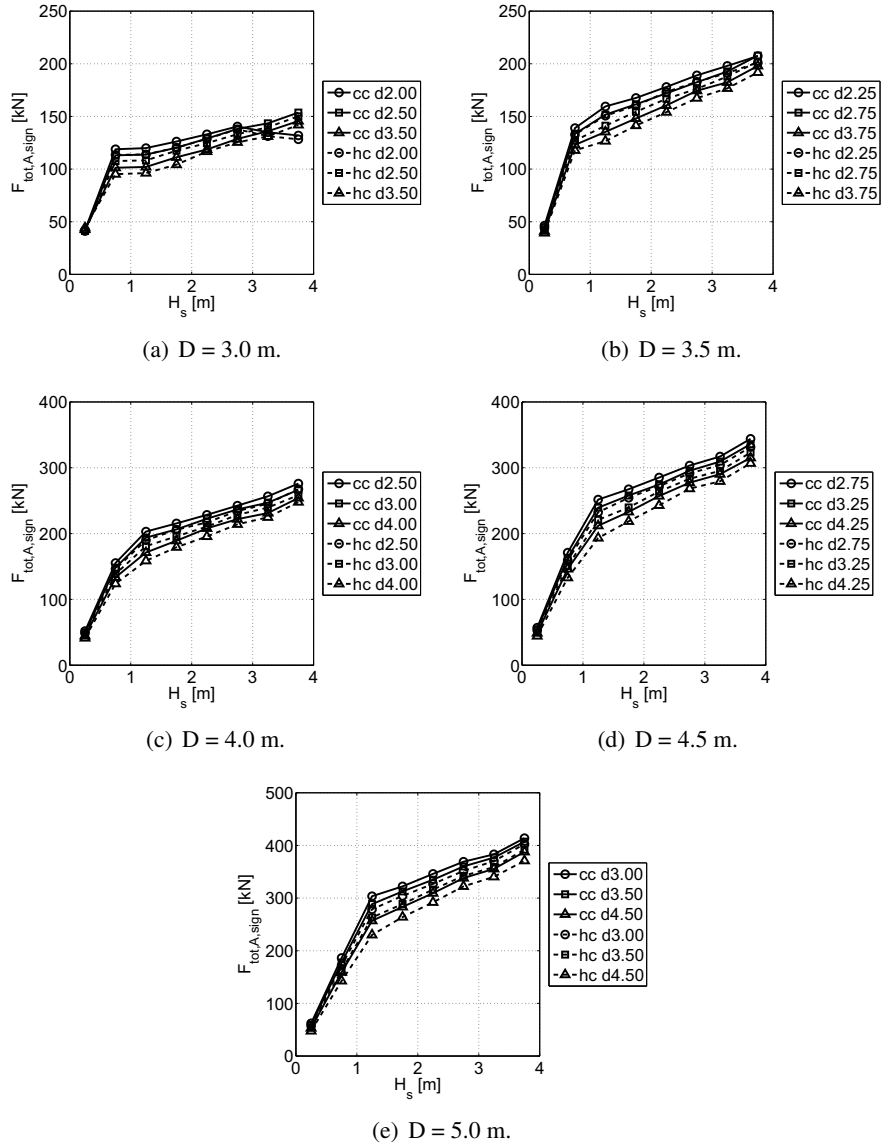


Figure C.14: Significant amplitude of the total control force as a function of the H_s -classes defined in Table 2.1. Constraints: slamming restriction; stroke restriction: $z_{A,sign,max} = 2.00$ m; no force restriction.

C.3 Constraint case 3

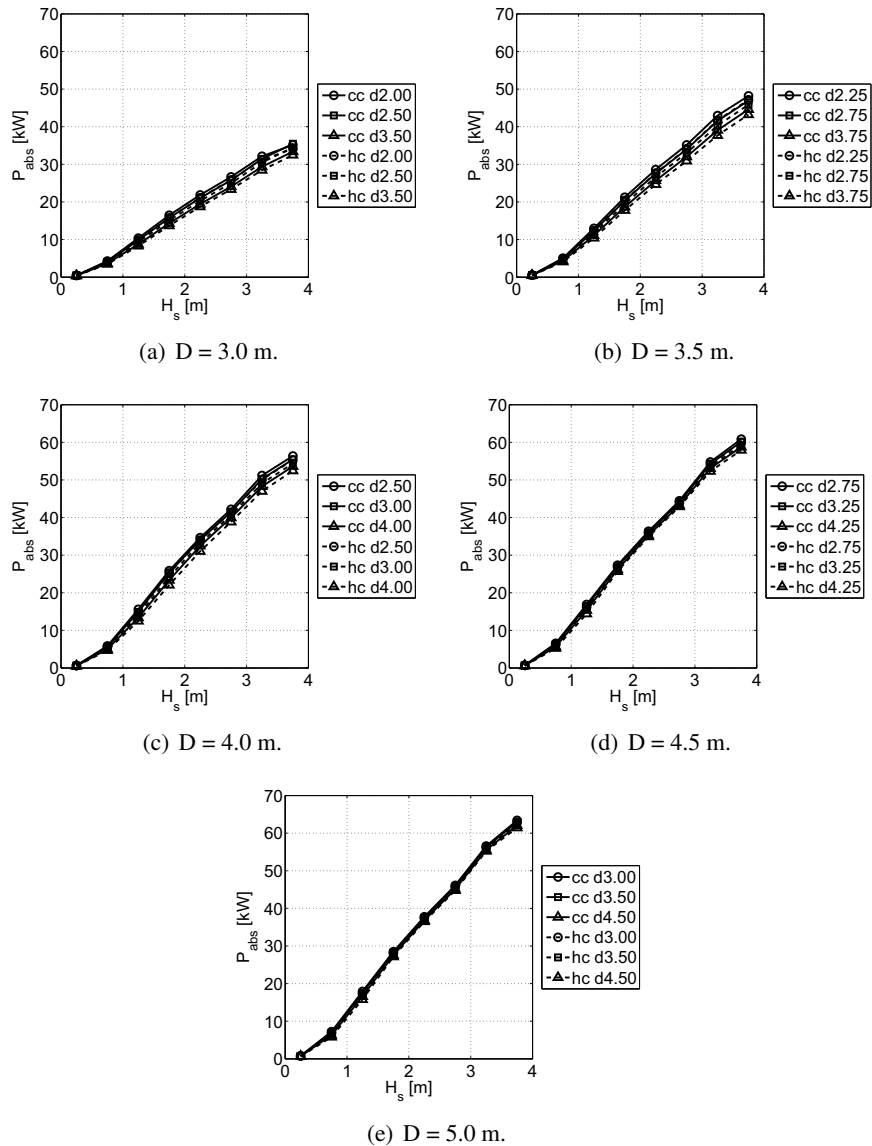


Figure C.15: Power absorption as a function of the H_s -classes defined in Table 2.1. Constraints: slamming restriction; stroke restriction: $z_{A,sign,max} = 2.00$ m; force restriction: $F_{tot,A,sign,max} = 200$ kN.

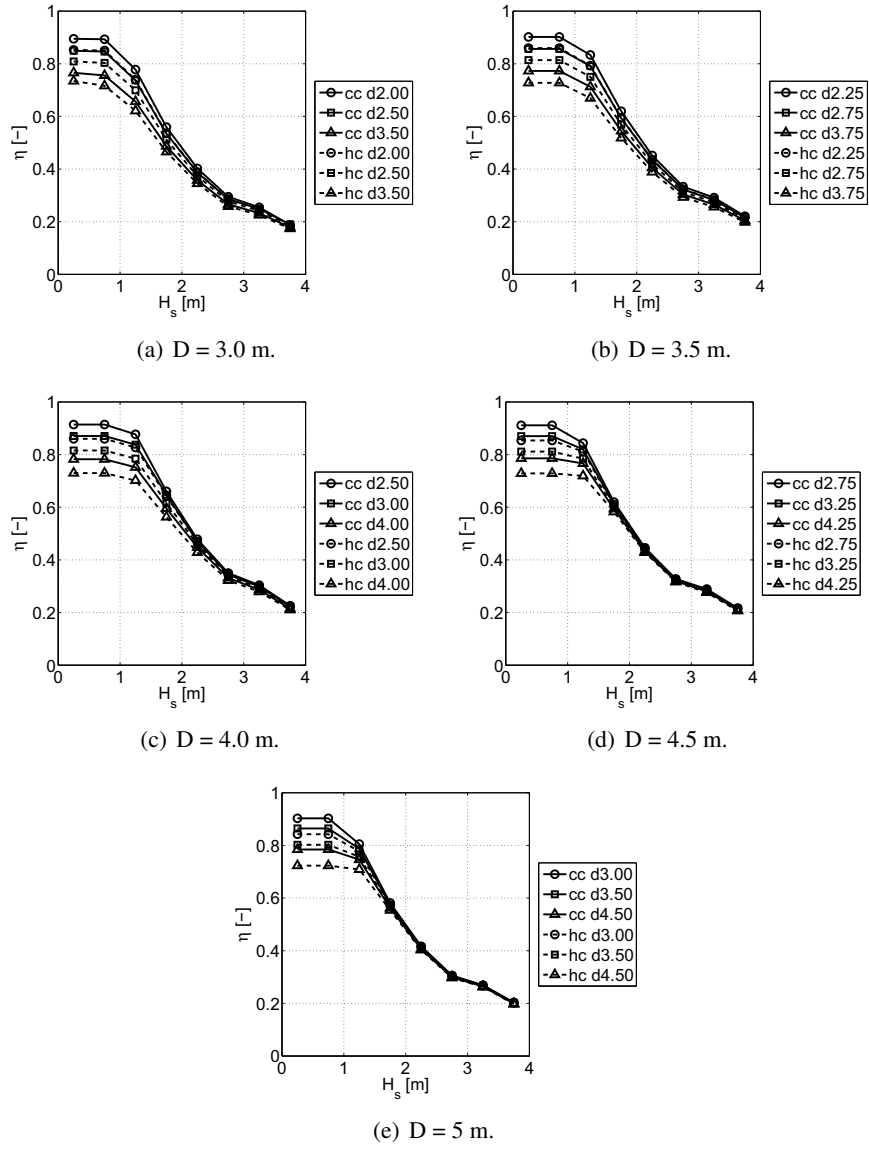


Figure C.16: Absorption efficiency as a function of the H_s -classes defined in Table 2.1. Constraints: slamming restriction; stroke restriction: $z_{A,sign,max} = 2.00\text{m}$; force restriction: $F_{tot,A,sign,max} = 200\text{ kN}$.

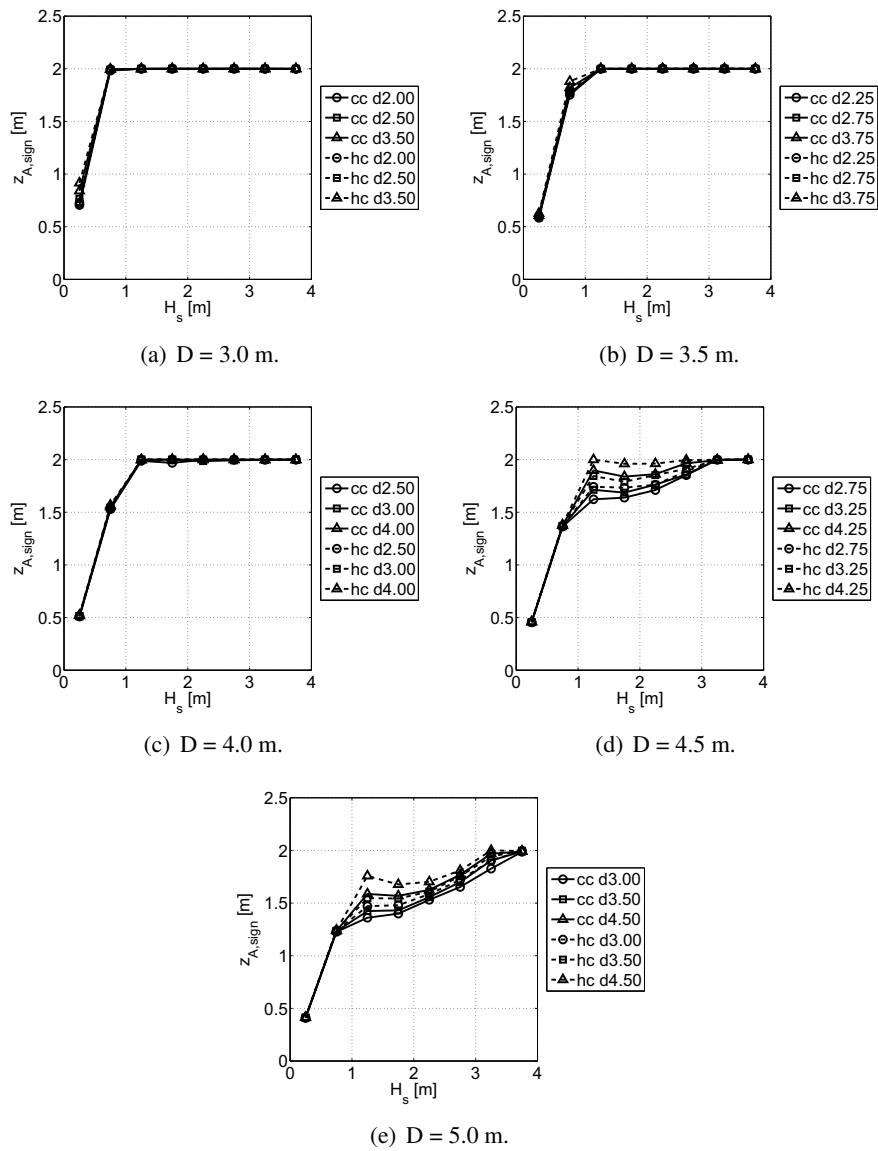


Figure C.17: Significant amplitude of the buoy position as a function of the H_s -classes defined in Table 2.1. Constraints: slamming restriction; stroke restriction: $z_{A,sign,max} = 2.00$ m; force restriction: $F_{tot,A,sign,max} = 200$ kN.

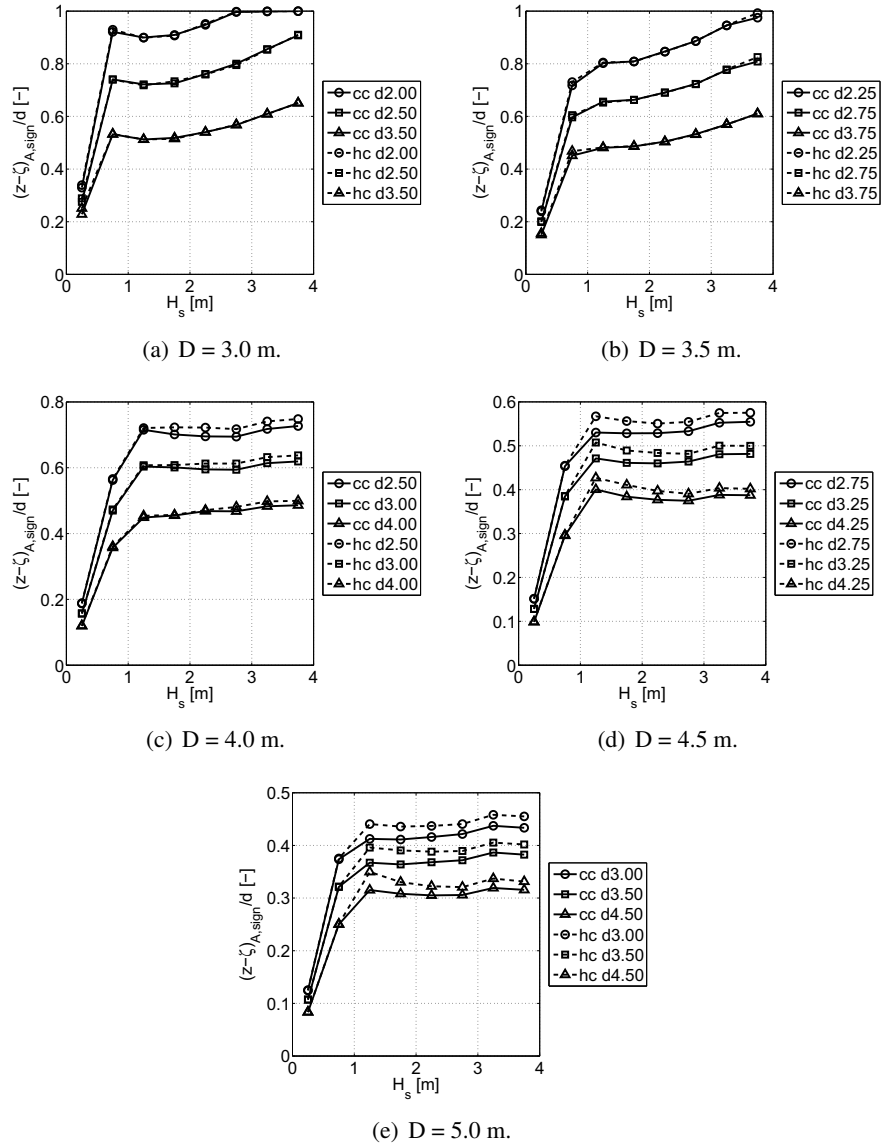


Figure C.18: Significant amplitude of the relative buoy position divided by the draft as a function of the H_s -classes defined in Table 2.1. Constraints: slamming restriction; stroke restriction: $z_{A,sign,max} = 2.00$ m; force restriction: $F_{tot,A,sign,max} = 200$ kN.

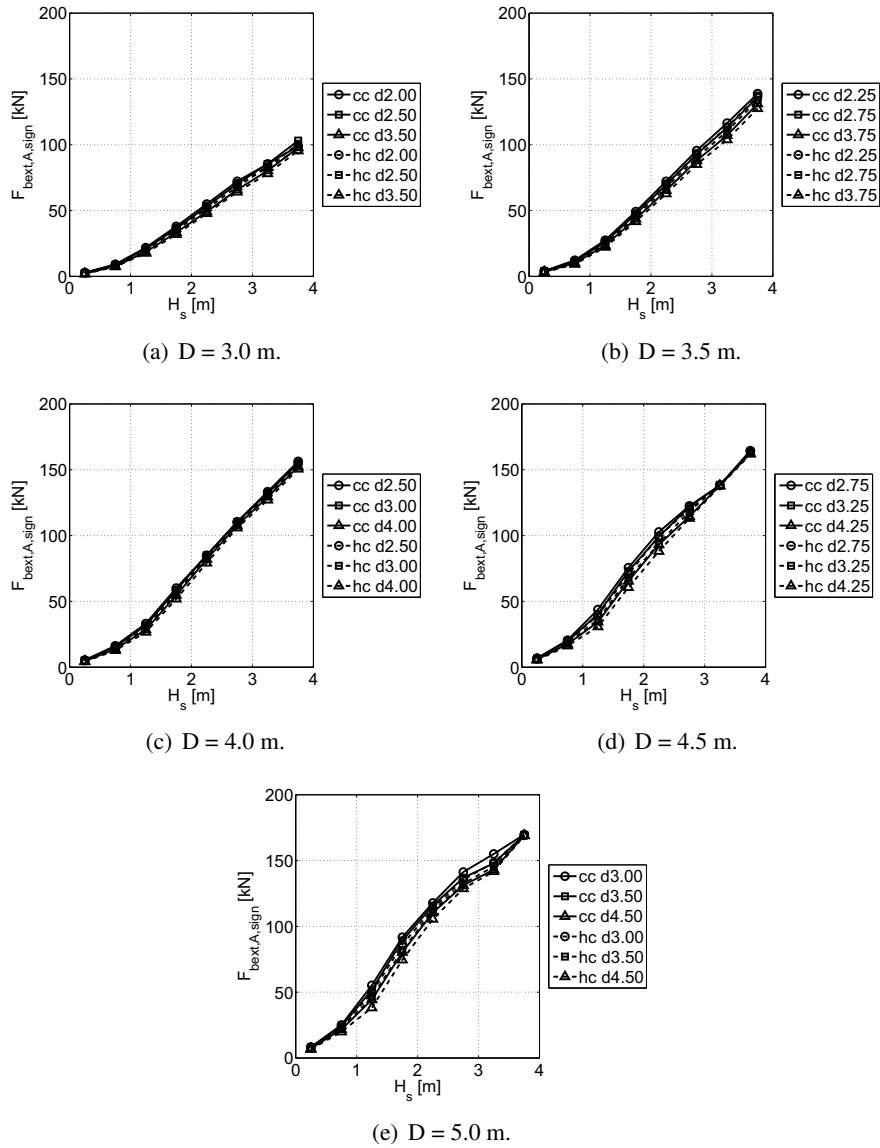


Figure C.19: Significant amplitude of the damping force as a function of the H_s -classes defined in Table 2.1. Constraints: slamming restriction; stroke restriction: $z_{A,sign,max} = 2.00$ m; force restriction: $F_{tot,A,sign,max} = 200$ kN.

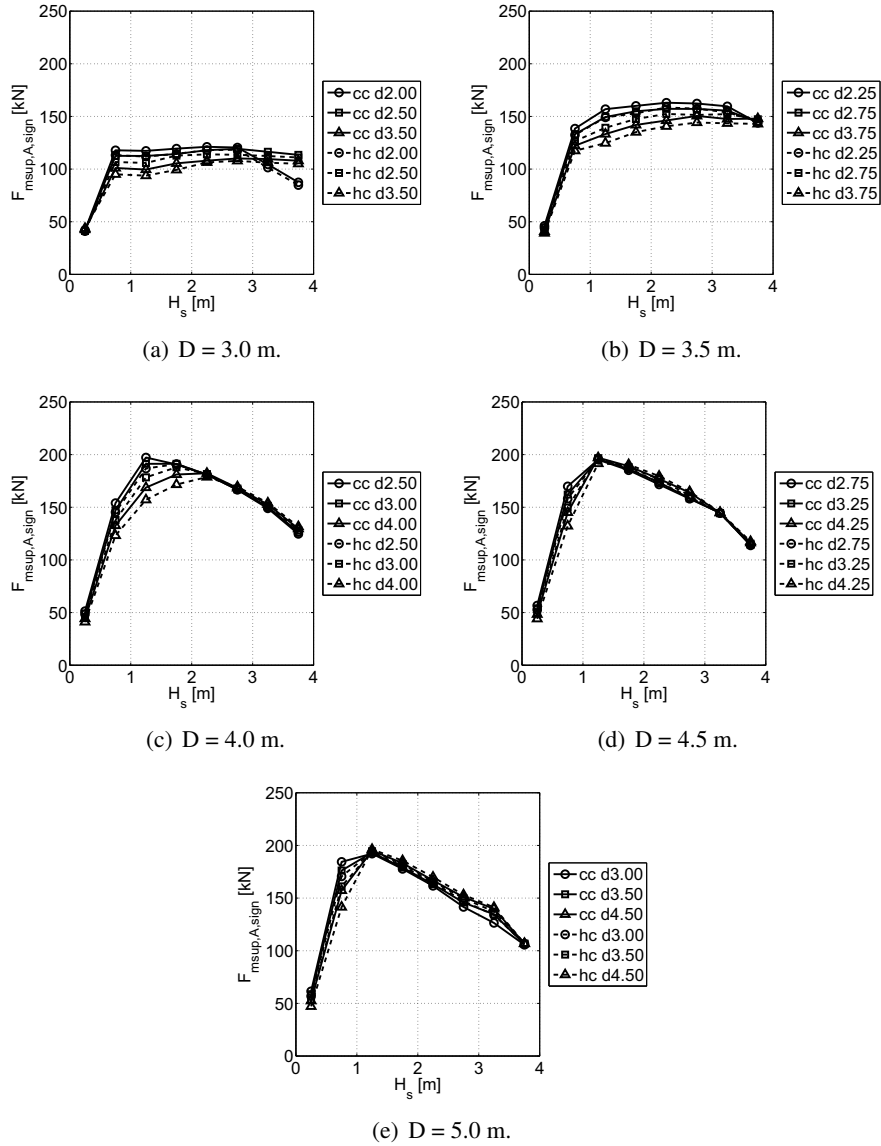


Figure C.20: Significant amplitude of tuning force as a function of the H_s -classes defined in Table 2.1. Constraints: slamming restriction; stroke restriction: $z_{A,sign,max} = 2.00$ m; force restriction: $F_{tot,A,sign,max} = 200$ kN.

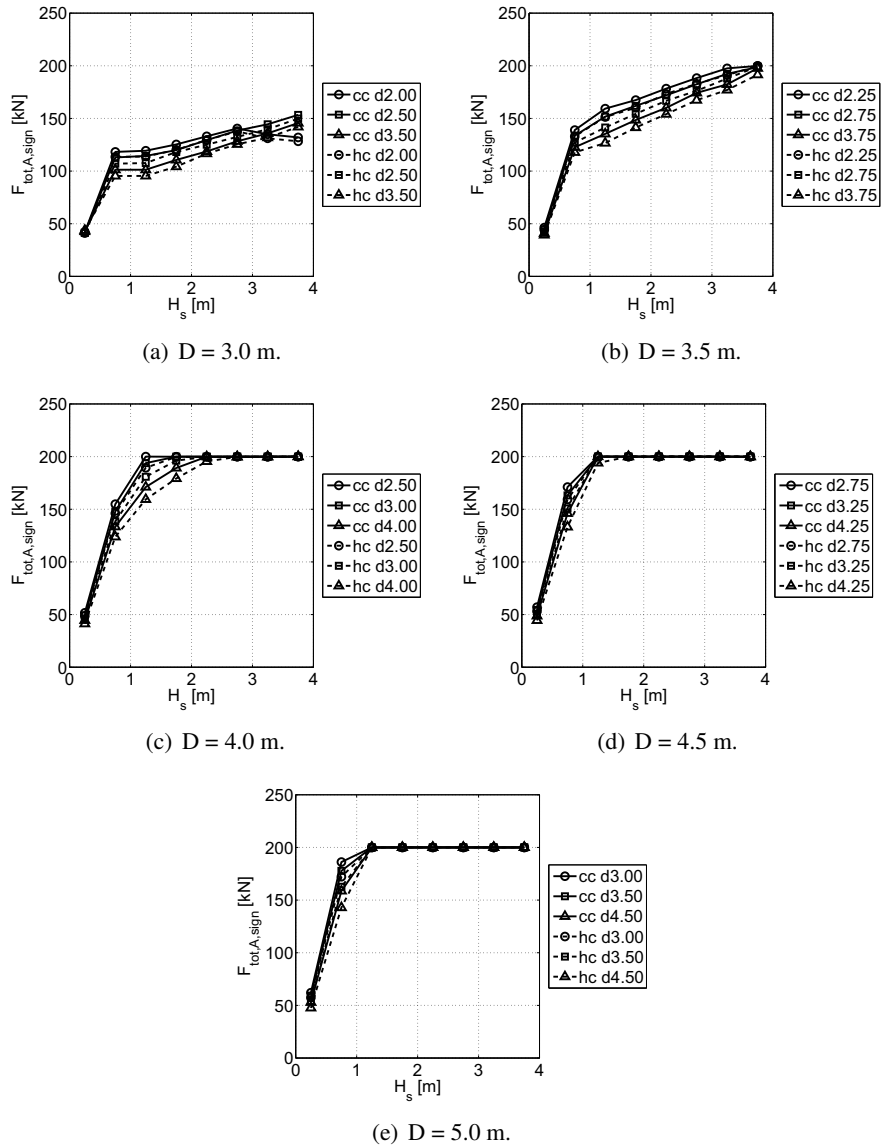


Figure C.21: Significant amplitude of the total control force as a function of the H_s -classes defined in Table 2.1. Constraints: slamming restriction; stroke restriction: $z_{A,sign,max} = 2.00$ m; force restriction: $F_{tot,A,sign,max} = 200$ kN.

APPENDIX D

Prony's method

Prony's method was developed by baron Gaspard Riche de Prony in 1795 and is still used to decompose an impulse response function in a set of complex exponential functions. The algorithm is included here for completeness.

Be $f(t)$ a real function, defined in the interval $[t_0, +\infty] \in \mathbb{R}$ with $\lim_{t \rightarrow +\infty} f(t) = 0$. These conditions are fulfilled for the known impulse response function (IRF). This function $f(t)$ will be approximated by a function $\tilde{f}(t)$ defined in an interval $[t_0, t_f]$, consisting of a sum of complex exponential functions:

$$\tilde{f}(t) = \sum_{i=1}^m \alpha_k e^{\beta_k t} \quad (\text{D.1})$$

If this function is known in n equally spaced points $t_i = t_0 + idt$, dt being the time step, equation (D.1) can be rewritten as, with $c_k = \alpha_k e^{\beta_k t_0}$ and $Q_k = e^{\beta_k dt}$:

$$\begin{bmatrix} Q_1 & \dots & Q_m \\ Q_1^2 & \dots & Q_m^2 \\ \dots & \dots & \dots \\ Q_1^n & \dots & Q_m^n \end{bmatrix} \cdot \begin{bmatrix} c_1 \\ c_2 \\ \vdots \\ c_m \end{bmatrix} = \begin{bmatrix} f(t_1) \\ f(t_2) \\ \vdots \\ f(t_n) \end{bmatrix} \quad (\text{D.2})$$

We define the polynomial R_m of degree m as:

$$R_m = \prod_{k=1}^m (q - Q_k) = \sum_{k=0}^m s_k q^{m-k}, s_0 = 1 \quad (\text{D.3})$$

If we multiply the first $m + 1$ lines of system (D.2) with the coefficients s_m, s_{m-1}, \dots, s_0 and find the sum of the equations, we get:

$$c_1 R_m(Q_1) + \dots + c_m R_m(Q_m) = s_m f(t_0) + \dots + s_0 f(t_m) \quad (\text{D.4})$$

Because Q_k are the roots of R_m , and because s_0 is equal to 1, the equation can be simplified to:

$$s_m f(t_0) + \dots + s_1 f(t_{m-1}) = -f(t_m) \quad (\text{D.5})$$

By repeating this process iteratively, however from another starting point, till a rank n so that $(n + 1) \geq m$ and $t_{m+n} \leq t_f$, we get:

$$\begin{bmatrix} f(t_0) & \dots & f(t_{m-1}) \\ f(t_1) & \dots & f(t_m) \\ \vdots & & \vdots \\ f(t_n) & \dots & f(t_{m+n-1}) \end{bmatrix} \cdot \begin{bmatrix} s_m \\ s_{m-1} \\ \vdots \\ s_1 \end{bmatrix} = - \begin{bmatrix} f(t_m) \\ f(t_{m+1}) \\ \vdots \\ f(t_{m+n}) \end{bmatrix} \quad (\text{D.6})$$

In practice, the number of points in which the function $f(t)$ is validated is quite high, e.g. $n = 3000$. However, the number of exponentials should be much smaller, because, the less exponential functions that are used, the less differential equations need to be solved. Therefore, m will be chosen a lot smaller than n , e.g. $m = 200$ and hence, the $(n + 1) \times m$ system (D.6) is an overdetermined system. The coefficients s_k can be found by applying the Singular Value Decomposition (SVD) algorithm on this system. When these coefficients are found, the polynomial R_m defined in equation (D.3) can be constructed and its roots Q_k can be determined. This allows us to calculate β_k immediately as: $\beta_k = \ln(Q_k)/dt$.

The coefficients c_k can be found by solving the overdetermined system (D.2), resulting in the coefficients α_k : $\alpha_k = c_k e^{-\beta_k t_0}$. It should be verified that the real part of the β values is always negative, since it is essential that also the approximated IRF, $\tilde{f}(t)$, approaches zero for time $\rightarrow +\infty$.

APPENDIX E

Reflection analysis

A reflection analysis has been carried out for the regular and irregular waves generated in the flume. The analysis is performed with the data analysis software tool WaveLab, developed at Aalborg University, Denmark. Wave trains of 360 s are considered for the analysis and the point absorber is removed from the wave flume.

At least three wave gauges need to be installed in the flume. The gauges are placed in front of the model, as shown in Fig. E.1.

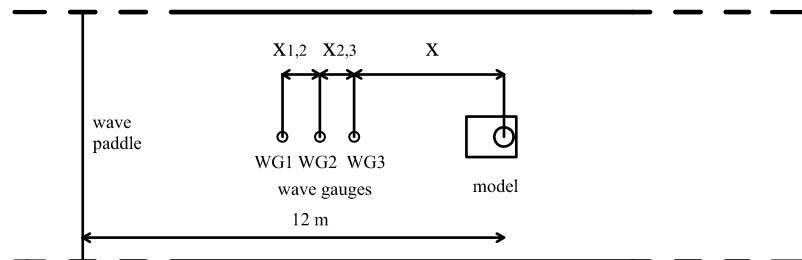


Figure E.1: Position of wave gauges in the flume (top view).

The distance x between the model and the third wave gauge, WG3, is equal to 2.4 m ($x > 0.4 L_n$). The distance between the wave gauges, $x_{1,2}$ and $x_{2,3}$ is based on the recommendations of Mansard and Funke [1]:

$$x_{1,2} = \frac{L_n}{10} \quad (\text{E.1})$$

$$\frac{L_n}{6} < x_{1,3} < \frac{L_n}{3} \quad (\text{E.2})$$

$$x_{1,3} \neq \frac{L_n}{5} \quad \text{and} \quad x_{1,3} \neq \frac{3L_n}{10} \quad (\text{E.3})$$

L_n is the wave length taking into account the water depth at the position of the wave gauges. For irregular waves, the subscript n corresponds with the peak frequency f_p , the low-cut frequency $f_{LC} = 1/3f_p$ and the high-cut frequency $f_{HC} = 3f_p$. Consequently, the lower and upper limits in Eq. E.2 correspond to f_{LC} and f_{HC} , respectively for each wave spectrum. The distance between the wave gauges is determined, taking into account the above mentioned requirements, in particular for the peak frequency for irregular waves. Table E.1 shows the selected interdistances. Reflection coefficients in the range of 9 % to 17% are found and displayed in Table E.2. Kim De Beule [2] performed reflection analyses in the same and other waves and obtained very similar reflection coefficients in the same range (all $C_r < 17\%$).

Table E.1: Distance between wave gauges

$x_{1,2}$ [m]	$x_{2,3}$ [m]	$x_{1,3}$ [m]
0.34	0.30	0.64

Table E.2: Generated waves and reflection coefficients

Regular waves	H [cm]	T [s]	L [m]	C_r [%]
	10.4	1.36	2.9	8.9
	10.2	1.60	3.8	16.6
Irregular waves	H_s [cm]	T_p [s]	L_p [m]	C_r [%]
	6.2	1.59	3.8	14.6

According to Klopman and van der Meer [3] a minimum distance of $0.4 L_n$ between the wave gauges and the intersection of the reflecting structure with SWL is required for applying the multigauge technique. (L_{LC} is the wave length at the toe, based on the corresponding water depth and based on f_{LC}). This requirement is satisfied for all waves.

Bibliography

- [1] Mansard E., Funke E., The measurement of incident and reflected spectra using a least square method. In: 17th Coastal Engineering Conference, Australia, 1980.
- [2] De Beule K., Experimental research on point absorber characteristics aiming at the optimization of energy absorption. Master dissertation. (in Dutch). Ghent University, Belgium, 2008.
- [3] Klopman G., van der Meer J., Random wave measurements in front of a reflective structure. *Journal of Waterway, Port, Coastal and Ocean Engineering* 1999;125(1):39–45.

APPENDIX F

Test matrices

F.1 Decay tests

Table F.1: Test matrix of decay tests on the hemisphere-cylinder.

d [cm]	m_{sup} [kg]
18.9	13.2
18.9	19.2
18.9	31.2
22.1	8.1
22.1	14.1
28.1	6.5
28.1	12.5

F.2 Heave exciting wave forces

Table F.2: Test matrix of heave wave exciting force tests on the cone-cylinder and hemisphere-cylinder.

d [cm]	H [cm]	T [s]
18.9	8.0	1.11
18.9	8.0	1.36
18.9	8.0	1.60
18.9	8.0	1.75
28.4	8.0	1.11
28.4	8.0	1.36
28.4	8.0	1.60
28.4	8.0	1.75

F.3 Power absorption tests

The masses placed on top of the mechanical brake are denoted by m_{br} . The letters ‘nc’ denote that the brake mechanism was ‘not connected’. Hence, in these tests only the friction force damps the buoy motion.

F.3.1 Regular waves

Table F.3: Test matrix of the cone-cylinder in regular waves.

No	d [cm]	H [cm]	Cone - cylinder			
			T [s]	m_{br} [kg]	m_{sup} [kg]	T_n/T [-]
1	18.9	10.2	1.60	0.50	23.9	0.87
2	18.9	10.2	1.60	nc	23.9	0.87
3	18.9	10.2	1.60	1.50	23.9	0.87
4	18.9	10.2	1.60	2.00	23.9	0.87
5	18.9	10.2	1.60	2.50	23.9	0.87
6	18.9	10.2	1.60	1.00	33.9	0.98
7	18.9	10.2	1.60	1.50	33.9	0.98
8	18.9	10.2	1.60	2.00	33.9	0.98
9	18.9	10.2	1.60	2.50	33.9	0.98
10	22.1	10.2	1.60	nc	18.5	0.83
11	22.1	10.2	1.60	0.50	18.5	0.83
12	22.1	10.2	1.60	1.00	18.5	0.83
13	22.1	10.2	1.60	1.50	18.5	0.83
14	22.1	10.2	1.60	2.00	18.5	0.83
15	22.1	10.2	1.60	2.50	18.5	0.83
16	22.1	10.2	1.60	3.00	18.5	0.83
17	22.1	10.2	1.60	0.50	24.5	0.90
18	22.1	10.2	1.60	1.00	24.5	0.90
19	22.1	10.2	1.60	1.50	24.5	0.90
20	22.1	10.2	1.60	2.00	24.5	0.90
21	22.1	10.2	1.60	2.50	24.5	0.90
22	22.1	10.2	1.60	3.00	24.5	0.90
23	22.1	10.2	1.60	0.50	30.5	0.96

No	d [cm]	H [cm]	T [s]	m_{br} [kg]	m_{sup} [kg]	T_n/T [-]
24	22.1	10.2	1.60	1.00	30.5	0.96
25	22.1	10.2	1.60	1.50	30.5	0.96
26	22.1	10.2	1.60	2.00	30.5	0.96
27	22.1	10.2	1.60	2.50	30.5	0.96
28	22.1	10.2	1.60	3.00	30.5	0.96
29	22.1	14.4	1.75	0.50	18.5	0.76
30	22.1	14.4	1.75	1.00	18.5	0.76
31	22.1	14.4	1.75	1.50	18.5	0.76
32	22.1	14.4	1.75	2.00	18.5	0.76
33	22.1	14.4	1.75	2.50	18.5	0.76
34	22.1	14.4	1.75	0.50	23.5	0.81
35	22.1	14.4	1.75	1.00	23.5	0.81
36	22.1	14.4	1.75	1.50	23.5	0.81
37	22.1	14.4	1.75	2.00	23.5	0.81
38	22.1	14.4	1.75	2.50	23.5	0.81
39	22.1	14.4	1.75	2.00	28.5	0.86
40	22.1	14.4	1.75	2.50	28.5	0.86
41	22.1	14.4	1.75	nc	18.5	0.96
42	22.1	14.4	1.75	0.50	18.5	0.96
43	22.1	14.4	1.75	1.00	18.5	0.96
44	22.1	14.4	1.75	1.50	18.5	0.96
45	22.1	14.4	1.75	2.00	18.5	0.96
46	28.4	14.4	1.75	nc	9.5	0.76
47	28.4	14.4	1.75	0.50	9.5	0.76
48	28.4	14.4	1.75	0.75	9.5	0.76
49	28.4	14.4	1.75	1.00	9.5	0.76
50	28.4	14.4	1.75	1.25	9.5	0.76
51	28.4	14.4	1.75	0.50	19.5	0.89
52	28.4	14.4	1.75	0.75	19.5	0.89
53	28.4	14.4	1.75	1.00	19.5	0.89
54	28.4	14.4	1.75	1.25	19.5	0.89

Table F.4: Test matrix of the hemisphere-cylinder in regular waves.

Hemisphere-cylinder						
No	d [cm]	H [cm]	T [s]	m_{br} [kg]	m_{sup} [kg]	T_n/T [-]
55	18.9	10.2	1.60	nc	13.2	0.77
56	18.9	10.2	1.60	0.50	13.2	0.77
57	18.9	10.2	1.60	1.00	13.2	0.77
58	18.9	10.2	1.60	1.50	13.2	0.77
59	18.9	10.2	1.60	0.50	23.2	0.89
60	18.9	10.2	1.60	1.00	23.2	0.89
61	18.9	10.2	1.60	1.50	23.2	0.89
62	18.9	10.2	1.60	2.00	23.2	0.89
63	22.1	10.2	1.60	nc	8.1	0.73
64	22.1	10.2	1.60	0.50	8.1	0.73
65	22.1	10.2	1.60	1.00	8.1	0.73
66	22.1	10.2	1.60	1.50	8.1	0.73
67	22.1	10.2	1.60	2.00	8.1	0.73
68	22.1	10.2	1.60	2.50	8.1	0.73
69	22.1	10.2	1.60	0.50	14.1	0.81
70	22.1	10.2	1.60	1.00	14.1	0.81
71	22.1	10.2	1.60	1.50	14.1	0.81
72	22.1	10.2	1.60	2.00	14.1	0.81
73	22.1	10.2	1.60	2.50	14.1	0.81
74	22.1	10.2	1.60	0.50	20.1	0.88
75	22.1	10.2	1.60	1.00	20.1	0.88
76	22.1	10.2	1.60	1.50	20.1	0.88
77	22.1	10.2	1.60	2.00	20.1	0.88
78	22.1	10.2	1.60	2.50	20.1	0.88
79	22.1	10.2	1.60	0.50	8.1	0.67
80	22.1	10.2	1.60	1.00	8.1	0.67
81	22.1	10.2	1.60	1.50	8.1	0.67
82	22.1	10.2	1.60	2.00	8.1	0.67
83	22.1	10.2	1.60	2.50	8.1	0.67
84	22.1	10.2	1.60	0.50	13.1	0.73

No	d [cm]	H [cm]	T [s]	m_{br} [kg]	m_{sup} [kg]	T_n/T [-]
85	22.1	10.2	1.60	1.00	13.1	0.73
86	22.1	10.2	1.60	1.50	13.1	0.73
87	22.1	10.2	1.60	2.00	13.1	0.73
88	22.1	10.2	1.60	2.50	13.1	0.73
89	22.1	10.2	1.60	0.50	18.1	0.79
90	22.1	10.2	1.60	1.00	18.1	0.79
91	22.1	10.2	1.60	1.50	18.1	0.79
92	22.1	10.2	1.60	2.00	18.1	0.79
93	22.1	10.2	1.60	2.50	18.1	0.79
94	22.1	10.2	1.60	nc	8.1	0.85
95	22.1	10.2	1.60	0.25	8.1	0.85
96	22.1	10.2	1.60	0.50	8.1	0.85
97	22.1	10.2	1.60	1.00	8.1	0.85
98	22.1	10.2	1.60	1.50	8.1	0.85
99	28.4	10.2	1.60	nc	6.5	0.78
100	28.4	10.2	1.60	0.50	6.5	0.78
101	28.4	10.2	1.60	1.00	6.5	0.78
102	28.4	10.2	1.60	1.50	6.5	0.78
103	28.4	10.2	1.60	0.50	16.5	0.90
104	28.4	10.2	1.60	1.00	16.5	0.90
105	28.4	10.2	1.60	1.50	16.5	0.90

F.3.2 Irregular waves

Table F.5: Test matrix of the cone-cylinder in irregular waves.

No	Cone-cylinder					
	d [cm]	H_s [cm]	T_p [s]	m_{br} [kg]	m_{sup} [kg]	T_n/T_p [-]
106	22.1	6.2	1.59	nc	18.5	0.83
107	22.1	6.2	1.59	0.50	18.5	0.83
108	22.1	6.2	1.59	0.75	18.5	0.83
109	22.1	6.2	1.59	1.00	18.5	0.83
110	22.1	6.2	1.59	1.25	18.5	0.83
111	22.1	6.2	1.59	1.50	18.5	0.83
112	22.1	6.2	1.59	0.50	22.5	0.88
113	22.1	6.2	1.59	0.75	22.5	0.88
114	22.1	6.2	1.59	1.00	22.5	0.88
115	22.1	6.2	1.59	1.25	22.5	0.88
116	22.1	6.2	1.59	0.50	26.5	0.92
117	22.1	6.2	1.59	0.75	26.5	0.92
118	22.1	6.2	1.59	1.00	26.5	0.92
119	22.1	6.2	1.59	1.25	26.5	0.92
120	22.1	6.2	1.59	0.50	30.5	0.97
121	22.1	6.2	1.59	0.75	30.5	0.97
122	22.1	6.2	1.59	1.00	30.5	0.97
123	22.1	6.2	1.59	1.25	30.5	0.97
124	18.9	6.2	1.59	0.50	31.9	0.96
125	18.9	6.2	1.59	0.75	31.9	0.96
126	18.9	6.2	1.59	1.00	31.9	0.96
127	18.9	6.2	1.59	1.25	31.9	0.96
128	18.9	9.6	1.83	0.50	23.9	0.76
129	18.9	9.6	1.83	1.00	23.9	0.76
130	18.9	9.6	1.83	1.50	23.9	0.76
131	18.9	9.6	1.83	2.00	23.9	0.76
132	18.9	9.6	1.83	1.00	31.9	0.84
133	18.9	9.6	1.83	1.50	31.9	0.84
134	18.9	9.6	1.83	2.50	31.9	0.84

Table F.6: Test matrix of the hemisphere-cylinder in irregular waves.

Hemisphere-cylinder						
No	d [cm]	H_s [cm]	T_p [s]	m_{br} [kg]	m_{sup} [kg]	T_n/T_p [-]
135	22.1	6.2	1.59	nc	8.1	0.74
136	22.1	6.2	1.59	0.50	8.1	0.74
137	22.1	6.2	1.59	0.75	8.1	0.74
138	22.1	6.2	1.59	1.00	8.1	0.74
139	22.1	6.2	1.59	1.25	8.1	0.74
140	22.1	6.2	1.59	1.50	8.1	0.74
141	22.1	6.2	1.59	0.50	12.1	0.79
142	22.1	6.2	1.59	0.75	12.1	0.79
143	22.1	6.2	1.59	1.00	12.1	0.79
144	22.1	6.2	1.59	1.25	12.1	0.79
145	22.1	6.2	1.59	0.50	16.1	0.84
146	22.1	6.2	1.59	0.75	16.1	0.84
147	22.1	6.2	1.59	1.00	16.1	0.84
148	22.1	6.2	1.59	1.25	16.1	0.84
149	22.1	6.2	1.59	0.50	20.1	0.89
150	22.1	6.2	1.59	0.75	20.1	0.89
151	22.1	6.2	1.59	1.00	20.1	0.89
152	22.1	6.2	1.59	1.25	20.1	0.89
153	22.1	6.2	1.59	1.50	24.1	0.93
154	22.1	6.2	1.59	1.75	24.1	0.93
155	22.1	6.2	1.59	2.00	24.1	0.93
156	18.9	6.2	1.59	0.50	21.2	0.87
157	18.9	6.2	1.59	0.75	21.2	0.87
158	18.9	6.2	1.59	1.00	21.2	0.87
159	18.9	6.2	1.59	1.25	21.2	0.87
160	18.9	6.2	1.59	0.50	13.2	0.68
161	18.9	6.2	1.59	1.00	13.2	0.68
162	18.9	6.2	1.59	1.50	13.2	0.68
163	18.9	6.2	1.59	2.00	13.2	0.68
164	18.9	6.2	1.59	0.50	21.2	0.76

No	d [cm]	H_s [cm]	T_p [s]	m_{br} [kg]	m_{sup} [kg]	T_n/T_p [-]
165	18.9	6.2	1.59	1.00	21.2	0.76
166	18.9	6.2	1.59	1.50	21.2	0.76
167	18.9	6.2	1.59	2.00	21.2	0.76

APPENDIX G

Large scale drop test results

G.1 Overview of performed tests

Tables G.1 and G.2 list the performed drop tests with the buoy with foam and buoy without foam, respectively. The Tables also present the measured peak pressures that are obtained with and without smoothing.

Buoy with foam	Drop height h [m]	Equiv. drop height h^* [m]	Sensor A07			Sensor A08			Comments
			Max with smoothing [bar]	Max without smoothing [bar]	Max without smoothing [bar]	Max with smoothing [bar]	Max without smoothing [bar]		
BMS1mB1	1.35	1.35	0.089	0.090	0.074	0.095	no acc signal, slightly oblique		
BMS1mB2	1.35	1.17	0.119	0.120	0.089	0.089	ok, no acc signal		
BMS1mB3	1.35	1.22	0.079	0.080	0.103	0.103	ok, no acc signal		
BMS1mB4	1.35	1.25	0.088	0.090	0.116	0.116	ok, no acc signal		
BMS1mB5	1.35	-	0.088	0.089	0.039	0.043	high speed camera prob		
BMS1mB6	1.00	1.07	0.072	0.076	0.064	0.065	ok		
BMS2mB1	2.35	2.34	0.071	0.073	0.072	0.089	ok		
BMS3mB1	3.35	3.30	0.195	0.201	0.168	0.183	acc and pressure signal probs		
BMS3mB2	3.35	3.33	0.154	0.160	0.215	0.216	ok		
BMS3mB3	3.35	3.28	0.156	0.157	0.200	0.204	ok		
BMS4mB1	4.35	4.21	0.223	0.229	0.236	0.237	ok		
BMS4mB2	4.35	4.44	0.227	0.233	0.268	0.274	ok, slightly oblique		
BMS4mB3	4.35	-					bad signal, oblique -> test omitted		

Table G.1: Table continues on next page.

Buoy with foam	Drop height h [m]	Equiv. Drop height h^* [m]	Sensor A07			Sensor A08			Comments
			Max with smoothing [bar]	Max without smoothing [bar]	Max with smoothing [bar]	Max without smoothing [bar]	Max with smoothing [bar]	Max without smoothing [bar]	
BMS5mB1	5.35	5.35	0.282	0.392	0.228	0.235		no acc signal	
BMS5mB2	5.35	5.49						oblique -> test omitted	
BMS5mB3	5.35	6.56							
BMS5mB4	5.35	6.03	0.293	0.294	0.503	0.522		ok	
BMS5mB5	5.35	6.10	0.281	0.364	0.518	0.758		ok	
BMS5mB6	5.35	5.67	0.311	0.322	0.419	0.746		ok	
BMS5mB7	5.35	5.79						quite oblique -> test omitted	
BMS5mB8	5.35	-	0.305	0.407	0.626	0.807		ok	
BMS5mB9	5.35	5.94	0.255	0.257	0.636	0.758		ok	
BMS5mB10	5.35	5.62	0.311	0.322	0.637	0.776		ok	
BMS5mB10	5.35	-	-	-	-	-		oblique -> test omitted	

Table G.1: Test results for buoy with foam.

Buoy without foam	Drop height h [m]	Equiv. Drop height h^* [m]	Sensor A07			Sensor A08			Comments
			Max with smoothing [bar]	Max without smoothing [bar]	Max without smoothing [bar]	Max with smoothing [bar]	Max without smoothing [bar]		
BZS1mB1	1.00	1.17	-	-	-	-	-	-	oblique -> test omitted
BZS1mB2	1.00	1.11	0.009	0.015	0.128	0.132	0.128	0.132	ok
BZS1mB3	1.00	1.13	0.054	0.061	0.118	0.126	0.118	0.126	slightly oblique
BZS1mB4	1.00	1.24	0.066	0.069	0.101	0.105	0.101	0.105	ok
BZS2mB1	2.00	2.37	0.070	0.103	0.190	0.194	0.190	0.194	slightly oblique
BZS3mB1	3.00	3.48	0.145	0.149	0.157	0.180	0.157	0.180	ok
BZS3mB2	3.00	3.32	0.151	0.160	0.221	0.228	0.221	0.228	ok
BZS3mB3	3.00	3.50	0.123	0.151	0.238	0.250	0.238	0.250	ok
BZS4mB1	4.00	4.68	-	-	-	-	-	-	data record problem
BZS4mB1bis	4.00	4.57	-	-	-	-	-	-	data record problem
BZS4mB2	4.00	4.82	0.228	0.239	0.309	0.359	0.309	0.359	ok

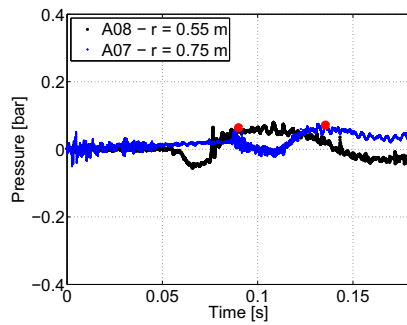
Table G.2: Table continues on next page.

Buoy without foam	Drop height h [m]	Equiv. Drop height h^* [m]	Sensor A07			Sensor A08			Comments
			Max with smoothing [bar]	Max without smoothing [bar]	Max with smoothing [bar]	Max without smoothing [bar]	Max with smoothing [bar]	Max without smoothing [bar]	
BZS5mB1	5.00	-	-	-	-	-	-	-	oblique -> test omitted
BZS5mB2	5.00	5.75	0.210	0.227	0.356	0.399	0.399	0.356	ok
BZS5mB3	5.00	5.81	0.231	0.306	0.425	0.541	0.541	0.425	ok
BZS5mB4	5.00	6.17	0.320	0.418	0.497	0.527	0.527	0.497	ok
BZS5mB5	5.00	5.29	0.222	0.264	0.498	0.567	0.567	0.498	ok
BZS5mB6	5.00	5.51	0.235	0.305	0.331	0.356	0.356	0.331	ok
BZS5mB7	5.00	5.94	-	-	-	-	-	-	oblique -> test omitted
BZS5mB8	5.00	6.06	0.222	0.370	0.420	0.545	0.545	0.420	ok
BZS5mB9	5.00	5.68	0.169	0.342	0.478	0.523	0.523	0.478	ok
BZS5mB10	5.00	-	-	-	-	-	-	-	oblique -> test omitted

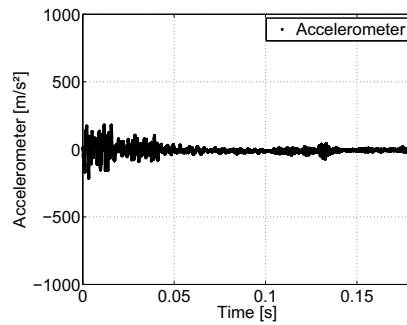
Table G.2: Test results for buoy without foam.

G.2 Drop test measurements

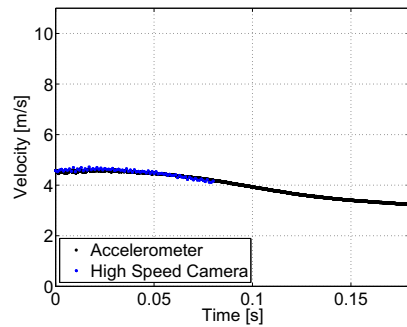
G.2.1 Buoy with foam



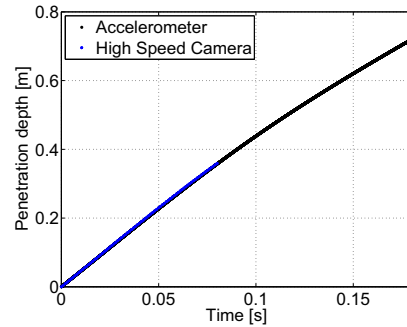
(a) Pressure time history (A08: black - A07: blue).



(b) Acceleration as a function of time.

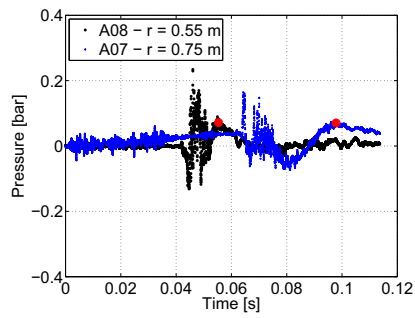


(c) Velocity as a function of time (Accelerometer: black - HSC: blue).

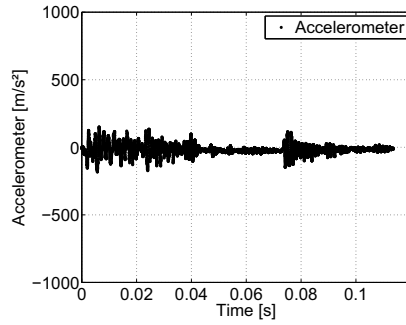


(d) Position as a function of time (Accelerometer: black - HSC: blue).

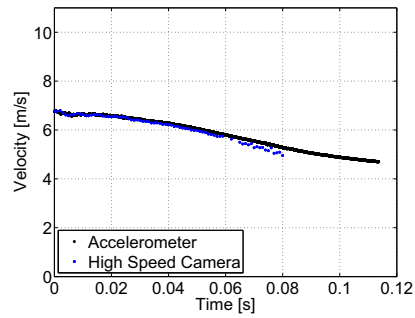
Figure G.1: Measured data on BWF, drop height 1.00 m.



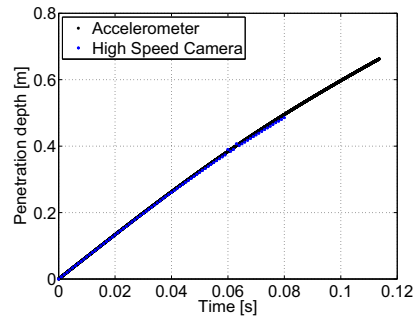
(a) Pressure time history (A08: black - A07: blue).



(b) Acceleration as a function of time.



(c) Velocity as a function of time (Accelerometer: black - HSC: blue).



(d) Position as a function of time (Accelerometer: black - HSC: blue).

Figure G.2: Measured data on BWF, drop height 2.35 m.

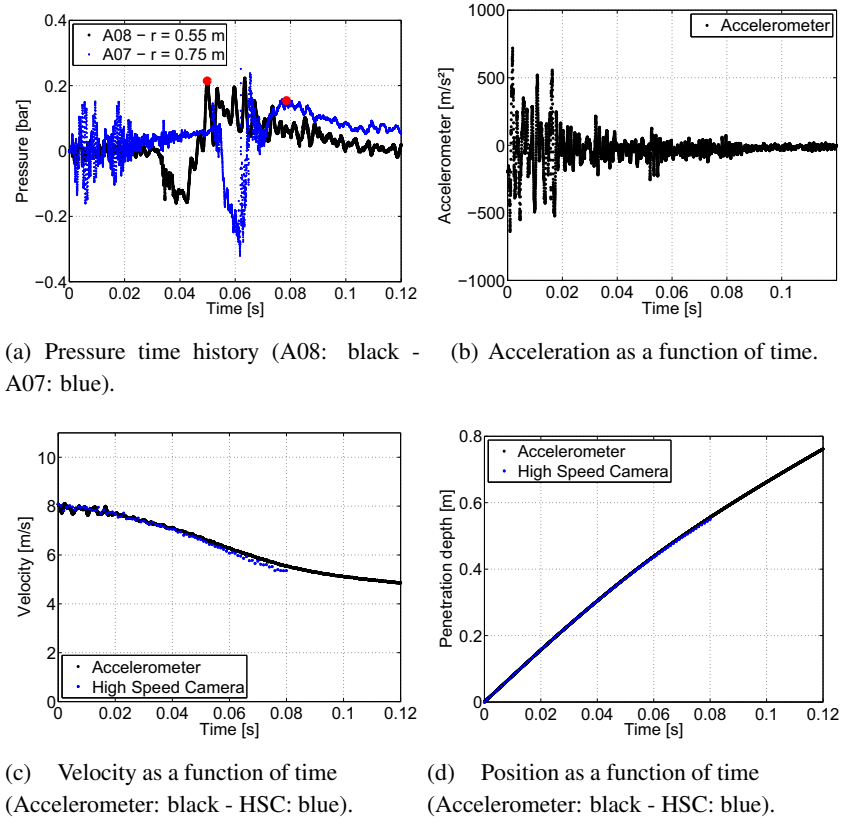
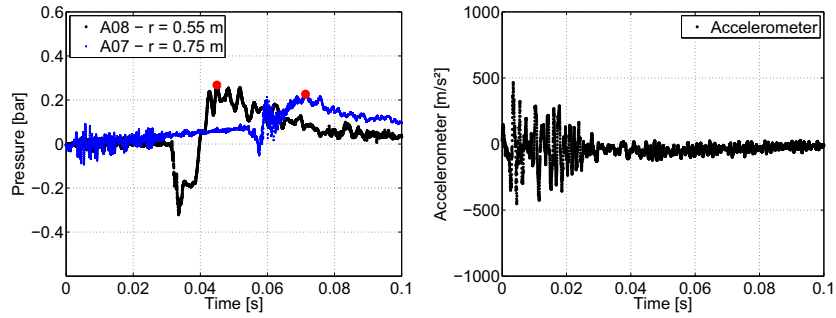
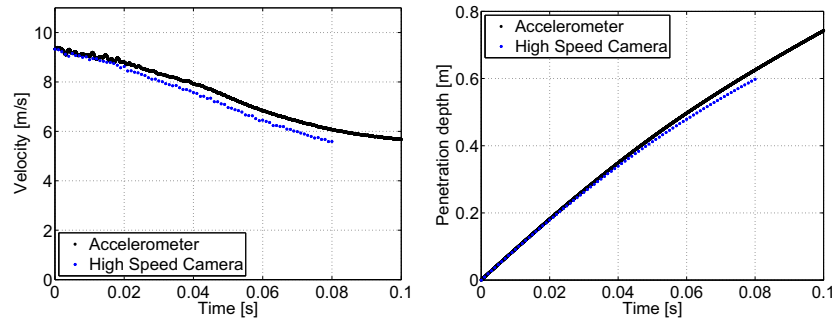


Figure G.3: Measured data on BWF, drop height 3.35 m.



(a) Pressure time history (A08: black - A07: blue).

(b) Acceleration as a function of time.



(c) Velocity as a function of time (Accelerometer: black - HSC: blue).

(d) Position as a function of time (Accelerometer: black - HSC: blue).

Figure G.4: Measured data on BWF, drop height 4.35 m.

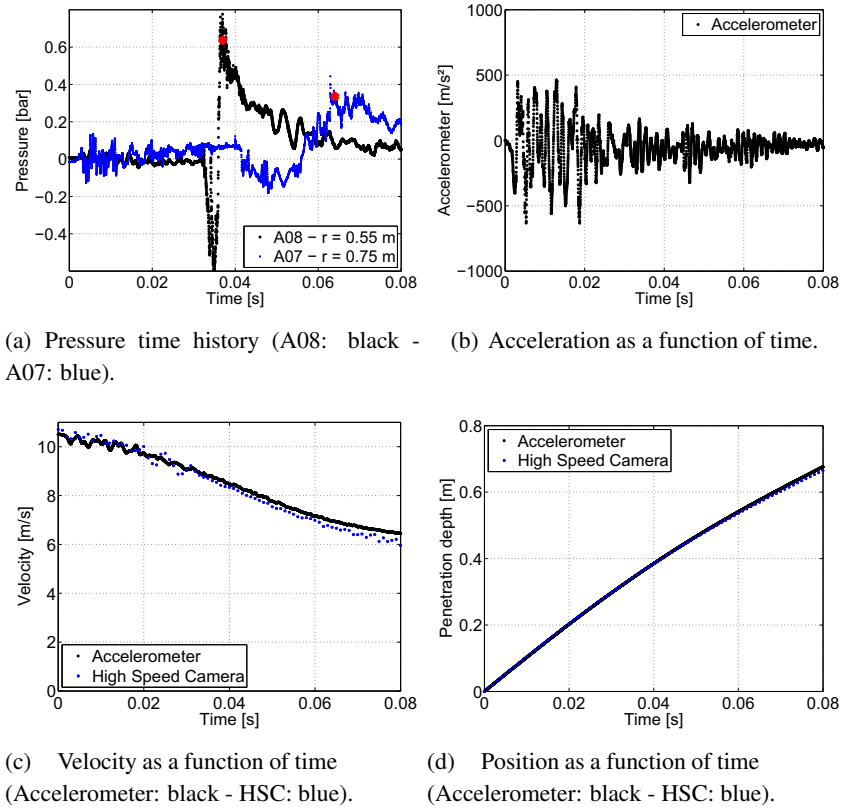
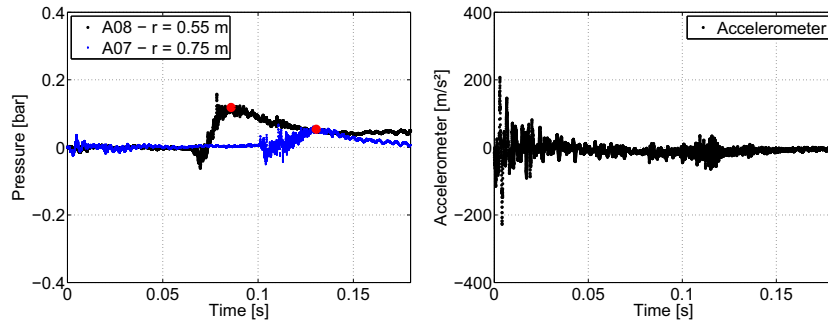
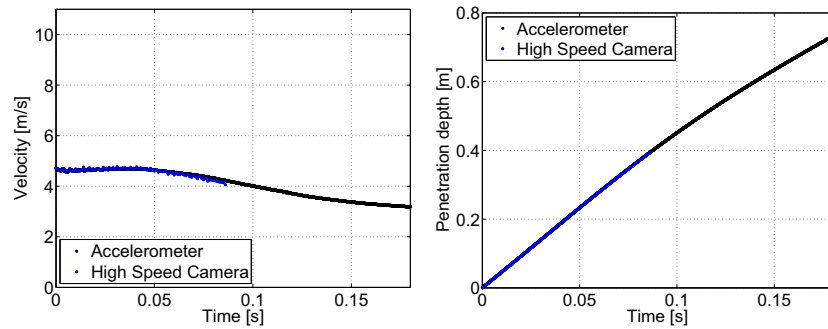


Figure G.5: Measured data on BWF, drop height 5.35 m.

G.2.2 Buoy without foam

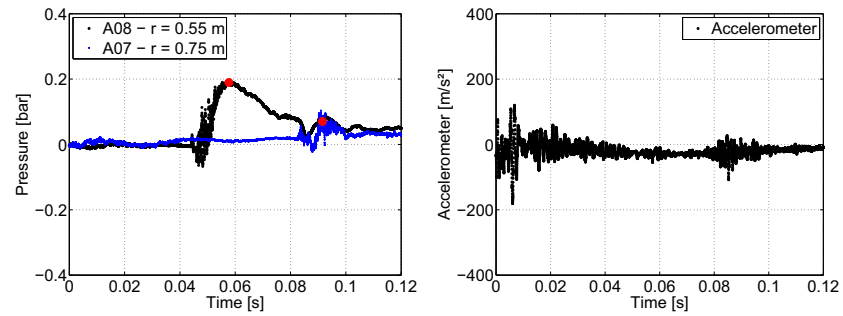


(a) Pressure time history (A08: black - A07: blue). (b) Acceleration as a function of time.

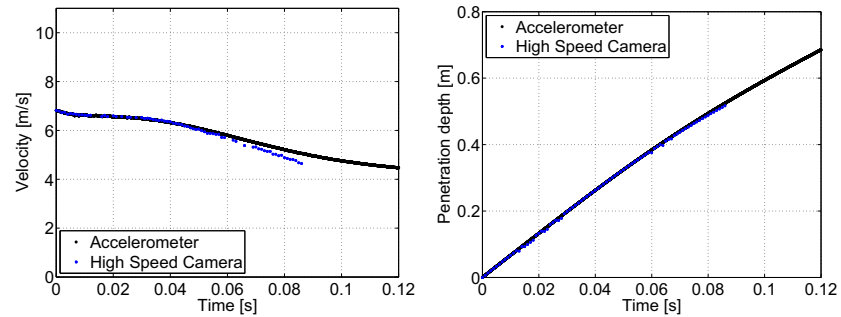


(c) Velocity as a function of time (Accelerometer: black - HSC: blue). (d) Position as a function of time (Accelerometer: black - HSC: blue).

Figure G.6: Measured data on BWO, drop height 1.00 m.

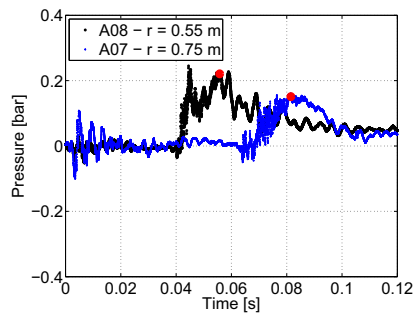


(a) Pressure time history (A08: black - A07: blue). (b) Acceleration as a function of time.

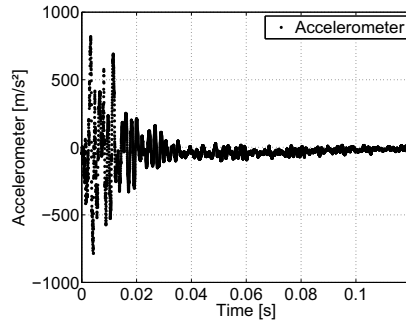


(c) Velocity as a function of time (Accelerometer: black - HSC: blue). (d) Position as a function of time (Accelerometer: black - HSC: blue).

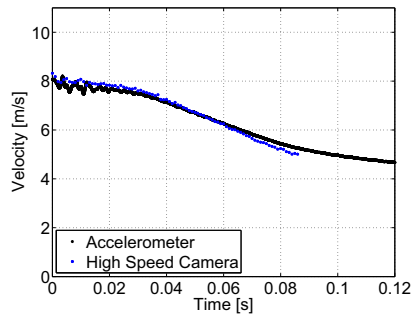
Figure G.7: Measured data on BWO, drop height 2.00 m.



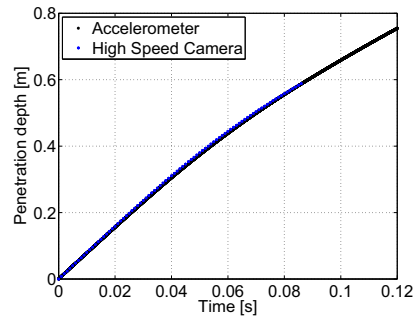
(a) Pressure time history (A08: black - A07: blue).



(b) Acceleration as a function of time.



(c) Velocity as a function of time (Accelerometer: black - HSC: blue).



(d) Position as a function of time (Accelerometer: black - HSC: blue).

Figure G.8: Measured data on BWO, drop height 3.00 m.

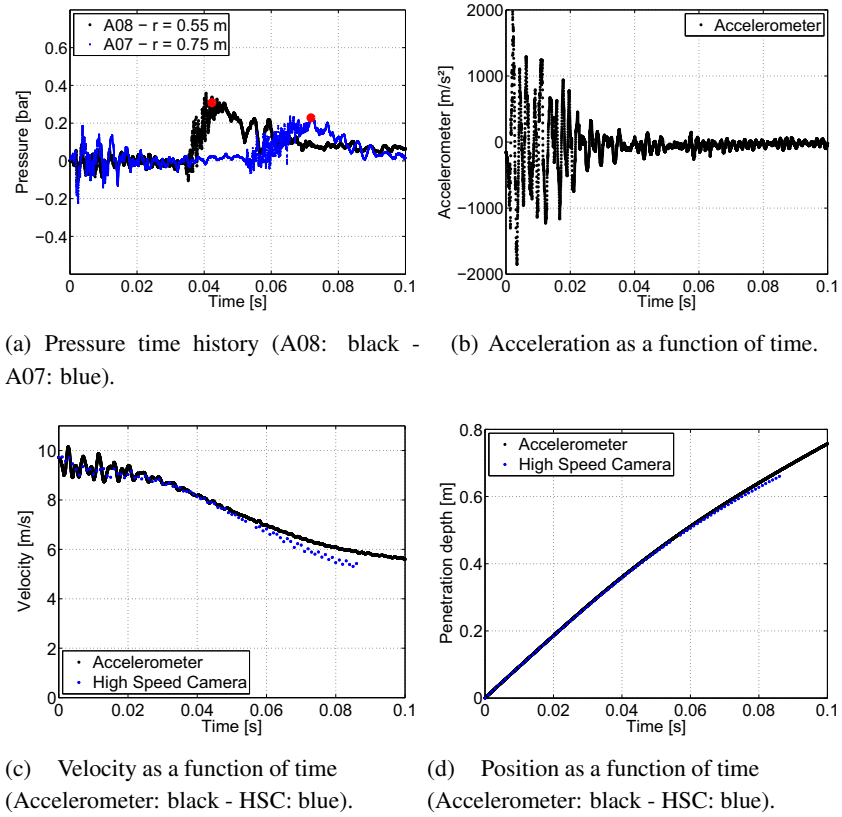


Figure G.9: Measured data on BWO, drop height 4.00 m.

Research funded by a PhD grant of the Institute for the Promotion of Innovation through Science and Technology in Flanders (IWT-Vlaanderen). This research partly fits into the EU project SEEWEC of the 6th Framework Programme. The additional support of the EU is gratefully acknowledged.

